

EUROPEAN ORGANIZATION FOR NUCLEAR RESEARCH

May 17, 2010

## COMPASS-II Proposal

*The COMPASS Collaboration*

# The COMPASS Collaboration

**Ruhr-Universität Bochum, Bochum, Germany**

*F. Gautheron, Ch. Heß, J. Koivuniemi, W. Meyer, G. Reicherz*

**Helmholtz-Institut für Strahlen- und Kernphysik, Universität Bonn, Bonn, Germany**

*J. Bisplinghoff, D. Eversheim, F. Hinterberger, R. Jahn, R. Joosten, T. Negrini*

**Physikalisches Institut, Universität Bonn, Bonn, Germany**

*J. Barth, F. Klein, S. Goertz, R. Panknin, J. Pretz, R. Windmolders*

**Institute of Scientific Instruments in Brno, Brno, Czech Republic**

*A. Srnka*

**Matrivani Institute of Experimental Research & Education, Calcutta, India**

*S. Dasgupta, L. Dhara, S. Sarkara, L. Sinha*

**JINR, Dubna, Russia**

*V. Yu. Alexakhin, G. D. Alexeev, V. A. Anosov, A. Antonov, A. Efremov, O. P. Gavrichtchouk,  
A. Guskov, Yu. Ivanshin, O. Ivanov, Yu. Kisilev, O. Kouznetsov, Z. Kroumchtein,  
G. V. Meshcheryakov, A. Nagaytsev, A. Olshevski, D. V. Peshekhonov, G. Pontecorvo, N. Rossiyskaya,  
M. G. Sapozhnikov, I. A. Savin, O. Yu. Shevchenko, A. N. Sissakian,<sup>1)</sup> G. I. Smirnov, O. V. Teryaev,  
L. G. Tkatchev, N. V. Vlassov, E. Zemlyanichkina*

**Universität Erlangen–Nürnberg, Erlangen, Germany**

*Ch. Adolph, Ch. Braun, W. Eyrich, A. Lehmann, A. Richter*

**Universität Freiburg, Freiburg, Germany**

*H. Fischer, F.-H. Heinsius,<sup>2)</sup> F. Herrmann, T. Guthörl, L. Lauser, K. Königsmann, F. Nerling,  
Ch. Schill, H. Wollny, K. Schmidt, S. Schopferer*

**CERN, Genève, Switzerland**

*G. K. Mallot, W.-D. Nowak,<sup>3)</sup> K. Schönning, M. Schott*

**Technical University of Liberec, Liberec, Czech Republic**

*M. Sulc*

**Laboratory of Instrumentation and Experimental Particles Physics, Lisbon, Portugal**

*P. Bordalo, C. Franco, A. S. Nunes, C. Quintans, S. Ramos, L. Silva, M. Stolarski*

**Universität Mainz, Mainz, Germany**

*J. Bernhard, D. Chaberny, N. du Fresne von Hohenesche, D. von Harrach, P. Jasinski, E. M. Kabuß,  
D.-H. Kang, M. Ostrick, J. Pochodzalla*

**P. N. Lebedev Physical Institute of the Russian Academy of Sciences, Moscow, Russia**

*Yu. Alexandrov, M. Zavertyaev*

**Technische Universität München, Munich, Germany**

*F. Böhmer, S. Dörheim, J. M. Friedrich, S. Gerassimov, S. Grabmüller, B. Grube, F. Haas,  
Ch. Höppner, B. Ketzer, I. Konorov, M. Krämer, A. Mann, T. Nagel, S. Neubert, S. Paul, L. Schmitt,<sup>4)</sup>  
S. Uhl*

---

<sup>1)</sup> deceased

<sup>2)</sup> also at Bochum University, Bochum, Germany

<sup>3)</sup> on leave of absence from DESY, Zeuthen, Germany

<sup>4)</sup> also at GSI, Darmstadt, Germany

**Ludwig Maximilian Universität München, Munich, Germany**

*M. Bettinelli, W. Dünnweber, M. A. Faessler, R. Geyer, J.-F. Rajotte, T. Schläter, I. Uman, A. Zvyagin*

**Charles University in Prague, Prague, Czech Republic**

*M. Finger, M. Finger jr., M. Slunecka*

**Czech Technical University in Prague, Prague, Czech Republic**

*V. Jary, M. Virius*

**IHEP, Protvino, Russia**

*S. V. Donskov, A. Filin, G. V. Khaustov, Yu. Khokhlov, V. Kolosov, V. Konstantinov, A. A. Lednev,  
Yu. V. Mikhailov, V. I. Nikolaenko, V. A. Polyakov, D. Ryabchikov, V. D. Samoylenko*

**CEA-Saclay, IRFU, Gif-sur-Yvette, France**

*Y. Bedfer, E. Burtin, A. Ferrero, N. d'Hose, F. Kunne, A. Magnon, N. Makke, C. Marchand,  
A. Morreale, D. Neyret, S. Platchkov, M. Vandenbroucke*

**Tel Aviv University, Tel Aviv, Israel**

*J. Lichtenstadt, M. A. Moinester*

**INFN, Sezione di Trieste, e Università di Trieste, Trieste, Italy**

*R. Birsa, F. Bradamante, A. Bressan, S. Dalla Torre, V. Duic, C. Elia, M. Giorgi, B. Gobbo,  
S. Levorato, A. Martin, G. Pesaro, E. Rocco, G. Sbrizzai, P. Schiavon, F. Sozzi, S. Tessaro,  
F. Tessarotto*

**INFN, Sezione di Torino, e Università di Torino, Turin, Italy**

*M. G. Alexeev, A. Amoroso, F. Balestra, R. Bertini, M. Chiosso, O. Denisov, R. Garfagnini, I. Gnesi,  
A. Grasso, A. Kotzinian, A. Maggiora, S. Melis,<sup>5)</sup> D. Panzieri,<sup>5)</sup> B. Parsamyan, G. Piragino, S. Sosio,  
S. Takekawa*

**Sołtan Institute for Nuclear Studies and University of Warsaw, Warsaw, Poland**

*B. Badelek, G. Brona, R. Gazda, K. Klimaszewski, K. Kurek, E. Rondio, A. Sandacz, P. Sznajder,  
W. Wislicki*

**Warsaw University of Technology, Warsaw, Poland**

*J. Marzec, M. Dziewiecki, R. Sulej, K. Zaremba, M. Ziembicki*

**Yamagata University, Yamagata, Japan**

*N. Doshita, T. Iwata, S. Ishimoto,<sup>6)</sup> N. Horikawa,<sup>7)</sup> K. Kondo, T. Matsuda,<sup>8)</sup> Y. Miyachi*

---

<sup>5)</sup> also at Università del Piemonte Orientale, Alessandria, Italy

<sup>6)</sup> also at KEK, Tsukuba, Japan

<sup>7)</sup> also at Chubu University, Kasugai City, Japan

<sup>8)</sup> also at University of Miyazaki, Miyazaki, Japan



# Contents

<b>Executive Summary</b>	<b>3</b>
<b>PHYSICS CASE</b>	<b>7</b>
<b>1 Hard exclusive photon and meson production</b>	<b>8</b>
1.1 Generalised parton distributions and hard exclusive reactions . . . . .	8
1.2 Kinematics and observables . . . . .	12
1.2.1 Kinematic domains . . . . .	12
1.2.2 Deeply virtual Compton scattering . . . . .	12
1.2.3 Deeply virtual meson production . . . . .	18
1.3 Simulations and projections . . . . .	19
1.3.1 The $t$ -slope of the DVCS cross section . . . . .	20
1.3.2 Beam charge & spin asymmetry and difference . . . . .	22
1.3.3 The $t$ -slope of the $\rho^0$ cross section . . . . .	25
1.3.4 Transverse target spin asymmetries . . . . .	29
1.4 A first look at exclusive photon production in 2008 . . . . .	30
1.4.1 Overall efficiency and performances to select BH and DVCS events	31
1.4.2 Improved analysis using ECAL timing information . . . . .	34
1.5 A first hint of “pure” DVCS events from the 2009 test run . . . . .	34
<b>2 Measurements of unpolarised PDFs and TMD effects in SIDIS</b>	<b>37</b>
2.1 Strange quark distribution function and quark fragmentation functions . .	37
2.1.1 Strange quark distribution function . . . . .	38
2.1.2 Quark fragmentation functions . . . . .	39
2.1.3 Expected statistical precision . . . . .	40
2.2 Transverse-momentum-dependent effects in SIDIS . . . . .	41
<b>3 Pion-induced Drell–Yan muon pair production</b>	<b>44</b>
3.1 Transverse spin-dependent structure of the nucleon . . . . .	44
3.2 SIDIS contributions to transversity and TMDs . . . . .	45
3.3 Drell–Yan formalism and observables . . . . .	46
3.3.1 Kinematics of the Drell–Yan process . . . . .	46
3.3.2 General expression for the Drell–Yan cross section . . . . .	48
3.3.3 Asymmetries in the LO QCD parton model . . . . .	49
3.3.4 Observables . . . . .	50
3.3.5 Study of the $J/\psi$ production mechanism and $J/\psi$ –DY duality . .	51
3.4 Kinematic domain and spectrometer acceptance . . . . .	52
3.5 Event rate and projected statistical precision . . . . .	55
3.5.1 Expected rate of Drell–Yan events . . . . .	55
3.5.2 Expected statistical precision and theory predictions for asymmetries	58
3.6 Feasibility of Drell–Yan measurements at COMPASS . . . . .	63
3.6.1 Results of 2007–2008 beam tests . . . . .	63
3.6.2 Preliminary results of 2009 beam test . . . . .	65
3.6.3 Background studies . . . . .	68
3.6.4 Systematic errors in the asymmetries . . . . .	69
3.7 Competition and complementarity . . . . .	71

<b>4 Experimental studies of chiral perturbation theory</b>	<b>74</b>
4.1 <i>Pion and kaon polarisability measurement</i>	74
4.2 <i>Primakoff reactions with neutral pions in the final state</i>	80
<b>HARDWARE UPGRADES</b>	<b>83</b>
<b>5 Muon trigger</b>	<b>84</b>
5.1 <i>Trigger hodoscopes</i>	84
5.2 <i>Veto system</i>	86
5.3 <i>Inclusive trigger</i>	87
5.4 <i>Trigger for Drell–Yan measurements</i>	88
<b>6 Target and proton recoil detector for the GPD programme</b>	<b>89</b>
6.1 <i>Liquid hydrogen target</i>	90
6.2 <i>Recoil Proton Detector</i>	91
<b>7 Upgrades of the electromagnetic calorimetry</b>	<b>97</b>
7.1 <i>ECAL1 and ECAL2 upgrades</i>	98
7.2 <i>Large-angle electromagnetic calorimeter ECAL0</i>	99
7.3 <i>Test of the new ECAL0 prototypes</i>	101
<b>8 Radiation Protection issues for Drell–Yan measurements</b>	<b>104</b>
<b>9 Transversely polarised target for Drell–Yan measurements</b>	<b>105</b>
<b>10 Absorber for Drell–Yan measurements</b>	<b>106</b>
10.1 <i>Concept and design</i>	106
10.2 <i>Results from the beam test in 2009</i>	108
<b>11 Pixelised Micromegas detectors</b>	<b>111</b>
<b>12 Upgrade of the RICH-1 gaseous photon detectors</b>	<b>112</b>
<b>13 Cost estimate</b>	<b>116</b>
<b>Acknowledgements</b>	<b>120</b>

## Executive Summary

The research fields of hadron spectroscopy and hadron structure are closely connected since their very beginnings. In 1964, spin-1/2 quarks were conjectured to be the building blocks of baryons and mesons in order to explain their quantum numbers observed in hadron spectroscopy. In 1969, when interpreting data from first direct studies of the structure of the proton, partons were hypothesised as its internal constituents and soon after identified with quarks. In the early 1970's, Quantum Chromodynamics (QCD) became accepted as the theory of strong interactions, explaining the observed weakening of the interquark forces at short distances or large momentum transfers. QCD not only describes hard processes through perturbative expansions, but also the non-perturbative dynamics of the strong interaction, down to soft and extremely soft processes which are involved in meson spectroscopy and linked to chiral perturbation theory.

Parton Distribution Functions (PDFs) describe the structure of the nucleon as a function of the nucleon momentum fraction carried by a parton of a certain species. They are studied primarily in Deeply Inelastic Scattering (DIS) where the longitudinal momentum structure of the nucleon is explored in the collinear approximation, *i.e.* neglecting transverse degrees of freedom. Up to now, PDFs were investigated independently from nucleon electromagnetic form factors that are related to ratios of the observed elastic electron–nucleon scattering cross section to that predicted for a structureless nucleon. The recently developed theoretical framework of Generalised Parton Distributions (GPDs) embodies both form factors and PDFs, such that GPDs can be considered as momentum-dissected form factors which provide information on the transverse localisation of a parton as a function of the fraction it carries of the nucleon's longitudinal momentum. Obtaining such a “3-dimensional picture” of the nucleon is sometimes referred to as “nucleon tomography”. In a complementary approach, the subtle effects of intrinsic transverse parton momenta are described by Transverse-Momentum-Dependent PDFs (TMDs). These effects become visible in hadronic Drell–Yan (DY) and Semi-Inclusive DIS (SIDIS) processes. The structure of hadrons can not yet be calculated in QCD from first principles. However, the deformation of the shape of a hadron in an external electromagnetic field, described by polarisabilities, can be predicted by chiral perturbation theory which is a low-energy expansion of the QCD Lagrangian.

More than 10 years ago, the COMPASS experiment was conceived as “COmmon Muon and Proton apparatus for Structure and Spectroscopy”, capable of addressing a large variety of open problems in both hadron structure and spectroscopy. As such, it can be considered as a “QCD experiment”. By now, an impressive list of results has been published concerning nucleon structure, while the physics harvest of the recent two years of hadron spectroscopy data taking is just in its beginnings. The COMPASS apparatus has been proven to be very versatile, so that it offers the unique chance to address in the future another large variety of newly opened QCD-related challenges in both nucleon structure and hadron spectroscopy, at very moderate upgrade costs. It consists of a high-precision forward spectrometer and either an unpolarised, longitudinally or transversely polarised target. It is located at the unique CERN SPS M2 beam line that delivers hadron or naturally polarised  $\mu^\pm$  beams in the energy range between 50 GeV and 280 GeV.

This proposal lays the ground for a new decade of fascinating QCD-related studies of nucleon structure and in hadron spectroscopy. It details the physics scope and related hardware upgrades for those topics for which data taking can be envisaged to start in 2012. This implies mainly studies of chiral perturbation theory, “unpolarised” generalised parton distributions, and transverse-momentum-dependent parton distributions.

More distant projects, as the whole complex of future QCD studies using hadron spectroscopy and also studies of “polarised” GPDs, will be described later in an addendum to this proposal. All these studies will significantly expand our knowledge on key aspects of hadron structure and spectroscopy which are inaccessible to any other facility existing or under construction.

The concept of GPDs attracted much attention after it was shown that the total angular momentum of a given parton species,  $J^f$  for quarks ( $f = u, d$  or  $s$ ) or  $J^g$  for gluons, is related to the second moment of the sum of the two GPDs  $H$  and  $E$ . As of today, it is by far not fully understood how the nucleon spin  $\frac{1}{2}$  is shared between the contributions of intrinsic and orbital angular momenta of quarks of various flavors and gluons. Constraining quark GPDs experimentally by measuring exclusive Deeply Virtual Compton Scattering (DVCS),  $\mu p \rightarrow \mu \gamma p$ , or Deeply Virtual Meson ( $M$ ) Production (DVMP),  $\mu p \rightarrow \mu M p$ , is the only known way to constrain the quark components of the nucleon’s spin budget  $\frac{1}{2} = \sum_{f=u,d,s} J^f + J^g$ . Such data will also be very important to experimentally validate GPD moments calculated from first principles through QCD calculations on the lattice. In order to ensure exclusivity of DVCS and DVMP events, a new recoil detector will surround a 2.5 m long liquid hydrogen target. The kinematic domain accessible with 160 GeV muon beams cannot be explored by any other facility in the near future. The DVCS cross section will be determined as a function of both the momentum transfer between initial and final nucleons and the fraction of the longitudinal nucleon momentum carried by the struck parton. A new electromagnetic calorimeter (ECAL0) will provide coverage of substantially higher values of this fraction as compared to the existing calorimeters ECAL1 and ECAL2. One key result will be the first, model-independent answer on the question how the transverse nucleon size varies gradually from the gluon/sea-quark region to that dominated by valence quarks. Only COMPASS can explore the kinematic region between the H1/ZEUS collider range and the HERMES/JLAB fixed-target range, so that particularly important results can be expected from 3-dimensional nucleon “tomography” within this kinematic domain. The transverse structure of the nucleon in the COMPASS kinematic range is considered to be important input for background simulations in proton-proton collisions at LHC. The second key result is information on the GPD  $H$ , obtained by separating the real and imaginary parts of the DVCS amplitude. This will be accomplished by combining data from positive and negative muon beams. The azimuthal dependence of the cross section will be used to isolate the contribution of the GPD  $H$ , which is of particular importance for the evaluation of the spin sum rule. The measurements with the liquid hydrogen target will mainly constrain  $H$ . An extension of the programme is envisaged using a transversely polarised target, mainly to constrain  $E$ . This will be subject of an addendum to this proposal. After completion of data taking, the combined DVCS and DVMP data set of H1, ZEUS, COMPASS, HERMES and JLAB will constrain the nucleon-helicity-conserving  $u$  and  $d$  quark GPDs over a wide kinematic range in parton longitudinal momentum versus parton transverse localisation, and virtual-photon resolution scale. It is expected that ongoing activities towards global fits of GPDs will lead to a reliable determination of total and also orbital quark angular momenta.

Simultaneously with the GPD programme, high-statistics data will be recorded on unpolarised semi-inclusive deep inelastic scattering,  $\mu p \rightarrow \mu h X$ . The pion and kaon multiplicities will be used to extract at leading order  $\alpha_s$  (LO) the unpolarised strange quark distribution function  $s(x)$  as well as fragmentation functions describing how a quark fragments into a hadron. Presently, the poor knowledge of these quantities is the limiting

factor in the determination of the polarisation of strange quarks from SIDIS data. These multiplicities will also represent important input to future global analyses beyond LO.

The transverse momentum of partons is a central element in understanding the 3-dimensional structure of the nucleon. From the measured azimuthal asymmetries of hadrons produced in unpolarised SIDIS and DY processes a sizable transverse momentum was derived. When this intrinsic transverse momentum is taken into account, several new functions are required to describe the structure of the nucleon. Transverse spin, in fact, couples naturally to intrinsic transverse momentum, and the resulting correlations are encoded in various transverse-momentum-dependent parton distribution and fragmentation functions. The SIDIS cross section contains convolutions of these two types of functions, while the convolutions in the DY cross section comprise only PDFs and/or TMDs. In spite of the widespread interest in this approach which goes beyond collinear QCD, the field is still in its infancy and only data can sort out which correlations are appreciably different from zero and relevant. Of particular interest are the correlations between quark transverse momentum and nucleon transverse spin, and between quark transverse spin and its transverse momentum in an unpolarised nucleon, which are encoded in the so-called Sivers and Boer–Mulders functions, both (naively)  $T$ -odd. The Boer–Mulders function contributes to the azimuthal modulations in the cross sections of unpolarised SIDIS and DY processes which have been observed since many years. We intend to accurately measure such modulations both in DY and in SIDIS (this last measurement in parallel to the GPD programme). Much attention in the recent years has been devoted to the Sivers function originally proposed to explain the large single-spin asymmetries observed in hadron–hadron scattering. From  $T$ -invariance arguments, for a long time it was believed to be zero. One of the main theoretical achievements of the recent years was the discovery that the Wilson-line structure of parton distributions, which is necessary to enforce gauge invariance of QCD, implies a sign difference between the  $T$ -odd distributions measured in SIDIS and the same distributions measured in DY. According to this “restricted universality”, the Sivers function can be different from zero but must have opposite sign in SIDIS and DY. There is a keen interest in the community to test this prediction which is rooted in fundamental aspects of QCD, and many laboratories are planning experiments just to test it. The Sivers function was recently measured by HERMES and COMPASS in SIDIS off transversely polarised targets and shown to be different from zero and measurable. In order to test its sign change, DY experiments with transversely polarised hadrons are required, but none were performed so far. The main goal of our DY programme is to measure for the first time on a transversely polarised target the process  $\pi^- p^\uparrow \rightarrow \mu^+ \mu^- X$ . This will be a unique measurement as at COMPASS energies the virtual photon originates mainly from the fusion of a  $\bar{u}$  quark from the pion and a  $u$  quark from the nucleon, both in valence-like kinematics. In two years of data taking with the 190 GeV  $\pi^-$  beam and the COMPASS spectrometer with the  $\text{NH}_3$  transversely polarised target, the fundamental prediction for the sign of the  $u$  quark Sivers function can be tested for the first time.

Measurements of exclusive final states produced by incoming high-energy pions at very small momentum transfer to the recoiling nucleus, explore the Primakoff region where the cross section is dominated by the exchange of a quasi-real photon. The initial  $\pi^- \gamma^*$  system may scatter into  $\pi^- \gamma$  (Compton reaction),  $\pi^- \pi^0$ ,  $\pi^- \pi^0 \pi^0$ ,  $\pi^- \pi^+ \pi^-$ , or final states containing more pions. In QCD, chiral Perturbation Theory (ChPT) predicts the low-energy behaviour for all these reactions at small intermediate-state masses  $m_{\pi\gamma}^2$ , from threshold to a few pion masses. The chiral expansion of the cross section contains

several low-energy constants which describe important physical properties of the pion. For the Compton reaction, the ChPT calculations result in deviations from the QED bremsstrahlung cross section that is exactly calculable for a point-like particle. The first term in the expansion in  $m_{\pi\gamma}$  originates from the electric and magnetic dipole polarisabilities of the charged pion,  $\alpha_\pi$  and  $\beta_\pi$ , and is proportional to their difference  $\alpha_\pi - \beta_\pi$ . In order to resolve these two polarisabilities independently, *i.e.* to also determine  $\alpha_\pi + \beta_\pi$ , it is necessary to measure the cross section differential in the centre-of-momentum scattering angle  $\theta_{cm}$ , in which the two contributions have a complementary functional dependence. At that level of precision, it is possible (and necessary) to also account for the most relevant combination of the pion quadrupole polarisabilities,  $\alpha_2 - \beta_2$ . Its effect has a similar  $\theta_{cm}$  dependence as that of  $\alpha_\pi - \beta_\pi$  but is proportional to  $m_{\pi\gamma}^4$  instead of  $m_{\pi\gamma}^2$ . The planned measurements will also allow for the determination of the two combinations  $\alpha_\pi + \beta_\pi$  and  $\alpha_2 - \beta_2$ , for the first time. The neutral (electromagnetic) trigger permits at the same time the precise measurement of final states containing one or more  $\pi^0$ . The threshold behaviour of  $\pi^-\pi^0$  determines the chiral anomaly constant  $F_{3\pi}$ , for which the new data set will allow a new level of experimental precision beyond that of the theoretical prediction of about 1%.

The physics programme described in this proposal covers a period of five years, one year for the tests of chiral perturbation theory and two years each for the GPD and DY programmes. The tentative schedule for the first three years is as follows:

- 2012: Tests of chiral perturbation theory,
- 2013: GPD programme,
- 2014: Drell–Yan programme.

On the basis of the results from the 2008 and 2009 hadron runs, an addendum to this proposal aiming at further hadron spectroscopy measurements will be submitted in due time. The schedule of these measurements will be considered together with that of the remaining parts of the proposed GPD and DY programmes, possibly taking into account extensions of the latter as sketched in the proposal.

## – PHYSICS CASE –

# 1 Hard exclusive photon and meson production

## 1.1 Generalised parton distributions and hard exclusive reactions

Generalised Parton Distributions [1–5] provide a novel and comprehensive description of the nucleon’s partonic structure and contain a wealth of new information. In particular, they embody both nucleon electromagnetic form factors, *i.e.* ratios of the observed elastic electron scattering to that predicted for a point-like nucleon, and Parton Distribution Functions (PDFs) measured in DIS, *i.e.* parton number and helicity densities. Very importantly, GPDs provide a novel description of the nucleon as an extended object, referred sometimes to as 3-dimensional “nucleon tomography” [6–8], which correlates (transverse) spatial and (longitudinal) momentum degrees of freedom of quarks and gluons. Moreover, the evaluation of GPDs may for the first time provide an insight into orbital momenta of quarks and gluons, another fundamental property of the nucleon [2, 3].

GPDs, just like ordinary PDFs, describe the structure of the nucleon independently of the specific reaction by which the nucleon is probed, *i.e.* they are expected to be universal quantities. The mapping of nucleon GPDs, which very recently became one of the key objectives of high-energy nuclear physics, requires a comprehensive programme of measuring various hard exclusive processes in a broad kinematic range, in particular Deeply Virtual Compton Scattering (DVCS). In addition, Deeply Virtual Meson Production (DVMP) is expected to add independent and complementary information.

The kinematic variables on which GPDs depend can be illustrated using the “handbag” diagram shown in Fig. 1 which describes the DVCS process at leading twist in the Bjorken limit ( $Q^2 \rightarrow \infty$  for fixed  $x_B$  and  $t$ , *i.e.*  $|t|/Q^2$  small). GPDs depend on the photon

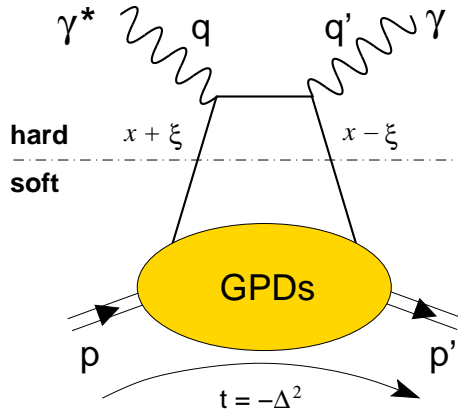


Figure 1: Handbag diagram for the DVCS process at leading twist.

virtuality  $Q^2 = -q^2$ , the total four-momentum squared  $t = (p-p')^2 = (q-q')^2$  transferred between initial and final nucleon states, and on  $x$  and  $\xi$ . The latter two variables represent respectively average and half the difference between the initial and final longitudinal momentum fractions of the nucleon, carried by the parton throughout the process. While in Deeply Inelastic Scattering (DIS), the momentum fraction  $x$  carried by the struck parton is identified with the Bjorken variable  $x_B = \frac{Q^2}{2p \cdot q}$ , in the hard exclusive DVCS and DVMP processes  $x$  is an internal variable that is integrated over in a convolution of the given GPD with a kernel describing the hard virtual-photon quark interaction (see, *e.g.* Eq. (12)). As such,  $x$  must not be identified with  $x_B$ , which in these kinematics is related to the skewness as  $\xi \simeq x_B/(2-x_B)$  in the Bjorken limit. Hence the skewness coverage

of a given lepton production measurement is approximately given by the range it covers in  $x_B$ .

Based on the factorisation theorem [9], the short-distance information specific to the virtual-photon quark interaction can be separated from the long-distance information about nucleon structure contained in the GPDs. In the handbag approximation of DVCS, GPDs can be understood as describing the quantum mechanical amplitude for “kicking out” a parton of the fast moving nucleon by the virtual photon and “putting it back” with a different momentum after it has radiated the real photon.

The DVCS final state is identical to that of the competing Bethe–Heitler (BH) (bremsstrahlung) process and hence both processes interfere on the level of amplitudes. The resulting interference term permits access to certain linear combinations of GPDs, which makes hard exclusive single-photon lepton production a powerful tool to study GPDs. Complementarily, DVMP will allow independent access to different bilinear combinations of GPDs.

The GPDs  $H^f$  and  $\tilde{H}^f$  ( $f = u, d, s, g$ ), which describe the case of nucleon-helicity conservation in the scattering process, include as limiting cases the well-measured parton density and helicity distributions  $q^f$  and  $\Delta q^f$ , respectively. The case of nucleon-helicity flip is described by the GPDs  $E^f$  and  $\tilde{E}^f$ , for which there are no such limiting cases. Gluon GPDs enter in DVCS only beyond leading order in  $\alpha_s$  (LO), analogous to DIS.

GPDs attracted much attention after it was shown that the total angular momentum of a given parton species  $f$  is related to the 2<sup>nd</sup> moment of the sum of the two GPDs  $H^f$  and  $E^f$  via the Ji relation [2]

$$J^f(Q^2) = \frac{1}{2} \lim_{t \rightarrow 0} \int_{-1}^1 dx \ x \ [H^f(x, \xi, t, Q^2) + E^f(x, \xi, t, Q^2)], \quad (1)$$

which holds for any value of  $\xi$ . This finding in 1997 was one of two major reasons that strongly boosted experimental and theoretical activities towards determinations of GPDs as it opened the way to constrain the contributions  $J^q$  from total quark angular momenta to the nucleon’s spin budget

$$\frac{1}{2} = \sum_{q=u,d,s} J^q(Q^2) + J^g(Q^2), \quad (2)$$

where  $J^g$  is the total gluon contribution to the nucleon spin. The Ji relation Eq. (1) is the only known—though not straightforward—way to constrain the quark total angular momentum contributions to the nucleon spin budget. Progress in its evaluation, on the one hand, will have to rely on global analyses of experimental data for various exclusive processes in the broadest possible kinematic range. Here, sufficient knowledge about the kinematic dependencies of GPDs in the full kinematic range is essential as *e.g.* unknown nodes in an unmeasured region would render reliable GPD fits impossible. On the other hand, QCD simulations on an Euclidean lattice have been used to determine the second moments of the GPDs  $H$  and  $E$  that enter the Ji relation. Using chiral perturbation theory to extrapolate to the physical pion mass, the results for  $u$  and  $d$  quarks are  $J^u = 0.236 \pm 0.006$  and  $J^d = 0.002 \pm 0.004$ . The uncertainties are only statistical, as some of the systematic uncertainties are very hard to quantify [10–12]. No practical way is known to evaluate the Ji relation for partons other than  $u$  and  $d$  quarks.

A particularly simple physical interpretation for GPDs as probability density exists in the limiting case  $\xi = 0$  where the parton carries the same longitudinal momentum fraction  $x$  in initial and final state and hence the momentum transfer  $t \equiv -\Delta^2 = -\Delta_L^2 - \Delta_\perp^2$

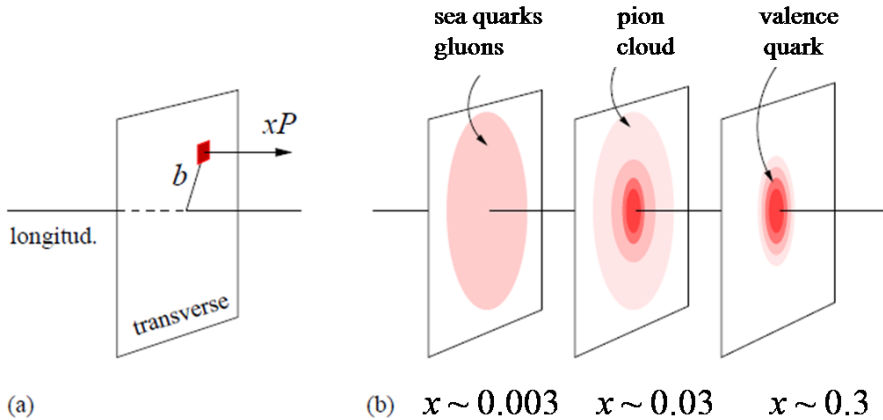


Figure 2: Nucleon tomography: (a) The Fourier transform of the  $-\Delta_\perp^2$  dependence of the GPD  $H^f(x, 0, -\Delta_\perp^2)$  for fixed  $x$  describes the distribution of the transverse distance  $b \equiv |\mathbf{b}_\perp|$  of partons carrying the fraction  $x$  of the nucleon's longitudinal momentum  $P$ , from the centre of momentum of the nucleon. (b) Sketch of tomographic views of the transverse spatial parton distribution in the nucleon at certain parton longitudinal momentum fractions  $x$ . Figure adapted from Ref. [13].

is purely transverse,  $t = -\Delta_\perp^2$ . In this case, in analogy to the case of form factors, the Fourier transform of the  $-\Delta_\perp^2$  dependence of the GPD  $H^f(x, 0, -\Delta_\perp^2)$  for fixed  $x$  describes the spatial distribution of partons of species  $f$  carrying the longitudinal momentum fraction  $x$ , with respect to their transverse distance  $\mathbf{b}_\perp$  from the centre of momentum of the nucleon (impact-parameter representation) [7]

$$q^f(x, \mathbf{b}_\perp) = \int \frac{d^2 \Delta_\perp}{(2\pi)^2} e^{-i \Delta_\perp \cdot \mathbf{b}_\perp} H^f(x, 0, -\Delta_\perp^2). \quad (3)$$

The “three-dimensional” impact-parameter-dependent parton distribution  $q^f(x, \mathbf{b}_\perp)$  can be interpreted as providing a set of “tomographic images” of the nucleon, as illustrated by the cartoon shown in Fig. 2. Nucleon tomography continues attracting great attention, more than 300 publications on both experimental and theoretical aspects have appeared over the last 10 years.

In the study of the transverse structure of the nucleon, there are two quantities of particular importance. The first one is the GPD at  $\xi = 0$  which does have a probabilistic interpretation. It is related via Fourier transform to the distribution in the impact-parameter  $b \equiv |\mathbf{b}_\perp|$ , which represents the transverse distance between struck quark and centre of momentum of the whole nucleon [7]. Lattice calculations can determine the expectation value of  $b$ , averaged over  $x$  with different weights  $x^n$  [14]. The transverse distance between the struck parton and the centre of momentum of the spectator system is given by  $r_\perp = b/(1-x)$  and provides an estimate of the overall transverse size of the nucleon. One expects that its expectation value remains finite due to confinement, which implies that the expectation value of  $b$  must tend to zero for  $x \rightarrow 1$ .

The second important quantity is the GPD at  $x = \xi$ . It has no probabilistic interpretation but nevertheless its Fourier transform is connected to the distance  $r_\perp$  between struck parton and spectator system [15, 16]. At leading order in  $\alpha_s$  (LO), the corresponding average  $\langle r_\perp^2(x) \rangle$  can be directly obtained from the imaginary part of amplitudes of exclusive processes. At small  $x_B$ , where amplitudes are predominantly imaginary, one

has the relation  $\langle r_\perp^2(x_B) \rangle \approx 2 \cdot B(x_B)$  if the exclusive cross section is parametrised as  $\frac{d\sigma}{dt} \propto \exp(-B(x_B)|t|)$ .

Results on the transverse size of the nucleon derived from measurements of the experimental electromagnetic form factor correspond to an average over the longitudinal momentum fractions  $x$  carried by the struck parton. The measured transverse r.m.s. charge radius of the nucleon is about 0.7 fm. The present understanding of the  $x$  dependence of the “partonic” transverse size of the nucleon is sketched in Fig. 2. At very large  $x$ , for  $x \rightarrow 1$ , the width of the distribution  $q^f(x, \mathbf{b}_\perp)$  in  $b \equiv |\mathbf{b}_\perp|$  is expected to vanish since the active parton becomes the centre of momentum of the entire nucleon. In the valence quark region, denoted by  $x \sim 0.3$  in Fig. 2, we expect to mainly “see” the core of valence quarks. Lattice calculations find average values of  $\langle b(x) \rangle$  decreasing from about 0.5 fm to about 0.25 fm for typical values of the longitudinal momentum fraction  $x$  ranging from about 0.2 to about 0.4 [10, 12, 17]. The low- $x$  range, denoted by “ $x \sim 0.003$ ” in Fig. 2, is dominated by sea quarks and gluons. This domain has been investigated by the HERA collider experiments ( $x_B = 10^{-2} \dots 10^{-3}$ ). An average transverse proton radius  $\langle r_\perp(x_B) \rangle$  of  $0.65 \pm 0.02$  fm was determined [18] from the  $t$ -slope  $B(x_B)$  of the DVCS cross section. Although this is a different quantity than the average  $b$  value determined on the lattice, an increase of about 20–30% in transverse nucleon size compared to the valence region is expected in a chiral-dynamics approach that is applicable for  $x \ll M_\pi/M_p \approx 0.15$ , with  $M_\pi$  ( $M_p$ ) the pion (proton) mass [19, 20]. This model predicts a corresponding increase in the transverse size of the nucleon due to the “pion cloud” which is expected to enhance the gluon density with decreasing  $x$ . The variation in transverse nucleon size vs.  $x$  was also investigated using model-dependent GPD fits based on most recent HERA DVCS measurements, confirming its growth with decreasing  $x$  [21]. However, absolute numbers from these fits still vary in the range 20–30% due to model uncertainties. We emphasise that there exists no direct measurement of  $\langle r_\perp(x_B) \rangle$  in the  $x_B$  range above  $10^{-2}$ .

The transverse distribution of partons with  $x > 0.01$  also plays an important role in the theory and phenomenology of high-energy  $p p / \bar{p} \bar{p}$  collisions with hard processes at the Tevatron and LHC. Because events with hard processes require binary parton–parton collisions, their centrality dependence and underlying event structure are generally very different from those of minimum-bias events [22]. Knowing the transverse distribution of the partons in the colliding protons from independent measurements through exclusive  $e p / \mu p$  scattering, one can calculate the centrality dependence and model the spectator interactions in much more detail. This is particularly important for estimating the rate of multijet production in  $p p$  collisions at LHC, which is expected to be high and represents an important background in  $p p$  events with new physics processes. Precise information about the transverse distribution of quarks and gluons with  $x > 0.01$  will be highly valuable for developing next-generation Monte Carlo generators for multijet events (for a recent summary see Ref. [23]), and for revealing dynamical multiparton correlations which enhance multiple hard processes beyond their geometric probability [24, 25]. The transverse distribution of partons also determines the rapidity gap survival probability [26] in central exclusive diffraction  $p p \rightarrow p + (\text{gap}) + H + (\text{gap}) + p$ , which is being considered as a clean channel for Higgs boson production at the LHC [27] (for a recent summary see Ref. [28]). The parton momentum fraction probed in production of a Standard Model Higgs boson of  $M_H \sim 10^2$  GeV at the LHC at central rapidity are  $x_{1,2} \sim M_H/\sqrt{s} \sim 10^{-2}$ , which is exactly the region where their transverse distribution will be measured in exclusive processes at COMPASS.

The transverse spatial distribution of partons measured in exclusive  $ep/\mu p$  scattering is an essential ingredient in studies of the regime of high parton densities in high-energy QCD (“saturation”) at RHIC, LHC and a future  $ep/eA$  collider [29]. The transverse distribution of quarks and gluons at  $x > 0.01$  defines the initial conditions for the non-linear QCD evolution equations [30–32] describing the approach to the saturation regime [33, 34]. We note that the transverse profile of partons in the nucleon also figures in the estimates of the nuclear enhancement of the saturation scale [35], which determines the region of applicability of these concepts in  $AA$  collisions at RHIC and LHC. The dynamically generated saturation scale  $Q_{\text{sat}}$  is proportional to the density of small- $x$  gluons in transverse area, and thus directly sensitive to the spatial distribution of colour charges in the initial condition at larger  $x$ . Present studies of saturation in the QCD dipole model [36, 37] rely on the limited data from exclusive  $J/\psi$  production at HERA [38, 39] for information on the transverse distribution of partons at  $x < 0.01$ . Measurements of exclusive processes with COMPASS would map the spatial distribution of partons in the unknown region  $x > 0.01$ , and separate the distributions of gluons and singlet quarks by comparing  $J/\psi$  and  $\gamma$  production (DVCS), and thus provide new information about the initial conditions for small- $x$  evolution.

## 1.2 Kinematics and observables

### 1.2.1 Kinematic domains

The COMPASS apparatus is located at the unique CERN SPS M2 beam line that is able to deliver high-energy (50–280 GeV) and highly-polarised  $\mu^\pm$  particles. It consists of a high-resolution forward spectrometer and an unpolarised, longitudinally or transversely polarised target. By installing a recoil proton detector around a liquid hydrogen target to ensure exclusivity of the DVCS and DVMP events, COMPASS would become a facility measuring exclusive reactions within a kinematic subspace ranging from  $x_B \sim 0.01$  to about 0.1, which cannot be explored by any other existing or planned facility in the near future (Fig. 3). COMPASS would thus explore the uncharted  $x_B$  domain between the HERA collider experiments H1 and ZEUS and the fixed-target experiments as HERMES and the planned 11 GeV extension of the JLAB accelerator [13].

### 1.2.2 Deeply virtual Compton scattering

Deeply Virtual Compton Scattering has the same final state as the competing Bethe–Heitler (BH) process, which is elastic lepton–nucleon scattering with a hard photon emitted by either the incoming or outgoing lepton. The differential cross section for hard exclusive muoproduction of real photons off an unpolarised proton target can be written as<sup>1)</sup>

$$\frac{d^4\sigma(\mu p \rightarrow \mu p \gamma)}{dx_B dQ^2 dt |t| d\phi} = d\sigma^{BH} + (d\sigma_{unpol}^{DVCS} + P_\mu d\sigma_{pol}^{DVCS}) + e_\mu (\text{Re } I + P_\mu \text{Im } I), \quad (4)$$

where  $P_\mu$  is the polarisation and  $e_\mu$  the charge in units of the elementary charge, of the polarised muon beam. The interference term  $I$  arises as the DVCS and BH processes interfere on the level of amplitudes. A characteristic feature of this cross section is its dependence on  $\phi$ , the azimuthal angle between lepton scattering plane and photon production plane (Fig. 4). Its integration over  $\phi$  and an analysis of its angular dependence in  $\phi$ , respectively, allows us to study the  $x_B$  dependence of the DVCS cross section  $\frac{d\sigma}{dt}$

---

<sup>1)</sup> For simplicity  $d\sigma$  is used in the following instead of  $\frac{d^4\sigma(\mu p \rightarrow \mu p \gamma)}{dx_B dQ^2 dt |t| d\phi}$ .

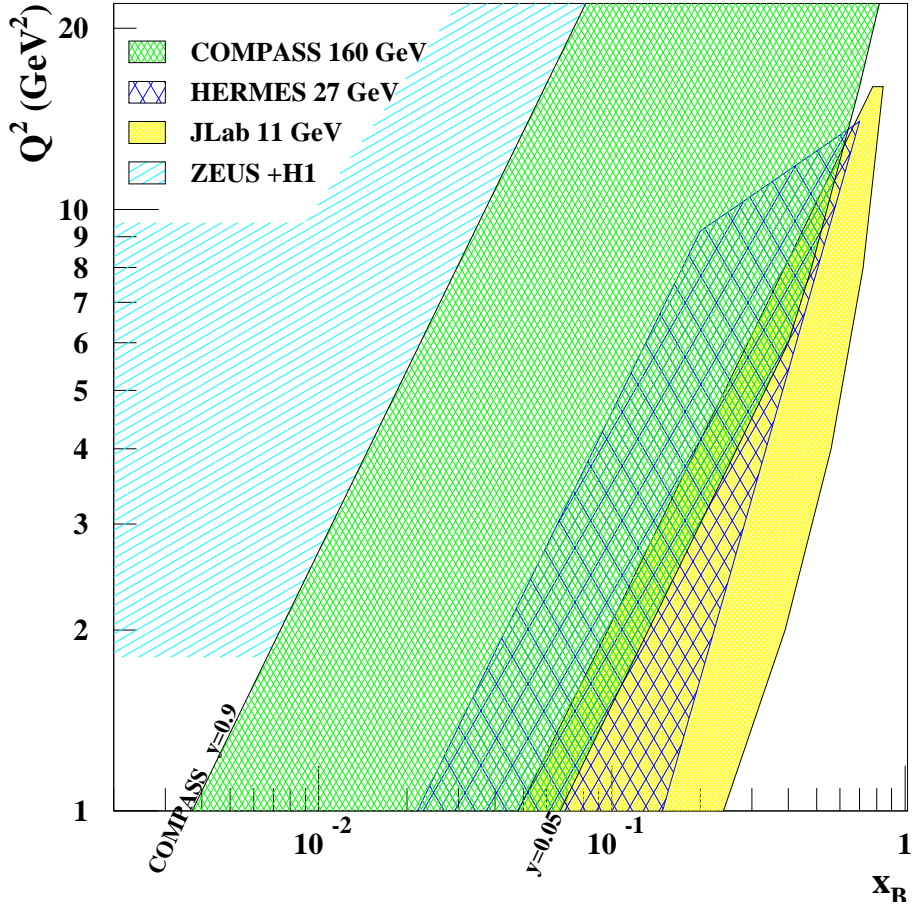


Figure 3: Kinematic domains for measurements of hard exclusive processes shown for the COMPASS (green area enclosed by the lines  $y = 0.9$  and  $y = 0.05$ ), HERMES and JLAB fixed-target experiments and the HERA collider experiments H1 and ZEUS. COMPASS will explore the uncharted territory in between the collider region and that of the lower-energy fixed-target HERMES and JLAB experiments.

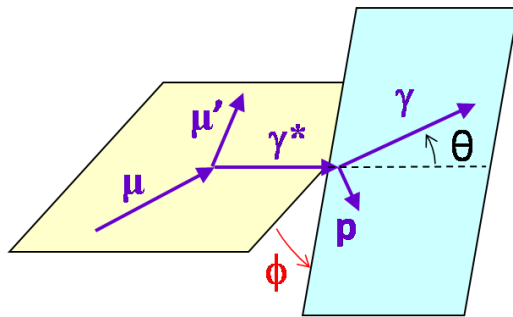


Figure 4: Azimuthal angle between lepton scattering plane (yellow, left) and photon production plane (blue, right) in exclusive single-photon production,  $\mu p \rightarrow \mu p \gamma$ . When both planes coincide, the virtual photon defines two half-planes. For  $\phi = 0$ , the real photon is emitted in the same half-plane as the two muons.

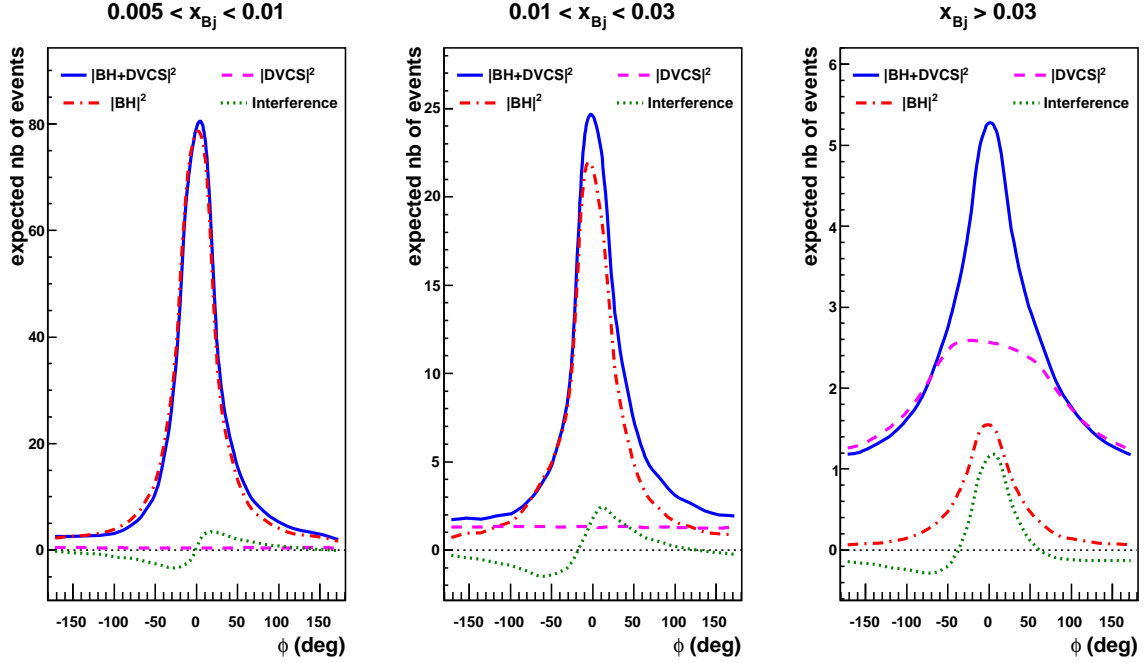


Figure 5: Monte Carlo simulation of the exclusive process  $\mu^+ p \rightarrow \mu'^+ p\gamma$  for  $Q^2 > 1 \text{ GeV}^2$ , showing the  $\phi$  angle distribution for three bins in  $x_B$ :  $0.005 < x_B < 0.01$  (left),  $0.01 < x_B < 0.03$  (middle) and  $0.03 < x_B$  (right). The event yield shown is normalised to the integrated luminosity of the 2009 DVCS test run, as described in Sect. 1.5. It is based on the acceptance of the presently existing COMPASS set-up, *i.e.*, using the existing calorimeters ECAL1 and ECAL2 (for more details see Sect. 1.3).

at a given  $Q^2$  and to isolate specific contributions that are sensitive to different linear combinations of quark GPDs as explained in the following.

The relative abundance of the BH and DVCS processes varies strongly over the COMPASS kinematic domain, as can be seen from Fig. 5. In the lower- $x_B$  region, the almost pure BH event sample is an excellent reference yield allowing precise monitoring of the global efficiency of the apparatus, as the BH amplitude is well known (it relies only on the knowledge of elastic nucleon form factors). The practically negligible contribution of the DVCS process in this region is ‘‘amplified’’ by the BH process, leading to a non-negligible contribution of the interference term, which grows with increasing  $x_B$ . Only in the highest accessible  $x_B$  region, DVCS events are produced at almost the same rate as BH events. In spite of the DVCS-over-BH yield ratio being small in most of the COMPASS kinematics, the study of the interference term through measurements of azimuthal dependencies of cross section differences and asymmetries will allow us to constrain various linear combinations of quark GPDs. When, in an alternative approach, the  $\phi$  dependence is integrated over, measuring the  $x_B$  dependence of the  $t$  slope of the cross section over the full experimentally accessible  $x_B$  range will allow us to draw conclusions on the tomographic partonic image of the nucleon. Both cases are described in more detail below and in Sect. 1.3.

COMPASS is presently the only facility that operates polarised leptons of either charge, namely polarised  $\mu^+$  and  $\mu^-$  beams. The natural polarisation of the muon beam produced from pion decay changes sign when the beam charge is reversed, *i.e.*  $\mu^+$  and  $\mu^-$  beams are polarised along opposite directions. As the BH process is independent of beam charge and polarisation, its contribution is removed when subtracting the yields

from two separate measurements performed using different beam charges. Hence with the same apparatus the COMPASS experiment can perform separate measurements for the two beam charge/polarisation states  $\leftarrow^+$  and  $\rightarrow^-$ , different combinations of which allow us to calculate various observables:

### (1) The beam charge & spin sum of cross sections

$$\mathcal{S}_{CS,U} \equiv d\sigma^{\leftarrow^+} + d\sigma^{\rightarrow^-} = 2(d\sigma^{BH} + d\sigma_{unpol}^{DVCS} + e_\mu P_\mu \text{Im } I), \quad (5)$$

contains both the mostly dominant BH contribution and the unpolarised DVCS contribution. The subscript  $CS$  indicates that both lepton charge and lepton spin are reversed simultaneously when changing from  $\mu^+$  to  $\mu^-$ , while  $U$  denotes the unpolarised target.

The DVCS process is considered to be the theoretically cleanest of the experimentally accessible hard exclusive processes because effects of next-to-leading order and subleading twist are under theoretical control. Its amplitude can be expanded in  $1/Q$  beyond leading twist-2 including all twist-3 contributions [40], leading to

$$\begin{aligned} \mathcal{S}_{CS,U} = & 2 \frac{\Gamma(x_B, Q^2, t)}{\mathcal{P}_1(\phi)\mathcal{P}_2(\phi)} \left( c_0^{BH} + c_1^{BH} \cos \phi + c_2^{BH} \cos 2\phi \right) \\ & + 2 \frac{e^6}{y^2 Q^2} \left( c_0^{DVCS} + \{c_1^{DVCS} \cos \phi + c_2^{DVCS} \cos 2\phi\} \right) \\ & + 2e_\mu P_\mu \frac{e^6}{x_B y^3 t \mathcal{P}_1(\phi)\mathcal{P}_2(\phi)} \left( s_1^I \sin \phi + \{s_2^I \sin 2\phi\} \right). \end{aligned} \quad (6)$$

Here,  $\mathcal{P}_1(\phi)$  and  $\mathcal{P}_2(\phi)$  represent the well known  $\phi$ -dependence of the BH lepton propagators. The coefficients  $c_n^{BH}$  are calculable in QED. The coefficients  $c_n^{DVCS}$  and  $s_n^I$  are related to certain combinations of Compton Form Factors (CFFs). A CFF  $\mathcal{F}$  is a sum over flavours  $f$ , of convolutions of the respective GPDs  $F^f$  with a perturbatively calculable kernel describing the hard  $\gamma^* q$  interaction. Note that each contribution in Eq. (6) and Eq. (10) shown between a pair of braces corresponds to higher-twist or higher-order effects.

When, on the one hand, the azimuthal dependence of  $\mathcal{S}_{CS,U}$  is integrated over, one gets rid of the complete interference term and also of the  $\phi$ -dependent terms of the DVCS contribution. Thus the DVCS leading twist-2 quantity  $c_0^{DVCS}$  can be isolated.

#### (1a) The $t$ slope of the DVCS cross section

can be determined from this quantity as a function of  $x_B$ , which leads to conclusions on the dependence of the transverse size of the nucleon on the fraction of nucleon momentum carried by the struck parton (“nucleon tomography”).

When, on the other hand, the azimuthal dependence of the sum or difference of measurements with different beam charge and/or polarisation is analysed, it is possible to select only the real or only the imaginary part of the complex DVCS amplitude.

#### (1b) The analysis of the azimuthal angular dependence

of the beam charge & spin sum  $\mathcal{S}_{CS,U}$  will provide the coefficients  $c_n^{DVCS}$  and

$s_n^I$ , from which constraints on GPDs can be derived. As an example, the leading (twist-2) contribution  $s_1^I$  is related to the imaginary part of a combination of CFFs

$$s_1^I \propto \text{Im} \left( F_1 \mathcal{H} + \xi(F_1 + F_2) \tilde{\mathcal{H}} - \frac{t}{4M^2} F_2 \mathcal{E} \right). \quad (7)$$

In the kinematics of COMPASS (and even HERMES), the kinematic factors in front of  $\tilde{\mathcal{H}}$  and  $\mathcal{E}$  are small, so that the contribution of  $\mathcal{H}$  is dominant and therefore  $s_1^I \propto \text{Im}(F_1 \mathcal{H})$ . In leading order  $\alpha_s$  (LO),  $\text{Im} \mathcal{H}$  gives direct access to the GPD  $H$  at particular kinematic conditions

$$\text{Im} \mathcal{H}(\xi, t, Q^2) \stackrel{\text{LO}}{=} \pi \sum_f e_f^2 (H^f(\xi, \xi, t, Q^2) \mp H^f(-\xi, \xi, t, Q^2)), \quad (8)$$

which allows one to constrain parametric models for the GPD  $H^f$  in the subspace ( $x = \xi, t$ ) at a given  $Q^2$ .

## (2) The beam charge & spin difference of cross sections

$$\mathcal{D}_{CS,U} \equiv d\sigma^+ - d\sigma^- = 2(P_\mu d\sigma_{pol}^{DVCS} + e_\mu \text{Re } I), \quad (9)$$

in which the BH contribution cancels, requires a precise control at the percent level, of the overall incoming  $\mu^+$  and  $\mu^-$  fluxes and of the corresponding detection efficiencies for exclusive photon production. Here, the azimuthal expansion of the cross section (Eq. (4)) yields

$$\begin{aligned} \mathcal{D}_{CS,U} &= 2P_\mu \frac{e^6}{y^2 Q^2} \left( \{s_1^{DVCS} \sin \phi\} \right) \\ &+ 2e_\mu \frac{e^6}{x_B y^3 t \mathcal{P}_1(\phi) \mathcal{P}_2(\phi)} \left( c_0^I + c_1^I \cos \phi + \{c_2^I \cos 2\phi + c_3^I \cos 3\phi\} \right). \end{aligned} \quad (10)$$

The analysis of the azimuthal angular dependence of  $\mathcal{D}_{CS,U}$  will provide the leading (twist-2) contributions  $c_0^I$  and  $c_1^I$ , which are directly related to the real part of same combination of Compton form factors as in Eq. (7)

$$c_1^I \propto \text{Re} \left( F_1 \mathcal{H} + \xi(F_1 + F_2) \tilde{\mathcal{H}} - \frac{t}{4M^2} F_2 \mathcal{E} \right). \quad (11)$$

Again, as in Eq. (7), the contribution of  $\mathcal{H}$  is dominant and therefore  $c_1^I \propto \text{Re}(F_1 \mathcal{H})$ . In leading order  $\alpha_s$ ,  $\text{Re}(F_1 \mathcal{H})$  is given by a convolution of the GPD  $H$  with a kernel describing the hard photon interaction

$$\text{Re} \mathcal{H}(\xi, t, Q^2) \stackrel{\text{LO}}{=} \sum_f e_q^2 \left[ \mathcal{P} \int_{-1}^1 dx H^f(x, \xi, t, Q^2) \left( \frac{1}{x-\xi} \mp \frac{1}{x+\xi} \right) \right], \quad (12)$$

where  $\mathcal{P}$  denotes Cauchy's principal value. We note that also  $c_0^I \propto \text{Re}(F_1 \mathcal{H})$ .

## (3) The beam charge & spin asymmetry of cross sections

$$\mathcal{A}_{CS,U} \equiv \frac{d\sigma^+ - d\sigma^-}{d\sigma^+ + d\sigma^-} = \frac{\mathcal{D}_{CS,U}}{\mathcal{S}_{CS,U}}, \quad (13)$$

where all the above mentioned quantities are involved, is i) easier to measure than the difference as certain systematics cancel and ii) expected to be (at least partially) less sensitive to theoretical corrections while it is less straightforward to interpret (see explanations for Fig. 9 in Sect. 1.3.2).

- (4) **Transverse-target beam charge & spin difference, sum and asymmetry** require measurements of muoproduction of real photons off a transversely polarised proton target (denoted by the subscript  $T$  below). In this case, there appears an additional azimuthal dependence, namely on the azimuthal angle  $\phi_S$  of the transverse target spin vector relative to the lepton scattering plane. The single-photon cross section can be decomposed as

$$d\sigma(\phi, \phi_S) = d\sigma_U(\phi) + S_T d\sigma_T(\phi, \phi_S), \quad (14)$$

where  $d\sigma_U$  is the cross section for the unpolarised target and  $S_T$  is the value of the transverse target polarisation.

As both beam and target are polarised, the transverse beam charge & spin difference is defined as a double difference, namely between differences of cross sections with the two opposite target spin orientations denoted by  $\phi_S$  and  $\phi_S + \pi$

$$\mathcal{D}_{CS,T} \equiv \left( d\sigma^{\pm}(\phi, \phi_S) - d\sigma^{\pm}(\phi, \phi_S + \pi) \right) - \left( d\sigma^{\mp}(\phi, \phi_S) - d\sigma^{\mp}(\phi, \phi_S + \pi) \right). \quad (15)$$

Correspondingly, the transverse beam charge & spin sum is given by

$$\mathcal{S}_{CS,T} \equiv \left( d\sigma^{\pm}(\phi, \phi_S) - d\sigma^{\pm}(\phi, \phi_S + \pi) \right) + \left( d\sigma^{\mp}(\phi, \phi_S) - d\sigma^{\mp}(\phi, \phi_S + \pi) \right). \quad (16)$$

The lepton-charge-average unpolarised cross section reads

$$\begin{aligned} \Sigma_{unpol} &\equiv \\ &\frac{1}{2} \left[ \left( d\sigma^{\pm}(\phi, \phi_S) + d\sigma^{\pm}(\phi, \phi_S + \pi) \right) + \left( d\sigma^{\mp}(\phi, \phi_S) + d\sigma^{\mp}(\phi, \phi_S + \pi) \right) \right. \\ &\left. + \left( d\sigma^{\pm}(-\phi, \phi_S) + d\sigma^{\pm}(-\phi, \phi_S + \pi) \right) + \left( d\sigma^{\mp}(-\phi, \phi_S) + d\sigma^{\mp}(-\phi, \phi_S + \pi) \right) \right] \end{aligned} \quad (17)$$

so that two asymmetries can be measured

$$\mathcal{A}_{CS,T}^D = \frac{\mathcal{D}_{CS,T}}{\Sigma_{unpol}} \text{ and } \mathcal{A}_{CS,T}^S = \frac{\mathcal{S}_{CS,T}}{\Sigma_{unpol}}. \quad (18)$$

As an example we give here the azimuthal expansion for the transverse beam charge & spin difference

$$\begin{aligned} \mathcal{D}_{CS,T} &= \sin(\phi - \phi_S) \\ &\times \left( 2e_\mu \frac{e^6}{x_B y^3 t \mathcal{P}_1(\phi) \mathcal{P}_2(\phi)} \left( c_{0T_-}^I + c_{1T_-}^I \cos \phi + \{c_{2T_-}^I \cos 2\phi + c_{3T_-}^I \cos 3\phi\} \right) \right. \\ &\quad \left. + 2P_\mu \left( \frac{e^6}{y^2 Q^2} \{s_{1T_+}^{DVCS} \sin \phi\} + \frac{\Gamma(x_B, Q^2, t)}{\mathcal{P}_1(\phi) \mathcal{P}_2(\phi)} s_{1T}^{BH} \sin 2\phi \right) \right) \\ &+ \cos(\phi - \phi_S) \\ &\times \left( 2e_\mu \frac{e^6}{x_B y^3 t \mathcal{P}_1(\phi) \mathcal{P}_2(\phi)} \left( s_{1T_+}^I \sin \phi + \{s_{2T_+}^I \sin 2\phi + s_{3T_+}^I \sin 3\phi\} \right) \right. \\ &\quad \left. + 2P_\mu \left( \frac{e^6}{y^2 Q^2} (c_{0T_+}^{DVCS} + \{c_{1T_+}^{DVCS} \cos \phi\}) \right. \right. \\ &\quad \left. \left. + \frac{\Gamma(x_B, Q^2, t)}{\mathcal{P}_1(\phi) \mathcal{P}_2(\phi)} (c_{0T}^{BH} + c_{1T}^{BH} \cos \phi) \right) \right). \end{aligned} \quad (19)$$

The analysis of the azimuthal angular dependence of  $\mathcal{D}_{CS,T}$  will provide the (leading) twist-2 contribution  $c_{1T_-}^I$  which gets contributions from both  $\mathcal{E}$  and  $\mathcal{H}$  on the same level

$$c_{1T_-}^I \propto \frac{t}{4M^2} \text{Im} \left[ (2 - x_B) F_1 \mathcal{E} - 4 \frac{1 - x_B}{2 - x_B} F_2 \mathcal{H} \right]. \quad (20)$$

At leading twist, the dominant coefficients in the azimuthal expansion, see Eqs. (19) and (20), are related to Compton form factors that involve the quark GPDs  $E^f$  unsuppressed relative to the GPDs  $H^f$ . This is in contrast to the case of an unpolarised target, see Eqs. (7) and (11), where the sensitivity to the GPD  $E^f$  was seen to be strongly reduced. It demonstrates the particular usefulness of (possible later) measurements of muoproduction of real photons off a transversely polarised proton target.

The attainable sensitivity to  $E^u$  and  $E^d$  was recently studied by HERMES [41] comparing data taken with a transversely polarised proton target to GPD-model-dependent predictions where  $E^u$  and  $E^d$  were parametrised in a model-dependent way as functions of the quark total angular momenta  $J^u$  and  $J^d$ , respectively.

### 1.2.3 Deeply virtual meson production

In DVMP, collinear factorisation was rigorously proven in the limit  $Q^2 \rightarrow \infty$  for amplitudes with longitudinal polarisation of the virtual photon [4, 42]. Applying it to data taken at moderate values of  $Q^2$  may not completely be justified, however. Moreover, recent data on the  $\pi\gamma$  transition form factor from BABAR [43] have cast serious doubts onto the collinear factorisation as such [44]. For amplitudes with transverse virtual-photon polarisation, collinear factorisation does not hold because of infrared singularities. Although there is no rigorous proof of  $k_\perp$  factorisation [45–48], it is perhaps an alternative applicable for moderate values of  $Q^2$  as it provides power corrections and also allows one to compute the amplitudes for transverse photon polarisation.

In vector meson production ( $\rho, \phi, \omega, \dots$ ), the longitudinal component can be isolated from the transverse one by using the self-analysing decay of the vector meson, under the assumption of  $s$ -channel helicity conservation which was found experimentally to be valid at the 10% level. We note that the production of  $\rho, \omega, \phi$  vector mesons is already under investigation at COMPASS.

Only the GPDs  $H^f$  and  $E^f$  are needed to describe the exclusive production of longitudinally polarised vector mesons ( $\rho_L^{0,\pm}, \omega_L, \phi_L, \dots$ ). In the description of exclusive production of pseudo-scalar mesons ( $\pi^{0,\pm}, \eta, \dots$ ) produced by longitudinally polarised virtual photons, only the GPDs  $\tilde{H}^f$  and  $\tilde{E}^f$  are involved but here no straightforward practical way is known to separate the transverse contribution.

Different vector mesons are described by different combinations of GPDs, for example

$$\begin{aligned} H_{\rho^0} &= \frac{1}{\sqrt{2}} \left( \frac{2}{3} H^u + \frac{1}{3} H^d + \frac{3}{8} H^g \right), \quad H_\omega = \frac{1}{\sqrt{2}} \left( \frac{2}{3} H^u - \frac{1}{3} H^d + \frac{1}{8} H^g \right), \\ H_\phi &= -\frac{1}{3} H^s - \frac{1}{8} H^g. \end{aligned}$$

Hard exclusive vector meson production can be considered complementary to DVCS as it provides access to various other combinations of GPDs. Note that in DVMP there exists no interference term and the corresponding CFFs appear in bilinear combinations as, *e.g.*

$\mathcal{H}\mathcal{H}^*$ . In contrast to DVCS, where gluon contributions enter only beyond leading order in  $\alpha_s$ , in DVMP both quark and gluon GPDs contribute at the same order, so that by combining the results for various mesons even conclusions on  $H^g$  may be extracted. It is foreseen to measure cross sections for a large set of mesons ( $\pi, \eta, \rho, \omega, \phi, J/\psi, \dots$ ), which are all sensitive to different combinations of quark and gluon GPDs. This rich data set will make model-dependent determinations of a variety of GPDs possible. In parallel, the  $x_B$  dependence of the  $t$  slope will be determined for the meson production cross sections, which will complement the information on the transverse size of the nucleon as obtained from DVCS data.

It has been shown that the “transverse target spin asymmetry” measured in vector meson production on a transversely polarised target is sensitive to the GPDs  $E^f$  [49]. A first measurement of this observable in hard exclusive  $\rho^0$  electroproduction by HERMES shows insufficient precision to draw clear conclusions [50]. Such measurements are foreseen for the envisaged extension of the GPD programme using a transversely polarised target.

### 1.3 Simulations and projections

In order to calculate projected statistical accuracies for the proposed measurements, the following parameters and assumptions were used:

- a polarised muon beam with an energy of 160 GeV,
- a 48 s SPS period with a 9.6 s spill duration (flat top),
- a  $\mu^+$  beam intensity of  $4.6 \times 10^8$  muons per spill,
- a three times lower intensity for the  $\mu^-$  beam,
- a new liquid hydrogen target of 2.5 m length (Sect. 6.1), yielding a luminosity of about  $10^{32} \text{ cm}^{-2}\text{s}^{-1}$  for the  $\mu^+$  beam,
- a new Recoil Proton Detector (RPD) surrounding the target (Sect. 6.2),
- an as continuous as possible polar and azimuthal photon detection coverage provided by the two existing electromagnetic calorimeters ECAL1 and ECAL2 (Sect. 7),
- a new large-angle calorimeter ECAL0 (Sect. 7.2),
- an overall “global” efficiency of  $\epsilon_{global} = 0.1$  including detection, tracking and reconstruction of events comprising an incoming and scattered muon, a high-energy photon and a recoiling proton within the RPD acceptance as well as beam and spectrometer availabilities (Sect. 1.4),
- a running time of 280 days (70 days with  $\mu^+$  and 210 days with  $\mu^-$ , in order to have as close as possible integrated luminosities for both data sets).

The acceptance for exclusive single-photon production is determined using the standard COMPASS program for reconstructing the simulated DVCS and BH events. Hard exclusive single-photon production, *i.e.* the interfering Bethe–Heitler and DVCS processes, is simulated employing two separate codes using two generators for the DVCS amplitude: one is based on the VGG model [51] and the other one on the Frankfurt–Freund–Strikman (FFS) model, which was modified for the proposed experiment [52].

The conditions listed above will allow for an accumulation of at least 300 DVCS events for those bins, in which the number of DVCS events reaches at least 10% of the number of BH events and for which  $Q^2 \leq 8 \text{ GeV}^2$ , as shown in Table 1. Such statistics are sufficient to perform a 2-dimensional analysis of the  $t$ -slope measurement with 6 bins in  $t$  and 5 bins in  $\phi$  (Sect. 1.3.1). It is worth noting that an increase in the number of muons per spill by a factor of 4 would extend the range in  $Q^2$  up to about 16  $\text{GeV}^2$ .

Table 1: Number of BH/DVCS events in  $6 \times 4$  bins in  $x_B$  and  $Q^2$  for  $0.05 \leq y = E_{\gamma^*}/E_\mu \leq 0.9$  projected for 280 days (70 days with  $\mu^+$  and 210 days with  $\mu^-$ ) with a global efficiency of 0.1 and using ECAL0, ECAL1 and ECAL2. The numbers of DVCS events are obtained using the VGG model. The modified FFS model yields numbers of DVCS events smaller by a factor 0.7. The geometrical acceptance for single-photon detection is indicated for each bin between parentheses. Bins containing at least 300 DVCS events, which also have to represent not less than 10% of the number of BH events, are marked by an asterisk.

$Q^2/\text{GeV}^2$	$0.005 \leq x_B \leq 0.01$	$0.01 \leq x_B \leq 0.02$	$0.02 \leq x_B \leq 0.03$	$0.03 \leq x_B \leq 0.07$	$0.07 \leq x_B \leq 0.13$	$0.13 \leq x_B \leq 0.27$
$8 \leq Q^2 \leq 16$	-	-	-	3280 / 51 (0.88)	1032 / 84 (0.91)	190 / 120 (0.93)
$4 \leq Q^2 \leq 8$	-	2512 / 18 (0.86)	4176 / 78 (0.87)	2371 / 309* (0.90)	269 / 347* (0.94)	66 / 501* (0.94)
$2 \leq Q^2 \leq 4$	6577 / 36 (0.86)	15258 / 368 (0.86)	1848 / 374* (0.90)	1050 / 1257* (0.93)	153 / 1466* (0.94)	29 / 933* (0.97)
$1 \leq Q^2 \leq 2$	44749 / 627 (0.86)	7684 / 1338* (0.86)	1187 / 1270* (0.90)	771 / 4420* (0.93)	68 / 2000* (0.94)	-

The acceptance for single-photon detection is seen to be always larger than 86%. It has to be noted that without ECAL0 the acceptance is smaller by a factor of two in the bin  $0.07 \leq x_B \leq 0.13$  and by a factor of seven in the bin  $0.13 \leq x_B \leq 0.27$ .

The choice of 160 GeV for the muon beam energy bears the advantage that there will be a sufficiently large number of  $(x_B, Q^2)$  bins where the DVCS contribution dominates over the BH one. The price to pay is the relatively low intensity of the  $\mu^-$  beam at this energy.

At a later date, measurements are envisaged using a transversely polarised NH<sub>3</sub> target (Sect. 1.3.4) which are planned to be described in more detail in an addendum to this proposal.

### 1.3.1 The $t$ -slope of the DVCS cross section

For the parametrisation of the  $x_B$  dependence of the  $t$ -slope parameter  $B(x_B)$  introduced in Sect. 1.1, the simple ansatz  $B(x_B) = B_0 + 2\alpha' \log(\frac{x_0}{x_B})$  is sufficient when disregarding the case  $x_B \rightarrow 1$  that is of no interest here. In this parametrisation, the  $x_B$ -slope  $\alpha'$  is a measure for the decrease in nucleon size with increasing  $x_B$ .

The COMPASS  $x_B$  region is uncharted territory also for the  $t$ -slope parameter  $B(x_B)$ . Data on  $B(x_B)$  exist only for smaller  $x_B$  values, namely for the HERA collider range  $10^{-4} < x_B < 10^{-2}$  [18, 53, 54]. Above the COMPASS  $x_B$  range, in the valence region, no experimental determinations of  $B(x_B)$  exist. The only information comes from fits adjusted to form factor data which give  $\alpha' \simeq 1 \text{ GeV}^{-2}$  [55, 56]. In this situation, the values  $B_0 = 5.83 \text{ GeV}^{-2}$ ,  $\alpha' = 0.125 \text{ GeV}^{-2}$  and  $x_0 = 0.0012$  are chosen for the simulation of a  $t$ -slope measurement inspired by the HERA data.

In Figure 6 are shown the projected statistical and systematic uncertainties for a measurement of the  $x_B$  dependence of the  $t$ -slope parameter  $B(x_B)$  for the range  $1 \leq Q^2 \leq 8 \text{ GeV}^2$ . As  $B(x_B)$  is obtained from the  $\phi$ -integrated beam charge & spin sum (Eq. (5)) after BH subtraction, it constitutes a direct measurement of the DVCS cross section. The statistical error in a  $(x_B, Q^2)$  bin is given by  $\sqrt{N_{BH} + N_{DVCS}}/N_{DVCS}$  where  $N_{BH}$  and  $N_{DVCS}$  are the numbers of BH and DVCS events collected in this bin (Table 1).

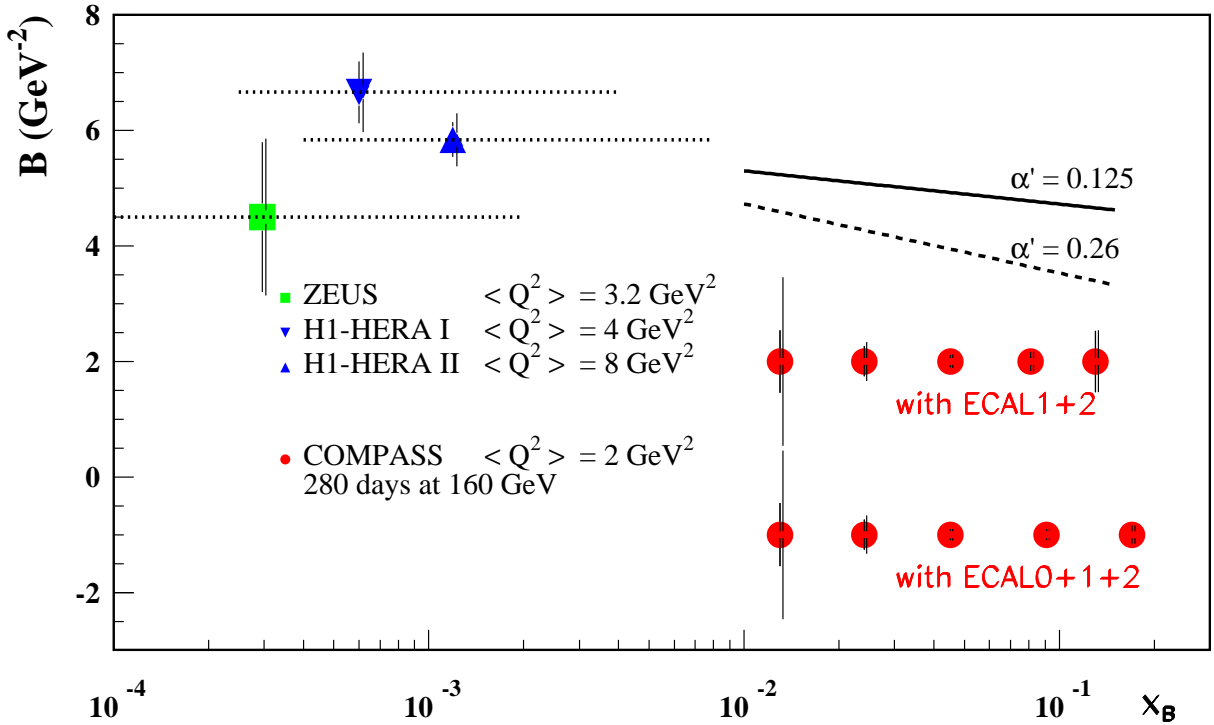


Figure 6: Projections for measuring the  $x_B$  dependence of the  $t$ -slope parameter  $B(x_B)$  of the DVCS cross section, calculated for  $1 < Q^2 < 8 \text{ GeV}^2$ . For comparison some HERA results with similar  $\langle Q^2 \rangle$  are shown [18, 53, 54], for which the horizontal dashed lines indicate their  $x_B$  range. The left vertical bar on each data point indicates the statistical error only while the right one includes also the quadratically added systematic uncertainty, using only ECAL1 and ECAL2 (first row) and also ECAL0 (second row). Two different parametrisations are shown using  $\alpha' = 0.125 \text{ GeV}^{-2}$  and  $0.26 \text{ GeV}^{-2}$ .

For this purpose, only those bins indicated by an asterisk in Table 1 are used for which  $N_{DVCS} \geq 0.1 \times N_{BH}$  is satisfied.

The dominant systematic uncertainty of the resulting DVCS contribution arises from the subtraction of the BH contribution. The BH contribution dominates the one of DVCS over a wide range in  $x_B$  and  $Q^2$ . In this region, the BH yield is obtained from the calculated BH cross section, taking into account radiative corrections, luminosity and detection efficiencies. Up to now, we assume that this BH yield will be known within 3%. It turns out that in such a case the resulting systematic uncertainty, which is  $0.03 \times N_{BH}/N_{DVCS}$ , is of relevance only for the first selected point in  $x_B$  for each  $Q^2$  domain where the BH contribution is more than twice as large as the DVCS contribution. When extrapolating the BH yield into the kinematic region where it has to be used for subtraction, an additional uncertainty can originate from possible kinematic-dependent detector efficiencies.

As the DVCS cross section dominates the one of the BH process at larger values of  $x_B$  (Fig. 5), the accuracy of the  $t$ -slope measurement profits considerably from the additional acceptance of a possible new large-angle calorimeter ECAL0. This becomes evident when comparing the two sets of points in Fig. 6 which describe the projected total uncertainties without and with ECAL0.

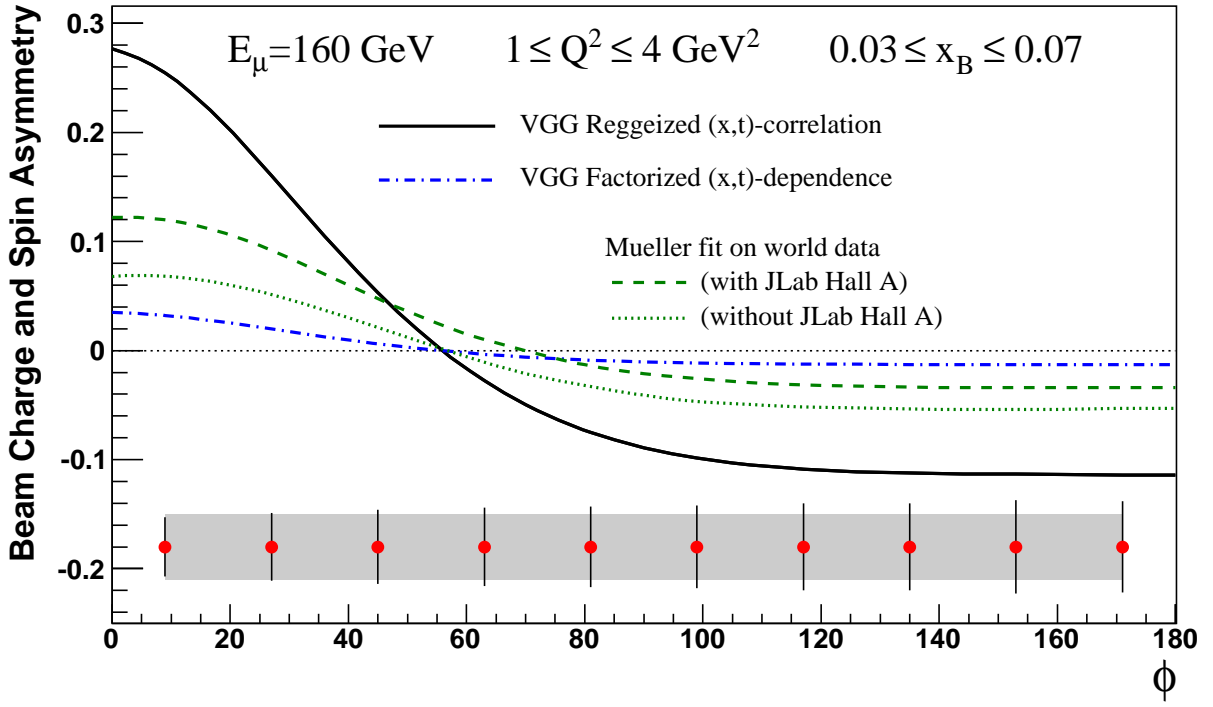


Figure 7: Projected statistical accuracy for a measurement of the  $\phi$  dependence of the beam charge & spin asymmetry. As an example, the 2-dimensional bin  $0.03 \leq x_B \leq 0.07$  and  $1 \leq Q^2 \leq 4 \text{ GeV}^2$  is shown. Predictions are calculated using the VGG model [51]. The black (solid) and blue (dash-dotted) curves correspond to two different variants of the VGG model (see text). The green curves show predictions based on the first fit of world data [21] including JLAB HALL A (dashed line) or not (dotted line).

Altogether, the measurement of the  $\phi$ -integrated beam charge & spin sum in DVCS will lead to a model-independent determination of the  $t$ -slope parameter  $\langle B(x_B) \rangle$  with a total accuracy of better than  $0.1 \text{ GeV}^{-2}$ , when averaged over the COMPASS  $x_B$  range. The measurement of its  $x_B$  dependence allows a direct determination of the  $x_B$  slope  $\alpha'$  with a total accuracy better than 2.5 sigma in the total projected uncertainty, should  $\alpha'$  possess a value above  $0.26 \text{ GeV}^{-2}$  and only the existing calorimeters ECAL2 and ECAL1 be used. With a new ECAL0 detector (Sect. 7.2), a 2.5-sigma determination of  $\alpha'$  is already possible when its value is above  $0.125 \text{ GeV}^{-2}$ . A visualisation of these two scenarios is also given in Fig. 6. In any case, new and significant information will be obtained in this uncharted  $x_B$  region, further elucidating the issue of “nucleon tomography” as it was described in Sect. 1.1.

### 1.3.2 Beam charge & spin asymmetry and difference

In Figures 7 and 8, the projected statistical accuracies are shown for a measurement of the azimuthal dependence of the beam charge & spin asymmetry  $\mathcal{A}_{CS,U}$  (Eq. (13)) and difference  $\mathcal{D}_{CS,U}$  (Eq. (9)) in a particular  $(x_B, Q^2)$  bin, calculated using the VGG GPD model [51] that is meant to be applicable mostly in the valence region. Two choices exist for the  $(x, t)$  dependence of GPDs, either factorised or ‘reggeised’, the latter corresponding to  $\alpha' \approx 0.8 \text{ GeV}^{-2}$ . Recent evidence from phenomenology (see, *e.g.* Ref. [55]) and experiment (see, *e.g.* Ref. [41]) indicates that the factorised ansatz is disfavoured. This favours larger

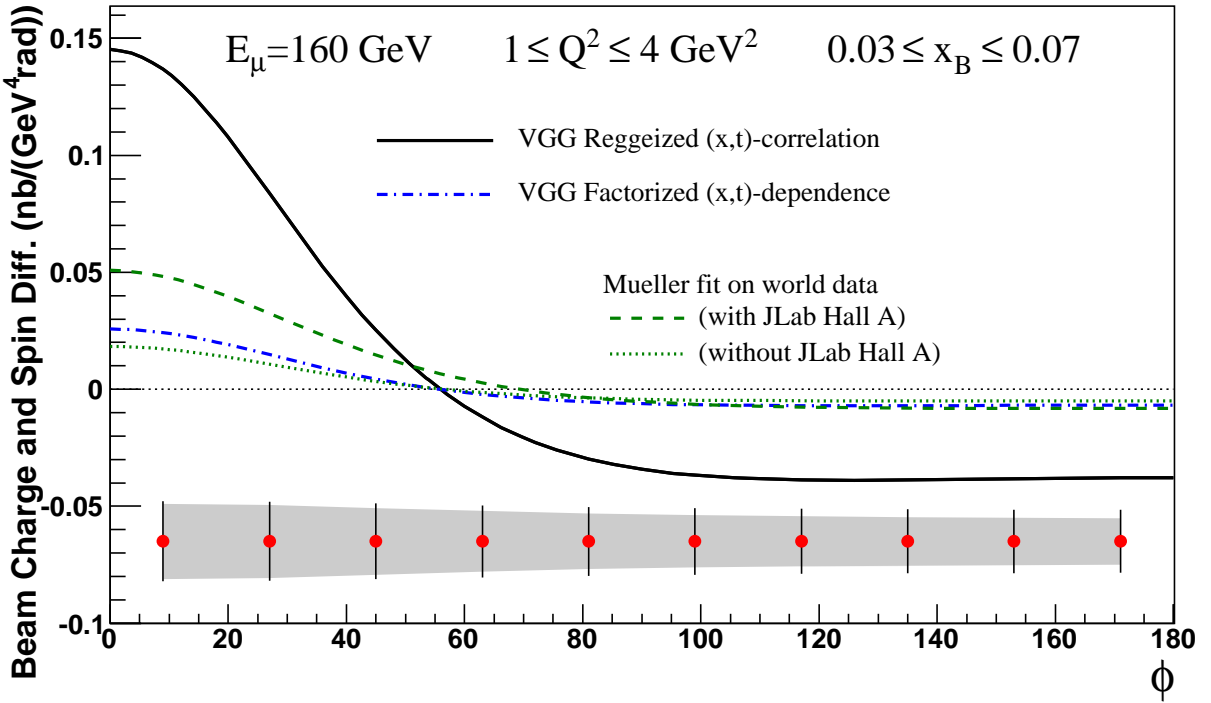


Figure 8: Projected statistical accuracy for a measurement of the  $\phi$  dependence of the beam charge & spin difference. For further explanations see caption of Fig. 7.

values of the beam charge & spin asymmetry (and difference), as can be seen by comparing the two VGG curves in the figures.

The statistics expected from the proposed two years of running with an unpolarised LH target will permit us to study a 2-dimensional dependence with, *e.g.* 6 bins in  $x_B$  combined with 6 bins in  $t$  or with 4 bins in  $Q^2$ . This choice is driven by the requirement to have enough statistics in each of the about 10  $\phi$  bins for a stable fit of the azimuthal dependence. In Figure 9 is shown the projected statistical accuracy for a measurement of the 2-dimensional ( $x_B, t$ ) dependence of the  $\cos \phi$  azimuthal modulation of the beam charge & spin asymmetry, leaning towards the analysis and interpretation techniques developed for azimuthal asymmetries at HERMES and described, *e.g.* in Ref. [41]. The asymmetry amplitude  $A_{CS,U}^{\cos \phi}$  is related through the coefficient  $c_1^I$  to the real part of the CFF  $\mathcal{H}$  (Eq. (11)). Such data will provide strong constraints for reliable future GPD models that must be able to simultaneously and consistently describe the full range in  $x_B$ . Presently, no such model exists.

A recent theoretical development exploits dispersion relations for Compton form factors. In this context, a fitting procedure including next-to-next-to-leading order (NNLO) corrections was developed and successfully applied to describe DVCS observables at very small values of  $x_B$ , which are typical for the HERA collider [57]. This technique was very recently extended [21] to include DVCS data from HERMES and JLAB (CLAS and HALL A), the fit yielding the  $x_B$ -dependence of  $xH(x, x, t)$  which was then used to predict the  $\phi$ -dependence of  $\mathcal{A}_{CS,U}$  shown as additional curves in Figs. 8, 7 and 9 (with and without the impact of the JLAB HALL A data). The asymmetry amplitude  $A_{CS,U}^{\cos \phi}$  is related via the coefficient  $c_1^I$  to the real part of the CFF  $\mathcal{H}$  (Eq. (11)). This real part was found positive at HERA and negative at HERMES and JLAB. The kinematic domain of COMPASS,

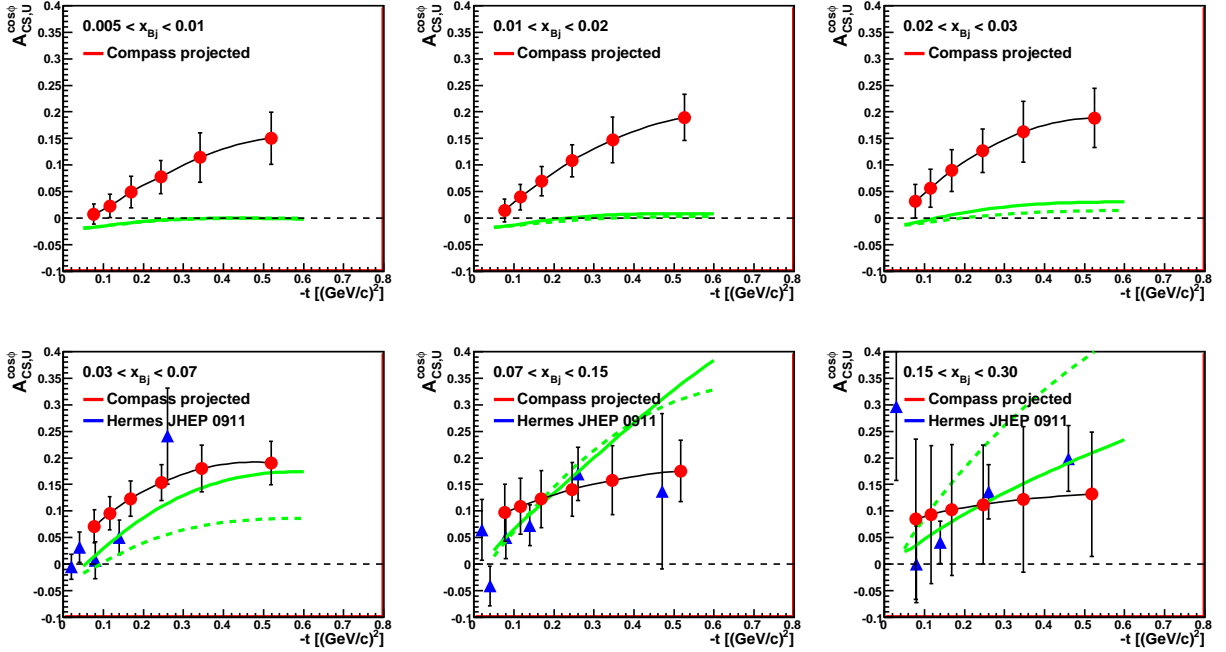


Figure 9: Projected statistical accuracy for the amplitude of the  $\cos \phi$  modulation of the beam charge & spin asymmetry using ECAL2+ECAL1+ECAL0. Projections calculated with the reggeised variant of the VGG model are shown for the  $t$  dependence in each of the six  $x_B$  bins. The blue triangles at large  $x_B$  show recent HERMES results [58]. The curves show the latest predictions based on the first fit on world data [21] including JLAb HALL A (solid line) or not (dotted line).

in particular the region  $0.005 < x_B < 0.03$  (see the 3 first panels of Fig. 9), is expected to allow the determination of the  $x_B$  position of the node of this function, which is important input for the fitting procedure.

The quantification of the systematic errors for the beam charge & spin difference (Eq. (9)) is a major issue. This difference of cross sections is calculated as

$$\mathcal{D}_{CS,U} = \frac{N^+}{F^+ \epsilon^+} - \frac{N^-}{F^- \epsilon^-},$$

where  $N^+$  and  $N^-$  are the number of events recorded using  $\mu^+$  and  $\mu^-$  beams,  $F^+$  and  $F^-$  are the corresponding integrated luminosities, and  $\epsilon^+$  and  $\epsilon^-$  are the factors taking into account acceptance and efficiencies for the two beam charges. The  $\mu^+$  and  $\mu^-$  measurements will be done successively by changing as often as possible from one setting to the other. The quantities  $F^+$  and  $F^-$  will have to be kept as close as possible to one another ( $F^+ \sim F^-$ ), which means that the duration of a  $\mu^-$  measurement will be about three times the duration of a  $\mu^+$  measurement in order to compensate for the different maximum beam intensities available.

When calculating the systematic errors on  $\mathcal{D}_{CS,U}$  one can distinguish between the normalisation factors which are independent of the beam charge and those which depend on it, the latter having more impact on the systematics than the former. For this purpose we consider the factor  $a^{+(-)} = F^{+(-)} \epsilon^{+(-)}$  and decompose the systematic errors on  $a^+$  and  $a^-$  into i) an error common to  $a^+$  and  $a^-$ , denoted as charge-independent error  $\Delta a_{ci}$ , and ii) an error which affects only the difference, denoted as charge-dependent error  $\Delta a_{cd}$

$$(\Delta \mathcal{D}_{syst})^2 = \left( \frac{\Delta a_{ci}}{a} \mathcal{D} \right)^2 + \left( \frac{\Delta a_{cd}}{a} \mathcal{S} \right)^2.$$

For simplicity, in this section the notation  $\mathcal{D}$  is used for  $\mathcal{D}_{CS,U}$  and  $\mathcal{S}$  for  $\mathcal{S}_{CS,U}$ . The relative contributions of  $|\text{BH}|^2$ ,  $|\text{DVCS}|^2$  and interference terms were shown in Fig. 5. Figures 10 and 11 show for 12 bins in  $(x_B, Q^2)$  the  $\phi$  variation of the sum  $\mathcal{S}$  and the difference  $\mathcal{D}$  of the hard-exclusive single-photon cross section. It becomes apparent that the ratio of  $\mathcal{D}$  over  $\mathcal{S}$  varies from below the percent level to values close to unity, so that for small values the determination of  $\mathcal{D}$  becomes more difficult.

The  $\mu^+$  and the  $\mu^-$  data are recorded during separate data taking periods, with different beam intensities and different beam line and spectrometer settings (all magnetic fields are reversed). Presently, there is no information on the magnitude of the charge-dependent error  $\Delta a_{cd}$ . We therefore chose to estimate what we consider a tolerable level and define the specifications required to achieve this goal. For the proposed running time and for most of the bins in  $(x_B, Q^2, \phi)$ , the statistical accuracy  $\Delta \mathcal{D}_{stat} = 1/\sqrt{N_{BH} + N_{DVCS}} \times \mathcal{S}$  is always above  $3\% \times \mathcal{S}$ . We therefore assume a value of 3% for the relative accuracy  $\frac{\Delta a_{cd}}{a}$  of the charge-dependent term, which results in the systematic error  $\Delta \mathcal{D}_{syst} = \frac{\Delta a_{cd}}{a} \mathcal{S}$  shown as the grey bands in Fig. 11. Except for small  $\phi$  angles and this only in two  $(x_B, Q^2)$  bins, the charge-dependent systematic error does not exceed the statistical one.

An illustration of the present understanding of systematic errors from existing data on absolute SIDIS cross sections is shown in Table 2. The table lists the different corrections with the corresponding errors which need to be applied to calculate the cross sections for semi-inclusive high  $p_T$  hadron muo-production at COMPASS. Concerning acceptance corrections, a present estimate for the muon detection (Source 7) gives a correction of 5–7%. Assuming a similar number for photon detection we expect for both a correction of 7–10%. The quoted error of 50% is conservative.

Putting aside the acceptance correction, which is still preliminary and should not depend on beam charge, the resulting systematics would reach a maximum of  $\sim 7\%$ , assuming it is similar for data taking in the GPD programme. Note that the dominant contributions are Source 2 and 4 (Table 2). It is presently not possible to evaluate which fraction of this systematics is beam-charge dependent. Therefore, an obvious goal is to have this fraction equal (or less) to the 3% assumed for the charge dependent systematic error  $\frac{\Delta a_{cd}}{a}$ .

In addition to a precise monitoring of the above mentioned corrections, the following quantities will need to be precisely controlled

- the beam position when using  $\mu^+$  or  $\mu^-$  beams,
- the symmetry of the two COMPASS spectrometer magnets with the two polarities,
- the Moller electron contamination which affect different parts of the detectors for the two beam charges.

### 1.3.3 The $t$ -slope of the $\rho^0$ cross section

Data on the exclusive production of vector mesons ( $\rho, \phi, \dots$ ), which will be recorded simultaneously to the DVCS measurements, will be used to determine the corresponding cross sections and  $t$ -slope parameters  $B(x_B)$ . As an example, we show here projections for the  $\rho^0$  vector meson. The simulations are based on a model developed for COMPASS [60] where the  $Q^2$  and  $\nu$  dependencies are taken from the parametrisation of NMC data [61] and the absolute normalisation is done according to predictions of Ref. [49]. The statistical

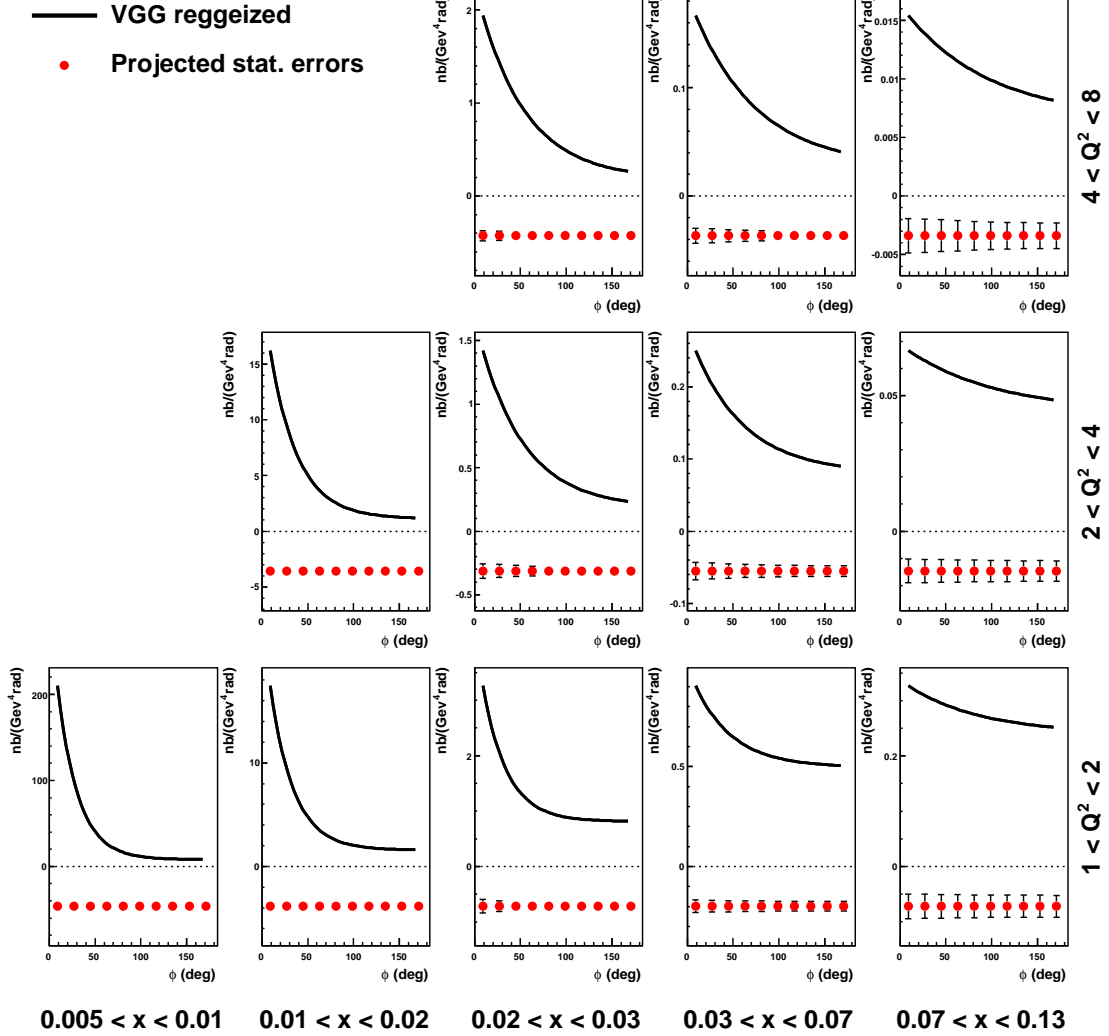


Figure 10: Simulated results for the sum  $\mathcal{S}$  (solid line), based on the reggeised variant of the VGG model, shown for 12 bins in  $(x_B, Q^2)$ . The error bars show the projected statistical errors.

Table 2: The corrections and corresponding errors affecting absolute SIDIS cross sections.

Source	Correction (relative error)	Resulting systematics
1 Missing events (errors in data processing)	$\leq 10\% (3\%)$	$\leq 0.3\%$
2 Detector instabilities (not full diagnostics)		$5\%$
3 DAQ dead time	$10\% (4\%)$	$0.4\%$
4 Beam Flux determination	$20\% (25\%)$	$5\%$
5 Veto dead time needs precise spill structure	$20\% (5-10\%)$	$1-2\%$
6 Radiative corrections	$10-20\% (10\%)$	$1-2\%$
7 Acceptance/Efficiency	$7-10\% (\leq 50\%)$	$\leq 3-5\%$

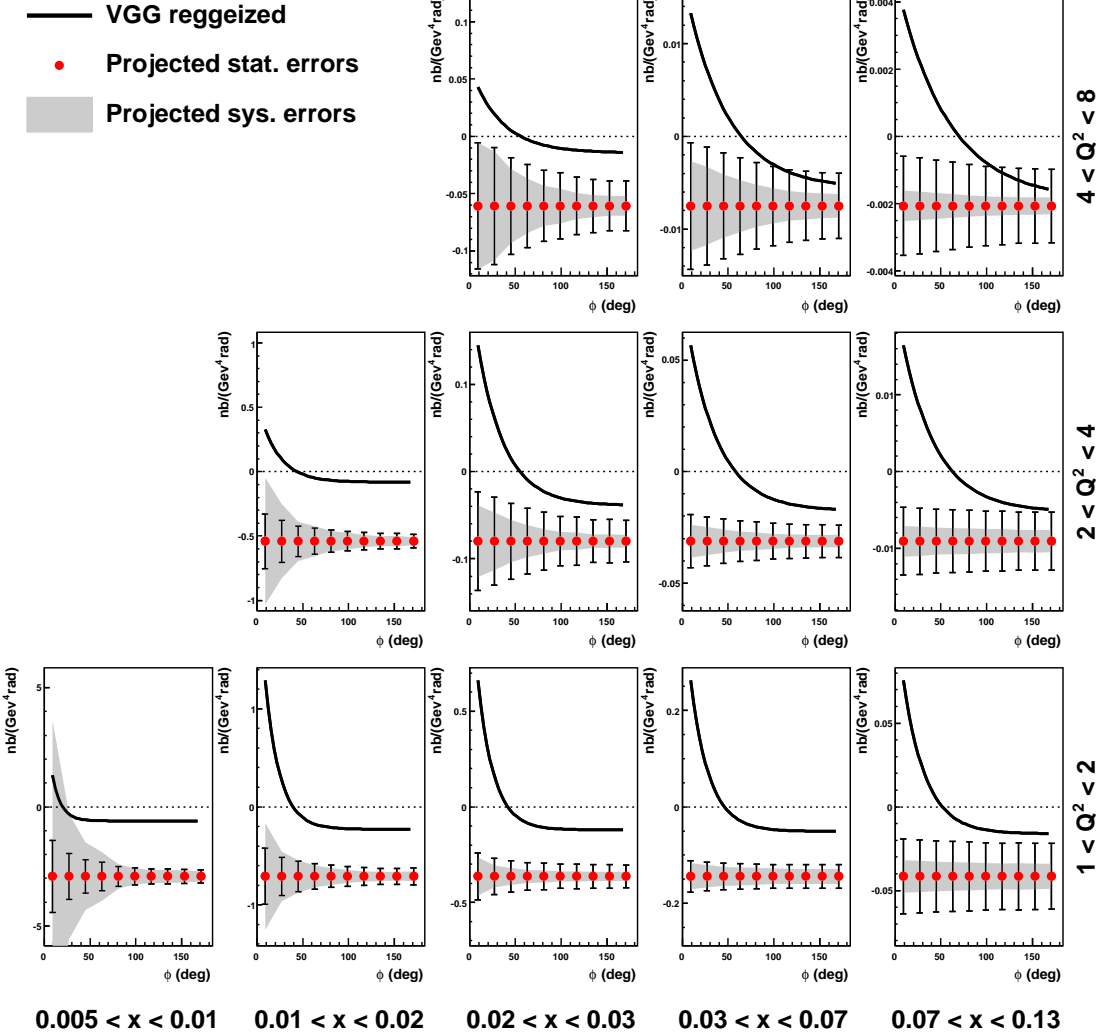


Figure 11: Simulated results for the difference  $\mathcal{D}$  (solid line), based on the reggeised variant of the VGG model, shown for 12 bins in  $(x_B, Q^2)$ . The error bars show the projected statistical errors, the grey bands show the systematic uncertainties expected when assuming 3% for the charge-dependent errors (see text).

accuracy expected for 280 days (70 days with  $\mu^+$  and 210 days with  $\mu^-$ ) at 160 GeV muon beam energy is shown in Fig. 12 for the  $x_B$  and  $Q^2$  bins given in Table 3. The data from ZEUS [59], which cover a lower  $x_B$  range, are shown for comparison. The only existing data in the COMPASS range are those from NMC, although with significantly lower precision. The  $t$ -slope parameter  $B(x_B)$  measured at HERA was found to decrease with increasing  $Q^2$  from  $B(x_B) \sim 8 \text{ GeV}^{-2}$  at  $Q^2 \sim 1 \text{ GeV}^2$  to  $B(x_B) \sim 5.5 \text{ GeV}^{-2}$  at  $Q^2$  larger than  $10 \text{ GeV}^2$ . The present simulation was performed assuming  $B(x_B) = 8 \text{ GeV}^{-2}$ ; a smaller value would decrease the error bars. It can be seen that the future DVMP data from COMPASS will cover a  $x_B$  range which is slightly shifted to lower values as compared to the DVCS data shown in Fig. 6. At  $x_B$  above 0.1, the statistics are reduced by the acceptance of the first spectrometer magnet SM1 and the central hole of the ECAL0 calorimeter. Data on exclusive production of heavier mesons, like  $\phi$ , are expected to provide additional measurements of  $B(x_B)$  in a similar kinematic range. The virtue of other mesons is to enhance the capability of disentangling not only different flavours, but also valence, sea

Table 3: Number of DVMP events for  $\rho$  production, shown for  $6 \times 4$  bins in  $x_B$  and  $Q^2$  for  $0.05 \leq y = E_{\gamma^*}/E_\mu \leq 0.9$ , using a global efficiency of 0.1 and the COMPASS set-up comprising the new large-angle calorimeter ECAL0 with small central hole, located directly behind the RPD. The acceptance for  $\rho$  detection is indicated for each bin between parentheses.

$Q^2/\text{GeV}^2$	$0.005 \leq x_B \leq 0.01$	$0.01 \leq x_B \leq 0.02$	$0.02 \leq x_B \leq 0.03$	$0.03 \leq x_B \leq 0.07$	$0.07 \leq x_B \leq 0.13$	$0.13 \leq x_B \leq 0.27$
$8 \leq Q^2 \leq 20$	-	-	-	538 (0.87)	569 (0.69)	103 (0.10)
$4 \leq Q^2 \leq 8$	-	303 (0.83)	1140 (0.86)	3224 (0.80)	716 (0.21)	11 (0.003)
$2 \leq Q^2 \leq 4$	1138 (0.82)	8427 (0.86)	6491 (0.86)	8148 (0.45)	308 (0.02)	0 (0.00)
$1 \leq Q^2 \leq 2$	31186 (0.84)	42496 (0.84)	18897 (0.57)	8763 (0.11)	38 (0.002)	- -

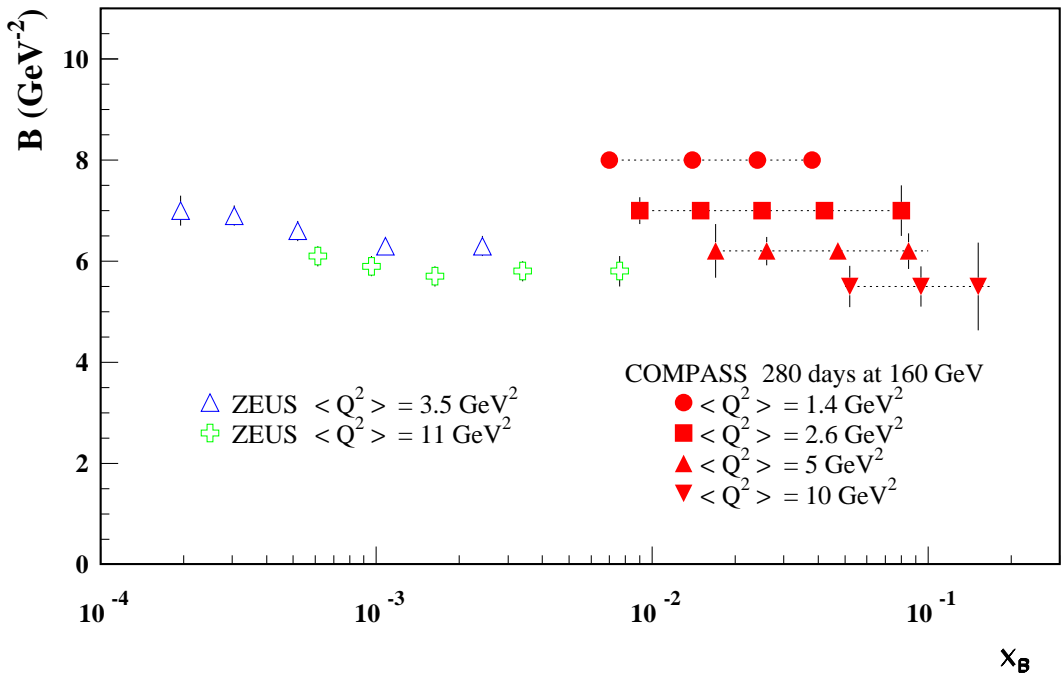


Figure 12: Projections for measuring the  $x_B$  dependence of the  $t$ -slope parameter  $B(x_B)$  in  $\rho^0$  vector meson production, calculated for  $1 \leq Q^2 \leq 20 \text{ GeV}^2$  and compared to ZEUS results with similar  $\langle Q^2 \rangle$  [59]. Only statistical uncertainties are shown.

and gluons. In particular, for  $\phi$  only sea and gluons contribute, whereas for  $\rho$  valence quarks have also to be taken into account, as explained in Sect. 1.2.3.

### 1.3.4 Transverse target spin asymmetries

Measurements of transverse target spin asymmetries for the proton are foreseen at a later stage. In this section, we present the corresponding projected statistical accuracies for the DVCS process in order to illustrate the potential of such measurements. The target will consist of transversely polarised ammonia, similar to the one used presently at COMPASS, with the density of the material in the target cells equal to  $0.5 \text{ g/cm}^3$ , the total length of the target cells equal to 120 cm and a diameter of up to 4 cm [62]. The target cells will be surrounded by a recoil proton detector (RPD) of a length that matches the length of the target. The present polarised target set-up based on the combination of two superconducting magnets, i) a 2.5 T large-diameter highly uniform solenoid and ii) a 0.6 T transverse dipole, leaves no space for a RPD of similar structure as the one foreseen for the measurements with a 2.5 m length liquid hydrogen target, as described in Sect. 6.2. Two hypothetical configurations are therefore considered here for polarised target and RPD. In configuration 1, a simplified and more compact version of an RPD could be installed inside the solenoid of the existing COMPASS polarised target. In configuration 2, an RPD similar to the new one but of shorter length would be used which necessitates a new technology for the polarised target magnet(s). Possible solutions to integrate a transversely polarised target into a complete RPD are under discussion [63]. They involve the construction of thin superconducting coils needed to perform the dynamic nuclear polarisation and to hold the transverse polarisation. Their structure would have to be compatible with that of the cryogenic and microwave equipments. We note that configuration 1 will most likely not provide the necessary resolution in recoil proton momentum  $P$  and consequently in momentum transfer  $t$  required for such measurements. Therefore it is very important to soon initiate R&D activities for configuration 2 of polarised target and RPD.

In a later analysis of data on hard-exclusive single-photon production on a transversely polarised target, the transverse spin-dependent part of the DVCS cross section will be obtained by calculating the difference of cross sections with opposite values of  $\phi_s$ , the azimuthal angle between lepton scattering plane and target spin vector, *i.e.*, with two opposite orientations of the transverse target spin vector. In order to minimise systematic effects the different target cells will have to be polarised in opposite directions and their polarisation will be reversed periodically using the method of dynamic nuclear polarisation, as it was done at COMPASS in the past.

In order to disentangle the contributions of the  $|\text{DVCS}|^2$  and the interference terms, which have the same azimuthal dependence, data with both  $\mu^+$  and  $\mu^-$  beams will have to be taken and the difference and sum of  $\mu^+$  and  $\mu^-$  cross sections will be calculated which permits to separate these contributions. The asymmetries for the difference and the sum of  $\mu^+$  and  $\mu^-$  transverse spin-dependent cross sections,  $A_{CS,T}^D$  and  $A_{CS,T}^S$  (Eqs. (15) to (18)), will be analysed separately.

Simulations were performed assuming the polarised ammonia target as described in Ref. [62], in order to estimate the expected statistical accuracy of transverse target spin asymmetries. The spectrometer set-up, parameters and fluxes of  $\mu^+$  and  $\mu^-$  beams, as well as the global efficiency were assumed to be the same as described earlier in this section. The fraction of all protons in the target, both polarised and unpolarised, was estimated to be equal to 0.57 and the dilution factor (fraction of polarised protons to all protons) equal to 0.26. The value assumed for the target polarisation was 0.9. Simulations were performed

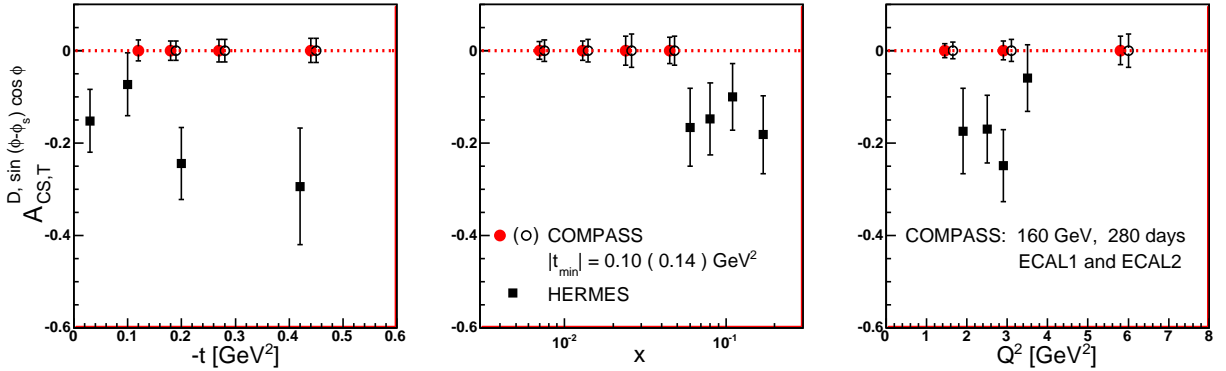


Figure 13: Expected statistical accuracy of  $A_{CS,T}^{D,\sin(\phi-\phi_s)\cos\phi}$  as a function of  $-t$ ,  $x_B$  and  $Q^2$  from a measurement in 280 days, using a 160 GeV muon beam and ECAL1+ECAL2. Solid and open circles correspond to the simulations for the two hypothetical configurations of the target region (see text). Also shown is the asymmetry  $A_{UT}^{\sin(\phi-\phi_s)\cos\phi}$  measured at HERMES [41] with its statistical errors.

for the two above assumed configurations of the target region. Due to the recoil-proton energy loss in the target, in the microwave cavity and in addition for configuration 2 also in the thin holding coil, the minimal value of  $|t|$  measured by the RPD is 0.10 (0.14)  $\text{GeV}^2$  for configuration 1 (2). In the exclusive-photon event generator, the DVCS amplitude was calculated according to the Frankfurt–Freund–Strikman (FFS) model which was modified for the COMPASS experiment [52].

As an example of the results from the simulations, the expected statistical accuracy of the asymmetry  $A_{CS,T}^{D,\sin(\phi-\phi_s)\cos\phi}$  is shown in Fig. 13 as a function of  $-t$ ,  $x_B$  and  $Q^2$  for the two hypothetical target/RPD configurations. This asymmetry is analogous to the asymmetry  $A_{UT}^{\sin(\phi-\phi_s)\cos\phi}$  measured with unpolarised electrons on a transversely polarised proton target, which is also shown in the figure. It is related to the leading (twist-2) contribution  $c_{1T-}^I$  (Eq. (20)).

Typical values for the statistical errors of  $A_{CS,T}^{D,\sin(\phi-\phi_s)\cos\phi}$ , as well as of the seven remaining asymmetries related to the twist-2 terms in the cross section, are expected to be about 0.03. This projected statistical accuracy for possible future COMPASS measurements of transverse target spin asymmetries represents a significant improvement compared to existing results. One should also mention that using  $\mu^+$  and  $\mu^-$  beams COMPASS can measure the whole set of eight transverse-spin-dependent twist-2 terms, whereas only four of them were previously determined by HERMES.

#### 1.4 A first look at exclusive photon production in 2008

Simulations have been performed for the projected DVCS measurements. However, for such complex apparatus like the COMPASS spectrometer, experience has shown that a check with data (whenever available) is mandatory. The precision of the final results will depend on:

- the achievable luminosity, which is a function of the LH target length and the maximum reachable  $\mu^+$  and  $\mu^-$  beam intensities,
- the global detection efficiency, which includes all possible hardware losses (trigger dead time etc.) and event reconstruction losses,
- the efficiency to identify and possibly reject background,

- how accurately the Bethe–Heitler (BH) contribution, which dominates in certain kinematic regions, can be subtracted,
- how accurately the measured yields can be translated into absolute cross sections.

There are common key issues to answer these questions quantitatively, namely:

- how accurately we know the detection efficiencies (absolute, and relative between  $\mu^+$  and  $\mu^-$ ) and how well we can monitor their stability versus time,
- what is the ultimate precision for the measurements of the incoming  $\mu^+$  and  $\mu^-$  flux measurements, which will determine the systematic accurately arising from the combination of both data sets.

The set-up used for a part of the COMPASS hadron programme makes use of a 40 cm long LH target, surrounded by a Recoil Proton Detector (RPD). It includes all detectors available including the ECAL1 and ECAL2 electromagnetic calorimeters for photon detection. Apart from the target length and the corresponding RPD length, this set-up has all the features of the one foreseen for the proposed future GPD programme, where the LH target length will be 2.5 m with the RPD length correspondingly adapted. The flexibility of the CERN/SPS M2 beam line allows one to tune either a hadron beam or a polarised muon beam, reaching in both cases the optimum performance within a few hours. This offered an excellent opportunity to perform DVCS test measurements with minimum disturbance of the ongoing hadron programme. Such measurements were performed in 2008 and 2009 using both  $\mu^+$  and  $\mu^-$  beams of 160 GeV energy, with an intensity of about 1/3 of the maximum in 2008 and close to the maximum intensity in 2009. In 2008, due to the short time slot available, the Beam Momentum Station (BMS) which determines with a precision of a few  $10^{-3}$  the incoming beam particle momentum but needs to be removed for running with hadron beam, could not be reinstalled. For the 2009 test run the BMS was reinstalled.

#### 1.4.1 Overall efficiency and performances to select BH and DVCS events

The first results from the 2008 test run on exclusive production of a high-energy single-photon in coincidence with a recoiling proton are presented in Ref. [64]. The pre-selection towards exclusive  $\mu p \rightarrow \mu' p \gamma$  events is requiring that:

- there are only two charged tracks ( $\mu, \mu'$ ) at the primary vertex,
- there is only one proton candidate in the Recoil Proton Detector (RPD) and it has a momentum of less than  $1 \text{ GeV}/c$ ,
- there is only one photon with energy  $E_\gamma \geq 5 \text{ GeV}$  in ECAL1 and no other photon with energy  $\geq 10 \text{ GeV}$  in ECAL2, or
- there is only one photon with energy  $E_\gamma \geq 10 \text{ GeV}$  in ECAL2 and no other photon with energy  $\geq 5 \text{ GeV}$  in ECAL1. These conditions correspond to the kinematic domain for DVCS displayed in Fig. 51.

We note that the events preselected in this way may have additional low-energy photons. At this first step of the analysis, the precise photon timing provided by the ECALs readout electronics to suppress the background was not available. The suppression of the main part of additional photons in this first analysis was accomplished by an appropriate choice of ECAL thresholds.

In Figure 14 correlations are illustrated between quantities derived from the particle detected in the RPD and those derived from the muon vertex reconstructed using the incoming and the scattered muons. The left panel shows the time difference  $\Delta t = t_\mu - t_{RPD}$  between the incoming muon and the RPD particle both evaluated at the muon vertex. The random noise in the 30 ns timing window is less than 2% and a Gaussian fit gives

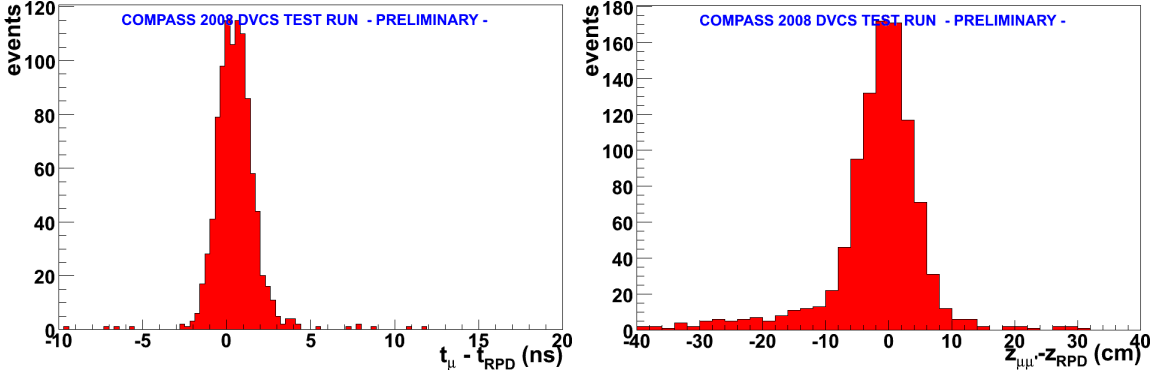


Figure 14: Differences in timing (left) and  $Z$  position along the beam direction (right) between the reconstructed  $\mu\mu'$  vertex and the single proton detected in the RPD. The resolutions of timing and position difference are better than 1 ns and 4 cm, respectively.

$\sigma_t \simeq 1$  ns. The right panel shows  $\Delta Z = Z_{\mu\mu' \text{vertex}} - Z_{RPD}$ , the difference between the longitudinal position of the muon vertex and the RPD particle's point of closest approach to the beam axis. It shows a peak with an approximately 8 cm width at half maximum and a tail present in the left part of the  $\Delta Z$  distribution; a Gaussian fit gives  $\sigma_Z \simeq 4$  cm. No cuts are applied yet since most of the events in this tail will be removed by the further application of exclusivity cuts.

In the absence of the BMS, the momentum of the incoming muon is not precisely known while its direction is well determined, hence it is relevant to work in the transverse plane. One can build the missing momentum  $\mathbf{P}_{miss} = \mathbf{P}_\mu - \mathbf{P}_{\mu'} - \mathbf{P}_\gamma$  and compare its projection in the transverse plane with the projection of  $\mathbf{P}_{proton}$ . This is shown in Fig. 15 together with correlation and difference between the azimuthal angles  $\phi_{miss}$  and  $\phi_{RPD}$ . Two exclusivity cuts,  $|\Delta P_\perp| < 0.2$  GeV and  $\Delta\phi < 36^\circ$  (*i.e.* 3  $\sigma$ ), are derived using these distribution and applied to improve the rejection of non-exclusive background. Assuming now that the selected events have a pure 3-particle final state  $up \rightarrow \mu' p\gamma$ , one can calculate the azimuthal angle  $\phi$  between the lepton plane spanned by the incoming and scattered muons and the “hadron” plane spanned by recoiling proton and produced photon, as illustrated in Fig. 4. Results are shown in Fig. 16 where the peak at  $\phi = 0$  is a characteristic feature of BH events which are dominant at small  $x_B$  (as shown in the left panel of Fig. 5). Applying the two previous exclusivity cuts  $|\Delta P_\perp| < 0.2$  GeV and  $\Delta\phi < 36^\circ$  reduces significantly the constant (non-exclusive) background, as illustrated in the right panel of Fig. 16.

Reliable simulations for the hard exclusive DVCS process are restricted to sufficiently large photon virtualities,  $Q^2 > 1$  GeV $^2$ . This restriction does not apply to the BH bremsstrahlung process, which dominates this sample of events at low values of  $x_B$ . Awaiting a simulation for BH production for this full kinematical phase space, a standard “2-Gaussian + constant” fit is applied to the background, as shown in Fig. 16. In order to compare with available simulations, a cut  $Q^2 > 1$  GeV $^2$  is eventually applied. The resulting  $\phi$  distribution is shown in Fig. 17, where 51 events are finally selected. We note that among the 51 selected events, 36 have an additional cluster with energy below 1 GeV in ECAL1 or below 2 GeV in ECAL2. Calculating the  $M_{\gamma\gamma}$  for the corresponding photon pair leads to an upper limit for a possible  $\pi^0$  contamination of the selected sample of  $16 \pm 6\%$ .

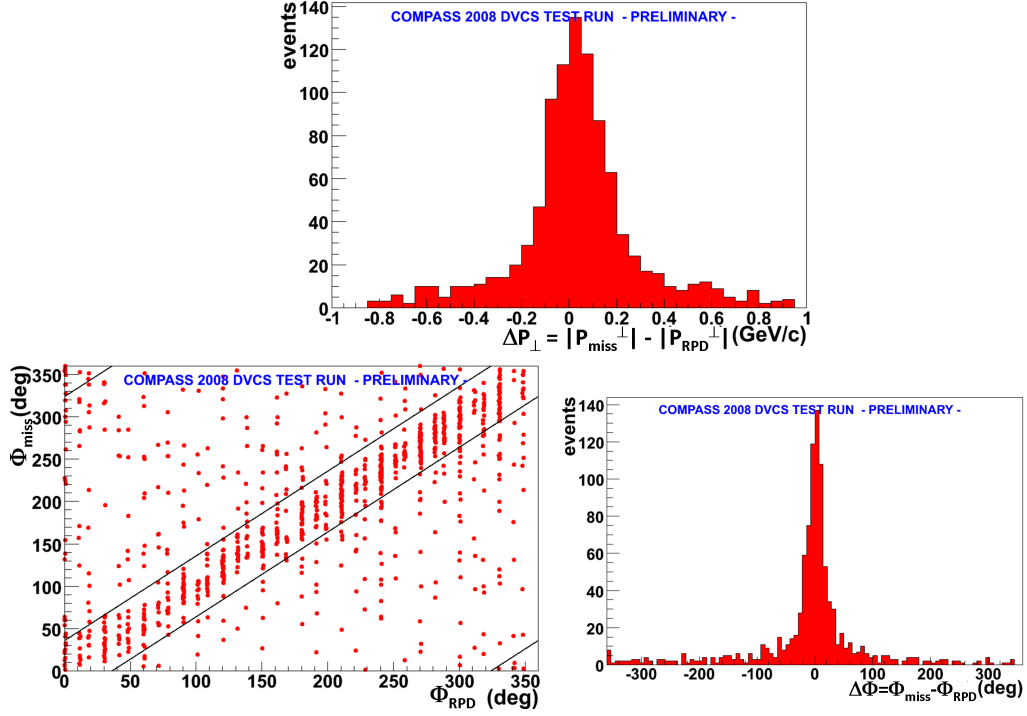


Figure 15: Top panel:  $\Delta P_{\perp} = |\mathbf{P}_{\text{miss}}^{\perp}| - |\mathbf{P}_{\text{RPD}}^{\perp}|$ . Bottom left: correlation between  $\phi_{\text{miss}}$  and  $\phi_{\text{RPD}}$ . Bottom right:  $\Delta\phi = \phi_{\text{miss}} - \phi_{\text{RPD}}$ .

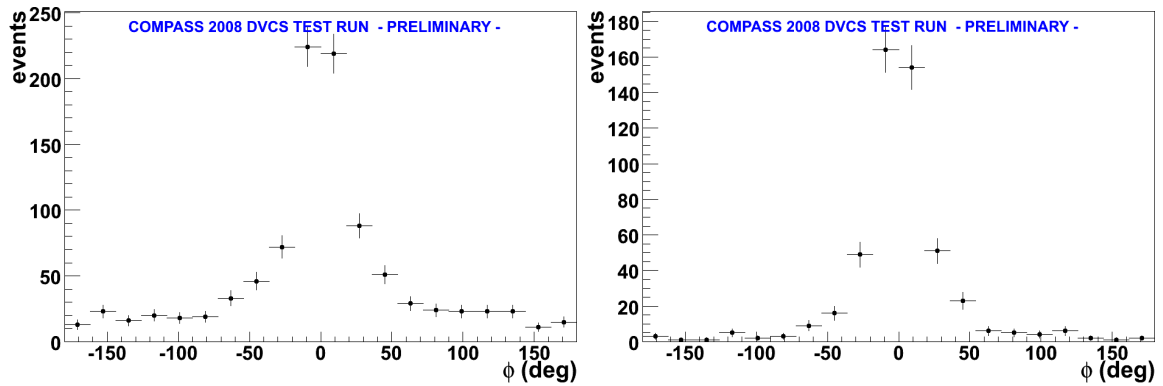


Figure 16: Azimuthal distribution in  $\phi$  of the measured exclusive  $\mu p \rightarrow \mu' p \gamma$  events before (left) and after (right) exclusivity cuts. This angular distribution exhibits a peak at  $\phi = 0$ , which is a characteristic feature of BH dominance at small  $x_B$ .

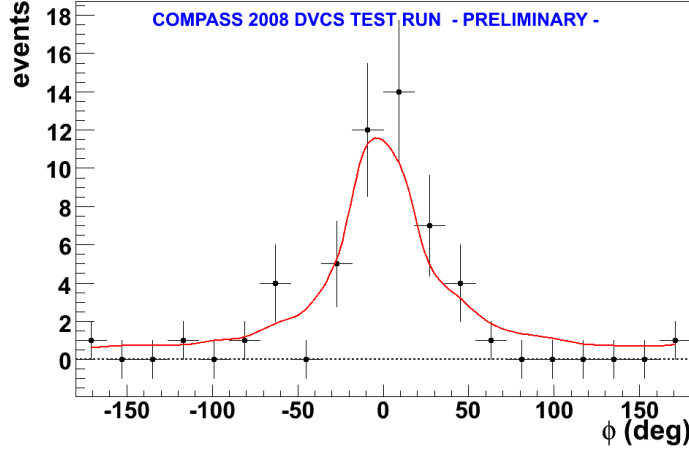


Figure 17: Azimuthal distribution in  $\phi$  of the measured exclusive  $\mu p \rightarrow \mu' p \gamma$  events for  $Q^2 > 1 \text{ GeV}^2$  and comparison with simulation. This distribution is rather similar to the distribution dominated by the BH contribution at small  $x_B$  (left panel of Fig. 5). In total, 51 events are selected.

We can now compare to the prediction for single-photon production which is still dominated, for this restricted kinematic region, by the BH process. The relative normalisation factor of the two distributions produced for equal luminosities provides the overall detection efficiency  $\epsilon = 0.32 \pm 0.13$ . The final global efficiency incorporates several additional factors which amount to  $\epsilon_{Add} \sim 0.4$ . Combining the two numbers provides the global efficiency  $\epsilon_{global} = 0.13 \pm 0.05$ . The value of 0.1 that was given in the Letter of Intent [65] to the SPSC is in excellent agreement with this first direct estimate.

#### 1.4.2 Improved analysis using ECAL timing information

Following the first analysis step described in the previous section, the 2008 DVCS test data were reproduced providing an improved cluster reconstruction and a precise cluster timing information from the ECALs. The issue of background from additional photons was solved in the new production as described in Ref. [66].

The reduction of additional photons was accomplished by imposing a cut on the ECALs' timing information, and also by a general improvement of the ECAL reconstruction software and calibration algorithm. Given the timing resolution for all photons in the ECALs, the optimum cut was found to be  $|t - t_0| \leq 3.5 \sigma_t$  with  $\sigma_t \sim 1.5 \text{ ns}$  and  $t_0$  the offset of the distribution from zero. This cut, which simultaneously maximises the number of selected events and drastically decreases the average multiplicities of the additional clusters, is a major improvement that opened the way to select exclusive single-photon events without applying any threshold on  $E_\gamma$  (besides the necessary hardware thresholds).

In Figure 18 is shown the azimuthal distribution of the final 52 exclusive  $\mu p \rightarrow \mu' p \gamma$  events which are obtained for  $Q^2 > 1 \text{ GeV}^2$  from the improved analysis using the photon timing information, *i.e.* without additional low-energy clusters. Possible reasons for any remaining  $\pi^0$  contamination in this sample are that one of the two photons is not detected in the ECALs or has an energy below the hardware threshold.

#### 1.5 A first hint of “pure” DVCS events from the 2009 test run

One of the main goals of the DVCS test run performed in 2009 was to provide a first evaluation of the relative contributions of the  $|DVCS|^2$  and  $|BH|^2$  terms, and of the

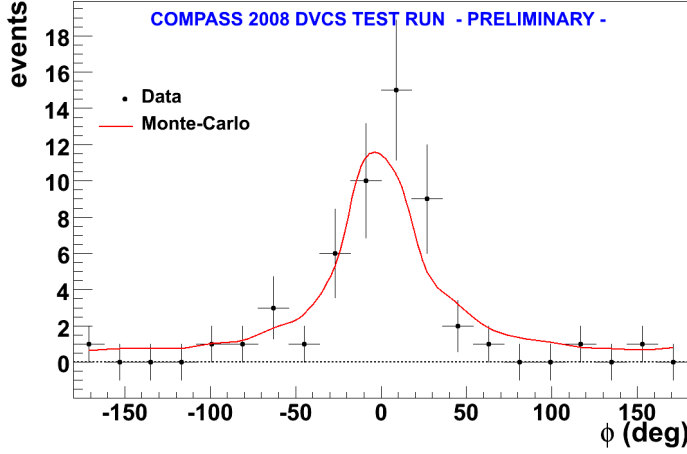


Figure 18: Same distribution as shown in Fig. 17 but from the new analysis with photon timing. In total, 52 purely exclusive single-photon events are selected.

DVCS-BH interference term at COMPASS kinematics. In comparison to the shorter 2008 test run, the 2009 test run was improved in several aspects:

- higher statistics,
- the three inclusive triggers (Middle, Ladder and Outer) were added to the trigger in coincidence with the RPD,
- the beam momentum station was reinstalled to measure the momentum of the incoming muon,
- the  $\mu$  beam intensity was increased by a factor of three,
- the data were taken with both  $\mu^+$  and a  $\mu^-$  beam.

The selection of exclusive single-photon production events and the use of the precise photon timing were performed as for the 2008 data analysis (see Sects. 1.4.1 and 1.4.2). Figure 19 shows, for three bins in  $x_B$  and after applying the cut  $Q^2 > 1 \text{ GeV}^2$ , the  $\phi$  distribution for a sample of exclusive single-photon events obtained with the  $\mu^+$  beam. In the low- $x_B$  bin we observe 278 events with a  $\phi$  distribution compatible with a BH-dominated sample. In the high- $x_B$  bin we observe 54 events. An extrapolation of the BH yield from the low- $x_B$  bin to the high- $x_B$  bin leads to  $\sim 10$  BH events, which suggests a significant contribution of DVCS events in the high- $x_B$  bin. This figure has to be compared to Fig. 5 that shows, in the same lay-out, a simulation of all contributions to hard exclusive single-photon production, namely pure BH ( $|\text{BH}|^2$ ), pure DVCS ( $|\text{DVCS}|^2$ ), DVCS-BH interference term and the resulting sum ( $|\text{BH} + \text{DVCS}|^2$ ).

Another goal of the 2009 DVCS test run is to learn about the possible limitations to reach a level of accuracy of a few percent, to which the overall luminosity, including acceptances and efficiencies, has to be controlled. This is a severe requirement for this physics programme and the study involves the use of inclusive  $\mu p \rightarrow \mu' X$  and semi-inclusive  $\mu p \rightarrow \mu' \pi^+ (\pi^-) (\pi^0) X$  channels as well as exclusive channels with a recoil proton detected, including  $\mu p \rightarrow \mu' p \gamma$ .

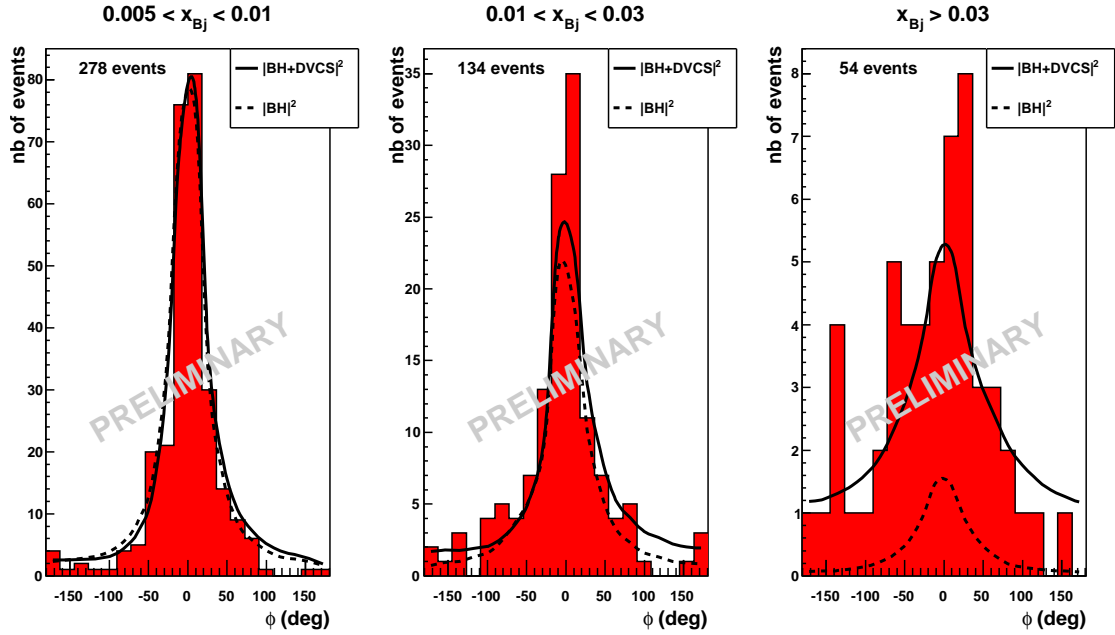


Figure 19: Distribution in the azimuthal angle  $\phi$  for measured exclusive single-photon events,  $\mu p \rightarrow \mu' p \gamma$  with  $Q^2 > 1 \text{ GeV}^2$ , in the same three  $x_B$  bins as in Fig. 5. Shown here is a Monte Carlo simulation of only the BH process ( $|\text{BH}|^2$ ) and of both the BH and DVCS processes ( $|\text{BH} + \text{DVCS}|^2$ ).

## 2 Measurements of unpolarised PDFs and TMD effects in SIDIS

High-statistics data on semi-inclusive deep inelastic scattering (SIDIS) on the proton,  $\mu p \rightarrow \mu h X$ , will be recorded simultaneously with the DVCS and DVMP measurements using the long liquid hydrogen target. Combined with existing COMPASS SIDIS data on the deuteron taken earlier with the  ${}^6\text{LiD}$  target, they will permit quark flavour separation. The new proton data will be obtained in a region of Bjorken- $x$  (denoted by  $x$  in the rest of this section), where measurements from other experiments are either not available or have limited precision.

Studying polarisation effects in SIDIS, a  $\text{NH}_3$  target could be used as proton target and the background from unpolarised nucleons could be subtracted. This, however, is not possible for the unpolarised case as the  $\text{NH}_3$  target is an almost isoscalar target with a fraction of only 10/17 protons. In addition, nuclear effects in nitrogen can be sizable[67]. Therefore, a liquid hydrogen target is mandatory to study unpolarised effects in SIDIS on the proton. As cross section measurements are foreseen, special attention will be devoted to all systematic effects related to normalisation. Finally, the capability of identifying both the charge and the nature of the outgoing hadrons is an advantage compared to some previous experiments. This will be addressed more in detail in Sect. 12, where upgrades of the RICH system will be discussed.

With the statistics expected from two years of running with the long liquid hydrogen target described in Sect. 6.1, it will be possible to study simultaneously 4-dimensional dependencies in the kinematic variables  $x, Q^2, p_T^2$  and  $z$ . The SIDIS data to be taken on the proton target will be used in global QCD analyses to constrain PDFs as well as quark Fragmentation Functions (FFs), which describe quark fragmentation into a hadron. The latter functions are a necessary ingredient for the determination of polarised parton distributions. Presently, FFs are still poorly known quantities which leads to ambiguities and/or systematic uncertainties in such determinations. The new proton data will also permit an LO determination of the unpolarised strange quark distribution function  $s(x)$  in the region  $0.001 < x < 0.2$ , where its shape is unknown.

In addition, using the same data, it will be possible to measure with high statistics asymmetries in the azimuthal distributions of hadrons produced in SIDIS on an unpolarised proton target. These measurements, already performed by COMPASS using a deuteron ( ${}^6\text{LiD}$ ) target, are sensitive to the  $T$ -odd transverse-momentum-dependent (TMD) Boer–Mulders function [68] and also to the Cahn effect [69], both depending on the intrinsic transverse momentum of quarks  $k_T$ . The Boer–Mulders function will also be measured in the Drell–Yan process, thereby allowing for a test of (restricted) universality, an important test of QCD (for more details see Sect. 3.3).

### 2.1 Strange quark distribution function and quark fragmentation functions

Hadron multiplicities can be measured at COMPASS for a large variety of produced hadrons,  $\pi^+, \pi^-, \pi^0, K^+, K^-, K^0, \Lambda$  and  $\bar{\Lambda}$  as a function of  $x, z$  and  $Q^2$ . Hadron multiplicities represent the number of hadrons of type  $h$  produced per DIS event. At LO, they can be written as

$$\frac{dN^h(x, z, Q^2)}{dN^{DIS}} = \frac{\sum_q e_q^2 q(x, Q^2) D_q^h(z, Q^2)}{\sum_q e_q^2 q(x, Q^2)}, \quad (21)$$

where  $q(x, Q^2)$  is the unpolarised PDF for flavour  $q$ ,  $D_q^h$  is the FF for a quark  $q$  fragmenting into a hadron  $h$ , and  $z$  is the fraction of virtual photon energy carried by the hadron. The

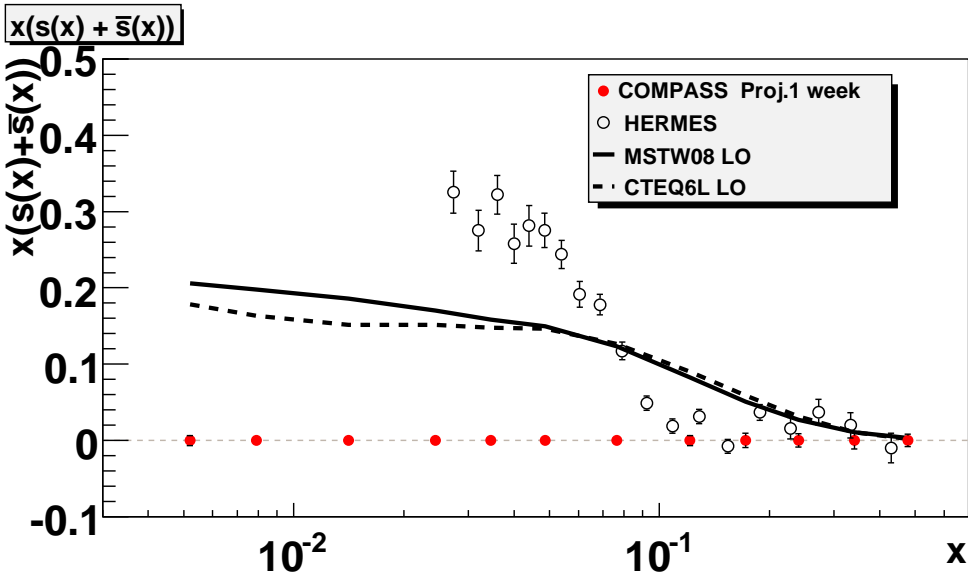


Figure 20: Projected statistical errors for  $s(x) + \bar{s}(x)$  for one week of data taking with a 2.5 m long liquid hydrogen target. Systematic errors are estimated to be of the order of 25% of the value of  $s$ . Also shown are the MSTW and CTEQ parametrisations at LO and the HERMES result.

multiplicities involve a product of PDFs and FFs. The possibility to disentangle them bases on factorisation, *i.e.*, PDFs depend only on  $x$  and FFs only on  $z$ .

An extensive and precise mapping of hadron multiplicities will be achieved for values of  $x$  as low as 0.004, *i.e.*, to a value ten times smaller than the lower  $x$  limit of HERMES which performed the only other SIDIS measurement. The data will be taken at higher average values of  $Q^2$  or  $W$ , which are a signature of the current fragmentation region. The particle identification by the RICH detector and by electromagnetic calorimeters will make it possible to identify various channels so that also the strange quark sector will be covered, for example  $K^+$ ,  $K^-$  and  $K^0$ .

The data will provide input to global analyses of FFs such as the one by DSS[70]. The advantage of SIDIS data is that they are sensitive to individual quark and antiquark flavours in the fragmentation process, which is not the case for  $e^+e^-$  annihilation data. In addition, the new data will be used on their own in a simple LO analysis to extract for instance  $s(x) + \bar{s}(x)$  and some poorly known FFs, as described below.

### 2.1.1 Strange quark distribution function

While light quark PDFs are well constrained, this is not the case for the strange quark and antiquark distribution functions  $s(x)$  and  $\bar{s}(x)$ , especially in the COMPASS  $x$  range. A better knowledge of  $s(x)$  is needed for the extraction of  $\Delta s$  from the measured quantity  $\Delta s(x)/s(x)$  and for physics issues relevant to LHC experiments.

Our present knowledge of PDFs comes from global analyses at NNLO (see Refs. [71, 72] and references therein) of inclusive data on hard scattering from fixed-target experiments and the HERA and Tevatron colliders. No semi-inclusive data are included in these analyses yet. The lack of knowledge on  $s(x)$  was reflected in the common practise of past PDF analyses to adopt the simplifying ansatz of  $s + \bar{s}$  being proportional to  $\bar{u} + \bar{d}$ . Only recently, PDF analyses started to treat  $s$  and  $\bar{s}$  separately including recent dimuon cross section data from NuTeV, which are sensitive to  $s$ .

HERMES [73] determined  $s(x) + \bar{s}(x)$  using SIDIS kaon data on a deuteron target and a simplified formula for the multiplicities at LO. The results disagree substantially with existing parametrisations. At  $x = 0.03$ , the HERMES value is twice higher than the CTEQ6L one and at  $x = 0.1$  it is close to zero, much below the CTEQ6L value (Fig. 20). COMPASS has taken similar data using the  ${}^6\text{LiD}$  target covering the range  $0.004 < x < 0.6$  that extends considerably to lower values than explored before. However, the proposed measurement on a pure hydrogen target will be substantially cleaner, as there will be no additional material in the target and secondary interactions will be less important.

We note another interesting possibility to determine  $s(x)$  and  $\bar{s}(x)$  separately by a measurement of the longitudinal spin transfer from polarised muons to  $\Lambda$  and  $\bar{\Lambda}$  hyperons, a measurement shown to be feasible at COMPASS [74].

### 2.1.2 Quark fragmentation functions

Our present knowledge on FFs is based on NLO analyses of single-inclusive hadron production which combine data from  $e^+e^-$  annihilation,  $pp$  collisions and deep inelastic lepton–proton scattering. The recent inclusion of SIDIS (HERMES) and  $pp$  (RHIC) data with charge identification [70] leads to significant progress, permitting to disentangle quark and antiquark fragmentation. However, there exist large discrepancies between various FF parametrisations. In particular, the huge uncertainties of FFs for fragmentation of light quarks into kaons and  $s$  quarks into any hadron are presently a major obstacle to the extraction of the strange-quark polarisation from polarised SIDIS data. An important piece of the nucleon spin puzzle is the contribution of strange quarks  $\Delta s$  to the total nucleon spin of 1/2. The first  $x$ -moment of  $\Delta s(x)$  was estimated to be significantly negative, of the order of  $-0.10$ , from inclusive polarised DIS measurements, while present semi-inclusive data from COMPASS and HERMES indicate values of the strange quark polarisation  $\Delta s(x)/s(x)$  that are very small or even compatible with zero in the measured  $x$  ranges [75]. This dilemma already caused theoretical debates [76]. However, COMPASS has shown that the SIDIS result on  $\Delta s(x)$  and the associated error can change by a factor of three depending on the choice of the quark-to-kaon FFs. In the next section, we show that with the proposed measurement on the hydrogen target kaon FFs can be determined with high statistical precision and a systematic uncertainty of the order of 25% of the signal value, already from a very short measurement. This will remove the above mentioned factor of three in the kaon FF uncertainty. Later, with the large data sets to be collected in the two years of the GPD programme, a multidimensional mapping of FFs as a function of (at least)  $x$  and  $z$  will be possible so that the systematic uncertainty will be drastically reduced.

When included in combined NLO analyses, the future SIDIS data on the proton for various identified hadrons will substantially increase the range in  $x$ ,  $Q^2$ , and  $z$  as well as the sensitivity of the FF parametrisation to the partonic flavours. Several additional results will be obtained on FFs. For instance, a model-independent method [77] can be used to derive non-singlet FFs using cross section differences between hadrons of opposite charges from a combination of proton and deuteron data.

Finally, it should be noted that the measurements of multiplicities are not limited by statistics but by systematic uncertainties. The dominant error comes from the determination of the acceptance of the apparatus. There will be mutual benefits with the GPD programme, for which an excellent understanding of the acceptance is mandatory.

### 2.1.3 Expected statistical precision

The final goal is to combine the measurements of all hadron multiplicities as a function of  $x$ ,  $z$  and  $Q^2$  obtained during the two years of data taking for the GPD programme, together with the existing deuteron data. The FFs and the PDFs will be extracted from global analyses. Already from a first sample of data collected in one week and using some reasonable assumptions, first physics results can be obtained. For instance, the unpolarised strange quark distribution function  $s(x) + \bar{s}(x)$  can be extracted from Eq. (21) using the charged kaon multiplicities as input and assuming that the non-strange PDFs  $u$ ,  $\bar{u}$ ,  $d$  and  $\bar{d}$  and all FFs are known. The expected statistical errors on  $s(x) + \bar{s}(x)$  were calculated using a Monte Carlo simulation based on LEPTO assuming one week of data taking with the 2.5 m long liquid hydrogen target in parallel to the data taking for the GPD programme. The values of the FFs  $D_u^K$ ,  $D_d^K$  and  $D_s^K$  were taken from DSS [70] and the non-strange PDFs  $u$ ,  $\bar{u}$ ,  $d$  and  $\bar{d}$  from MRST [78], all in LO. The resulting projections are shown in Fig. 20 together with the MSTW08 and CTEQ6L parametrisations and the HERMES results [73] obtained from kaon multiplicities on a deuterium target. It can be seen that COMPASS can reach small statistical errors already in one week. However, at that moment the dominant uncertainties will be the systematic ones which are essentially coming from the uncertainties on the fragmentation functions. If FFs will be known with an uncertainty of, *e.g.*, 25% as it will be discussed further below, this will affect the systematic uncertainty on  $s$  by the same amount. As a pure proton target will be used, no systematic uncertainties from nuclear effects exist.

Using the same initial sample of data and integrating over the variable  $z$ , one can extract the FFs at LO assuming that all PDFs are known. As an example, we show below how to extract quark-to-kaon FFs from the measured kaon multiplicities on the proton. In the following,  $D_q^K$  stands for  $\int D_q^K(z)dz$  for simplicity. Using Eq. (21) to describe separately the  $K^+$  and the  $K^-$  multiplicities, we obtain two equations involving twelve FFs. Assuming charge conjugation invariance in the fragmentation and assuming that all unfavoured FFs are equal, we are left with only three unknown FFs, namely

$$\begin{aligned} D_1 &= D_{\bar{s}}^{K^+} = D_s^{K^-} \\ D_2 &= D_u^{K^+} = D_{\bar{u}}^{K^-} \\ D_3 &= D_{\bar{u}}^{K^+} = D_d^{K^+} = D_{\bar{d}}^{K^+} = D_u^{K^-} = D_d^{K^-} = D_{\bar{d}}^{K^-} = D_s^{K^+} = D_{\bar{s}}^{K^-} \end{aligned}$$

Since FFs do not depend on  $x$  while the multiplicities and all PDFs do, the measured multiplicities of  $K^+$  and  $K^-$  in 12  $x$  bins provide 24 equations with 3 unknowns,  $D_1$ ,  $D_2$  and  $D_3$ . Note that the known  $Q^2$  dependence of the FFs can be taken into account in the calculation.

In order to estimate the statistical errors obtained on FFs from one week of data taking, the kaon multiplicities were calculated using a Monte Carlo simulation based on LEPTO with non-strange FFs taken from DSS and all PDFs from MRST. The simulation gives  $D_1 = 0.39 \pm 0.03$ ,  $D_2 = 0.11 \pm 0.002$  and  $D_3 = 0.03 \pm 0.012$ . As can be seen, very small statistical errors will already be obtained in one week, especially for the favoured FFs  $D_1$  and  $D_2$ . However, systematic errors on the acceptance determination are expected to dominate here. As an example, an uncertainty of the order of 25% is expected for  $D_1$  if kaon multiplicities are determined with a precision of 5%. Nevertheless, the result of such a short run has already an impact because presently the various predictions for  $D_1$  differ by a factor of three. The uncertainty on the unpolarised strange quark distribution

function will propagate directly into that of  $D_1$ . We note that a similar extraction can be done for the  $s$ -to-pion FF. Once high-statistics data will be available after two years of running, it will be possible to extract for the first time the FFs in a multidimensional binning in  $x$ ,  $z$ , and  $Q^2$ . Combining the new proton data with the existing deuteron data, more FFs will be determined in the analysis without assumptions.

## 2.2 Transverse-momentum-dependent effects in SIDIS

In SIDIS on an unpolarised target, hadron azimuthal asymmetries arise that give access to the distribution of intrinsic quark transverse momentum as encoded in the  $T$ -odd Boer–Mulders function (see also Sect. 3.2) and also to higher-twist effects.

The cross section for hadron production in SIDIS of longitudinally polarised leptons on unpolarised nucleons can be written as [79]

$$\frac{d\sigma}{dxdy d\phi_h} = \frac{\alpha^2}{xyQ^2} \frac{1 + (1 - y)^2}{2} \left[ F_{UU} + \varepsilon_1 \cos \phi_h F_{UU}^{\cos \phi_h} + \varepsilon_2 \cos 2\phi_h F_{UU}^{\cos 2\phi_h} + \lambda_\mu \varepsilon_3 \sin \phi_h F_{LU}^{\sin \phi_h} \right],$$

where  $\phi_h$  is the azimuthal angle of the outgoing hadron in the  $\gamma^*$ –nucleon system,  $\lambda_\mu$  is the value of the longitudinal beam polarisation and the  $\varepsilon_i$  are kinematical factors depending on  $y$ . In the three structure functions  $F_{UU}^{\cos \phi_h}$ ,  $F_{UU}^{\cos 2\phi_h}$ , and  $F_{LU}^{\sin \phi_h}$  the first and second subscripts denote beam and target polarisation, respectively, as earlier used in this document. In cross section asymmetries corresponding azimuthal asymmetries arise which can be extracted by fitting the  $\phi_h$  distribution.

At COMPASS energies, the azimuthal asymmetry  $A^{\cos \phi_h}$  arises mainly due to the Cahn effect [69] describing the non-collinear quark kinematics. It contains information on the mean value on the intrinsic quark transverse momentum [80]. The Boer–Mulders function is expected to yield an important contribution to the asymmetry  $A^{\cos 2\phi_h}$ , in which it appears coupled to the Collins fragmentation function that is now known to be different from zero. At hadron transverse momenta smaller than  $1 \text{ GeV}/c$ , the only other relevant contribution to this asymmetry is that from the Cahn effect. The measurement of  $A^{\cos 2\phi_h}$  and  $A^{\cos \phi_h}$  would thus allow the extraction of the Boer–Mulders function, once the Collins fragmentation function will be known sufficiently well. The third asymmetry involved in this measurement,  $A^{\sin \phi_h}$ , is expected to contain twist-3 TMDs.

In the past, these azimuthal asymmetries were measured by the EMC [81, 82], E665 [83] and ZEUS [84] experiments. The precision of these measurements was limited and all results were produced without separating hadrons according to their charge. Recently, COMPASS has produced preliminary results [85] on  $A^{\cos \phi_h}$ ,  $A^{\cos 2\phi_h}$  and  $A^{\sin \phi_h}$  from data collected with the 160 GeV muon beam and the  ${}^6\text{LiD}$  target which consists essentially of two deuterons and one  $\alpha$  particle. For the first time, separate results were given for positive and negative hadrons. The results for  $A^{\cos \phi_h}$  and  $A^{\cos 2\phi_h}$  as a function of  $x$  are shown by the black filled points in Fig. 21 in the upper and lower rows, respectively. The left (right) panels are for positive (negative) hadrons. The bands show the systematic uncertainties, which are mainly due to the correction for the apparatus acceptance, which is needed for these kind of asymmetries. As can be seen, the asymmetries are different from zero and different for positive and negative hadrons, indicating Boer–Mulders functions being different from zero. The asymmetry  $A^{\sin \phi_h}$  (not shown in Fig. 21) is consistent with zero. HERMES has recently produced preliminary results for charged pions from data collected with  $p$  and  $d$  targets and a 27.5 GeV electron beam [86]. In their data, the measured

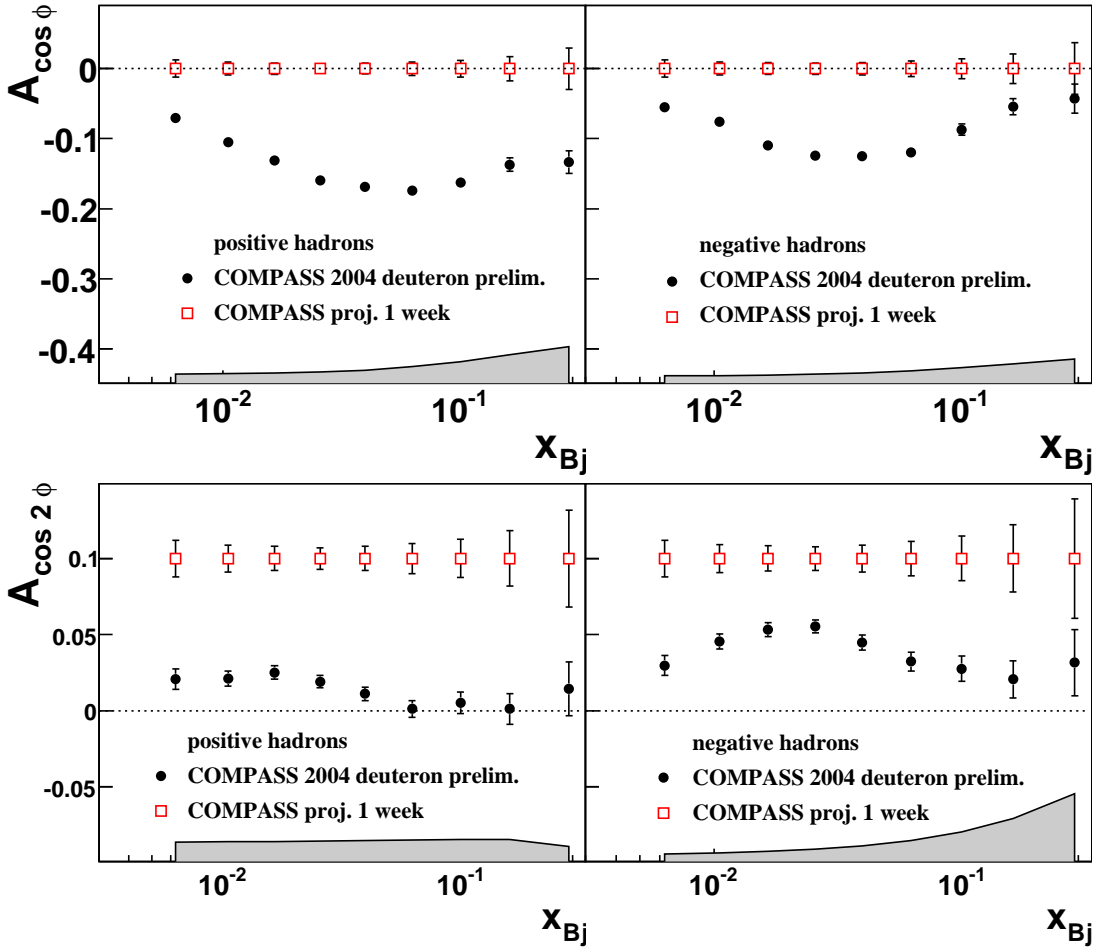


Figure 21: Projected statistical errors (red open squares) for  $A_{\cos\phi}$  (upper plots) and  $A_{\cos^2\phi}$  asymmetries (lower plots) for positive (left) and negative (right) hadrons for one week of data with the LH target. The black closed spheres with the grey bands for systematic errors correspond to preliminary results on  ${}^6\text{LiD}$  [85]. For the new measurement the systematic errors are expected to be considerably reduced.

values for  $A^{\cos\phi_h}$  and  $A^{\cos^2\phi_h}$  are quite similar for proton and deuteron. They are different from zero and differ between positive and negative pions. The results on  $A^{\cos^2\phi_h}$  from COMPASS and HERMES have already been used for a first, model-dependent extraction of the Boer–Mulders functions [87].

Given the relevance of TMD effects for the understanding of nucleon structure, measurements of all these azimuthal asymmetries in SIDIS on unpolarised protons at high energies are highly desirable, and only COMPASS could perform them in the near future. The data already collected by COMPASS with the polarised proton target can not be used by averaging the polarisation, since the target material is  $\text{NH}_3$ . In order to study the feasibility of such a measurement in parallel with the GPD programme, we have estimated the expected statistical error for one week of running (corresponding to  $6 \times 10^{12}$  integrated muons on the target) with the 2.5 m long liquid hydrogen target. The result is shown as red open squares in Fig. 21. The estimation is based on the previous analysis [85] and was done assuming the same data selection. This includes the standard DIS cuts ( $Q^2 > 1 \text{ (GeV}/c^2)$ , mass of the hadronic final state  $W > 5 \text{ GeV}/c^2$ ,  $0.1 < y < 0.9$ ) and the detection of at

least one hadron in the final state with  $0.2 < z < 0.85$  and transverse momentum between  $0.1 \text{ GeV}/c$  and  $1.5 \text{ GeV}/c$ . For one week of running, the statistical errors are expected to be larger than those in Ref. [85] by a factor of 1.8. The systematic uncertainties are expected to be considerably reduced with respect to those shown in Fig. 21 because the geometrical acceptance will be known much better than in the past runs. The new measurement will thus produce accurate results for these azimuthal asymmetries, and the study of their dependence on various kinematic variables will also be possible.

The use of the RICH detector for particle identification will allow the measurement of these azimuthal asymmetries for charged pions and kaons separately, which is an important ingredient for flavour separation. Since the percentage of identified pions (kaons) is of the order of 70% (10%), the statistical errors on the modulations shown in Fig. 21 will be larger by a factor of 1.2 and 3.2 for identified pions and kaons, respectively.

### 3 Pion-induced Drell–Yan muon pair production

#### 3.1 Transverse spin-dependent structure of the nucleon

Spin and transverse momentum dependent semi-inclusive hadronic processes have attracted much interest from both experiment and theory in recent years. These processes provide more opportunities than inclusive hadronic processes to study Quantum Chromodynamics (QCD) and the internal structure of hadrons. Single transverse spin asymmetries (SSAs) were observed in various reactions, such as  $H_a + H_b \rightarrow H + X$ ,  $l + H \rightarrow H' + X$ ,  $H_a + H_b \rightarrow l + l' + X$  and  $l^+ + l^- \rightarrow H_a + H_b + X$  [88–99] where a hadron (lepton) is indicated by  $H$  ( $l$ ). This stimulated remarkable theoretical developments; among them two approaches in the QCD framework have been most explored: the transverse momentum dependent approach and the higher-twist collinear factorisation approach. The first one deals with TMDs in the QCD transverse-momentum-dependent (QCD-TMD) factorisation approach that is valid at small transverse momentum  $k_T \ll Q$  (see Refs. [79, 100] and references therein). Such functions generalise Feynman’s original parton picture, where the partons only carry a longitudinal momentum fraction of the parent hadron’s momentum. In the second approach [101] the spin-dependent differential cross sections can be calculated in terms of collinear twist-3 quark–gluon correlation functions in the formalism of collinear factorisation. This approach is applicable for large transverse momentum  $k_T \gg \Lambda_{QCD}$ . Recently, it was shown that the above sketched two approaches are consistent in the intermediate transverse momentum region  $\Lambda_{QCD} \ll k_T \ll Q$ , where both apply [101]. Since Drell–Yan events are expected to occur at COMPASS mainly at small transverse momentum we will discuss in the following only the first, namely the QCD-TMD factorisation based approach.

At leading twist, the quark structure of the hadron is completely described by three PDFs: the unpolarised distribution function  $f_1(x)$  describing the probability of finding a quark with a fraction  $x$  of the longitudinal momentum of the parent hadron regardless of its spin orientation, the helicity distribution  $g_1(x)$  describing the difference between the number densities of quarks with spin parallel and antiparallel to the spin of the longitudinally polarised parent hadron, and transversity  $h_1(x)$ , a function similar to  $g_1(x)$  but for transversely polarised hadrons. The latter is chiral-odd [102], *i.e.* it mixes left-handed and right-handed partons, while QCD in massless and collinear approximation, as it is actually calculable with perturbative methods, preserves helicity. There exist several experimental observations of large azimuthal and spin asymmetries (also at beam energies of 184 GeV and 252 GeV) which perturbative QCD at leading twist (twist-2) in collinear approximation can not explain. In particular, large asymmetric azimuthal distributions of final-state leptons measured in high-energy collisions of pions and antiprotons with nuclei [103–105] show a striking deviation from the so-called Lam-Tung sum rule [106, 107] that is based on collinear perturbative QCD, and seem to indicate the need to go beyond the collinear approximation. When considering non-zero quark transverse momentum  $\mathbf{k}_T$  with respect to the hadron momentum, the nucleon structure is described at leading twist by eight PDFs:<sup>2)</sup>  $f_1(x, \mathbf{k}_T^2)$ ,  $g_{1L}(x, \mathbf{k}_T^2)$ ,  $h_1(x, \mathbf{k}_T^2)$ ,  $g_{1T}(x, \mathbf{k}_T^2)$ ,  $h_{1T}^\perp(x, \mathbf{k}_T^2)$ ,  $h_{1L}^\perp(x, \mathbf{k}_T^2)$ ,  $h_1^\perp(x, \mathbf{k}_T^2)$  and  $f_{1T}^\perp(x, \mathbf{k}_T^2)$ . The first three functions, when integrated over  $\mathbf{k}_T^2$ , yield  $f_1(x)$ ,  $g_1(x)$  and  $h_1(x)$ , respectively. The last two are  $T$ -odd PDFs. The Boer–Mulders function  $h_1^\perp(x, \mathbf{k}_T^2)$  describes the correlation between transverse spin and transverse momentum of the quark in an unpolarised nucleon. The Sivers function  $f_{1T}^\perp(x, \mathbf{k}_T^2)$  describes the influence of the transverse spin of the nucleon onto the quark transverse momentum

<sup>2)</sup> We are using the so called Amsterdam notations [68]

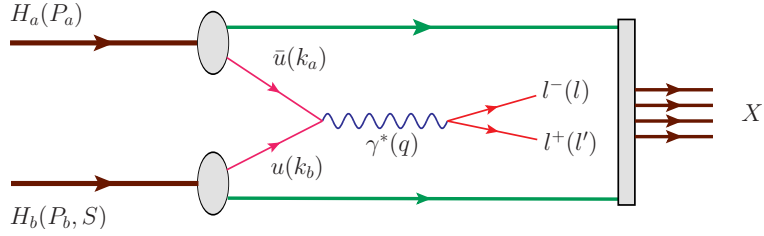


Figure 22: Feynman diagram of the Drell–Yan process: annihilation of a quark–antiquark pair into a lepton pair.

distribution. A correlation between  $\mathbf{k}_T$  and the transverse polarisation of a parton/hadron is intuitively possible only for non-vanishing orbital angular momentum of the quarks themselves. Hence, determinations of  $h_1^\perp$  and  $f_{1T}^\perp$  as well as of  $h_1$  are of great interest to further reveal the partonic (spin) structure of hadrons (see, *e.g.* Ref. [102] for a review). In this proposal, we concentrate mainly on transversity  $h_1$ , and the  $T$ -odd Boer–Mulders ( $h_1^\perp$ ) and Sivers ( $f_{1T}^\perp$ ) functions.

The Drell–Yan quark–antiquark annihilation process is an excellent tool to study transversity and  $\mathbf{k}_T$ -dependent  $T$ -odd PDFs. In the DY process (Fig. 22) quark and antiquark annihilate into a lepton pair. Other kinds of hard processes can also access chirally odd PDFs, like semi-inclusive deep-inelastic scattering (SIDIS) where chirality is conserved through the convolution of PDFs with polarised quark fragmentation functions. There exist no fragmentation process in DY. In order to access spin structure information a high-intensity hadron beam and a large-acceptance set-up as well as a high-performance polarised target are required. These features are provided by the multipurpose large-acceptance COMPASS spectrometer in combination with the SPS M2 secondary beam line and the large-acceptance polarised target. In more detail, the COMPASS experiment is characterised by the availability of:

- a transversely polarised solid-state proton target with a high polarisation and a long relaxation time in frozen-spin mode,
- intense secondary hadron beams of intensities up to  $10^9$  hadrons/spill,
- a detection system designed to stand high particle fluxes.

### 3.2 SIDIS contributions to transversity and TMDs

Much of the information that exists today about transversity and TMDs comes from SIDIS measurements with unpolarised and polarised beams and targets. In the SIDIS cross section, transversity and TMDs appear in azimuthal asymmetries which are convolutions of PDFs and fragmentation functions (FFs) and which can be obtained from angular distributions of final-state hadrons. Thus, if the FFs are known, one can access the PDFs for different quark flavours from SIDIS measurements of identified hadrons, produced with different polarised targets. As will become clear in the next sections, these measurements are complementary to those by DY experiments which measure convolutions of only PDFs without involving FFs.

In the past eight years, first measurements of SIDIS with transversely polarised targets were performed by the COMPASS and the HERMES Collaborations at beam energies of 160 GeV and 27.5 GeV, respectively. The measurements of the Collins asymmetry on the deuteron (found compatible with zero) by COMPASS [93, 108, 109] and on the proton (found clearly different from zero both for positive and negative pions) by HERMES

[92, 110], together with the results on azimuthal asymmetries in  $e^+e^- \rightarrow h^\pm h^\mp X$  produced by the BELLE Collaboration [98, 99] provide a consistent phenomenological picture which permitted the extraction of the Collins FF and of the  $u$  and  $d$  quark transversity functions [111]. COMPASS [93, 108, 109] and HERMES [112] have also measured the Sivers asymmetries on the deuteron and the proton. The asymmetries were found to be different from zero only on the proton, for positive pions and kaons. From global fits to these data, first extractions of the Sivers functions have been performed [113].

Very recently, COMPASS has finalised the analysis of the entire set of data collected in 2007 with transversely polarised protons and a 160 GeV muon beam [114]. The Collins asymmetry is found to be different from zero in the valence region both for positive and negative hadrons also at this higher energy. Thus it is not a higher-twist effect. For what concerns the Sivers asymmetry, the preliminary results [115], based on about half of the collected statistics, were found to be compatible with zero. The final results [114] from the full sample are still compatible with zero for negative hadrons while for positive hadrons they show a positive signal, smaller but still compatible with that measured by HERMES, and suggest a possible dependence of the Sivers asymmetry on the invariant mass of the hadronic final state. These open questions will be further elucidated by the new, higher precision measurement COMPASS/ will perform in 2010. When averaging over the target polarisation, azimuthal asymmetries for an unpolarised target can also be extracted. COMPASS [85] and HERMES [86] have already produced preliminary results for the  $\cos 2\phi_h$  asymmetry, to which the Boer–Mulders function contributes. From these data a first model-dependent extraction of the Boer–Mulders function has been performed [87]. For these spin-independent azimuthal asymmetries on the proton, significant measurements will be performed in parallel with the DVCS measurement proposed earlier in this document.

In summary, a lot of progress has been made in understanding the transverse spin and momentum structure of the nucleon by SIDIS measurements. However, since in SIDIS and DY the amplitudes of azimuthal modulations are convolutions of PDFs and FFs on the one hand, and of only PDFs on the other, pursuing both types of measurements with the same apparatus will be unique at COMPASS.

### 3.3 Drell–Yan formalism and observables

#### 3.3.1 Kinematics of the Drell–Yan process

Here we describe notations, the choice of reference frames and the general expression for the Drell–Yan cross section closely following the article by Arnold, Metz and Schlegel [100]. We only consider the reaction with an unpolarised beam ( $H_a$ ) and a polarised target ( $H_b$ )

$$H_a(P_a) + H_b(P_b, S) \rightarrow \gamma^*(q) + X \rightarrow l^-(l) + l^+(l') + X, \quad (22)$$

where  $P_{a(b)}$  is the momentum of the beam (target) hadron;  $l$ ,  $l'$  and  $q = l + l'$  are the momenta of the lepton, the antilepton and of the virtual photon, respectively, and  $S$  is the 4-vector of the target polarisation. Further, the following kinematical variables will be used:

$s = (P_a + P_b)^2,$	the total centre-of-mass energy squared,
$x_{a(b)} = q^2/(2P_{a(b)} \cdot q),$	the momentum fraction carried by a parton from $H_{a(b)}$ ,
$x_F = x_a - x_b,$	the Feynman variable,
$M_{\mu\mu}^2 = Q^2 = q^2 = s x_a x_b,$	the invariant mass squared of the dimuon.

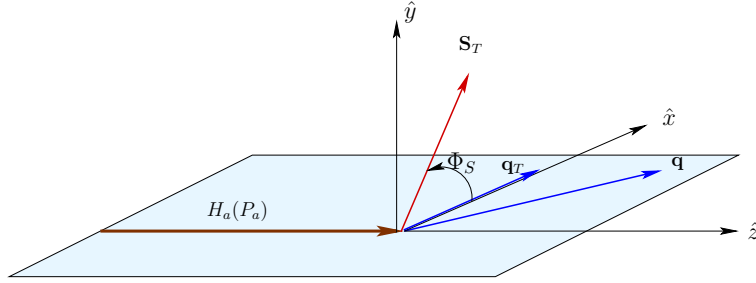


Figure 23: Definition of the azimuthal angle  $\phi_S$  of transverse target spin  $\mathbf{S}_T$  in the target rest frame.

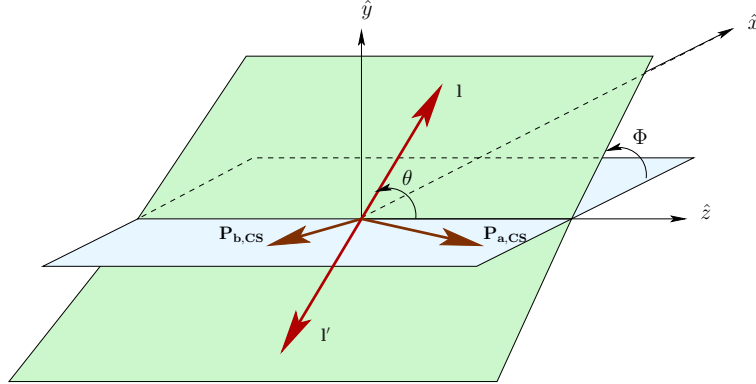


Figure 24: Definition of polar and azimuthal angles  $\theta$  and  $\phi$  of the lepton momenta in the Collins–Soper frame.

The dependence of the DY cross section on the target spin and on the polar and azimuthal angles of the out-going leptons is commonly described using two coordinate systems:

1. The target rest frame (TF) is defined by the unit vectors  $\hat{z}$  along the momentum of the beam hadron,  $\hat{x}$  along the transverse component  $q_T$  of the virtual photon momentum and finally  $\hat{y} = \hat{z} \times \hat{x}$  (Fig. 23), yielding

$$P_{a,TF}^\mu = (P_{a,TF}^0, 0, 0, P_{a,TF}^3), \quad (23)$$

$$P_{b,TF}^\mu = (M_b, 0, 0, 0), \quad (24)$$

$$q_{TF}^\mu = (q_{TF}^0, q_T, 0, q_{TF}^3), \quad (25)$$

$$S_{TF}^\mu = (0, S_T \cos \phi_S, S_T \sin \phi_S, S_L), \quad (26)$$

where the polarisation vector is normalised as  $S^2 = -1$ .

2. The Collins–Soper frame (CS) is the rest frame of the virtual photon. It is obtained from the TF by boosting first along  $\hat{z}$  and then along  $\hat{x}$  so that both the longitudinal and the transverse momenta of the virtual photon vanish (Fig. 24). Neglecting the lepton mass, the lepton and antilepton momenta in this frame are given as

$$l_{CS}^\mu = \frac{q}{2} (1, \sin \theta \cos \phi, \sin \theta \sin \phi, \cos \theta), \quad (27)$$

$$l'_{CS}^\mu = \frac{q}{2} (1, -\sin \theta \cos \phi, -\sin \theta \sin \phi, -\cos \theta). \quad (28)$$

In the following we shall use the azimuthal angle  $\phi_S$  of the target polarisation vector  $\mathbf{S}_T$  in the TF (Fig. 23), and the polar and azimuthal angles  $\theta$  and  $\phi$  of the lepton momentum in the CS frame (Fig. 24).

### 3.3.2 General expression for the Drell–Yan cross section

The general form for the Drell–Yan cross section with polarised nucleons in the initial state, expressed in the above described angular variables, can be found in Ref. [100]. We are interested in the case when only the target nucleon is polarised. Then (for details see Ref. [116]), the general expression looks simpler

$$\begin{aligned} \frac{d\sigma}{d^4q d\Omega} &= \frac{\alpha_{em}^2}{F q^2} \hat{\sigma}_U \left\{ \left( 1 + D_{[\sin 2\theta]} A_U^{\cos \phi} \cos \phi + D_{[\sin^2 \theta]} A_U^{\cos 2\phi} \cos 2\phi \right) \right. \\ &\quad + S_L \left( D_{[\sin 2\theta]} A_L^{\sin \phi} \sin \phi + D_{[\sin^2 \theta]} A_L^{\sin 2\phi} \sin 2\phi \right) \\ &\quad + |\mathbf{S}_T| \left[ \left( D_{[1]} A_T^{\sin \phi_S} + D_{[\cos^2 \theta]} \tilde{A}_T^{\sin \phi_S} \right) \sin \phi_S \right. \\ &\quad + D_{[\sin 2\theta]} \left( A_T^{\sin(\phi+\phi_S)} \sin(\phi + \phi_S) + A_T^{\sin(\phi-\phi_S)} \sin(\phi - \phi_S) \right) \\ &\quad \left. \left. + D_{[\sin^2 \theta]} \left( A_T^{\sin(2\phi+\phi_S)} \sin(2\phi + \phi_S) + A_T^{\sin(2\phi-\phi_S)} \sin(2\phi - \phi_S) \right) \right] \right\}, \end{aligned} \quad (29)$$

where  $F = 4\sqrt{(P_a \cdot P_b)^2 - M_a^2 M_b^2}$  represents the flux of incoming hadrons, the solid angle  $\Omega$  specifies the orientation of the lepton and the depolarisation factor is given by

$$D_{[f(\theta)]} = \frac{f(\theta)}{1 + A_U^1 \cos^2 \theta}. \quad (30)$$

In Eq. (29) the part of the cross section which survives after integration over the azimuthal angles  $\phi$  and  $\phi_S$ ,

$$\hat{\sigma}_U = (F_U^1 + F_U^2)(1 + A_U^1 \cos^2 \theta), \quad (31)$$

is factored out. The azimuthal asymmetries<sup>3)</sup>  $A_P^{f(\phi,\phi_S)}$  (ten in total) are given as ratios of combinations of structure functions  $F_P^{f(\phi,\phi_S)}$  to  $F_U^1 + F_U^2$  with  $P = U, T, L$ . These structure functions appear in the decomposition of the hadronic tensor characterising the process of Eq. (22) in the one-photon-exchange approximation. In general, they depend on three independent variables, for example, on the Lorentz-invariant ones  $P_a \cdot q$ ,  $P_b \cdot q$ , and  $q^2$ , *i.e.*  $F_U^1 = F_U^1(P_a \cdot q, P_b \cdot q, q^2)$  etc. and do not depend on the polar angle  $\theta$  and the azimuthal angles  $\phi$  and  $\phi_S$ . In Eqs. (29)–(31) the subscript of structure functions and asymmetries corresponds to the polarisation state of the target nucleon ( $U$  for target-polarisation-independent contributions,  $L$  and  $T$  for contributions from longitudinal and transverse target polarisations, respectively) and the superscript describes the azimuthal modulation. The relations between our notation and the structure functions introduced in Ref. [100] are given in a separate note [116]. Explicit expressions for asymmetries in the LO QCD parton model are given in Sect. 3.3.3.

We note that upon integration over the lepton azimuthal angle  $\phi$  only one azimuthal asymmetry survives in Eq. (29), namely the transverse spin-dependent  $\sin \phi_S$  asymmetry.

---

<sup>3)</sup> For unpolarised azimuthal asymmetries often another notation is used:  $\lambda = A_U^1$ ,  $\mu = A_U^{\cos \phi}$  and  $\nu = 2 A_U^{\cos 2\phi}$  [106, 117].

### 3.3.3 Asymmetries in the LO QCD parton model

According to the factorisation theorem, the structure functions of Drell–Yan processes can be expressed at high energies ( $s, Q^2 \gg M_a^2, M_b^2$ ) and small transverse momentum of the virtual photon ( $q_T \ll q$ ) as a convolution over TMDs [100]. These convolutions are defined in intrinsic-transverse-momentum space as

$$\begin{aligned} \mathcal{C} [w(\mathbf{k}_{aT}, \mathbf{k}_{bT}) f_1 \bar{f}_2] &\equiv \frac{1}{N_c} \sum_q e_q^2 \int d^2 \mathbf{k}_{aT} d^2 \mathbf{k}_{bT} \delta^{(2)}(\mathbf{q}_T - \mathbf{k}_{aT} - \mathbf{k}_{bT}) w(\mathbf{k}_{aT}, \mathbf{k}_{bT}) \times \\ &\quad \left[ f_1^q(x_a, \mathbf{k}_{aT}^2) f_2^{\bar{q}}(x_b, \mathbf{k}_{bT}^2) + f_1^{\bar{q}}(x_a, \mathbf{k}_{aT}^2) f_2^q(x_b, \mathbf{k}_{bT}^2) \right], \end{aligned} \quad (32)$$

where  $N_c = 3$  is the number of colours.

For the case of a transversely polarised target and keeping only terms surviving in the LO QCD parton model, Eq. (29) simplifies to

$$\begin{aligned} \frac{d\sigma}{d^4 q d\Omega} &\stackrel{\text{LO}}{=} \frac{\alpha_{em}^2}{F q^2} \hat{\sigma}_U \left\{ \left( 1 + D_{[\sin^2 \theta]} A_U^{\cos 2\phi} \cos 2\phi \right) \right. \\ &+ |S_T| \left[ A_T^{\sin \phi_S} \sin \phi_S + D_{[\sin^2 \theta]} \left( A_T^{\sin(2\phi + \phi_S)} \sin(2\phi + \phi_S) \right. \right. \\ &+ \left. \left. A_T^{\sin(2\phi - \phi_S)} \sin(2\phi - \phi_S) \right) \right] \left. \right\}, \end{aligned} \quad (33)$$

where

$$\hat{\sigma}_U \stackrel{\text{LO}}{=} F_U^1 (1 + \cos^2 \theta) \quad (34)$$

and the depolarisation factor depends only on the lepton polar angle  $\theta$

$$D_{[f(\theta)]} \stackrel{\text{LO}}{=} \frac{f(\theta)}{1 + \cos^2 \theta}. \quad (35)$$

The non-vanishing asymmetries at LO are given as ratios of corresponding structure functions to the unpolarised structure function

$$F_U^1 \stackrel{\text{LO}}{=} \mathcal{C} [f_a \bar{f}_a] \quad (36)$$

as

$$A_U^{\cos 2\phi} \stackrel{\text{LO}}{=} \mathcal{C} \left[ \left( 2(\mathbf{h} \cdot \mathbf{k}_{aT})(\mathbf{h} \cdot \mathbf{k}_{bT}) - \mathbf{k}_{aT} \cdot \mathbf{k}_{bT} \right) h_1^\perp \bar{h}_1^\perp \right] / M_a M_b F_U^1, \quad (37)$$

$$\begin{aligned} A_T^{\sin \phi_S} &\stackrel{\text{LO}}{=} \tilde{A}_T^{\sin \phi_S} \\ &\stackrel{\text{LO}}{=} \mathcal{C} [\mathbf{h} \cdot \mathbf{k}_{bT} f_1 \bar{f}_{1T}^\perp] / M_b F_U^1, \end{aligned} \quad (38)$$

$$\begin{aligned} A_T^{\sin(2\phi + \phi_S)} &\stackrel{\text{LO}}{=} -\mathcal{C} \left[ \left( 2(\mathbf{h} \cdot \mathbf{k}_{bT}) [2(\mathbf{h} \cdot \mathbf{k}_{aT})(\mathbf{h} \cdot \mathbf{k}_{bT}) - \mathbf{k}_{aT} \cdot \mathbf{k}_{bT}] - \mathbf{k}_{bT}^2 (\mathbf{h} \cdot \mathbf{k}_{aT}) \right) h_1^\perp \bar{h}_{1T}^\perp \right] \\ &/ 4 M_a M_b^2 F_U^1, \end{aligned} \quad (39)$$

$$A_T^{\sin(2\phi - \phi_S)} \stackrel{\text{LO}}{=} -\mathcal{C} [\mathbf{h} \cdot \mathbf{k}_{aT} h_1^\perp \bar{h}_1] / 2 M_a F_U^1, \quad (40)$$

where  $\mathbf{h} = \mathbf{q}_T/q_T$ . The arguments of the PDFs,

$$x_a = \frac{q^2}{2P_a \cdot q} \quad \text{and} \quad x_b = \frac{q^2}{2P_b \cdot q}, \quad (41)$$

can be interpreted as the fraction of the light-cone momentum carried by the interacting parton in the incoming hadrons  $H_a$  and  $H_b$ , respectively. We see from Eqs. (37)–(40) that the measurement of the asymmetry:

- $A_U^{\cos 2\phi}$  gives access to the Boer–Mulders functions of the incoming hadrons,
- $A_T^{\sin \phi_S}$  to the Sivers function of the target nucleon,
- $A_T^{\sin(2\phi+\phi_S)}$  to the Boer–Mulders function of the beam hadron and to  $h_{1T}^\perp$ , the pretzelosity function of the target nucleon,
- $A_T^{\sin(2\phi-\phi_S)}$  to the Boer–Mulders function of the beam hadron and  $h_1$ , the transversity function of the target nucleon.

Within the QCD TMDs approach, the remaining asymmetries in the general expression for the Drell–Yan cross section Eq. 29 can be interpreted as kinematic corrections of higher order in  $q_T/q$  or as contribution of non-leading twist PDFs.

### 3.3.4 Observables

The Sivers and Boer–Mulders TMDs are  $T$ -odd objects. Their field-theoretical definition involves a non-local quark–quark correlator which contains the so-called gauge-link operator. While ensuring the colour-gauge invariance of the correlator, this gauge-link operator makes the Sivers and the Boer–Mulders functions process dependent. In fact, on general grounds it is possible to show that the  $f_{1T}^\perp$  and the  $h_1^\perp$  functions extracted from Drell–Yan processes and those obtained from semi-inclusive DIS should have opposite sign [118], *i.e.*

$$f_{1T}^\perp \Big|_{DY} = -f_{1T}^\perp \Big|_{DIS} \quad \text{and} \quad h_1^\perp \Big|_{DY} = -h_1^\perp \Big|_{DIS}. \quad (42)$$

It is important to note that sensitivity to the sign of the Boer–Mulders function exists only in the polarised Drell–Yan process. For the unpolarised Drell–Yan process the azimuthal  $\cos 2\phi$  asymmetry contains a convolution of two Boer–Mulders functions, while in the polarised DY process the Boer–Mulders function appears also coupled to other TMDs, *e.g.* transversity. A clear observation of a non-zero Sivers distribution has been reported by the HERMES [91, 110] and COMPASS [93] Collaborations. The global analysis of these data [113] led to the extraction of  $f_{1T}^\perp \Big|_{DIS}$ . By measuring the asymmetry  $A_T^{\sin \phi_S}$ , which is given by a convolution of the pion  $f_1$  PDF and the nucleon Sivers function (Eq. (38)). We shall perform the first experimental verification of the sign-reversal property of the Sivers function.

Also the asymmetry related to transversity was rather well measured in polarised SIDIS by HERMES [91, 110] and COMPASS [93]. A global analysis combining those data with that of BELLE [98, 99] already exists [119, 120]. Preliminary results on the SIDIS asymmetry related to pretzelosity were reported by COMPASS for the polarised deuteron [121]. As mentioned in the previous section, the measurement proposed in this document will allow us to access the pretzelosity and transversity functions  $h_{1T}^\perp$  and  $h_1$ , respectively (Eqs. (39) and (40)). To this end, the knowledge of the Boer–Mulders function of the pion is needed. There are two different scenarios to evaluate this function:

1. measure the asymmetry  $A_T^{\sin(2\phi-\phi_S)}$  and use the parametrisation of  $h_1$  from Refs. [119, 120] to extract the Boer–Mulders functions of the pion;
2. use the already existing information on  $A_U^{\cos 2\phi}$  and the information on the Boer–Mulders function of the target nucleon. This asymmetry was measured in the unpolarised  $\pi + N$  Drell–Yan process by the NA10 and E615 Collaborations [103, 105, 122] two decades ago and recently by the E866/NuSea Collaboration at FNAL [123, 124] in the  $p + N$  Drell–Yan reaction. Recently, the first extraction of the proton Boer–Mulders function from the analysis of E866/NuSea data was reported [125]. Also in SIDIS, the nucleon Boer–Mulders function is expected to generate the same

kind of asymmetry and the recently released COMPASS [85, 126] and HERMES [86] data [68] confirm this expectation. The very recent analysis [87] of these data shows that one can constrain the valence quark Boer–Mulders function of the proton.

By performing measurements of target-spin-(in)dependent asymmetries in the Drell–Yan reaction and comparing the results with the ones measured in SIDIS we will be able to verify the universality of the TMD approach for the description of these reactions. This would constitute an important test of QCD in the non-perturbative regime.

### 3.3.5 Study of the $J/\psi$ production mechanism and $J/\psi$ –DY duality

In spite of the large amount of experimental data on  $J/\psi$  production in various reactions accumulated so far, the production mechanism is still unclear. The data on the unpolarised  $J/\psi$  production cross sections in the process  $H_a H_b \rightarrow J/\psi X \rightarrow l^+ l^- X$ , integrated over the angles  $\theta$  and  $\phi$  (polar and azimuthal angles of the positive lepton in the dilepton centre of mass frame) allows one to construct models that use the usual unpolarised quark and gluon PDFs  $q(x)$  and  $g(x)$ . The most popular, widely used model is the “gluon evaporation” model (see Ref. [127] and references therein). For the angle-integrated cross section this model predicts for  $x_F > 0$

$$\sigma \Big|_{H_a H_b \rightarrow J/\psi X \rightarrow l^+ l^- X} = \sigma_{q\bar{q}} + \sigma_{gg}, \quad (43)$$

$$\sigma_{q\bar{q}(gg)} = \int_{4m_c^2}^{4m_D^2} dQ^2 \int_0^{1 - \frac{Q^2}{s}} dx_F \sigma^{q\bar{q}(gg) \rightarrow c\bar{c}}(Q^2) \frac{x_a x_b}{Q^2(x_a + x_b)} F_{q\bar{q}(gg)}^{H_a H_b}, \quad (44)$$

where the quark–antiquark and gluon–gluon fluxes  $F_{q\bar{q}}^{H_a H_b}$  and  $F_{gg}^{H_a H_b}$  are given by

$$F_{q\bar{q}}^{H_a H_b} = \sum_{q=u,d,s} [q^{H_a}(x_a)\bar{q}^{H_b}(x_b) + \bar{q}^{H_a}(x_a)q^{H_b}(x_b)], \quad F_{gg}^{H_a H_b} = g^{H_a}(x_a)g^{H_b}(x_b) \quad (45)$$

and the  $c\bar{c}$  and open charm thresholds are  $2m_c = 3.0$  GeV and  $2m_D = 3.74$  GeV, respectively. The elementary cross sections  $\sigma^{q\bar{q} \rightarrow c\bar{c}}$  and  $\sigma^{gg \rightarrow c\bar{c}}$  are proportional to  $\alpha_s(Q^2)$  and can be found, *e.g.* in Ref. [127] (Eqs. (3) and (4) therein). It is important to note that the application of Eq. (43) allows to quantitatively control the quark and gluon contributions and to estimate when the former becomes dominant (which leads to the simple and very useful “duality” model, see below). If the angular dependencies are included, the lack of data does not allow to construct a model like Eq. (43) and produce quantitative predictions even in the purely unpolarised case. In the absence of a general theoretical model that can quantitatively describe the  $J/\psi$  production mechanism, a model based on the close analogy (duality) between the Drell–Yan process  $H_a H_b \rightarrow \gamma^* X \rightarrow l^+ l^- X$  and  $J/\psi$  production  $H_a H_b \rightarrow J/\psi X \rightarrow l^+ l^- X$  attained much interest [128–130]. It is assumed that such an analogy/duality occurs at relatively low energies when the quark–antiquark ( $\bar{q}q$ ) fusion mechanism dominates over the gluon–gluon ( $gg$ ) fusion mechanism in  $J/\psi$  production. Since the  $J/\psi$  is a vector particle like the  $\gamma$  and the helicity structure of  $\bar{q}q(J/\psi)$  and  $(\bar{q}q)\gamma^*$  couplings is the same, one can obtain the  $J/\psi$  production cross section from the DY cross section applying the simple replacements

$$16\pi^2 \alpha^2 e_q^2 \rightarrow (g_q^{J/\psi})^2 (g_\ell^{J/\psi})^2, \quad \frac{1}{M^4} \rightarrow \frac{1}{(M^2 - M_{J/\psi}^2)^2 + M_{J/\psi}^2 \Gamma_{J/\psi}^2}, \quad (46)$$

where  $M^2 \equiv Q^2$  is the squared mass of the dilepton pair,  $M_{J/\psi}^2 \simeq 9.59$  GeV $^2$  is the squared  $J/\psi$  mass and  $\Gamma_{J/\psi}$  is the full  $J/\psi$  width. It is believed that the duality model Eq. (46)

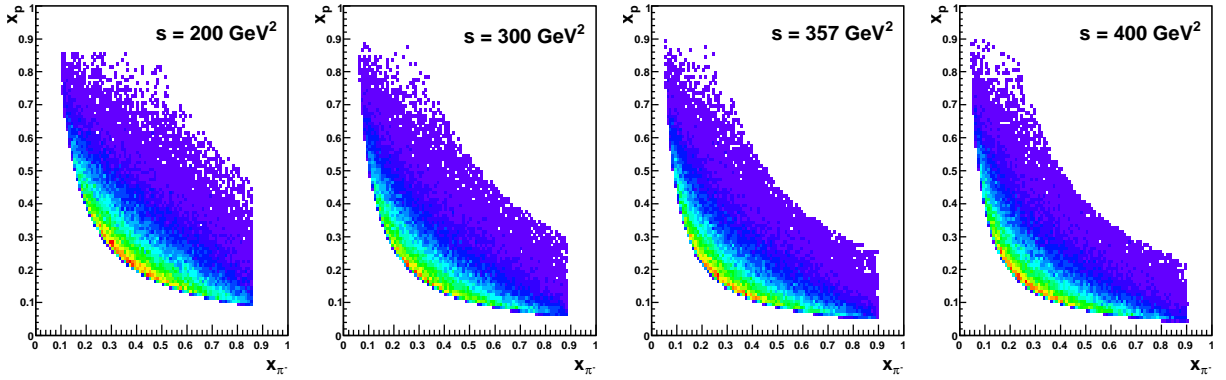


Figure 25: Phase space for the Drell–Yan process  $\pi^- p^+ \rightarrow \mu^+ \mu^- X$  in the dimuon mass range  $4 \text{ GeV}/c^2 < M_{\mu\mu} < 9 \text{ GeV}/c^2$ , for different values of centre of mass energy squared:  $s = 200 \text{ GeV}^2$ ,  $s = 300 \text{ GeV}^2$ ,  $s = 357 \text{ GeV}^2$  and  $s = 400 \text{ GeV}^2$  (corresponding to the beam momenta of  $106 \text{ GeV}/c$ ,  $160 \text{ GeV}/c$ ,  $190 \text{ GeV}/c$  and  $213 \text{ GeV}/c$ , respectively).

can be applied in both unpolarised [129] and polarised [128] cases. The latter is due to the identical helicity and vector structure of the  $\gamma^*$  and  $J/\psi$  elementary channels (all  $\gamma^\mu$  couplings). The duality model was exploited in particular in Ref. [128] in the double-polarised case where both hadrons in the initial state are transversely polarised. The important feature of the duality model is that in the region of  $u$ -quark dominance (large Bjorken  $x$ ) all couplings exactly cancel in the ratios of cross sections (like asymmetries), so these ratios become the same for the DY and  $J/\psi$  production processes. Thus in this kinematic region for the extraction of  $u$  quark PDF it does not matter where the dilepton events come from, from the continuum or the  $J/\psi$  production region. Certainly, such a possibility to use  $J/\psi$  production for the extraction of PDFs is very attractive because the dilepton production rate in the  $J/\psi$  production region is a factor of 30 higher than in the continuum region above the  $J/\psi$  mass.

### 3.4 Kinematic domain and spectrometer acceptance

The acceptance of the COMPASS spectrometer for Drell–Yan events with  $\mu^+ \mu^-$  pairs in the final state was evaluated using a Monte Carlo simulation based on the PYTHIA 6.2 [131] generator and COMGEANT, the COMPASS Monte Carlo simulation program based on GEANT 3.21 [132]. Drell–Yan production proceeds via the annihilation of the valence  $u$  quark from the proton and the  $\bar{u}$  quark from the  $\pi^-$ . We generated events in the invariant mass intervals  $4 \text{ GeV}/c^2 < M_{\mu^+ \mu^-} < 9 \text{ GeV}/c^2$  and  $2 \text{ GeV}/c^2 < M_{\mu^+ \mu^-} < 2.5 \text{ GeV}/c^2$ , which are considered to be the regions for Drell–Yan analysis, avoiding the large combinatorial background that shall dominate at lower dimuon masses, and excluding the  $\phi$ ,  $J/\psi$  and  $\Upsilon$  vector-meson resonances. The higher-mass region provides a cleaner sample of DY events because of the very small contribution from combinatorial and  $D\bar{D}$  decay background, while the DY cross section is almost a factor of 10 smaller than in the lower-mass region. In order to minimise the systematic errors in the asymmetries, the target is segmented into two identical cylindrical cells polarised in opposite directions, each 55 cm long and with a diameter of 2 cm. The target material to be used in the experiment will be ammonia ( $\text{NH}_3$ ).

The probability density functions for the sea quarks fall steeply with increasing  $x_1$  and  $x_2$ , which are the momentum fractions of the annihilating antiquark and quark

Table 4: Average (second column) and partial acceptances (columns 3 to 5) of the spectrometer for dimuons belonging to the two mass ranges.

Mass range ( $\text{GeV}/c^2$ )	Average acceptance (%)	LAS	LAS+SAS	SAS
4–9	35	64	40	4
2–2.5	43	32	54	20

from the projectile  $\pi^-$  and from the target proton, respectively. When both  $x_1$  and  $x_2$  are larger than 0.1, the valence quark contributions are dominant in the parton distribution functions. In order to be sensitive to the transverse polarisation of the target proton one has to stay in the region  $x_2 > 0.1$ . We choose the momentum of the  $\pi^-$  beam in order to select events falling into the valence (anti)quarks region but keeping at the same time cross sections large enough to provide reasonable statistics in the dimuon mass interval between  $4 \text{ GeV}/c^2$  and  $9 \text{ GeV}/c^2$ . Figure 25 presents the phase-space covered by Drell–Yan events with dimuon masses of  $4 \text{ GeV}/c^2 < M_{\mu\mu} < 9 \text{ GeV}/c^2$ , generated by PYTHIA for different  $\pi^-$  beam energies. As the energy increases, the phase space coverage extends to the low- $x$  non-valence region. The value  $s = 357 \text{ GeV}^2$ , corresponding to a pion beam momentum of  $190 \text{ GeV}/c$ , seems to be a convenient choice. Hence, the studies of the COMPASS spectrometer acceptance are presented for DY muons pairs generated at  $s = 357 \text{ GeV}^2$ .

The simulated set-up includes a hadron absorber placed downstream of the polarised target. As will be discussed in more detail in Sect. 10, this absorber shall be made of  $\text{Al}_2\text{O}_3$  (150 cm) and stainless steel (60 cm). In the centre, along the beam direction, it contains a conical beam stopper of tungsten (with 180 cm total length, starting 30 cm downstream inside the absorber). We select pairs of oppositely charged reconstructed muon tracks coming from the primary vertex. The identification of muons in COMPASS is performed by two dedicated muon filters, the first one in the Large Angle Spectrometer (LAS), the second one in the Small Angle Spectrometer (SAS). The LAS muon detector (MW1) includes a 60 cm thick iron absorber placed in between the two tracking stations with eight planes of Mini Drift Tubes (MDT) each. It covers the angular acceptance of the first dipole magnet (SM1), which is about  $\pm 165$  mrad horizontally, and about  $\pm 110$  mrad vertically, assuming that the upstream end of the target is 690 cm upstream of the SM1 magnet. In the SAS the muon filtering system makes use of the tracking detectors behind SM2 in combination with a concrete wall absorber (2.4 m thick) followed by two dedicated muon wall stations (MW2) and three stations of Multi-Wire Proportional Chambers type B (MWPC B) [133].

The spectrometer acceptance for the generated DY events is calculated requiring that each muon in the pair is detected at least by one of the two muon filtering systems. We assume that the muon is inside the LAS acceptance if the particle has produced at least 5 hits in the second station of MW1. If the muon has produced at least 7 hits in MW2 or at least 5 hits in MWPC B then the particle is counted as being in the SAS acceptance. As it was discussed above, two regions of the  $\mu^+\mu^-$  invariant mass are considered. The average geometrical acceptance of dimuons in the mass range  $4\text{--}9 \text{ GeV}/c^2$  is 35%. From the pairs which are found to be inside the spectrometer acceptance, 64% are with both muons in LAS, and 4% with both muons in SAS. In 40% of the cases, one of the muons is accepted in the first spectrometer and the other in the second one. Note that there is

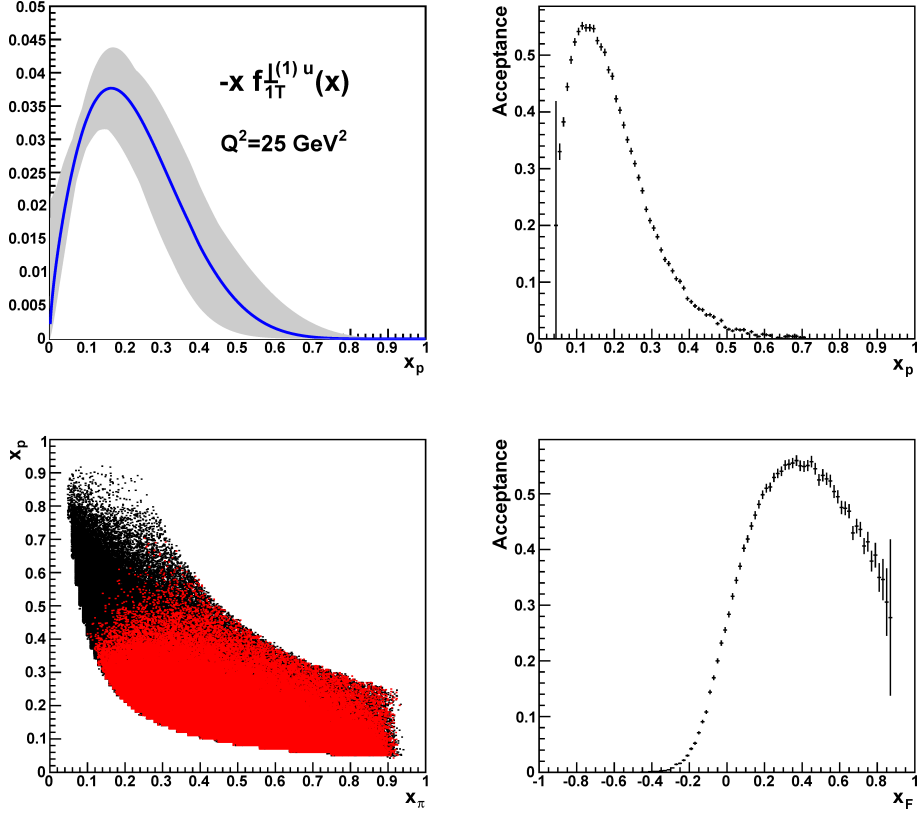


Figure 26: Dimuon mass range  $4\text{--}9 \text{ GeV}/c^2$ . The left upper panel shows the first  $\mathbf{k}_T$ -moment of the  $u$ -quark Sivers PDF calculated at  $Q^2 = 25 \text{ GeV}^2$  from Ref. [134]. The left lower panel shows the covered kinematic region in  $x_p$  versus  $x_\pi$  (in red). In the right upper and lower panels the COMPASS acceptance is shown as a function of  $x_p$  and  $x_F$ , respectively.

a probability that the same muon was registered in both the SAS and the LAS, therefore the sum of three contributions can exceed 100%.

The geometrical acceptance is calculated as the ratio between the number of events inside the acceptance to the total number of generated events, in the same kinematic window. In Figure 26, the acceptance is shown as a function of  $x_p$ ,  $x_p$  versus  $x_\pi$ , and  $x_F$ , where  $x_F = x_\pi - x_p$ , for  $4 \text{ GeV}/c^2 < M_{\mu^+\mu^-} < 9 \text{ GeV}/c^2$ . In the same figure the  $x_p$ -dependence of the first  $\mathbf{k}_T$ -moment of the Sivers function is also shown for comparison. The COMPASS kinematics is in the valence region of both the  $u$  quark from the proton and the  $\bar{u}$  antiquark from the pion. In the same figure, the  $x_p$  dependence of the Sivers function [134] is also shown for comparison. Its value is expected to be largest where the acceptance is largest.

The average acceptance for dimuons in the mass range  $2\text{--}2.5 \text{ GeV}/c^2$  is 43%. Among the pairs found inside the spectrometer acceptance, 32% are with both muons in LAS and 20% with both muons in SAS. In 54% of the cases, one of the muons is accepted in the first spectrometer and the other in the second one. Also here there is a probability that the same muon was registered in both COMPASS spectrometers. A summary on the apparatus acceptance for dimuons belonging to two mass ranges is shown in Table 4.

In Figure 27 the first  $\mathbf{k}_T$ -moment of the Sivers function and the COMPASS acceptance are shown as function of  $x_p$ ,  $x_p$  versus  $x_\pi$ , and  $x_F$  in the region  $2 \text{ GeV}/c^2 <$

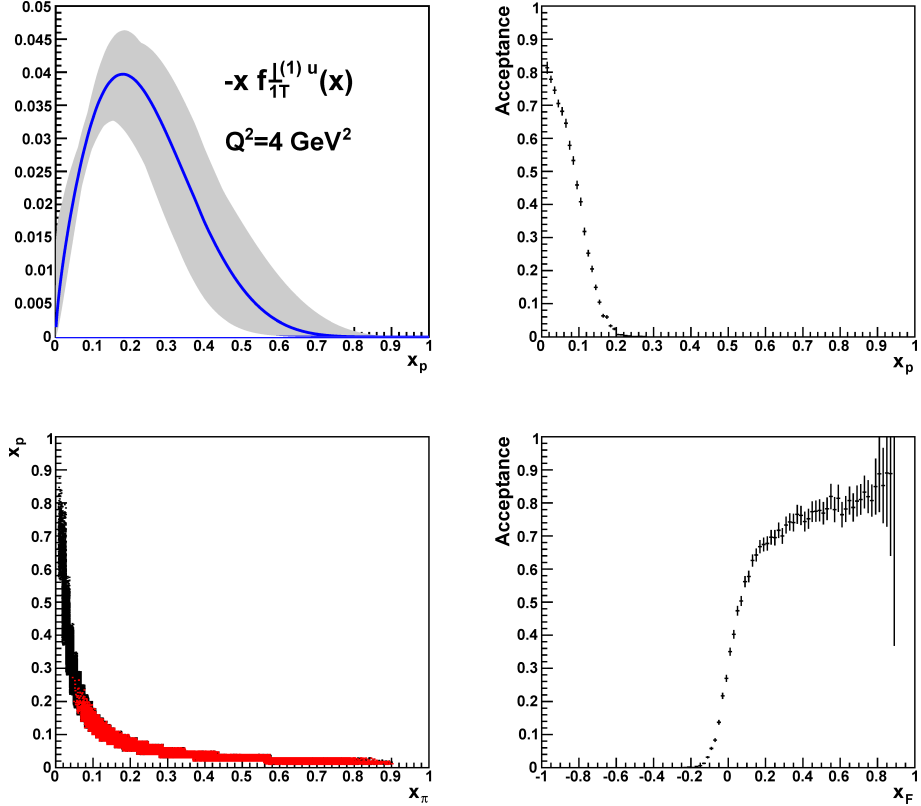


Figure 27: Dimuon mass range  $2\text{--}2.5 \text{ GeV}/c^2$ . The left upper panel shows the first  $k_T$  moment of the  $u$ -quark Sivers PDF calculated at  $Q^2 = 4 \text{ GeV}^2$  from Ref. [134]. The left lower panel shows the covered kinematic region in  $x_p$  versus  $x_\pi$  (in red). In the right upper and lower panels the COMPASS acceptance is shown as a function of  $x_p$  and  $x_F$ , respectively.

$M_{\mu^+\mu^-} < 2.5 \text{ GeV}/c^2$ . The conclusions from the simulations in this mass region are similar to those obtained for the high mass range: the maximal expected asymmetry value nearly corresponds to the maximal acceptance of the spectrometer.

### 3.5 Event rate and projected statistical precision

#### 3.5.1 Expected rate of Drell–Yan events

In this section we present detailed estimations of the achievable luminosity and Drell–Yan event rates for the two dimuon mass regions of interest. In these estimations a total  $\text{NH}_3$  target length of 110 cm is considered together with a  $\pi^-$  beam intensity of  $I_{beam} = 6 \times 10^7 \text{ s}^{-1}$ . The resulting expected instantaneous luminosity is given by

$$\mathcal{L} = L_{eff} \frac{\rho_{\text{NH}_3} F_f N_A}{A_{eff}} I_{beam}. \quad (47)$$

The corresponding effective target length is only  $L_{eff} = 90.36 \text{ cm}$  due to consecutive beam interactions along the target [135]. These calculations assume that the density of the ammonia material is  $\rho_{\text{NH}_3} = 0.85 \text{ g/cm}^3$  and that the packing factor (*i.e.* the correction factor to the density of the solid state target material per unit volume) is  $F_f = 0.50$  (as measured by COMPASS in 2007). The effective mass number of ammonia is  $A_{eff} = 11.71 \text{ g/mol}$ , calculated as in Ref. [132]. This leads to an expected luminosity of  $\mathcal{L} = 1.18 \times 10^{32} \text{ cm}^{-2}\text{s}^{-1}$ .

Table 5: The PYTHIA Drell–Yan  $\pi^- p$  and  $\pi^- n$  cross sections for a proton and a neutron target in the  $\mu^+ \mu^-$  decay channel integrated over two regions of the  $\mu^+ \mu^-$  invariant mass (in  $\text{GeV}/c^2$ ) and given for various beam pion momenta.

$\pi^-$ momentum ( $\text{GeV}/c$ )	$\sigma_{\pi^- p}^{DY \rightarrow \mu\mu}$ (nb)		proton
	$2 < M_{\mu\mu} < 2.5$	$4 < M_{\mu\mu} < 9$	
106	0.537	0.082	
160	0.605	0.126	
190	0.631	0.145	
213	0.647	0.159	

	$\sigma_{\pi^- n}^{DY \rightarrow \mu\mu}$ (nb)		neutron
	$2 < M_{\mu\mu} < 2.5$	$4 < M_{\mu\mu} < 9$	
106	0.340	0.037	
160	0.405	0.062	
190	0.431	0.074	
213	0.450	0.083	

Table 6: The PYTHIA Drell–Yan  $\pi^- \text{NH}_3$  cross sections for an ammonia target in the  $\mu^+ \mu^-$  channel for two regions of the  $\mu^+ \mu^-$  invariant mass (in  $\text{GeV}/c^2$ ) and given for various pion beam momenta.

$\pi^-$ momentum ( $\text{GeV}/c$ )	$\sigma_{\pi^- \text{NH}_3}^{DY \rightarrow \mu\mu}$ (nb)		$\text{NH}_3$
	$2 < M_{\mu\mu} < 2.5$	$4 < M_{\mu\mu} < 9$	
106	5.147	0.702	
160	5.922	1.109	
190	6.231	1.291	
213	6.428	1.419	

The Drell–Yan cross sections in the two ranges of dimuon invariant mass and for different energies of the incoming beam were calculated using the PYTHIA generator. Fixed-target  $\pi^- p$  and  $\pi^- n$  collisions were simulated, using the GRS 98 LO PDF set for the proton and GRS-L PDF set for the pion. The parameters controlling the  $k_T$  distribution of partons inside the hadrons were tuned in order to have the average transverse momentum of high-mass reconstructed dimuons matching the  $p_T$  distributions measured by the NA3 experiment in  $\pi^- W$  collisions at 194  $\text{GeV}/c$  [136]. An average  $p_T$  of 1.1  $\text{GeV}/c$  was used for dimuons in the mass range 4–9  $\text{GeV}/c^2$ . The results are shown in Table 5.

The obtained hadron–hadron cross sections were then combined as

$$\sigma_{\text{NH}_3}^{\mu\mu} = Z\sigma_{\pi^- p}^{\mu\mu} + N\sigma_{\pi^- n}^{\mu\mu}, \quad (48)$$

where  $Z$  and  $N$  stand for the number of protons and neutrons in the ammonia molecule, respectively. Nuclear effects in the nitrogen atom are neglected here. Nevertheless, we take into account the fact that this is a compound material, and that there is a difference between the protons inside the nitrogen nucleus and the quasi-free hydrogen atoms by using  $Z_{\text{eff}}$  and  $N_{\text{eff}} = A_{\text{eff}} - Z_{\text{eff}}$  as calculated in Ref. [135] instead of  $Z$  and  $N$ . The estimated values for the  $\pi^- \text{NH}_3$  DY cross section in the dimuon channel are presented in Table 6.

Table 7: Summary of experimental factors entering the DY event rate calculation.

$L_{\text{NH}_3}$ (target)	110 cm
$L_{\text{eff}}$ (target)	90.36 cm
$A_{\text{eff}}(\text{NH}_3)$	11.71 g/mol
$\rho_{\text{NH}_3}$	0.85 g/cm <sup>3</sup>
$F_f(\text{NH}_3)$	0.50
$I_{\text{beam}}$	$6 \times 10^7 \pi^-/\text{s}$
$\mathcal{L}$	$1.18 \times 10^{32} \text{ cm}^{-2}\text{s}^{-1}$
$E_{\text{SPS}}$	0.8
$\Omega$	0.4
$E_{\text{rec}}$	0.8
$E_{\text{trig}}$	0.81
$E_{\text{spec}}$	0.85
$E_{\text{tot}}$	0.17
$d_{\text{spill}}$	9.6 s
$n_{\text{spill}}$	1800/day
$K_{\text{DY}}$	2

As it is known since the 1980's, the leading-order Drell–Yan cross section as calculated here by PYTHIA is underestimated with respect to the measured experimental value by a so-called  $K_{\text{DY}}$  factor. This factor was measured to be about two. It must be applied to the values in Table 6, in order to obtain the expected experimental cross section. A cross-check of the PYTHIA-generated DY cross sections against experimental data has also been performed and good agreement was found [135].

It is important to note that in the case of the NH<sub>3</sub> target only the fraction of DY events originating from one of the polarised protons in the hydrogen atoms is polarisation-sensitive while the remaining fraction (DY processes originating from one of the 7 protons or 7 neutrons of the nitrogen nucleus) are background events which cannot be separated on an event-by-event basis. For this reason, we will give in this section the total DY event rates (polarisation sensitive or not) and then, as normally done in COMPASS, we will take into account the dilution factor  $f$  for the calculation of the expected statistical error on asymmetries (Sect. 3.5.2).

The event rate per day is calculated according to the expression

$$R = \mathcal{L} \sigma_{\pi^- - \text{NH}_3} K_{\text{DY}} d_{\text{spill}} n_{\text{spill}} E_{\text{tot}}, \quad (49)$$

where  $\mathcal{L}$  is the luminosity as calculated above,  $\sigma_{\pi^- - \text{NH}_3}$  the DY cross section for  $\pi^- - \text{NH}_3$  collisions in the dimuon decay channel as obtained from PYTHIA simulations,  $K_{\text{DY}} = 2$  is the scaling factor as measured from previous experiments,  $d_{\text{spill}} = 9.6$  s is the duration of the SPS spill, and  $n_{\text{spill}} = 1800$  is the maximum number of spills per day assuming the typical SPS supercycle of 48 s. The overall efficiency of the measurement  $E_{\text{tot}}$  is given by

$$E_{\text{tot}} = \Omega E_{\text{rec}} E_{\text{trig}} E_{\text{SPS}} E_{\text{spec}}, \quad (50)$$

where  $\Omega \approx 0.4$  is the acceptance of the COMPASS apparatus in the dimuon mass range  $4 \text{ GeV}/c^2 < M_{\mu\mu} < 9 \text{ GeV}/c^2$ ,  $E_{\text{rec}} = 0.8$  is the reconstruction efficiency,  $E_{\text{trig}} \approx 0.9 \times 0.9 = 0.81$  is the dimuon trigger efficiency,  $E_{\text{SPS}} \approx 0.8$  is the accelerator efficiency, and

Table 8: Number of Drell–Yan events per day ( $R$ ), depending on the dimuon mass range considered (in  $\text{GeV}/c^2$ ), and for different beam momenta (in  $\text{GeV}/c$ ).

$\pi^-$ momentum ( $\text{GeV}/c$ )	$R$ (/day)	
	$2 < M_{\mu\mu} < 2.5$	$4 < M_{\mu\mu} < 9$
106	4013	440
160	4617	695
190	4858	809
213	5012	889

$E_{\text{spec}} \approx 0.85$  the spectrometer availability. The latter estimate includes the trigger dead time, the run start-stop procedure and the DAQ availability. Taking all these factors into account, the estimated overall efficiency  $E_{\text{tot}}$  is 17%.

Table 7 summarises all the factors that are used in the event rates estimate together with the theoretical values on  $\sigma_{\text{DY}}$  taken from Table 6. The Drell–Yan event rates expected to be observed in the experiment per day are presented in Table 8 for the two mass regions of interest. Thus considering a typical run of 140 days per year, in two years of data-taking we can collect about 230 thousand Drell–Yan events in the dimuon high-mass range and 1.4 million events in the medium-mass range. A conservative pion beam intensity of  $6 \times 10^8$  hadrons/spill was used for the estimation of the DY event yield. The possibility to increase the beam intensity up to  $10^9$  pions/spill is presently under discussion.

### 3.5.2 Expected statistical precision and theory predictions for asymmetries

Here we present, as an example, a simple expressions for the Sivers asymmetry extraction at LO (see for details Ref. [116])

$$A_T^{\sin \phi_S}(x_a, x_b) = \frac{2}{f |\mathbf{S}_T|} \frac{\int d\phi_S d\phi \frac{dN(x_a, x_b, \phi, \phi_S)}{d\phi d\phi_S} \sin \phi_S}{N(x_a, x_b)}.$$

The statistical accuracy in the assumption of a flat acceptance of the apparatus in the azimuthal angles  $\phi_S$  and  $\phi$ , and the polar angle  $\theta$ , is then given by

$$\delta A_T^{\sin \phi_S}(x_a, x_b) = \frac{1}{f |\mathbf{S}_T|} \frac{\sqrt{2}}{\sqrt{N(x_a, x_b)}}.$$

In our calculations of the projected statistical errors of asymmetries we use  $|\mathbf{S}_T| = 90\%$  for the polarisation of the target material and  $f = 0.22$  for the dilution factor. Table 9 presents the expected statistical errors for the unpolarised and the three transverse-spin-dependent asymmetries that we can access, using only one bin in  $x_F$  and a beam momentum of 190  $\text{GeV}/c$ . The statistical errors of the asymmetries are calculated independently for the three mass ranges considered. For the  $J/\psi$  mass region, the fraction of  $q\bar{q}$ -produced  $J/\psi$ 's was assumed to be 60%, as will be discussed later, and the tail of the open-charm contamination was neglected except in the lowest mass region.

For a measurement in the DY high-mass region of the four asymmetries discussed above, the projected statistical errors are shown in Fig. 28 together with some theoretical predictions. In the case of the Sivers asymmetry, all data are combined in one bin in order to allow the best possible conclusion on its sign. Two error bars are shown with the smaller one being the systematic error, together with the theoretical prediction [137] (the only

Table 9: Expected statistical errors for various asymmetries assuming two years of data taking and a beam momentum of  $190 \text{ GeV}/c$ .

Asymmetry	Dimuon mass ( $\text{GeV}/c^2$ )		
	$2 < M_{\mu\mu} < 2.5$	$J/\psi$ region	$4 < M_{\mu\mu} < 9$
$\delta A_U^{\cos 2\phi}$	0.0020	0.0013	0.0045
$\delta A_T^{\sin \phi_S}$	0.0062	0.0040	0.0142
$\delta A_T^{\sin(2\phi + \phi_S)}$	0.0123	0.008	0.0285
$\delta A_T^{\sin(2\phi - \phi_S)}$	0.0123	0.008	0.0285

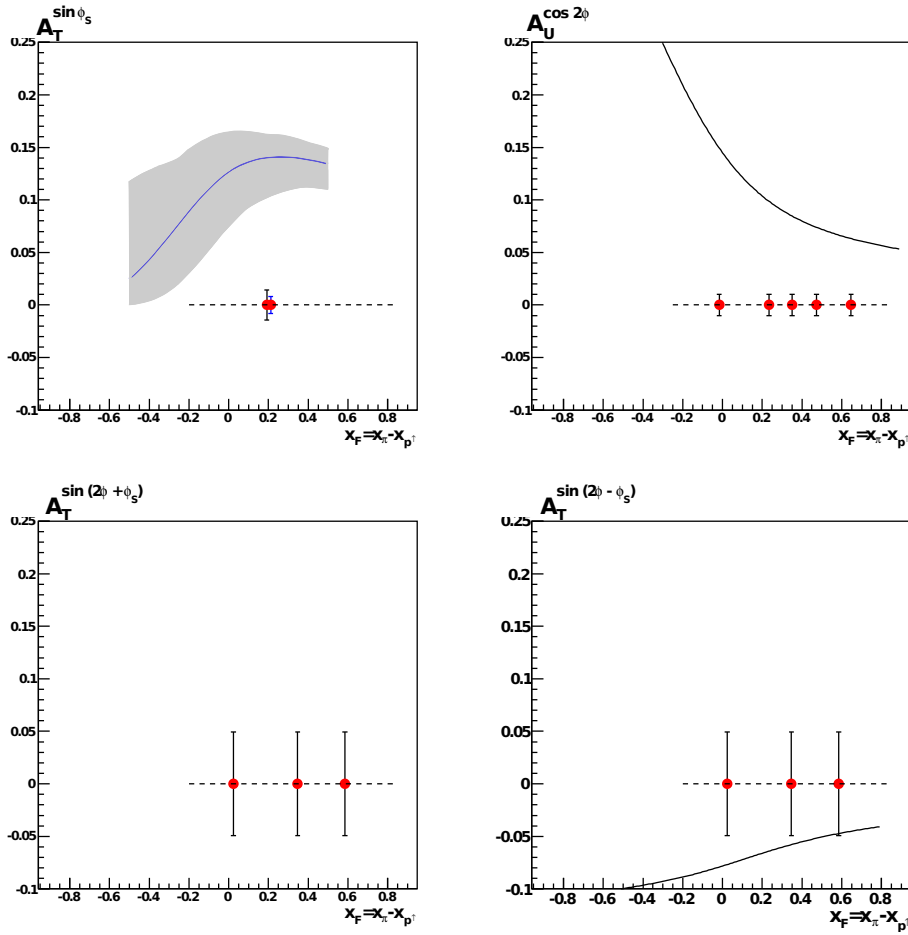


Figure 28: Theoretical predictions and expected statistical errors on the Sivers (top-left), Boer–Mulders (top-right),  $\sin(2\phi + \phi_S)$  (bottom-left) and  $\sin(2\phi - \phi_S)$  (bottom-right) asymmetries for a DY measurement  $\pi^- p \rightarrow \mu^+ \mu^- X$  with a  $190 \text{ GeV}/c$   $\pi^-$  beam in the high-mass region  $4 \text{ GeV}/c^2 < M_{\mu\mu} < 9 \text{ GeV}/c^2$ . In case of the Sivers asymmetry also the systematic error is shown (smaller error bar).

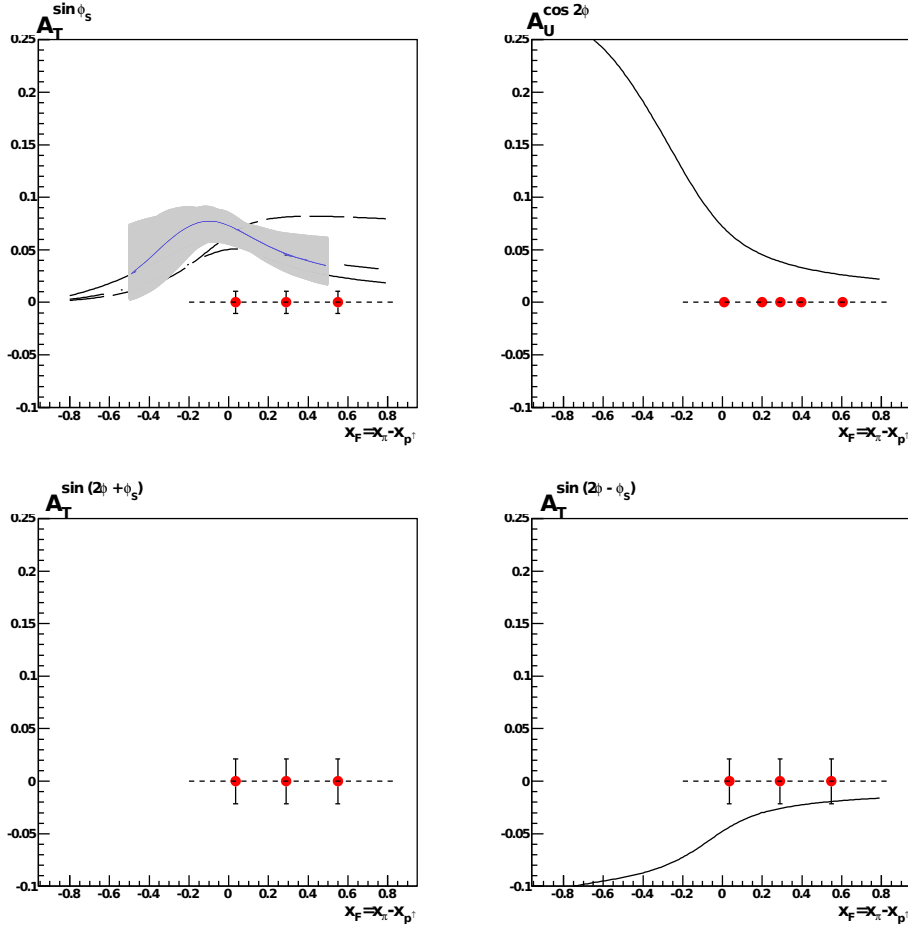


Figure 29: Theoretical predictions and expected statistical errors for the four asymmetries in the DY process  $\pi^- p \rightarrow \mu^+ \mu^- X$  with 190 GeV/c beam momentum, for the intermediate dimuon mass region  $2 \text{ GeV}/c^2 < M_{\mu\mu} < 2.5 \text{ GeV}/c^2$ .

existing prediction that is given together with its uncertainties, which are derived from a fit to the experimental data). For the other three asymmetries, equipopulated bins in  $x_F$  are chosen. In the case of the Boer-Mulders (BM) asymmetry  $A_U^{\cos 2\phi}$ , the theoretical predictions were obtained using the Boer-Mulders function of the pion extracted from NA10 data [138] and a parametrisation of the Boer-Mulders function of the proton from Ref. [139]. These predictions were also produced for medium-mass and  $J/\psi$ -mass ranges and are shown in Figs. 29 and 30, respectively. In the case of the Boer-Mulders-transversity asymmetry  $A_T^{\sin(2\phi - \phi_S)}$ , the theoretical predictions were obtained using the Boer-Mulders model for the pion BM function [102] and the evolution model for the transversity function [140]. The predictions for the BM-transversity asymmetry were also produced for both lower mass ranges and are also shown in Figs. 29 and 30, respectively.

In Figure 31, all available theoretical predictions on the Sivers asymmetry are shown in one graph, again together with the already shown projected statistical and systematic errors of the proposed measurement. The solid blue line in the centre of the grey shaded band of uncertainties is the same as in the previous figure. The predictions are evaluated at  $\langle M_{\mu\mu} \rangle \simeq 5 \text{ GeV}$ . The black solid and dashed lines correspond to fits of the Sivers function [141] to a parametrisation of experimental data (Fit I and II below), while the dot-dashed line shows a fit from Ref. [142] (Fit III). The fits are given by:

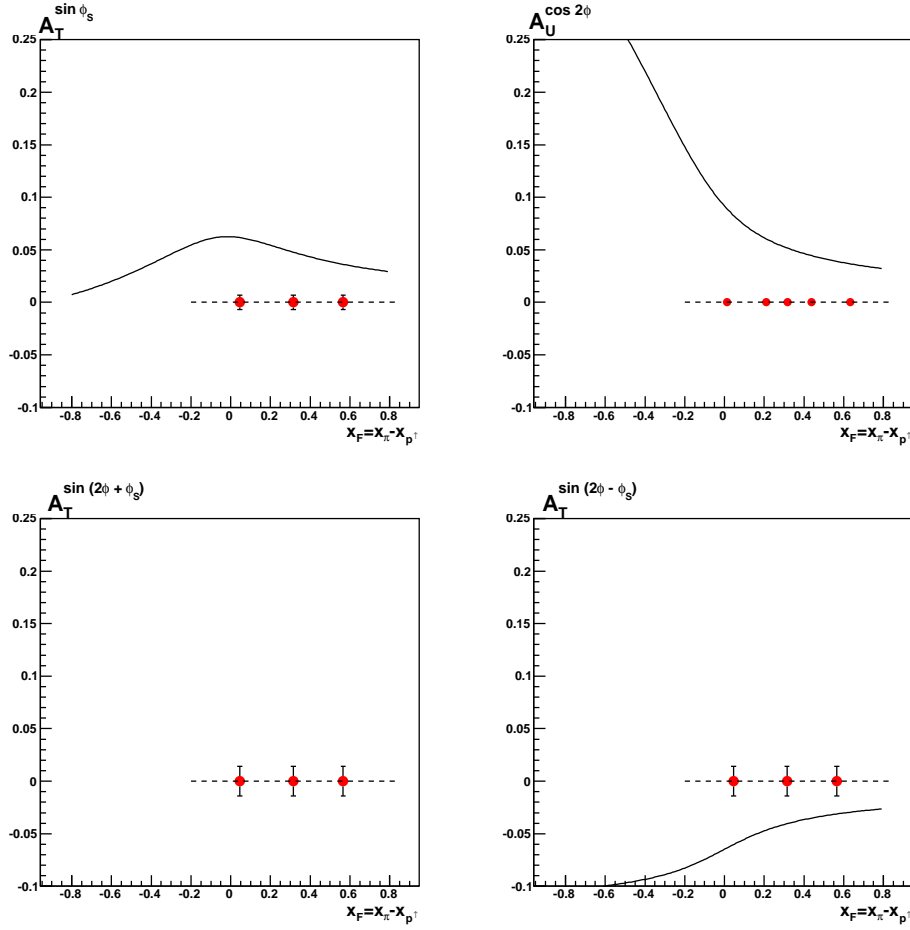


Figure 30: Expected statistical errors for the Sivers (top-left), Boer–Mulders (top-right),  $\sin(2\phi - \phi_S)$  (bottom-left) and  $\sin(2\phi + \phi_S)$  (bottom-right) asymmetries respectively, in the process  $\pi^- p \rightarrow \mu^+ \mu^- X$  with 190 GeV/c beam for the  $J/\psi$  mass region  $2.9 \text{ GeV}/c^2 < M_{\mu\mu} < 3.2 \text{ GeV}/c^2$ .

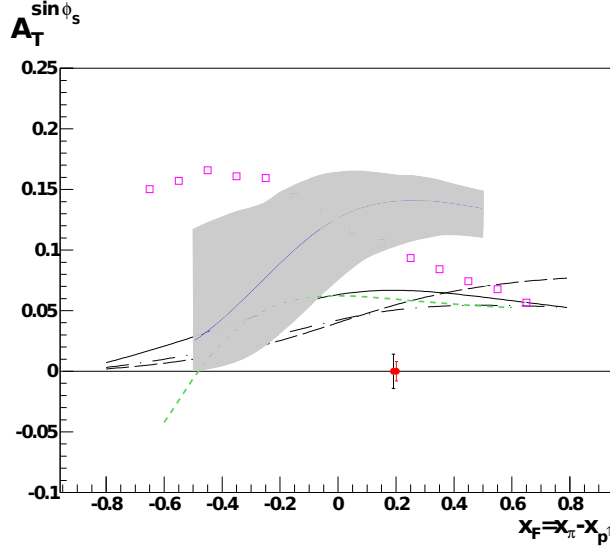


Figure 31: Theoretical predictions and expected statistical (left) and systematic (right) error for a measurement of the Sivers asymmetry in the high-mass region  $4 < M_{\mu\mu} < 9 \text{ GeV}/c^2$ .

Table 10: Expected statistical errors for the four asymmetries from events in the  $J/\psi$  mass region events, shown for various fractions of the  $q\bar{q}$  process .

Asymmetry	fraction of $q\bar{q}$		
	$\alpha = 0.1$	$\alpha = 0.6$	$\alpha = 0.9$
$\delta A_U^{\cos 2\phi}$	0.0060	0.0013	0.0009
$\delta A_T^{\sin \phi_S}$	0.0188	0.0040	0.0027
$\delta A_T^{\sin(2\phi + \phi_S)}$	0.0375	0.0080	0.0054
$\delta A_T^{\sin(2\phi - \phi_S)}$	0.0375	0.0080	0.0054

$$\begin{aligned} \text{Fit I: } & xf_{1T}^{\perp(1)u} = -xf_{1T}^{\perp(1)d} = 0.4x(1-x)^5, \\ \text{Fit II: } & xf_{1T}^{\perp(1)u} = -xf_{1T}^{\perp(1)d} = 0.1x^{0.3}(1-x)^5, \\ \text{Fit III: } & xf_{1T}^{\perp(1)u} = -xf_{1T}^{\perp(1)d} = (0.17 \dots 0.18)x^{0.66}(1-x)^5. \end{aligned}$$

The predictions from Refs. [143, 144] are shown by squares and as short-dashed line, respectively. We note that, although the asymmetries estimated in Refs. [141, 142] are  $q_T$  integrated (as a factor  $\frac{q_T}{M_N}$  is present in the asymmetry), the ones used in Fig. 28 were given by the authors as  $q_T$  non-integrated to facilitate the comparison of various models. The abscissa value of the experimental points used to indicate the projected statistical error is calculated from the  $x_F$  distribution of Drell–Yan events simulated in the COMPASS apparatus. The  $x_F$  range covered ( $-0.2 < x_F < 0.85$ ) was divided into bins of almost equal statistics and the weighted mean value of the corresponding bins in the generated variable was computed.

The expected asymmetry values in the intermediate dimuon mass region  $2 \text{ GeV}/c^2 < M_{\mu\mu} < 2.5 \text{ GeV}/c^2$  are presented in Fig. 29 together with projected statistical errors. In the case of the Sivers asymmetry, the black solid and dashed lines correspond to fits of the Sivers function in Ref. [141], while the dot-dashed line shows a fit from Ref. [142] (see fit function parameters of Fit I–III above). Contrary to the high-mass region which is practically free of background, we expect in this region a signal-to-background ratio of about unity so that the expressions for the statistical error, like the one in Eq. 51, were corrected by a factor  $\sqrt{1 + \frac{N_{D\bar{D}} + N_{C\bar{D}}}{N_{DY}}} = 1.4$ . Here, the two most important sources of physics background in this region, namely the open-charm decays to muons as well as combinatorial background, were taken into account.

As it was seen in Sect. 3.3.5, single spin asymmetries can be extracted also from  $J/\psi$  events if the DY– $J/\psi$  duality holds. In this case, the statistical error achievable for asymmetries is much more favourable due to the higher  $J/\psi$  cross section. On the other hand, in the energy range of this experiment which is relatively low, one assumes a dominance of the quark–antiquark mechanism over the gluon–gluon fusion mechanism for  $J/\psi$  production, but the exact fraction of one process with respect to the other is unknown. We have assumed for Table 9 that this fraction is  $\alpha = 0.6$ , while in Table 10 we give the statistical errors also for the extreme cases  $\alpha = 0.1$  and  $\alpha = 0.9$ . The expected number of  $J/\psi$  events is estimated taking into account its production cross section in the dimuon channel measured by the NA3 experiment. This experiment published results for  $200 \text{ GeV}/c \pi^-$  collisions with a  $H_2$  target [145],  $B_{\mu\mu}\sigma^{J/\psi}(x_F) = 6.3 \pm 0.8 \text{ nb/proton}$ . The expected rate of  $J/\psi$  events per day is given by

$$N_{J/\psi} = \sigma^{J/\psi} f_{abs} \mathcal{L} d_{spill} n_{spill} E_{tot}, \quad (51)$$

where  $f_{abs} = A^{0.925}$  takes into account the fact that some fraction of the produced  $J/\psi$ 's is absorbed in the target. Thus the total cross section is not  $A\sigma^{J/\psi}$  but  $A^{0.925}\sigma^{J/\psi}$  [146]. On the other hand, the acceptance for dimuons in the  $J/\psi$  mass range is estimated to be 47%, as obtained from Monte Carlo simulations. This results in an expected  $J/\psi$  rate of 25180 events per day, or a total of 7.05 million  $J/\psi$ 's in two years of data taking.

A Drell–Yan contribution under the  $J/\psi$  peak should also be considered as signal, as according to the duality assumption it contains the same physics information as the quark–antiquark generated  $J/\psi$ 's. On the other hand, the  $J/\psi$ 's generated by gluon–gluon fusion constitute a background that must be taken into account. Thus a correction factor of  $\sqrt{1 + N_{J/\psi gg}/(N_{J/\psi q\bar{q}} + N_{DY})} = 1.274$  must be applied. The expected number of Drell–Yan events under the  $J/\psi$  was calculated from the PYTHIA Drell–Yan cross section in the mass range  $2.9 \text{ GeV}/c^2 < M_{\mu\mu} < 3.2 \text{ GeV}/c^2$ , and amounts to 291000 events in the two-year period. Table 10 presents the expected statistical precision for the four considered asymmetries to be extracted from  $J/\psi$  events in the three considered scenarios of  $\alpha = 0.1$ ,  $\alpha = 0.6$  and  $\alpha = 0.9$ .

Figure 30 shows the projected statistical precision for the four considered asymmetries, extracted from events in the  $J/\psi$  mass region under the assumption that 60% of the produced  $J/\psi$  events result from a  $q\bar{q}$  process. In the case of the Sivers asymmetry, the black solid lines correspond to fits of the Sivers function in Ref. [141] (see fit function parameters of Fit I above).

### 3.6 Feasibility of Drell–Yan measurements at COMPASS

#### 3.6.1 Results of 2007–2008 beam tests

In order to establish the feasibility of the proposed polarised Drell–Yan programme at COMPASS and to evaluate in a realistic way the achievable statistical accuracies, short beam tests were performed in 2007, 2008 and 2009.

In the 2007 beam test at COMPASS a negative pion beam of  $160 \text{ GeV}/c$  momentum impinged on a  $\text{NH}_3$  target and an open configuration of the spectrometer was used, *i.e.* without hadron absorber downstream of the target. The beam intensity was  $2 \times 10^6$  to  $4 \times 10^6$  particles per second. The polarised-target system comprised three target cells with a total length of 120 cm placed inside the superconducting solenoid. The cells were longitudinally polarised during data taking. A simple dimuon trigger was set up with the requirement of a coincidence between one muon detected in SAS (via identification in the trigger hodoscopes) and one muon detected in LAS. The muon trigger in LAS is absent in the standard running mode. For the purpose of this test, it was built from setting two thresholds in the HCAL1 response, corresponding to  $0.7 \text{ mip} < \text{signal} < 2.5 \text{ mip}$ . According to the simulations performed, such trigger can only detect 40% of all the dimuons in the acceptance. Additionally, its efficiency is estimated to be of only 50%. The dimuon trigger was prescaled by a factor of five during the test.

The main goals of this test were to measure the radiation conditions inside the experimental hall and the temperature raise of the polarised target when using an incident hadron beam as well as to observe the behaviour of the spectrometer under “Drell–Yan conditions”.

Dimuon trigger data were collected during approximately 12 effective hours corresponding to 95 million events, from which about 90000 contained a  $\mu^+\mu^-$  pair. In such a short time interval, no Drell–Yan events are expected to be observed in the high mass range  $4 \text{ GeV}/c^2 < M_{\mu\mu} < 9 \text{ GeV}/c^2$ . Instead, the  $J/\psi$  events having a cross section higher than that of Drell–Yan by a factor 30, were used to judge about the experimental feasibil-

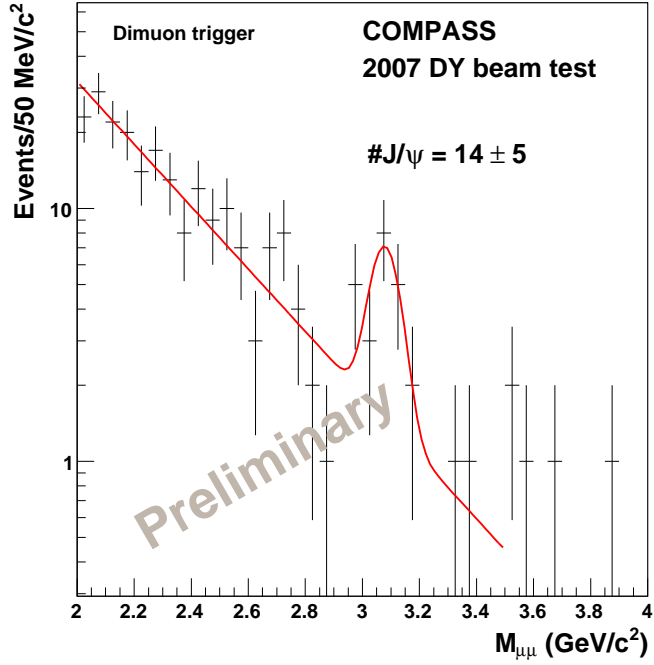


Figure 32: Dimuon mass spectrum from the 2007 beam test obtained with the requirement of a dimuon trigger. The number of fitted  $J/\psi$ 's is  $14 \pm 5$ , compatible with the  $20 \pm 8$  expected.

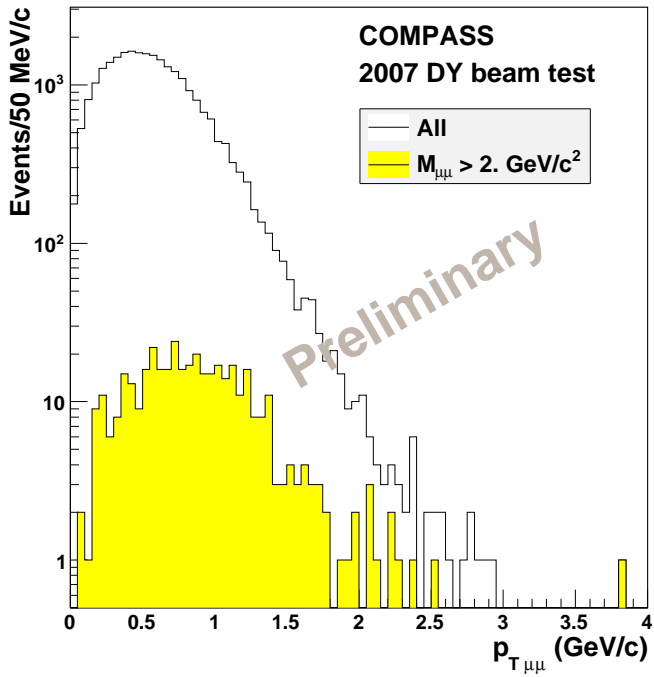


Figure 33: Dimuon transverse momentum distribution after all cuts are applied (white), and with the additional requirement that  $M_{\mu\mu} > 2 \text{ GeV}/c^2$  (yellow).

ity of the measurement. The analysis of the data after all cuts applied led to  $14 \pm 5$   $J/\psi$  events with dimuon trigger present. The number expected on the basis of  $J/\psi \rightarrow \mu^+ \mu^- X$  cross section measured by the NA3 experiment under similar conditions [145], amounts to  $20 \pm 8$ . Figure 32 shows the fitted dimuon mass spectrum. Figure 33 shows the dimuon transverse momentum distribution after all cuts are applied but without the dimuon trigger requirement and with the additional requirement of the invariant mass being larger than  $2 \text{ GeV}/c^2$ . By selecting higher dimuon masses, the  $p_T$  distribution shifts to higher values as expected, as both the  $J/\psi$  and DY events are known from past experiments to have an average  $p_T$  of about  $1\text{--}1.1 \text{ GeV}/c$ .

The 2007 beam test led to radiation conditions that were shown to be below the CERN safety limits. The high-intensity beam causes multiple nuclear interactions in the target with production of a large amount of secondary particles. This contributes to an increase of the target temperature and shortens the spin relaxation time of the material. The measurements of the target temperature during the test indicated no problems for the beam intensities studied. Concerning the spectrometer behaviour, the analysed data showed that, although the occupancy in the LAS detectors closest to the target was high, there was no apparent loss of events in the tracking and reconstruction, as the physics signal (number of  $J/\psi$  events) obtained was in agreement with what was expected.

In 2008 a second beam test was performed, also with an open configuration of the spectrometer, a  $\pi^-$  beam of  $190 \text{ GeV}/c$  momentum, and a polyethylene target with  $25\% \lambda_{int}$ . The goal of this test was to further clarify the occupancy of the detectors and the DAQ capability to handle the high data rates produced. Data were collected with a single muon trigger. Additionally, radiation measurements were performed again. By increasing gradually the beam intensity up to  $6.5 \times 10^6$  particles per second an increase in the current drawn by various detectors was visible, approaching their trip limit. The detectors placed closer to the target had occupancies above 5% even if the conditions of the test correspond to only 1/3 of the instantaneous luminosity required for the Drell–Yan measurement proposed in this document.

The overall conclusion from these two beam tests is that a configuration with a hadron absorber placed immediately after the target is the best choice. Although the universality of the spectrometer is lost, limiting the physics output to dimuons in the final state has the important advantage of preserving the highest efficiency of the detectors. In these conditions, the luminosity can be increased, while the combinatorial background will be significantly reduced.

### 3.6.2 Preliminary results of 2009 beam test

A three-day Drell–Yan beam test was performed at the end of the data-taking period of 2009. A  $\pi^-$  beam with momentum  $190 \text{ GeV}/c$  was used. The small angle part of the spectrometer comprising the SM2 magnet, the Muon Wall-1 and other tracking devices was positioned 3 m downstream of its nominal position (hadron run configuration). The polarised target cells were simulated by two cylinders of polyethylene ( $\text{CH}_2$ ) separated by 20 cm. The length of each cylinder was 40 cm and the diameter 5 cm. The total length of the dummy target was equal to about one interaction length, which corresponds to that of the polarised target. A hadron absorber was installed downstream of the target. The upstream part the absorber consisted of 100 cm concrete, while the downstream part was made of 100 cm stainless steel. The transverse dimensions of the absorber were  $80 \times 80 \text{ cm}^2$ . The main purpose of the hadron absorber was to suppress the flux of a secondary hadrons produced in the interactions of the  $\pi^-$  beam with the polyethylene target. The choice of

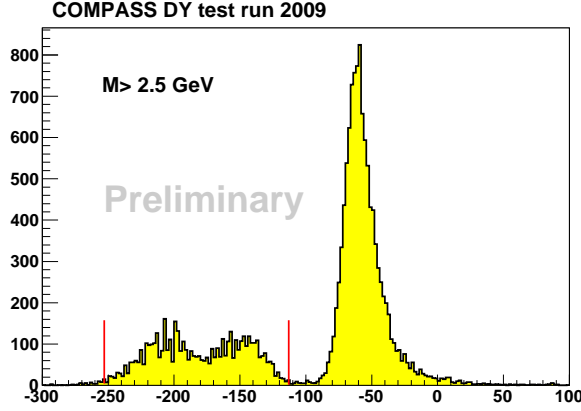


Figure 34: Vertex distribution along the beam direction for  $M_{\mu\mu} > 2.5 \text{ GeV}/c^2$ .

the material and the geometry of the absorber were constrained by the total cost as well as by construction and assembly time. In the centre of the absorber, along the beam axis, a beam plug made of tungsten was installed in order to stop the non-interacting beam. The test set-up consisting of the dummy target and the hadron absorber replaced the recoil proton detector, which was used during hadron spectroscopy data taking.

The beam intensity was  $8 \times 10^7$  pions/spill (spill length of 9.6 s), except for two runs when it was eventually increased to  $1.5 \times 10^8$ /spill. Two dimuon triggers were set up, one using the hodoscopes in the SAS (Middle, Ladder and Outer hodoscopes) in coincidence with a signal from the HCAL1 trigger in the LAS, the other using two signals in coincidence from the HCAL1 trigger in the LAS. The latter used a window discriminator with two sets of thresholds in order to select minimum ionising particles  $0.7 \text{ mip} < \text{signal} < 2.5 \text{ mip}$ . All collected data were analysed leading to a total processed statistics of 4935 spills. The corresponding beam flux is  $3.7 \times 10^{11}$  pions. In order to select events with a dimuon in the final state the following cuts were applied:

- only events with one positive and one negative particle, marked as muons, were accepted;
- the momentum of the negative muon is below  $100 \text{ GeV}/c$ . This cut rejects muons from the decay of beam pions  $\pi^- \rightarrow \mu^- + \bar{\nu}_\mu$ . The minimal energy of such muons is approximately  $E_{beam} m_\mu^2 / m_\pi^2 \approx 109 \text{ GeV}$ ;
- the position of the vertex reconstructed from the muon tracks is in the range  $-253 \text{ cm}$  to  $-113 \text{ cm}$  along the nominal beam line (Fig. 34);
- the distance from the nominal beam line is less than  $5 \text{ cm}$ ;
- the minimal distance between the muon tracks is less than  $4 \text{ cm}$ ;
- the difference between the values of the mean track time for muon tracks is below  $12 \text{ ns}$ . This cut is effective against background events induced by pile-up effects.

The expected yield of  $J/\psi$  and DY events can be estimated using the procedure applied in the Sect. 3.3.5. It is based on the DY cross section, target length, beam intensity, apparatus acceptance, reconstruction and trigger efficiencies and spectrometer availability. The number of expected  $J/\psi$  is  $3600 \pm 600$ , the number of DY events in the mass range  $4 \text{ GeV}/c^2 < M_{\mu\mu} < 9 \text{ GeV}/c^2$  is  $110 \pm 22$ . These numbers were obtained taking into account three important factors:

- a correction for the trigger inefficiency ( $\approx 1.8$ ),

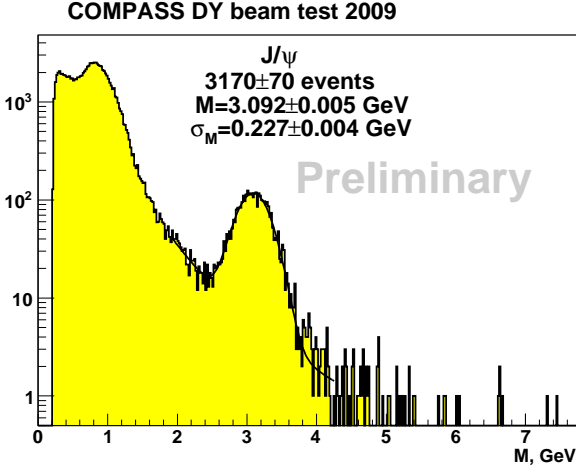


Figure 35: The measured  $\mu^+\mu^-$  invariant mass distribution. The number of events is obtained from the fit in the  $J/\psi$  region.

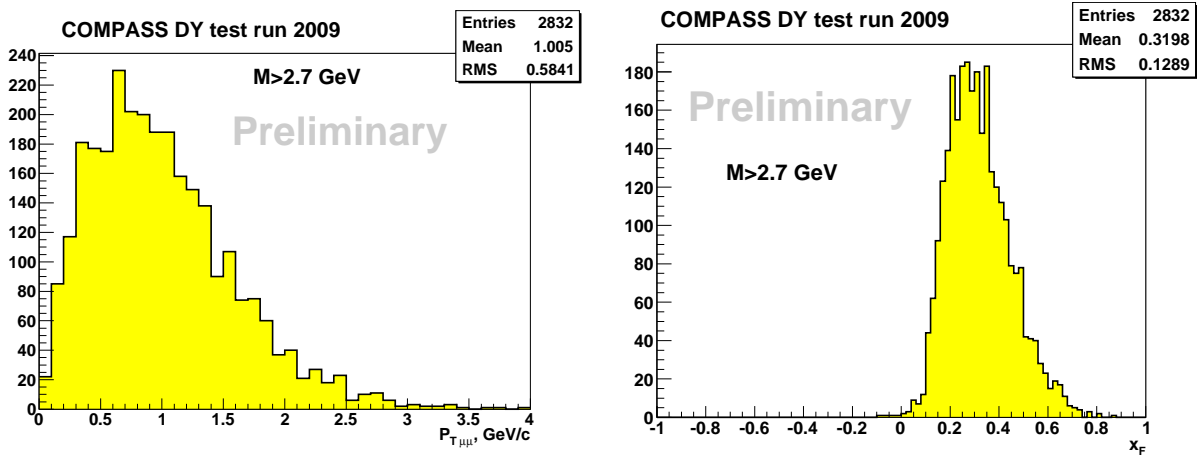


Figure 36:  $p_T$  (left) and  $x_F$  (right) of the dilepton for  $M_{\mu\mu} > 2.7$  GeV/ $c^2$ .

- a correction of the apparatus acceptance correction as in 2009 the SM2 magnet located 3 m downstream of its nominal position ( $\approx 15\%$  events less for  $J/\psi$  and  $\approx 20\%$  for DY dimuon mass range),
- a reduction of statistics by about 20% due to the applied cuts.

The number of found  $J/\psi$ 's is  $3170 \pm 70$  (Fig. 35), in good agreement with the expected  $J/\psi$  yield (Sect. 3.3.5) as is also the number of DY events of  $84 \pm 10$  found in the range  $4$  GeV/ $c^2 < M_{\mu\mu} < 9$  GeV/ $c^2$ . Correspondingly the measured ratio of the  $J/\psi$ -to-DY event yield of  $37.7 \pm 5.0$  agrees well with the expectation of  $33.3 \pm 5.0$ . In the further analysis only data from the two dedicated Drell-Yan triggers were used.

The  $p_T$  and  $x_F$  distributions for events with  $M_{\mu\mu} > 2.7$  GeV/ $c^2$  are shown in Fig. 36. The mean value of  $p_T$  is about 1 GeV/ $c$ . This makes COMPASS sensitive to TMDs, which are expected to be accessible up to  $p_T \approx 2$  GeV/ $c$ .

The  $x_a$  versus  $x_b$  distributions are shown in Fig. 37 for the two considered mass ranges of the dimuon. As one can see in the high-mass range of the dimuon,  $M_{\mu\mu} > 4$  GeV/ $c^2$ , both annihilating quarks belong to the valence quark range. In case of the  $J/\psi$ , the contribution of valence quarks is also dominant.

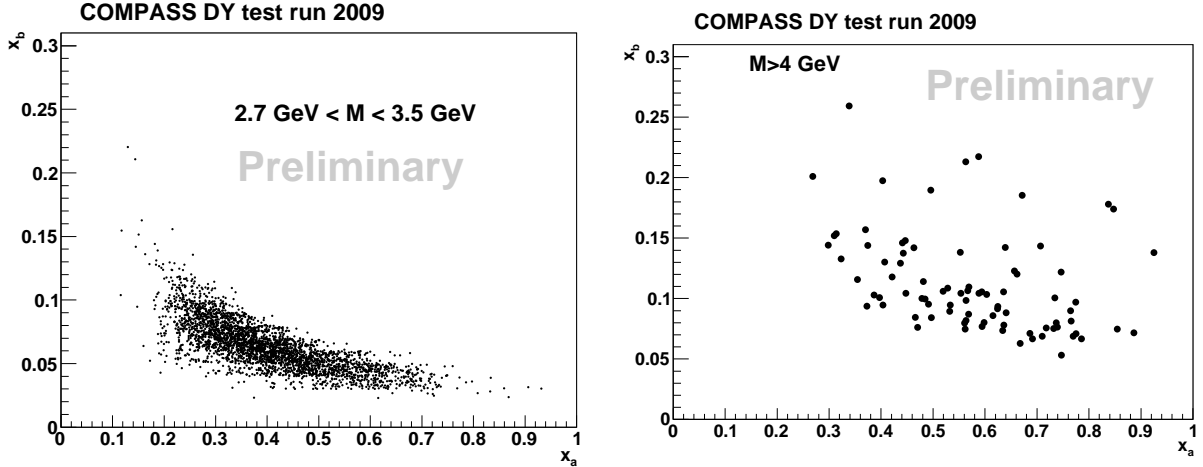


Figure 37: The  $(x_a, x_b)$  coverage for the  $J/\psi$  (left) and  $M_{\mu\mu} > 4 \text{ GeV}/c^2$  (right) mass range.

The high intensity of the incoming pion beam and the long exposition time prevents us from using silicon detectors for the beam definition (beam telescope) in the future Drell–Yan measurement. One possible alternative solution is to substitute them by scintillating fibres (corresponding detectors are under development in the Erlangen–Bonn group). They offer a sufficiently high space resolution of  $\approx 300 \mu\text{m}$  and a time resolution of 500 ps will allow a good rejection of pile-up events, a very important feature for beam intensities of  $10^9$  hadron/spill.

### 3.6.3 Background studies

According to the experience gained in several unpolarised Drell–Yan experiments performed so far, two contributions can be identified as competing processes to Drell–Yan, especially in the intermediate mass range 2–2.5  $\text{GeV}/c^2$ :

- uncorrelated combinatorial muon background, originating from pion and kaon decays,
- open-charm semi-leptonic decays.

The combinatorial background can be minimised by optimising the hadron absorber located downstream of the target, as described in Sect. 10.2. Of particular importance is a proper dumping of the non-interacting beam particles in a heavy beam plug placed in the central part of the absorber.

The measurement of the combinatorial background was one of the main goals of the 2009 Drell–Yan beam test (Sect. 3.6.2). The conditions of the test (hadron absorber and beam plug implemented in the set-up downstream of the target) allowed to increase the beam intensity up to  $1.5 \times 10^8 \pi^-$  per spill, which is a factor 4 lower than the beam intensity of the proposed DY measurement. The combinatorial background was measured by studying  $\mu^+\mu^-$  and  $\mu^-\mu^-$  invariant mass distributions. The combinatorial background in the  $\mu^+\mu^-$  invariant mass spectra is calculated according to the formula

$$N_{BC_{\mu^+\mu^-}} = 2\sqrt{N_{\mu^-\mu^-} N_{\mu^+\mu^+}}. \quad (52)$$

A comparison of the  $\mu^+\mu^-$  invariant mass spectra and the combinatorial background is shown in Fig. 38. It shows that the contribution of the combinatorial background is suppressed by a factor of about 10 with respect to the  $\mu^+\mu^-$  invariant mass spectrum at

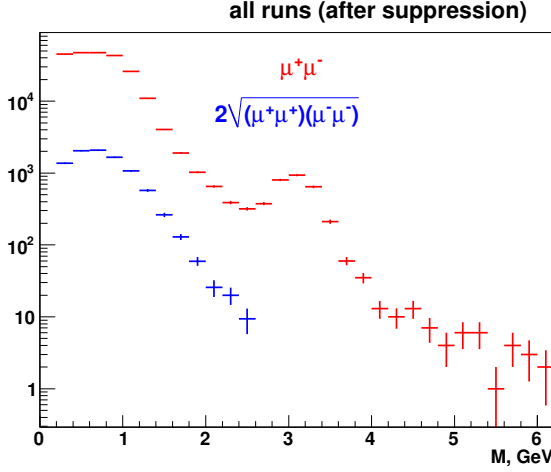


Figure 38: Upper points (red): invariant  $\mu^+\mu^-$  mass spectrum, lower points (blue): combinatorial background calculated according to Eq. (52).

$M_{\mu\mu} = 2 \text{ GeV}^2$ , so that even in the intermediate mass region  $2 \text{ GeV}/c^2 < M_{\mu\mu} < 2.5 \text{ GeV}^2$  there is a good probability to have a rather clean DY signal when running at the full beam intensity of  $6 \times 10^8$  pions per spill.

Open-charm decays, *i.e.*  $D^0$  and  $\bar{D}^0$  decays into muons, cannot be avoided or suppressed by using the hadron absorber. They constitute a source of dimuons that is correlated to some extent, as  $D^0$  and  $\bar{D}^0$  are produced from the partonic processes  $q\bar{q} \rightarrow c\bar{c}$  and  $gg \rightarrow c\bar{c}$ . The open-charm processes are simulated using PYTHIA and the generated dimuon events are propagated through a GEANT 3 simulation of the experimental apparatus. These Monte Carlo events are then reconstructed and the obtained distributions are compared with the corresponding ones for the Drell–Yan process. The contamination from open-charm dimuon events is seen to be negligible in both the high-mass region  $4 \text{ GeV}/c^2 < M_{\mu\mu} < 9 \text{ GeV}/c^2$  and the intermediate-mass region  $2 \text{ GeV}/c^2 < M_{\mu\mu} < 2.5 \text{ GeV}/c^2$ . The separation of open-charm and Drell–Yan events is likely to be improved by proper muon angular cuts.

### 3.6.4 Systematic errors in the asymmetries

Various systematic effects have been considered. Here we discuss the contributions from the most relevant ones:

1. The combinatorial background and the intrinsic charm contributions are negligible in the region of the dimuon invariant mass between  $4 \text{ GeV}/c^2 < M_{\mu\mu} < 9 \text{ GeV}/c^2$ . The data obtained from the 2009 beam test (Sect. 3.6.2) and MC simulations show that both are certainly not dominant in the intermediate dilepton mass range  $2 \text{ GeV}/c^2 < M_{\mu\mu} < 2.5 \text{ GeV}/c^2$ .
2. The migration of events from one cell to another, which results in a dilution of the asymmetries, depends on the experimental vertex resolution along the beam and on the separation between the two target cells. The distance between the two cells has been increased from the previous 10 cm to 20 cm in order to reduce this effect and to compensate for the decrease in vertex resolution caused by multiple scattering in the absorber. The final decision on the distance between the two target cells will be taken after the analysis of the 2009 beam test data will have been finished. The

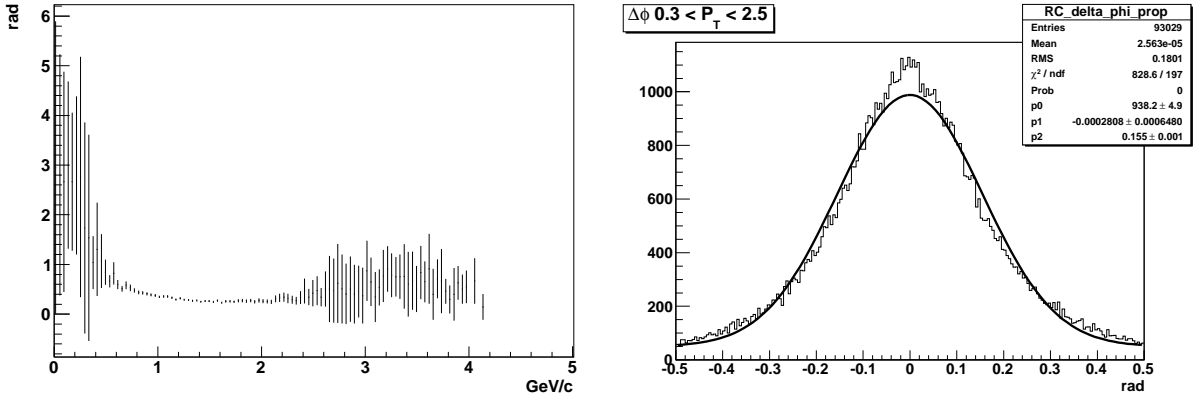


Figure 39: The profile plot for the resolution on  $\phi_S$  versus transverse momentum  $q_T$  of the virtual photon for the mass range  $4 < M_{\mu\mu} < 9 \text{ GeV}/c^2$  (left) and the average resolution in  $\phi_S$  for the mass range  $4 < M_{\mu\mu} < 9 \text{ GeV}/c^2$  and  $0.3 < q_T < 2.5 \text{ GeV}$  (right).

final goal for the cell-to-cell distance optimisation is to keep the contribution to the systematic error from the migration of events from one cell to another below the 1% level.

3. The resolution in  $\phi_S$  (for the definition see Fig. 23) determines the choice of the number of  $\phi_S$  bins to be used for the azimuthal asymmetries measurements. We have to minimise the bin-to-bin migration, on the one hand, and to have a sufficient number of bins in  $\phi_S$  for the fit, on the other. Exploiting the COMPASS experience in the azimuthal analysis of SIDIS data, where the resolution  $\sigma_{\phi_S} \approx 70 \text{ mrad}$  and 16 bins in total were used with a bin width of  $\approx 390 \text{ mrad}$  or  $\approx 5.6 \sigma_{\phi_S}$ , we conclude that for the DY analysis a bin width of  $5 \sigma$  will be sufficient to keep the bin-to-bin event migration under control. According to the experience of a previous Drell–Yan experiment (E615) in the analysis of the  $\cos 2\phi$  or Boer–Mulders asymmetry, 5 to 10 bins in  $\phi_S$  will be sufficient to reliably extract the modulations. The dependence of the resolution in  $\phi_S$  on the transverse momentum of the virtual photon is shown in Fig. 39. As one can see, the resolution is uniform almost over the whole  $q_T$  momentum range covered by the COMPASS spectrometer ( $0.3 – 2.5 \text{ GeV}$ ). In Figure 39 also is shown the  $\phi_S$  resolution averaged over this  $q_T$  region, as obtained in the Monte Carlo simulations with the hadron absorber (see Sect. 10.1 for a description of the absorber). The resulting  $\sigma_{\phi_S}$  is  $\approx 150 \text{ mrad}$ , thus a safe bin width will be 750 mrad which corresponds to 8 bins in  $\phi_S$ .
4. The influence of acceptance variations on the measured asymmetries has been checked in detail in the analysis of SIDIS data and a long list of tools has been built in order to both use estimators minimising the effects and give upper limits to the systematic error. The two cells of the COMPASS polarised target used for the Drell–Yan measurements will allow us to collect data with both polarisations at the same time. In transverse mode, the polarisation of a cell is reversed only every 3–5 days. The small difference in the acceptance of the two cells, which have their centres separated by 75 cm, does not allow the extraction of asymmetries from a single period of data taking. Therefore the data from two periods have to be combined in order to cancel acceptance and efficiency effects in the asymmetries. It is therefore important to monitor and keep as constant as possible the experimental conditions

over two consecutive periods with reversed spin configurations. One has to keep in mind that stability is also an essential ingredient for the DVCS and unpolarised DY measurements. Many tools were developed in previous years to check this stability of the data and the statistical compatibility of the results obtained in consecutive periods is a powerful test to check the presence of small systematic effects. The overall small upper limit for the systematic error obtained for the full data taking period with the  ${}^6\text{LiD}$  deuteron target proves that this systematics can be kept under control. Based on previous experience, a level of about 1% can be assumed for the systematic effects arising from potential instabilities of the data taking conditions.

5. For the unpolarised asymmetries, one needs to correct the measured distribution for the experimental acceptance. This is done by using a full Monte Carlo simulation of the apparatus which starts from the event generation performed by PYTHIA, simulates the experimental set-up and the particle interactions in the passive and active material of the detectors (also including the detector response done by COMGEANT), and ends with the reconstruction of the generated events by the same program (CORAL) used to analyse the real data. The quality of this chain is evaluated by comparing distributions of real data and of generated events. Moreover, a modification of the parameters in the event generator allows us to check the influence of the event phase space on the acceptance. Given the improvements in the Monte Carlo description of the apparatus which are foreseen and the improved stability of the apparatus over all the data taking periods, the expected contribution to the systematic error is considerably smaller than in the past.

Altogether, it can be concluded that there is no reason to expect a larger systematic error in asymmetry measurements using the DY reaction than in SIDIS measurements.

Two options are under discussion now to further reduce those systematic errors in the Drell–Yan experiment which are connected with the hadron absorber:

- the hadron absorber can be constructed entirely from alumina ( $\text{Al}_2\text{O}_3$ );
- an additional tracking station can be installed in between the polarised target and the hadron absorber.

What concerns the first option, the radiation length of the hadron absorber can be reduced by almost factor of two (from  $55.4 X_0$  of the current design of 150 cm  $\text{Al}_2\text{O}_3 + 60$  cm of stainless steel, down to  $35 X_0$  for 250 cm of only  $\text{Al}_2\text{O}_3$ ) when a 40 cm longer absorber is used. Due to the reduced multiple scattering in the absorber this would allow us to improve by a factor of about two the spatial, angular and mass resolution. The second option was studied by simulating an additional tracking detector plane at about  $z = -100$  cm in the standard COMPASS Monte Carlo program coordinate system, *i.e.* about 90 cm downstream of the second polarised target cell and about 20 cm upstream of the front edge of the absorber (Sect. 10.1). For simplicity, a standard MicroMega station was used as additional tracking detector (pitch size of 0.04 cm, no dead region simulated). In Table 11, a preliminary comparison is shown of various kinematic characteristics of dimuon events when reconstructed with or without such an additional tracking station. It appears that by using an additional tracking station one can improve by a factor of about five the resolution of the vertex reconstruction and significantly also the mass and angular resolutions.

### 3.7 Competition and complementarity

There are plans for future polarised Drell–Yan experiments at BNL, CERN, Fermilab, GSI, J-PARC and JINR. Some of them are presented in Table 12. Only PAX at FAIR (GSI-Darmstadt) and NICA at JINR (Dubna) plan to measure transverse doubly-

Table 11: Comparison of the resolution on various kinematical parameters in spectrometer configuration with and without additional MicroMega-like tracking station downstream of the target.

	present geometry	with $x$ - $y$ , $u$ - $v$ planes (preliminary)
$\sigma_{Vz}$	12.5 cm	1.8 cm
$\sigma_{Vx}$	0.6 cm	0.1 cm
$\sigma_M$	240 MeV	190 MeV
$\sigma_{P_T}$ (lab)	200 MeV/c	140 MeV/c
$\sigma_{\phi_\gamma}$ (lab)	148 mrad	90 mrad
$\sigma_{\theta_\gamma}$ (lab)	2 mrad	1.4 mrad
$\sigma_{\phi_{\mu^+}}$ (lab)	34 mrad	14 mrad
$\sigma_{\theta_{\mu^+}}$ (lab)	3 mrad	1 mrad
% reconstructed events	32%	56%

Table 12: Future Drell–Yan experiments.

Facility	Type	$s$ (GeV $^2$ )	Time-line
RHIC (STAR, PHENIX) [147]	collider, $p^\uparrow p^\uparrow$	200 $^2$ , 500 $^2$	> 2014
RHIC(internal target) [148]	fixed target, $p^\uparrow p^\uparrow$	500	> 2015
E906 (Fermilab) [149]	fixed target, $pp$ ,	226	> 2010
J-PARC [150]	fixed target, $pp^\uparrow$	60 $\div$ 100	> 2015
GSI(PAX) [151]	collider, $\bar{p}^\uparrow p^\uparrow$	200	> 2017
GSI (Panda) [152]	fixed target, $\bar{p}p$	30	> 2016
NICA [153]	collider, $p^\uparrow p^\uparrow, d^\uparrow d^\uparrow$	676	> 2014
COMPASS (this Paper)	fixed target, $\pi^- p^\uparrow$	300 $\div$ 400	> 2012

polarised Drell–Yan processes, in the long-term future. In Dubna it is proposed to study the Drell–Yan process in proton–proton or deuteron–deuteron polarised-beam collisions, which give access only to interactions between valence quarks and sea antiquarks. The PAX Collaboration plans to polarise antiprotons to study the interactions between valence quarks and valence antiquarks. However, the possibility to get a beam of polarised antiprotons still has to be demonstrated. Both collaborations plan to study  $e^+e^-$  final states. The Drell–Yan programmes at RHIC and J-PARC both foresee to measure single- and double-spin asymmetries in the Drell–Yan process, but unlike COMPASS they have only access to valence-quark–sea-quark interactions in  $pp$  collisions. The E906 project is oriented to the study of the sea quark distribution in the proton and can be considered as a complementary measurement with respect to the COMPASS DY plans. The Panda experiment is designed to study the  $J/\psi$  formation mechanism rather than Drell–Yan physics, because of the very low antiproton beam energy (15 GeV). The future experiment that is most similar to COMPASS, the PAX experiment, is designed to reach a luminosity of at most  $5 \times 10^{31}$  cm $^{-2}$  s $^{-1}$ . Thus the COMPASS experiment would be the first one to perform measurements of single-spin asymmetries in Drell-Yan processes to access spin-dependent PDFs in the valence quark region with high statistical significance. The first-ever data

on the  $J/\psi$  formation mechanism in  $\pi^- p$  interactions will be also obtained, which is very important for the understanding of hadron–hadron interaction dynamics.

## 4 Experimental studies of chiral perturbation theory

From the earliest attempts to understand the strong interaction more than 70 years ago, the pion and its properties have played a key role, first as an exchange particle in the nucleon–nucleon interaction, and later as the lightest quark–gluon bound state of Quantum Chromodynamics (QCD). Revealing and explaining the pion’s global properties and the details of the internal structure, is still a challenge for experimental and theoretical particle physics, specifically in verifying the validity of QCD for the dynamics of non-perturbative bound states and low-energy reactions.

Exploiting the smallness of the  $u, d, s$  quark masses, the approximate chiral symmetry of the QCD Hamiltonian,  $SU(3)_L \times SU(3)_R$ , can be used to construct the low-energy effective field theory, which allows to expand the strong interactions systematically in the particle momenta. This approach is called Chiral Perturbation Theory (ChPT). According to the Goldstone theorem, the spontaneous breaking of the chiral symmetry in the QCD vacuum manifests itself in the occurrence of (almost) massless pseudoscalar Nambu–Goldstone bosons. These are identified with the observed pions and kaons (and the eta). Within this theory, their small masses originate from the non-vanishing quark masses, which break the chiral symmetry explicitly. The first complete treatment of ChPT up to one-loop order has been presented by Gasser and Leutwyler in Ref. [154], where also references to earlier work can be found. For a recent overview of the current status of ChPT in the meson sector, see Ref. [155].

The crucial feature of ChPT is to establish various connections between physical observables as a consequence of the (approximate) chiral symmetry of QCD, often referred to as low-energy theorems. Working out the systematic corrections, ChPT can give firm predictions for the strong interaction dynamics of the Goldstone bosons, which is often very difficult to determine experimentally. The most striking example concerns the long-standing problem of the pion electromagnetic polarisabilities. In ChPT, the (dominant) difference of the electric and magnetic polarisabilities is directly related to the strength of the radiative pion decay. Beyond that, higher-order corrections and a theoretical error estimate have been worked out recently in Ref. [156]. The pion polarisabilities (together with chiral loop contributions) give rise to deviations of the pion Compton cross section  $\sigma(\pi\gamma \rightarrow \pi\gamma)$  from the QED expectation valid for a structureless spin-0 particle, as discussed in detail in Sect. 4.1.

Moreover, within ChPT the coupling constants for reactions including more pions in the final state are equally well controlled, *e.g.* the chiral anomaly driving the low-energy behaviour of the reaction  $\pi^\pm\gamma \rightarrow \pi^\pm\pi^0$ . The potential of measuring also those reactions, closely related to the Compton reaction and consequently measurable in parallel as reviewed in Ref. [157], is addressed in Sect. 4.2.

### 4.1 Pion and kaon polarisability measurement

The pion electric and magnetic dipole polarisabilities  $\alpha_\pi$  and  $\beta_\pi$  characterise the response of a (charged) pion, as a composite  $q\bar{q}$  system, to external electromagnetic fields in the low-frequency limit. Clearly these are fundamental structure parameters of the pion, and the comparison between theoretically predicted and directly measured values provides a stringent test for various theoretical approaches, like ChPT, dispersion sum rules, QCD sum rules and quark confinement models. The theoretical predictions disagree markedly with each other and lie in the range  $(2 - 8) \times 10^{-4} \text{ fm}^3$  for the absolute values of  $\alpha_\pi$  and  $\beta_\pi$  [157–159]. Several attempts were made in the past to measure these quantities (see, *e.g.* Ref. [160]) using different experimental approaches. The results obtained are affected

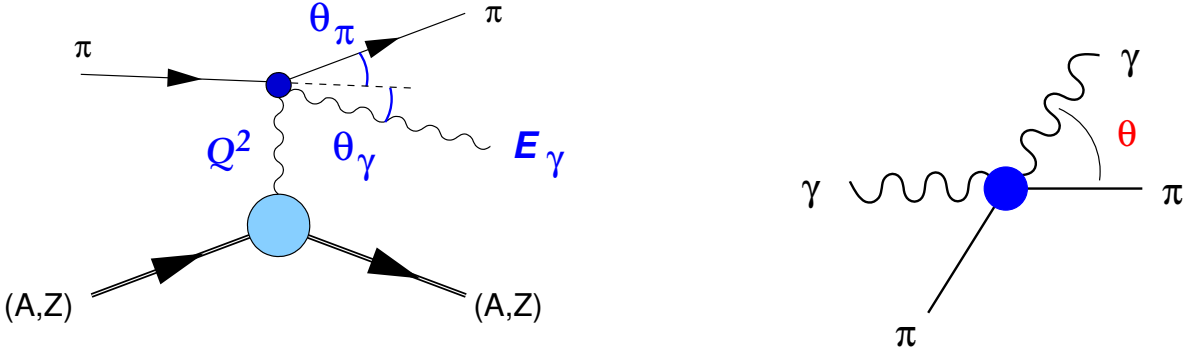


Figure 40: Pion Compton reaction (right graph) embedded in the Primakoff reaction (left graph) on a nucleus of charge  $Z$ . Kinematical quantities in the laboratory and the CM scattering angle are indicated.

by large uncertainties and there are even large discrepancies between them. The ongoing dispute about the compatibility of the ChPT results for the pion polarisabilities with those of the dispersion relation approach, as expressed in Refs. [161, 162], demonstrates once more the urgent need for experimental clarification.

The COMPASS experiment provides unique tools to measure precisely the pion polarisabilities in the Primakoff reaction

$$\pi^- Z \rightarrow \pi^- Z \gamma \quad (53)$$

embedding the pion Compton scattering reaction as depicted in Fig. 40. The cross section for the Primakoff reaction (53), treating the nuclear vertex in the equivalent photon approximation [163] is given by

$$\frac{d\sigma}{ds dt dQ^2} = \frac{\alpha}{\pi(s - m_\pi^2)} \cdot F_{\text{eff}}^2(Q^2) \cdot \frac{Q^2 - Q_{\min}^2}{Q^4} \cdot \frac{d\sigma_{\pi\gamma}}{dt} \quad (54)$$

where  $Q_{\min} = (s - m_\pi^2)/2E_{\text{beam}}$ ,  $s$  and  $t$  are the Mandelstam variables in the  $\pi\gamma$  system. Using the threshold expansion for the  $\pi\gamma$  subprocess, the polarisabilities are introduced at the level of Compton amplitudes (following Ref. [156])

$$\frac{\alpha}{m_\pi} H_{+\mp}(t, s = m_\pi^2) = (\alpha_\pi \pm \beta_\pi) + \frac{t}{12} (\alpha_2 \pm \beta_2) + \dots \quad (55)$$

where the leading Born terms are subtracted to obtain the reduced (spin-flip and spin-nonflip) helicity amplitudes  $H_{+\mp}$ . This leads (to linear order) to the pion polarisability term  $\mathcal{P}$  for the differential cross section

$$\frac{d\sigma_{\pi\gamma}}{d\Omega_{cm}} = \frac{\alpha^2 (s^2 z_+^2 + m_\pi^4 z_-^2)}{s(s z_+ + m_\pi^2 z_-)^2} - \frac{\alpha m_\pi^3 (s - m_\pi^2)^2}{4s^2 (s z_+ + m_\pi^2 z_-)} \cdot \mathcal{P} \quad (56)$$

which is given by

$$\mathcal{P} = z_-^2 (\alpha_\pi - \beta_\pi) + \frac{s^2}{m_\pi^4} z_+^2 (\alpha_\pi + \beta_\pi) - \frac{(s - m_\pi^2)^2}{24s} z_-^3 (\alpha_2 - \beta_2) \quad (57)$$

and  $z_\pm = 1 \pm \cos \theta_{cm}$ ,  $\theta_{cm}$  the scattering angle in the CM system of the outgoing  $\pi\gamma$  pair. The last term accounts for the quadrupole polarisability difference  $\alpha_2 - \beta_2$ , which

emerges in a consistent treatment in the same order as the dipole polarisability sum  $\alpha_\pi + \beta_\pi$ . The full expansion in  $s = m_{\pi\gamma}^2$  to the given order requires terms quadratic in the polarisabilities. They are omitted here as they do not change the salient features given by the linear terms.

The effect of the difference of electric and magnetic polarisability ( $\alpha_\pi - \beta_\pi$ ) is strongest under backward angles (for this reason, this quantity is also called backward polarisability), while the forward polarisability ( $\alpha_\pi + \beta_\pi$ ) influences the cross section mostly at large  $\cos\theta$ . While the latter forward polarisability is expected to assume small values, it is enhanced in the cross section by the prefactor  $s^2/m_\pi^4$ . As a consequence, measuring the energy and angular dependence of the cross section allows to extract the two dipole polarisabilities separately. Furthermore, within ChPT the 1- and 2-loop contributions are to be taken into account for a correct interpretation of the experimental cross section.

The effect of the polarisabilities as given by Eq. (56) is depicted in Fig. 41, also showing the kinematical relation with the laboratory quantities. The physically interesting region includes photons with energies in the range from 20 to 180 GeV at angles from 0 to 8 mrad with respect to the incoming beam pion direction.

The study of Primakoff reactions in COMPASS was first started in the pilot hadron run in 2004 using 190 GeV  $\pi^-$  and  $\mu^-$  beams impinging on a solid Pb target, segmented in longitudinal direction. Additional samples for Cu and C targets were also collected. The total amount of pion Primakoff events from the lead target was about 60,000 events with photon energies above 40 GeV. Instabilities in the amplification of many cells of the electromagnetic calorimeter connected with saturation effects and some features of the Primakoff trigger, including a missing row in the sensitive central region, turned out to cause significant systematic uncertainties of the measurement and do not allow to extract a reliable value for the pion polarisabilities from the 2004 data. However, the measurement allowed to address the full measurement procedure and established the feasibility of a much improved measurement.

The most important achievements of the present analysis are, on the one hand, the selection of Primakoff reactions as exclusive  $\pi\gamma$  events (Fig. 42), the identification of the Primakoff peak and the diffractive background in the  $Q^2$  distribution (Fig. 42) allowing to confirm the  $Z^2$  dependence of the Primakoff peak following the theoretical prediction (Fig. 43). On the other hand, we determined important parameters of our setup such as resolutions and Monte Carlo control of detector efficiencies and identified the main sources of background, both, non separable physics processes (the ratio of Primakoff signal to diffractive background for different targets is shown in Fig. 42) and backgrounds stemming from beam impurities for which a set of procedures for background reduction has been developed. Corrections to the pure tree level Primakoff cross section come from the Compton vertex, multiple photon exchange, vacuum polarisation, nuclear charge screening by atomic electrons and contribution of nuclear form factor and have now also been calculated [164, 165]. The full  $Q^2$  dependence was also investigated within the Glauber model in the work of [166, 167], incorporating the influence of the strong interaction.

In the recent Primakoff data taking in November 2009, several of the learnings from the 2004 run have been taken into account, with the perspective of extracting a reliable value for  $\alpha_\pi - \beta_\pi$  from a statistics of about a factor three larger than the one of 2004. Those include

- Usage of an unsegmented target with the thickness of  $0.3X_0$ . This target provides the opportunity to collect large statistics with high data quality (good resolution for  $Q^2$ , low background from beam kaon decays due a shorter fiducial volume cut).

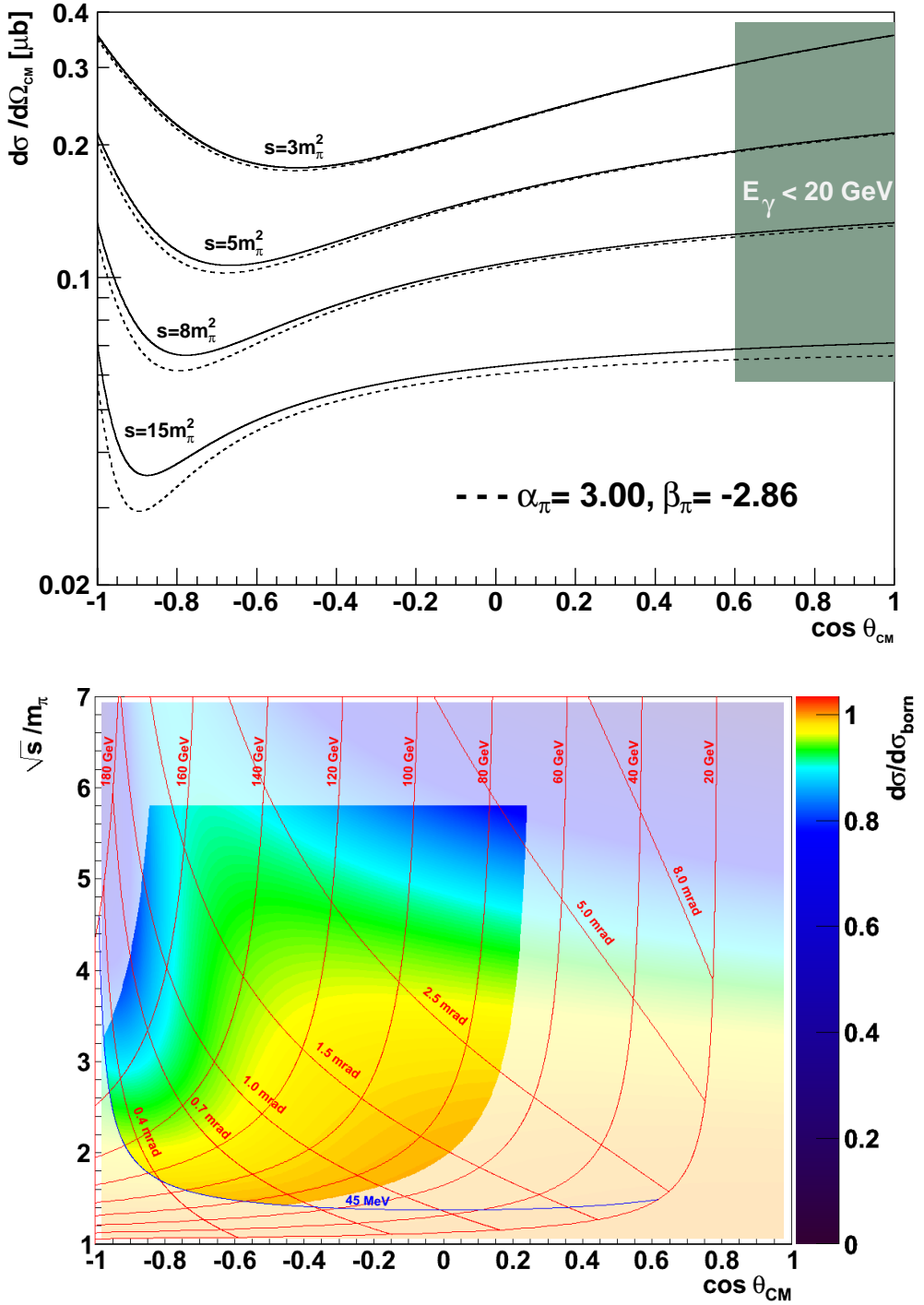


Figure 41: Top: Pion Compton scattering cross section (continuous line: point-like case) and polarisability effect (dashed line: prediction of chiral perturbation theory). Bottom: relation to the photon kinematics (energy and production angle) in the laboratory. In colour, the relative effect of the dipole polarisabilities (ChPT values) on the cross section is shown (in light colour saturation, the region outside of the kinematical cuts is indicated).

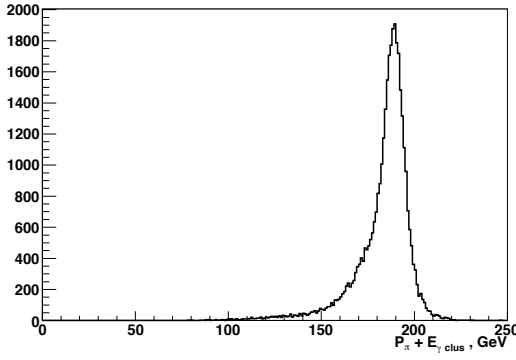


Figure 42: Exclusivity peak of  $E_\gamma + E_\pi$  for  $\pi\gamma$  events.

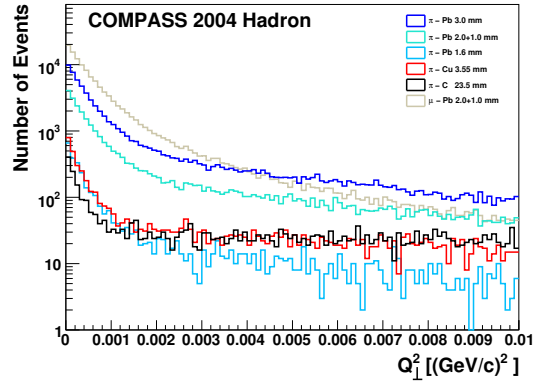


Figure 42:  $Q^2$  distribution for different targets. The Primakoff peak at  $Q^2 = 0$  is nicely visible.

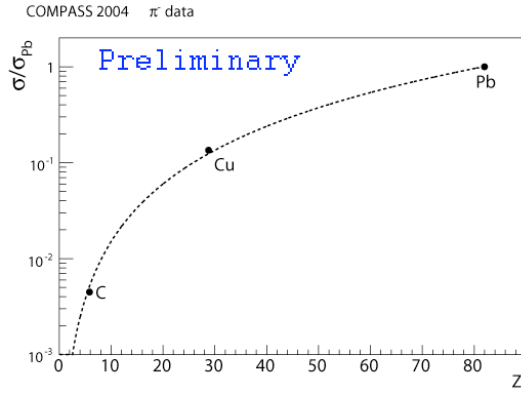


Figure 43:  $Z^2$  dependence of the Primakoff cross section.

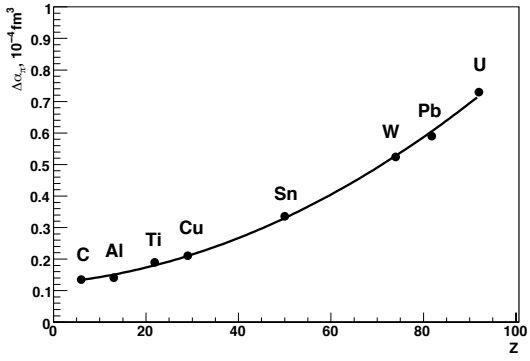


Figure 43: Systematic shift of  $\alpha_\pi$  due to radiative corrections.

Replacing Pb by Ni as target material reduces the effect radiative corrections more significantly for lead, and the correction related to the nuclear form factor. The spin-0  $^{58}\text{Ni}$  nucleus simplifies the estimation of radiative corrections.

- The layout of the target region was kept similar to the hadron run 2009, with the hydrogen target being replaced by a solid target. The present geometrical positions of silicon and PixelGEM detectors allow to measure the scattering angle of pions with the required precision of  $\Delta p_T < 10$  MeV, and to also collect the statistics for beam kaons decay up- and downstream of the target, which is important for  $K^- \rightarrow \pi^-\pi^0$  background determination, though kaon background will be much reduced owing to the CEDARs.
- The new digital ECAL2 trigger on the Primakoff photons was installed. As these photons are concentrated in the central part of ECAL2, it was sufficient to include the  $12 \times 12$  central cells. For the other processes of interest, as outlined in the next section, will require a larger active ECAL area to be included in the trigger.
- The trigger hodoscopes downstream of the concrete wall, used in the muon program in order to provide particle identification in the range  $15 \text{ GeV}/c < p < 20 \text{ GeV}/c$ , was activated in order to provide muon–pion separation.

Table 13: Proposed running time, the respective total beam flux for pions and muons, and expected total errors on the pion polarisabilities (units  $10^{-4}$  fm $^3$ , except quadrupole polarisability values in units of  $10^{-4}$  fm $^5$ ).

Days	$\pi$ beam, days	$\mu$ beam, days	Flux $\pi, 10^{11}$	Flux $\mu, 10^{11}$	$\alpha_\pi - \beta_\pi$ $\sigma_{tot}$	$\alpha_\pi + \beta_\pi$ $\sigma_{tot}$	$\alpha_2 - \beta_2$ $\sigma_{tot}$				
120	90	30	59	12	$\pm 0.27$	fixed	fixed				
					$\pm 0.26$	$\pm 0.016$	fixed				
					$\pm 0.66$	$\pm 0.025$	$\pm 1.94$				
					ChPT prediction						
					5.70	0.16	16				

- CEDARs are required for beam kaon identification. Their performance in 2009 is still to be studied.
- An optimised electron converter was installed on the beam line to decrease the admixture of the electrons in the hadron beam. It is positioned close to the last major bending dipoles or downstream of CEDAR 2.
- The VetoBox surrounding the target and used in 2004 was replaced by the new recoil proton detector, serving as veto system. The forward sandwich veto suppresses reactions of particles under large angles.

One of the key features for this measurement within COMPASS is the study of systematic effects using a well known calibration process, Primakoff scattering by muons. In the following we assume all of the systematic effects to be measured using muons, thereby neglecting for the moment effects on beam shape and intensity, secondary interactions and systematic effects based on concurring physics processes different for the two particle species. In order to keep the systematic uncertainty below the statistical one, we need to collect data shared between pion and muon beams as given in Table 13. Using a  $0.3X_0$  Ni target and beam intensities of  $4 \times 10^7$  per spill for pions and  $4 \times 10^8$  per spill for muons we have calculated event rates and uncertainties, where we assume the geometrical acceptance for Primakoff events and the efficiency of our selecting cuts to be the same as in 2004 (but which improved performance of ECAL 2 and trigger hodoscopes). Collecting 10 full runs (1000 spills) per day, as was realised in the previous beam times, we give the corresponding values for beam fluxes and the total uncertainties for different periods of data taking in Table 13, subdivided into three different ways to fit the polarisabilities: Fixing the subleading contributions  $\alpha_\pi + \beta_\pi$  and  $\alpha_2 - \beta_2$  to some value decreases the statistical uncertainty on the free parameter(s) as given in the first two rows. This, however, will lead to an unknown shift of the fitted value(s) due to the correlation between them (especially  $\alpha_\pi - \beta_\pi$  and  $\alpha_2 - \beta_2$ ). Since none of the polarisability combinations is constraint in principle, only the full 3-parameter fit (3<sup>rd</sup> row) is regarded as the goal for this measurement. For the quadrupole contribution, the full 2-loop result is given [156]. If the 1-loop contribution ( $12 \times 10^{-4}$  fm $^5$ ) is explicitly taken out, as has been done for the dipole polarisability extraction in the Serpukhov data analysis [168], the ChPT prediction reads  $4 \times 10^{-4}$  fm $^5$ . In Table 13, time needed for detector commissioning is not included. Small data samples with empty target which will help to study the systematic effects are also not included, however their collection should take just a few hours.

So far all experiments performed have only been able to address a combination of electric and magnetic polarisability (namely  $\alpha_\pi - \beta_\pi$ ). COMPASS can, for the first time,

Table 14: Expected precision of the kaon polarisability measurement obtained in parallel with the proposed running time in Table 13 (units  $10^{-4} \text{ fm}^3$ ).

$\pi/K$ beam days	Flux $\pi, 10^{11}$	Flux $K, 10^{11}$	$\alpha_K - \beta_K$ $\sigma_{tot}$	$\alpha_K + \beta_K$ $\sigma_{tot}$	$\alpha_{K,2} - \beta_{K,2}$ $\sigma_{tot}$
90	59	1.4	$\pm 0.08$	fixed	fixed
			ChPT prediction		
			1.0	-	-

also perform an independent measurement of  $\alpha_\pi$  and  $\beta_\pi$  using the information about both, energy and scattering angle of Primakoff photons. Within the proposed data taking, we can expect a statistical uncertainty on the level of  $0.66 \times 10^{-4} \text{ fm}^3$  on the difference of dipole polarisabilities, and  $0.025 \times 10^{-4} \text{ fm}^3$  for their sum. Here, it should be stressed that the investigation of the full  $s$  dependence includes to account for the 1- and 2-loop contributions predicted by Chiral Perturbation Theory, which are also viewed as dynamic polarisability  $\alpha_\pi(s)$ , in contrast to the  $s$ -averaged measurements discussed so far. The range of  $s$  accessible for COMPASS includes also the region of  $\rho$  meson decays, which contains interesting information, as the radiative width of the  $\rho$ , by itself.

In addition to the precise measurement of the pion polarisabilities, we can observe Primakoff scattering with charged kaons for the first time and thus obtain the kaon polarisability. For the proposed data taking, we expect about 4000 Primakoff events with kaons in the sensitive range  $0.5 < \omega < 0.9$ . Thus a first and coarse measurement of the kaon polarisability can also be obtained in parallel to the high precision determination of the pion polarisability outlined above due to the usage of CEDARs for separation of kaons and pions in the beam (Table 14).

The experimental setup has to be optimised in the following ways for the proposed data taking:

- In order to ensure high redundancy in the tracking of incoming and outgoing pions, an additional tracking station will be installed downstream of the target. Precision in the scattering angle requires distances smaller than 1 m between target and closest tracking stations.
- The measurement of the kaon polarisabilities require an improvement in kaon identification by the CEDAR system, which has to be optimised or rebuilt.
- The RICH beam pipe has to be replaced by a solution which minimises the conversion probability for photons and the multiple scattering for charged particles.
- The digital trigger electronics, which came as a very new installation to the 2009 data taking, has to be finalised.

## 4.2 Primakoff reactions with neutral pions in the final state

In parallel to the Primakoff Compton scattering Eq. (53) COMPASS also aims to measure Primakoff reactions with neutral mesons in the final state, already been observed in the 2004 pilot run:



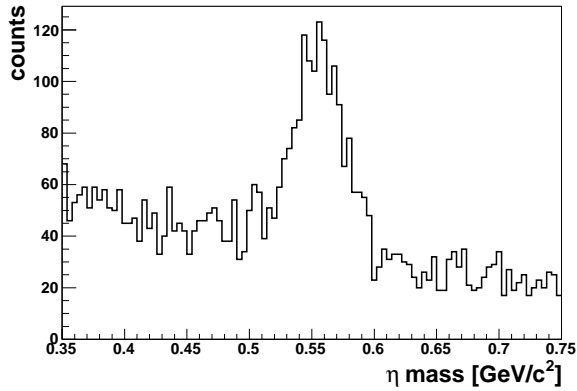


Figure 44:  $\eta$  mass spectrum for the  $\pi^- \eta$  final state (no background subtraction, very coarse cut set).

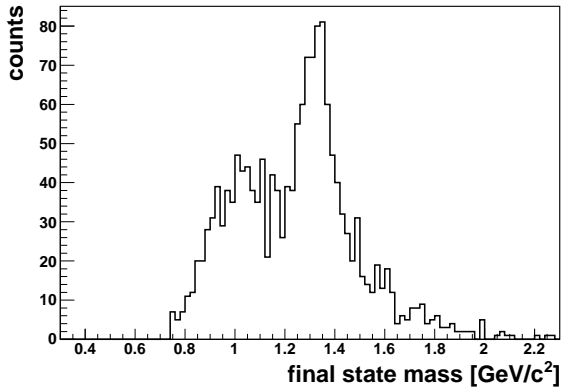


Figure 44: The mass spectrum of the  $\pi^- \eta$  final state for  $Q^2 < 0.002 \text{ GeV}^2$  (no background subtraction, very coarse cut set) is dominated by  $a_2(1320)$ . Improving event selection and subtraction of background is expected to clear up the picture.

The measurement of Eq. (58) allows to determine the chiral anomaly amplitude  $F_{3\pi}$ , for which Chiral Perturbation Theory (ChPT) makes an accurate prediction by relating the process to the  $\pi^0$  decay constant  $f_\pi$  and the electric coupling constant  $\alpha_{em}$ . This constitutes a test of higher-order ChPT. The reaction Eq. (59) is calculable directly at tree level ChPT [157], using the pion scattering lengths  $a_0, a_2$ , combined with the electromagnetic coupling  $\alpha$ . Here, the ChPT expansion should be reliable on the percent level, and so, the experiment constitutes a strong test of  $\chi PT$  at tree level and goes much beyond the determination of low energy constants.

Reaction Eq. (58) has already been examined by the Serpukhov experiment [169], however in the relevant region of  $s < 10 m_\pi^2$  only about 200 events were obtained. Reaction Eq. (59) has not been determined up to now.

Reaction Eq. (60) allows the direct observation of  $1^-(1^{+-})$  exotics created in photoproduction as the selection of Primakoff events removes  $a_0$  decaying to the same final state (Figs. 44 and 44).

All of these channels have been identified in the 2004 pilot run with effectively three days of COMPASS beam on a segmented 2+1 mm Pb target. About 320 events with exclusive single  $\pi^0$  production with  $s < 10 m_\pi^2$  (Fig. 45), and 85 events with exclusive double  $\pi^0$  in the interesting range  $s < 22 m_\pi^2$  have been reconstructed (Fig. 45). The cut on exclusivity was  $\pm 10 \text{ GeV}$  for the reaction of Eq. (58) and  $\pm 15 \text{ GeV}$  for that of Eq. (59) around the nominal beam energy, obtained as exclusivity peak in the sum of the outgoing pion energies. The quasi-real photon exchange was selected with cuts of  $Q^2 < 0.001 \text{ GeV}^2$  and  $Q^2 < 0.005 \text{ GeV}^2$  for reactions of Eqs. (58) and (59), respectively. Background has been subtracted using an adjacent  $Q^2$  side band. A new measurement should aim for at least 10,000 events in the  $s < 10 m_\pi^2$  range for the  $\pi^0$  channel, as it was also originally proposed for COMPASS. We expect about 2,500 events for the  $\pi^0 \pi^0$  channel at the same time.

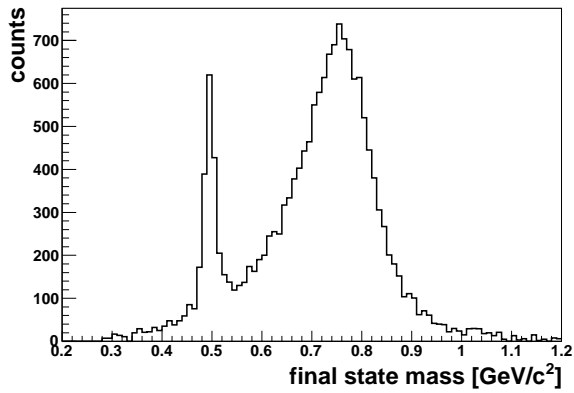


Figure 45: The invariant mass spectrum of  $\pi^-\pi^0$  is dominated by  $\rho^-$  photo-production. On its left side the decay of beam  $K^-$  gives rise to a narrow kaon line. Still further to lower masses, anomalous  $\pi^0$  production can be seen as a rising slope starting at  $2 m_\pi$ .

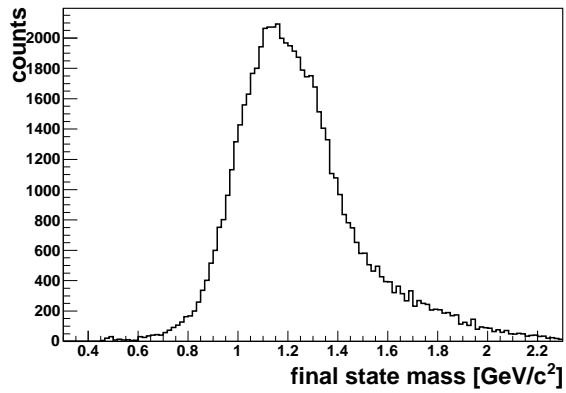


Figure 45: In the invariant mass spectrum of  $\pi^-\pi^0\pi^0$ , the  $a_1$  photo-production peak is interfering with direct  $\pi^0\pi^0$  production, most easily observed close to the  $3 m_\pi$  threshold.

## **– HARDWARE UPGRADES –**

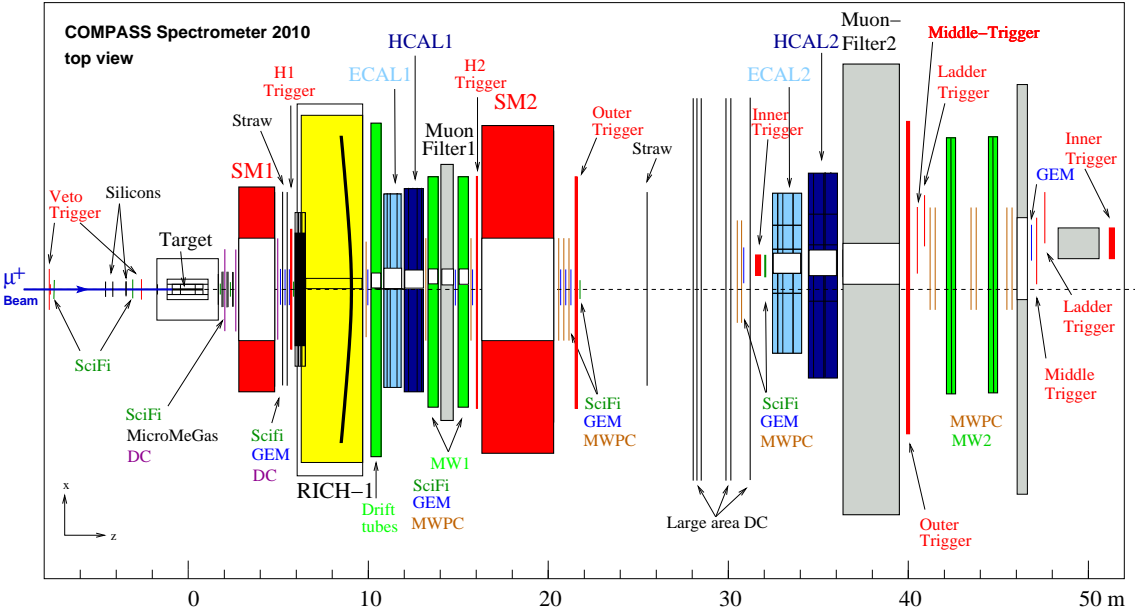


Figure 46: Top view of the 2010 COMPASS spectrometer setup.

### The 2010 lay-out of the COMPASS apparatus

Except otherwise noted, all hardware upgrades described in this document refer to the set-up used in 2010 with the muon beam and the polarised  $\text{NH}_3$  target. The 2010 spectrometer is shown in Fig. 46 and a detailed discussion of most of the components can be found in Ref. [133].

## 5 Muon trigger

For both DVCS and DY measurements the trigger relies on the detection of muons with fast scintillator hodoscopes. In case of the DVCS measurement, the detection of the scattered muon in a very large kinematic range of  $Q^2$  and  $x_B$  is mandatory, whereas for the Drell–Yan programme triggering of pairs of oppositely charged muons is needed.

Muons are detected behind thick concrete or iron absorbers for muon identification either by measuring their scattering angle in a plane perpendicular to the dipole bending plane (*target pointing trigger*) or by measuring the energy loss using the deflection in the dipole fields (*energy loss trigger*). Target pointing needs horizontal scintillator elements with a width given by the distance to the target; the energy loss trigger has vertical strips with a width determined by the distance to the dipole magnets.

### 5.1 Trigger hodoscopes

The measurements will make use of the existing hodoscope system selecting inclusive events which is operated since 2002 at the COMPASS experiment [170] and which was continuously improved during the recent years. A further upgrade is prepared for the transverse data taking in 2010.

Due to the large variation of counting rates, different trigger systems are being used for different kinematic regions. These parts are:

- the *Ladder trigger* covering low  $Q^2$  and high  $y$ ,
- the *Middle trigger* covering low  $Q^2$  and all  $y$ ,
- the *Outer trigger* covering intermediate  $Q^2$  and all  $y$ ,
- the *LAS trigger* covering large  $Q^2$  and high  $x_B$ .

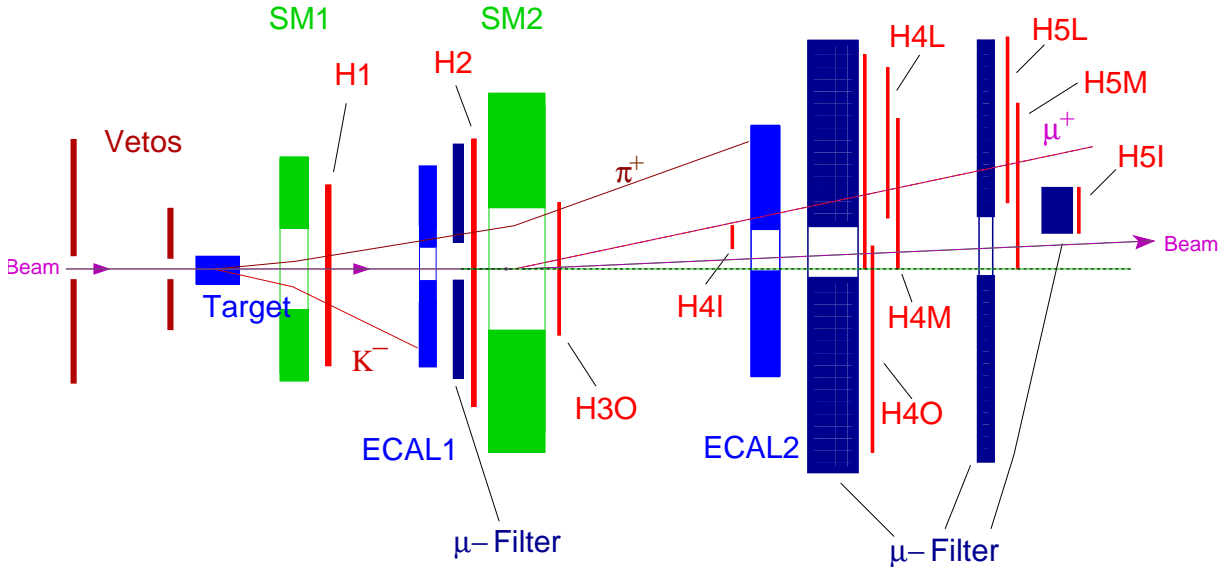


Figure 47: Location of the components relevant for the trigger (schematically), see also Table 15. The inner trigger system (H4I and H5I) will not be used for DVCS and DY data taking.

In order to guarantee triggering on muons only, at least one of the two hodoscopes is located behind an absorber (muon filter). In each case, the hodoscopes are put as close as possible to the absorber to minimise effects due to multiple Coulomb scattering in the absorber. Details on the hodoscopes are given in Table 15 and a sketch of their positions is shown in Fig. 47.

*Ladder trigger (H4L, H5L):* The ladder trigger selects muons with small scattering angles but high energy losses. To achieve this selection, both hodoscopes are located behind the spectrometer magnets bending particles in the horizontal plane. Both hodoscopes consist of short vertical strips read out on both sides by PMTs. Using a coincidence of two hodoscope strips in H4L and H5L, muons with a large deflection in the magnets but very small scattering angle are selected yielding events with a large energy loss, but small  $Q^2$ .

*Middle trigger (H4M, H5M):* The middle trigger combines the features of an energy loss trigger using vertical elements with a target pointing trigger using a second layer of horizontal strips for each of the two hodoscopes. The vertical strips are readout on one side by PMTs while the horizontal ones are read on both sides. The middle system covers a relative energy transfer  $y$  from 0.1 to 0.7 at small scattering angles.

*Outer trigger (H3O, H4O):* The outer system consists of a horizontal hodoscope plane at the exit of the second spectrometer magnet (H3O) and a second one behind the hadron absorber in the SAS (H4O) to obtain vertical target pointing. It is divided into two halves to avoid very long strips. The size of the second hodoscope is matched to the size of the muon wall MW2 chambers used to reconstruct muon tracks. All strips are read out by two PMTs. The outer system covers all  $y$  and large  $Q^2$  up to 10  $(\text{GeV}/c)^2$ .

Table 15: The trigger hodoscopes and their main parameters. The overlaps between neighbouring strips guarantee high trigger efficiency.

system	hodoscope	# of strips	width (mm)	overlap (mm)	z-pos. (m)	area ( $x \times y$ ) (cm $^2$ )
ladder	H4L	32	22 – 67	1 – 3	40.65	128.2×40
	H5L	32	27 – 87	1 – 3	48.05	168.2×47.5
middle	H4MV (top)	20	62	1.5	40.3	120×102
	H4MV (bot)	20	62	1.5	40.3	
	H4MH	32	21.5 – 25	1.5	40.4	
	H5MV (top)	20	77	1.5	47.7	150×120
	H5MV (bot)	20	77	1.5	47.7	
	H5MH	32	25 – 30	1.5	47.8	
outer	H3O	16	70	5	23	200×100
	H4O	2×16	150	10	40.0	480×225
LAS	H1	32	60	0	5.5	230×192
	H2	2×32	136	5	15.5	500×419.2

*LAS trigger (H1, H2):* The LAS trigger system will be set up for the 2010 transverse data taking. It consists of two horizontal hodoscope planes, H1 in front of the RICH and H2 after the first hadron absorber and the muon wall MW1 modules. The size of the second hodoscope is matched to the size of the MW1 chambers measuring the tracks behind the first muon filter. The second hodoscope is split into two halves to avoid too long strips and to allow an easy triggering on muon pairs in the DY programme. All scintillator elements are read out by two PMTs. Similar to the outer system the LAS system makes use of vertical target pointing. The main purpose of this system is the extension of the muon trigger system to the largest  $Q^2$  and high  $x_B$ .

## 5.2 Veto system

Due to the sizable muon beam emittance and a (near plus far) halo fraction of about 25% at 160 GeV beam energy many muons not interacting in the target would cause a trigger. Those muons are rejected using a system of veto counters in front of the target. It consists mainly of two segmented scintillation counters of about 30 cm diameter upstream of the target, with a central hole of about 4 cm leaving the central beam region uncovered. These counters veto tracks with a slope larger than 8 mrad. A third counter, V<sub>bl</sub>, located 20 m upstream of the target (not shown in Fig. 48) rejects halo muons having smaller slopes. The first veto counter is supplemented by additional strips covering an area of about 250 cm × 320 cm to veto also the far muon halo. Details of the counters are summarised in Table 16.

The drawback of a veto system is the dead time associated to it. The dead time of the full veto system which has to be applied to all inclusive triggers is about 25% at the nominal beam intensity for a reasonably well debunched beam. For the future it is desirable to run with a smaller veto dead time, also in view of the possibility to use a 100 GeV muon beam which has a larger halo fraction. For this case, a more modular veto system is under study, which only will veto those regions in the vicinity of the muon that cause an inclusive trigger. In order to achieve this goal the central veto counters need a higher granularity and coincidence matrices similar to the ones used in the hodoscope

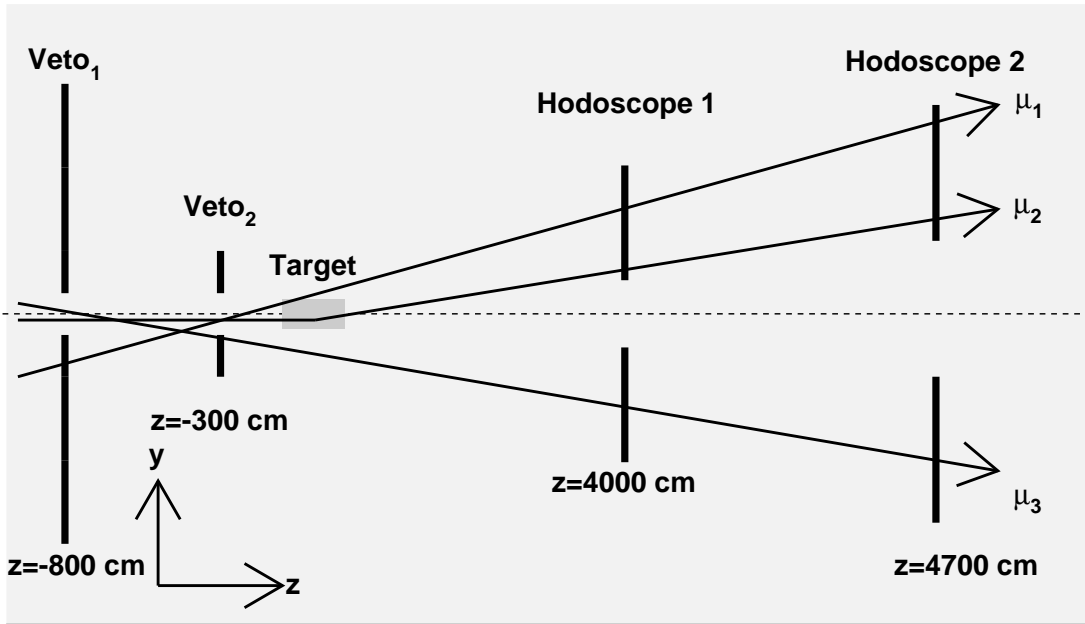


Figure 48: Schematic layout of the veto system. The tracks  $\mu_1$  and  $\mu_3$  are vetoed, whereas the track  $\mu_2$  fulfils the inclusive trigger condition.

system. The new trigger electronics developed for the LAS trigger system can be used. As the veto system is mainly needed for measurements with the muon beam due to its large halo, the conditions can be relaxed for measurements with a pion beam.

### 5.3 Inclusive trigger

For the DVCS measurements a fully inclusive trigger is necessary, especially when measurements of unpolarised PDFs and FFs are planned in parallel. Thus the detection of a muon in one of the four hodoscope subsystems is required. For this purpose, the signals of all hodoscopes are fed into constant-fraction discriminators followed by mean timers for the elements read out on both sides. The signals are then distributed to F1 TDCs and to custom-made coincidence matrices with adjustable delays to obtain a trigger signal from each of the subsystems. For the new hodoscopes H1 and H2 new mean timer and

Table 16: Main components of the veto system. In the second column, the outer dimensions and the diameters/sizes of the inner holes are given. The symbol  $\circ$  stands for a circular,  $\square$  for a quadratic hole.  $V_{bl}$  is the additional veto hodoscope placed further upstream in the beam line to veto tracks passing through both holes in Veto<sub>1</sub> and Veto<sub>2</sub>. The rates were determined during the 2009 DVCS test beam.

	dimensions/ cm	$z$ -pos./ cm	no. of elements	rate/ $10^6/\text{spill}$
single hodoscopes				
Veto <sub>1</sub>	$250 \times 320, \circ 4$	-800	34	80
Veto <sub>2</sub>	$30 \times 30, \circ 4$	-300	4	57
$V_{bl}$	$50 \times 50, \square 10 \times 10$	-2000	4	32
combination				
$V_{\text{tot}} = V_{\text{Veto}_1} + V_{\text{Veto}_2} + V_{bl}$				90

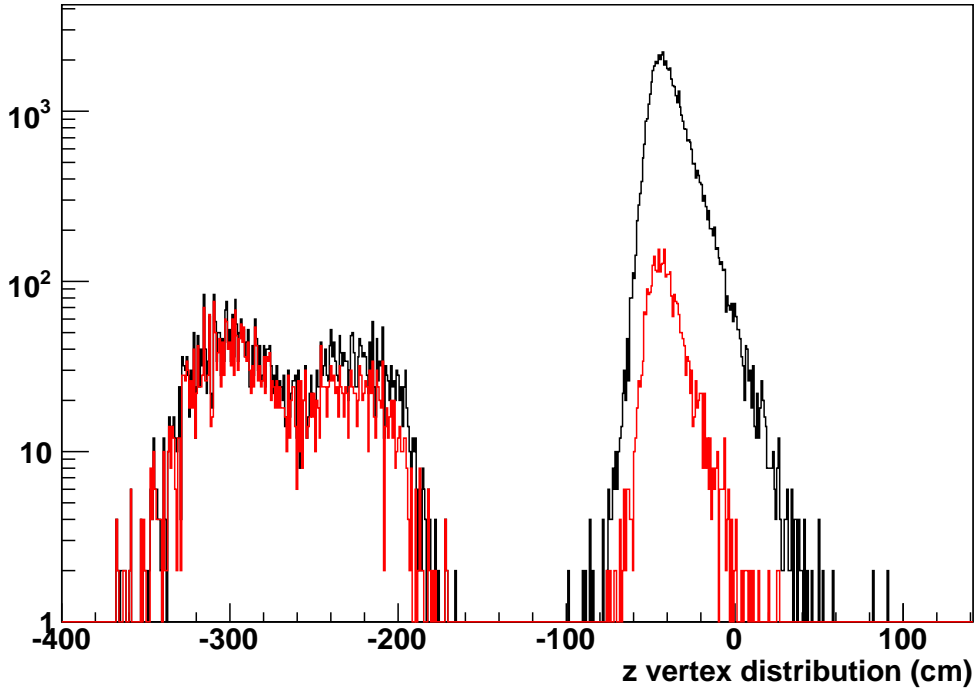


Figure 49: Vertex distribution for simulated Monte Carlo events with muon pairs without and with a LAS trigger. Note the strong suppression of the absorber events.

a coincidence matrix based on FPGAs (see GANDALF module, Sect. 6.2) are currently being developed. This flexible system will allow to select at the trigger level either a single scattered muon for the DVCS programme or an oppositely charged muon pair above a selected invariant mass for the DY measurements.

#### 5.4 Trigger for Drell–Yan measurements

For the DY measurements the selection of a pair of oppositely charged muons stemming from the target region is mandatory. Among all muon pairs in the spectrometer acceptance, 39% have one muon in LAS and one in SAS. Both muons are detected in the LAS hodoscopes in 57% of all cases while for the remaining 4% both muons are crossing the SAS hodoscopes.

Thus a trigger on muon pairs is needed for the LAS plus a trigger on a single muon in the LAS and a single muon in the SAS. For the latter, the inclusive sub triggers discussed in the previous subsection can be used requiring in addition a coincidence between the LAS hodoscope trigger and an OR of the outer, ladder, and middle triggers.

The LAS hodoscope system was designed to enable triggering on muon pairs as the second hodoscope H2 is split into parts. In addition, the distinction between muon pairs from the target region and the hadron absorber is done with the help of target pointing. The granularity of H2 was chosen such that only a small amount of muon pairs from the absorber enters the trigger as illustrated in Fig. 49; only 4% of the events in the absorber cause a LAS trigger.

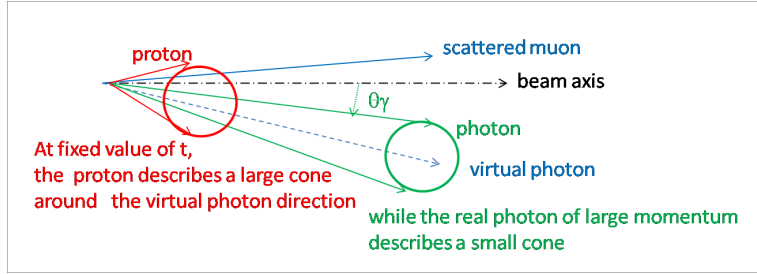


Figure 50: Sketch of the DVCS laboratory kinematics in the lepton plane. At fixed values of  $Q^2$ ,  $x_B$  and  $t$ , the real photon stays in the half plane opposite to the scattered muon (*i.e.*  $\theta_\gamma$  negative) when  $t$  is not too large.

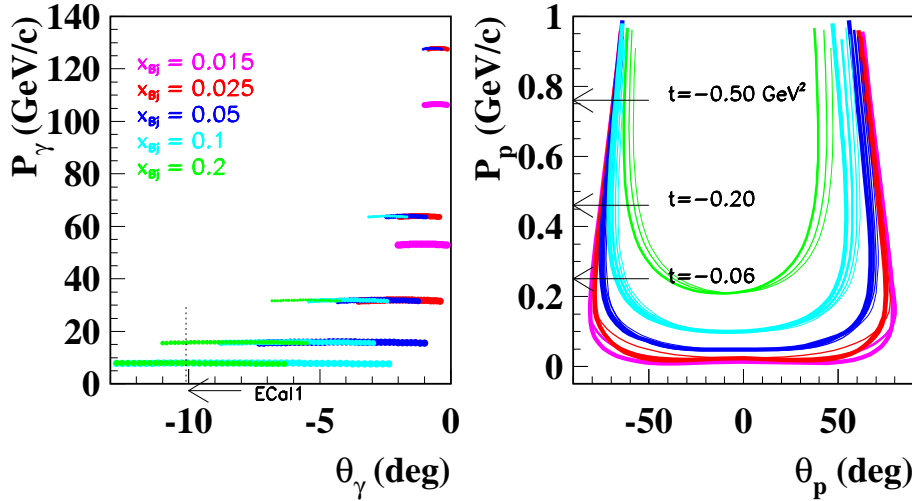


Figure 51: Polar angle and momentum ranges in the lepton plane for DVCS photon (left) and recoil proton (right), produced at  $|t| < 0.7 \text{ GeV}^2$  in the kinematics studied at COMPASS (pink for  $x_B = 0.015$ , red for  $x_B = 0.025$ , blue for  $x_B = 0.05$ , cyan for  $x_B = 0.1$  and green for  $x_B = 0.2$ ). For each colour (*i.e.*  $x_B$ ) the curve thickness decreases as  $Q^2$  increases ( $Q^2 = 1.5, 3, 6$  and  $12 \text{ GeV}^2$ ).

## 6 Target and proton recoil detector for the GPD programme

The laboratory kinematics for DVCS is illustrated in Fig. 50. The ranges for polar angle and momenta of outgoing proton and photon (or meson) are displayed in Fig. 51 assuming an incident muon energy of 160 GeV. As can be seen from the left panel Fig. 51, for values of  $x_B$  below  $10^{-1}$  the outgoing photon (or meson) is emitted at a polar angle below  $10^\circ$ . This is for a photon within the angular acceptance of the two electromagnetic calorimeters ECAL1 and ECAL2 and, similarly, for charged particles well within the acceptance of all tracking and PID devices including the RICH detector. In order to access higher  $x_B$  values for DVCS, a larger polar angular acceptance for photon detection is required. For this purpose, a new ECAL0 is presently under study (Sect. 7.2).

At COMPASS energies, the evaluation of the missing mass using the energy balance of the incoming and scattered muons and the photon (or meson) has an uncertainty of a few GeV, which is not sufficient to obtain a precise signature of exclusive events. Therefore, the spectrometer will be equipped with a Recoil Proton Detector (RPD) that has a large polar and full azimuthal angular acceptance. The projected uncertainties for

the proposed measurements, presented in Sect. 1.3, are based on the presently maximum possible muon beam intensities and a liquid hydrogen (LH) target of 2.5 m length, resulting in a luminosity of about  $10^{32} \text{ cm}^{-2}\text{s}^{-1}$ . In order to match the LH target length, an RPD of about 4 m length is needed. Every possible increase in the maximum  $\mu^+$  and  $\mu^-$  fluxes will increase the statistics correspondingly, thereby also extending the  $Q^2$  range. Therefore all existing or newly designed equipment should stand such an anticipated flux increase.

## 6.1 Liquid hydrogen target

The detection of recoil protons puts severe constraints on the structure of the target and the amount of material to be traversed. The full target length is equivalent to 0.29 radiation length. The thickness of the cryostat wall has to be minimised in order to collect low-momentum protons and, importantly, to minimise the absorption of produced (hard) photons emitted under forward angles of a few degrees. On the other hand, a minimum amount of material is needed to quench the flux of low energy  $\delta$ -ray electrons which, if too large, generates high occupancy in the RPD detector. Simulations of  $\delta$ -ray flux and absorption are ongoing to finalise certain critical target parameters.

The proposed physics programme to study nucleon tomography and generalised parton distributions requires to combine data of separate measurements with  $\mu^+$  and  $\mu^-$  beams, in order to be able to evaluate difference and sum of DVCS cross sections, and also the asymmetry as their ratio. While it is not required to measure absolute cross sections at the percent level, the evaluation of the key physics quantities requires to control the relative normalisation at the percent level. In addition, when calculating the difference of cross sections, all possible beam-charge-dependent effects, including the ones originating from the large difference in the  $\mu^+$  and  $\mu^-$  beam intensities, have to be monitored at the percent level. A relative precision of the order of 3% or better is required on the luminosity, *i.e.* incoming flux times target density. This constraint enters directly the technical specifications for the target.

In order to match the transverse size of the beam, the 2.5 m long LH<sub>2</sub> target should have a diameter of at least 40 mm. For such a long target, minimising the unavoidable gas-phase volume present at the target top is not trivial. This requirement enters directly into the specification for the cryogenic design and several options are presently envisaged. One of them is a powerful cooling based on an exchanger with liquid <sup>4</sup>He which should guarantee the required uniformity and stability of the target gas density.

Ongoing simulations (Sect. 1.3) take as initial configuration the 40 cm long LH<sub>2</sub> target that was used for COMPASS running with hadron beams in 2008 and 2009. It has the following characteristics:

- a target cell of 35 mm diameter made of 125  $\mu\text{m}$  Mylar foil,
- a 200 mm diameter Al cryostat of 1.8 mm thickness, and
- a global target thermal shield made of 250  $\mu\text{m}$  Mylar foil.

The extrapolation to the envisaged new 2.5 m long target comes with two additional requirements:

- **threshold for proton momentum detection:** the lowest value of the recoil proton momentum to be detected in the RPD is presently 262 MeV/c at 90° emission angle. In order to decrease this value the thickness of the Al cryostat tube should be reduced or lighter material should be used,
- **detection of forward photons:** given the 200 mm diameter of the present cryostat, photons emitted above 1.8° will traverse a large amount of material in the cryostat wall, resulting in significant absorption.

Table 17: Transmission factors for a photon as a function of the photon angle  $\theta_\gamma$

$\theta_\gamma$	$H_2$	$C_{CERN}$ $\varnothing 80 \text{ mm}$ th = 2 mm	$C_{Japan}$ $\varnothing 80 \text{ mm}$ th = 1 → 2 mm	Al $\varnothing 80 \text{ mm}$ th = 1 → 1.5 mm	Scintillator A $\varnothing 500 \text{ mm}$ th = 4 mm
0.45°	0.80				
0.88°	0.90	0.75	0.81 → 0.67	0.57 → 0.43	
1.1°	0.91	0.80	0.85 → 0.73	0.64 → 0.51	
2°	0.95	0.88	0.92 → 0.84	0.78 → 0.69	
3°	0.97	0.92	0.94 → 0.89	0.85 → 0.78	
4°	0.975	0.94	0.96 → 0.92	0.88 → 0.83	
5.4°	0.98	0.95	0.97 → 0.93	0.91 → 0.87	0.92
10°	0.99	0.975	0.98 → 0.96	0.95 → 0.93	0.96
17°	0.995	0.99	0.99 → 0.98	0.97 → 0.96	0.975

Ongoing studies and simulations indicate that a small-diameter ( $\leq 100 \text{ mm}$ ) cryostat is preferable. Three different options are being investigated:

- a cryostat of 80 mm diameter made of cellulose paper with phenolic resin of 2 mm thickness ( $C_{CERN}$ ),
- a cryostat of 80 mm diameter made of carbon fibre of 1 mm to 2 mm thickness ( $C_{Japan}$ ) and
- a cryostat of 80 mm diameter made of 1 mm to 1.5 mm thickness aluminium (Al).

Table 17 shows the transmission factors for a photon as a function of the photon angle  $\theta_\gamma$  for these options. The options  $C_{CERN}$  and  $C_{Japan}$  appear as the preferred ones. We note that on its path through the spectrometer the photon has to traverse additional material. The main components and corresponding transmission factors are 0.76 for tracking devices, 0.9 to 0.8 for the RICH detector and 0.94 for air. This optimisation will need as input a more precise knowledge of backgrounds, such as  $\delta$ -rays and also exclusive  $\pi^0$  background, which depending on its amplitude may (or may not) impose severe constraints on the photon absorption for measurements of DVCS.

## 6.2 Recoil Proton Detector

For a precise signature of exclusive single-photon or DVMP events, the detection of the recoiling proton is mandatory. Moreover, an accurate measurement of the momentum transfer  $t$  is required, in particular for the cross section measurement to study the transverse size of the nucleon. This requires to perform precise Time-of-Flight (ToF) measurements of the recoiling proton with a precision of 300 ps or better.

For the proposed measurements with the 2.5 m long liquid hydrogen target, *i.e.* in Phase-I of the GPD programme, a 4 m long Recoil Proton Detector (RPD) is required to fully cover the recoil-proton kinematics. Recoil proton detection is based on a ToF measurement between two barrels of 24 scintillator slats read out at both ends. The inner barrel (of 2.75 m length) with a diameter of 50 cm and surrounding directly the target, is made of slats of 4 mm thickness to allow low-momentum-proton detection down to about 260 MeV/c. The outer barrel is made of 3.6 m long and 5 cm thick slats and has a diameter of 2.2 m. A preliminary sketch is shown in Fig. 52 and the available space and the installation constraints are illustrated in Fig. 53.

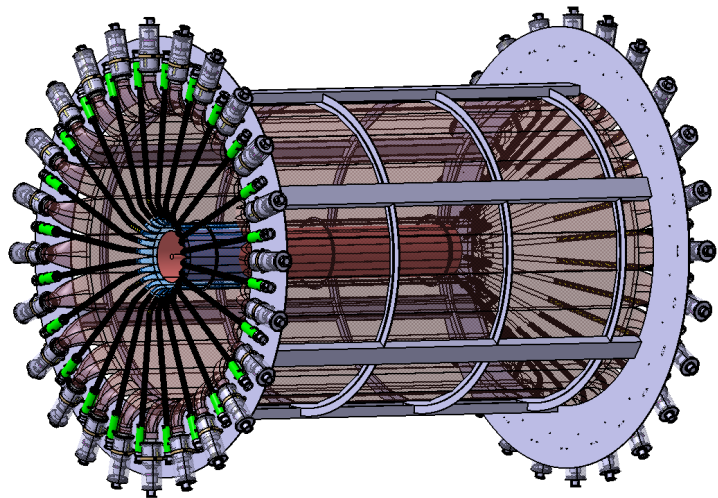


Figure 52: The 4 m long Recoil Proton Detector.

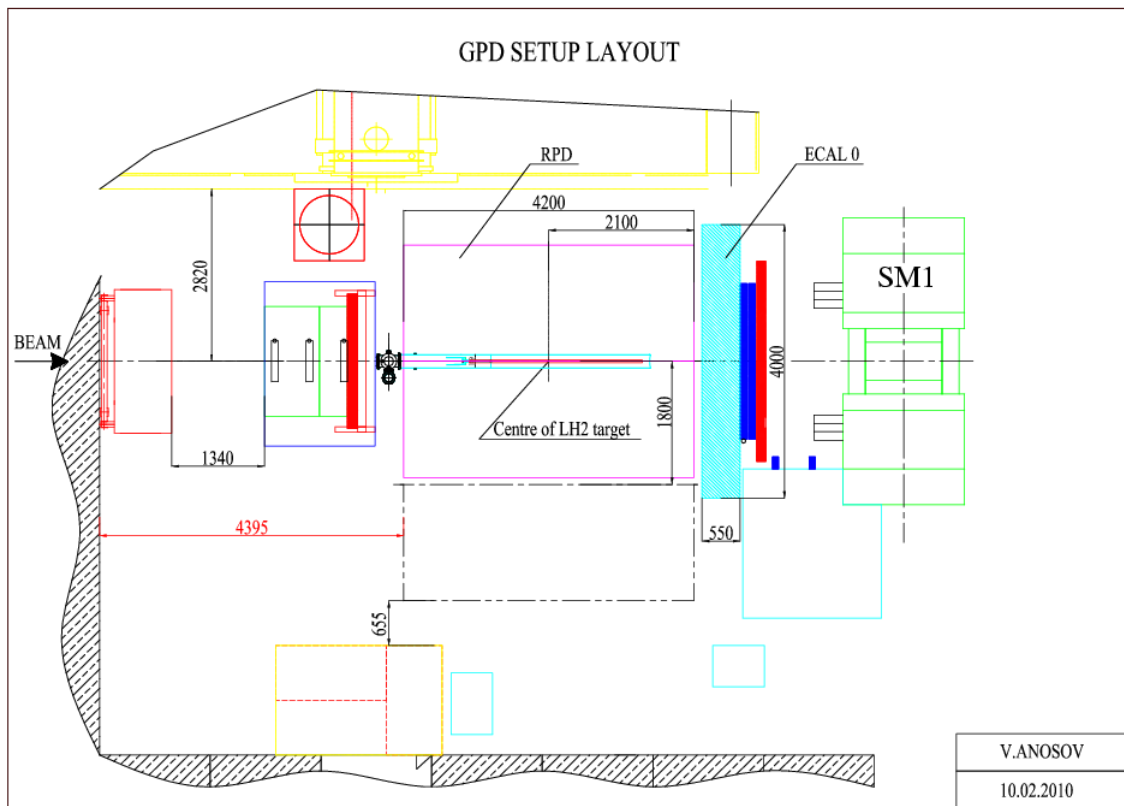


Figure 53: Available space for RPD and LH<sub>2</sub> target. The RPD can be displaced in the transverse direction (garage position: target axis off by 1800 mm) allowing the target to enter the RPD from the upstream side.

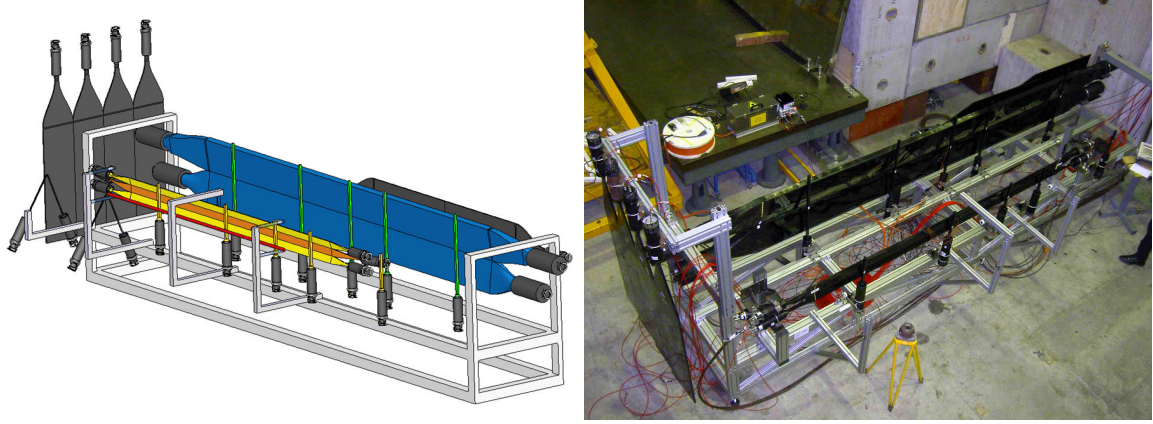


Figure 54: The 4 m long 30° sector prototype, named MuRex. Left: schematic drawing. Right: (photo) in the COMPASS hall during calibration using the muon beam halo. The laser system for calibration is also visible.

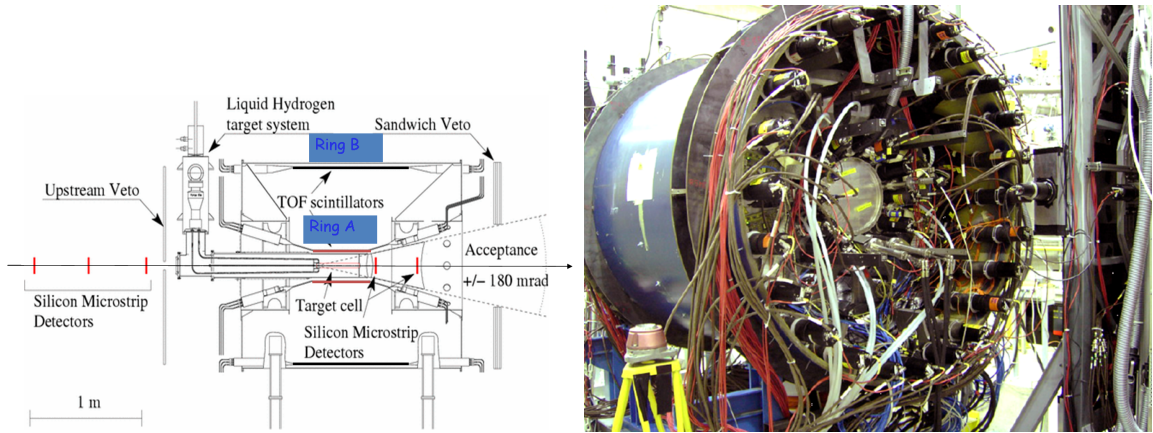


Figure 55: The 1 m long RPD used for COMPASS hadron running in 2008 and 2009 and also for a feasibility test of hard exclusive single-photon production at COMPASS. Left: schematic drawing of RPD with the cryogenic target and the silicon detectors. Right: (photo) seen from downstream where the 2 rings of phototubes as well as the window of the cryostat are visible.

Significant input to the expected performances and to the choice of certain critical parameters for the proposed RPD came from two studies that were performed with:

- the 30° sector of a 4 m long prototype, named MuRex, shown in Fig. 54 and
- the 1 m long RPD shown in Fig. 55 which was used together with the COMPASS spectrometer for 2008 and 2009 running with hadron beams. This RPD surrounded the 40 cm long LH<sub>2</sub> target and included a conical cryostat containing two cold silicon stations. It was also used for dedicated tests of the capability of COMPASS to measure hard exclusive single-photon production, as described in Sect. 1.4.

For this study using the hadron set-up, a recoil proton candidate is defined as a particle crossing two facing scintillator slats from the inner and outer barrel, which is coincident in time and position (at the vertex) with an outgoing pion of elastic scattering. Figure 56 (left) shows the energy loss  $\Delta E$  in the outer barrel as a function of the reconstructed velocity  $\beta$  of the particle, using the timing information collected at each end of the hit scintillators. A very similar proton signature obtained in parallel with the first observation

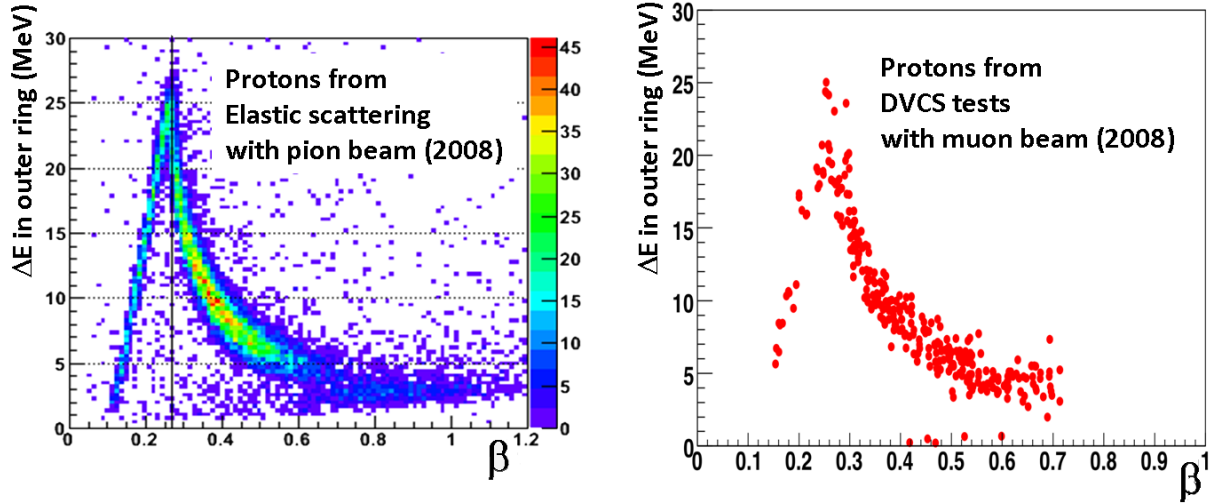


Figure 56: Proton identification in 2008 data using the present 1 m long RPD in elastic scattering with a pion beam (left) and in exclusive single-photon production during the DVCS tests (right).

of exclusive single-photon production during the 2008 DVCS test [64] is shown in the right panel of Fig. 56. The ToF measurement in the present 1 m long RPD has shown to yield an excellent selection of recoiling protons. Table 18 shows the timing resolutions achieved in the two studies.

The scintillator for the MuRex A layer is long and thin, delivering only 60 photo-electrons. This explains the worse resolution compared to the one obtained for the RPD A layer. On the contrary, the resolution of the MuRex B layer is improved compared to that of the RPD B since we deal with a thick element of material with a long attenuation length. The larger thickness of the MuRex B layer is also important to better separate proton and pion since the stopping power is higher.

The experimental resolution in recoil proton momentum  $\Delta P/P$  obtained during the 2008 hadron run is shown as open circles in the top left panel of Fig. 57. It is in good agreement with the estimate

$$\frac{\Delta P}{P} = \frac{1}{1 - \beta^2} \frac{\sin^2 \theta}{d_{AB}} \sqrt{\cos^2 \theta (\Delta z_A^2 + \Delta z_B^2) + \beta^2 c^2 \Delta t_{AB}^2}, \quad (61)$$

shown as filled circles in the same panel, where  $\theta$  is the polar angle of the track,  $d_{AB}$  the distance between layers A and B and  $\Delta z_A$ ,  $\Delta z_B$ ,  $\Delta t_{AB}$  are the position resolutions in layer A and B, and the ToF resolution (all these values are given in Table 18.) The bottom left panel shows the corresponding estimated resolution  $\Delta t/t$

$$\frac{\Delta t}{t} = \frac{\Delta P}{P} \frac{4M_p^2 - t}{2M_p^2 - t} \simeq 2 \frac{\Delta P}{P}. \quad (62)$$

Estimations for the future RPD are also shown in the same figure, in the two right panels. The improvement in resolution is mainly due to the larger distance between the A and B barrels.

A preliminary simulation using Geant Monte Carlo shows high counting rates in all elements of the RPD, in particular in ring A where the dominant source is the production

Table 18: Key parameters of the MuRex prototype and the 2008 RPD.

	MuRex (2006)	RPD (2008)
A material	BC408	BC404
A length	284 cm	50 cm
A thickness	0.4 cm	0.5 cm
PMT	XP20H0	EMI 9813B
attenuation length	2 m	0.7 m
B material	BC408	IHEP production
B length	400 cm	106 cm
B thickness	5 cm	1 cm
PMT	XP4512	EMI 9813B
attenuation length	4 m	0.7 m
$d_{AB}$ = distance between A and B	85 cm	63 cm
$\Delta z_A$ = position resol in A	3.5 cm	2.3 cm
$\Delta z_B$ = position resol in B	2.5 cm	3.8 cm
$\Delta t_A$ = timing resol in A	270 ps	180 ps
$\Delta t_B$ = timing resol in B	200 ps	300 ps
$\Delta t_{AB}$ = ToF resolution	310 ps	350 ps

of  $\delta$ -rays in target material and walls. Given the time window of about 150 ns dictated by the dispersion in proton momentum, vertex position along the target and light propagation in the scintillators, a high occupancy is expected. As a consequence, a high segmentation (24 sectors) is mandatory for both the A and B scintillator layers of the RPD. Simulations show that half of the elements receive at least one hit in this time window. A line-shape analysis of the PMT signal is foreseen to obtain precise ToF information and improve background rejection. Given the expected high counting rates, a dedicated readout called GANDALF, based on a 1 GHz digitiser was proposed and is under study.

The GANDALF 6U VME/VXS system has been designed to perform multiple electronic readout tasks in high energy physics experiments such as analog or time-to-digital conversions, coincidence matrix formation and fast trigger generation. As a transient recorder the GANDALF module can digitise eight analog channels with 1 Giga-samples per second and has a maximum dynamic range of 14 bit. Also 16 channels per module are possible at half sampling rate. The extraction of timing information is performed for both unipolar and bipolar signal shapes in a large dynamic range from a few millivolt up to 4 V. A timing resolution of better than 50 ps is achieved even for fast pulses with rise times down to 3 ns. The baselines of the 500 MHz bandwidth analog input circuits are adjustable by 16 bit DACs independently.

Enormous numerical capabilities are provided by the implementation of a Virtex5-SXT FPGA to perform algorithms for dead-time free timing measurements and pulse shape integration. Pile-up pulses with a minimal time distance of twice the rise time can be disentangled by numerical algorithms. A fast and deep memory extension provided by QDRII+ (144 Mbit) and DDR2 (4 Gbit) devices buffer data for numerical processes and output.

The modularity of the board design allows the implementation of a 128 channel TDC module. Here the time digitisation process is done inside the V5 FPGA and reaches timing resolution of up to 125 ps. The same hardware set-up can be used to implement

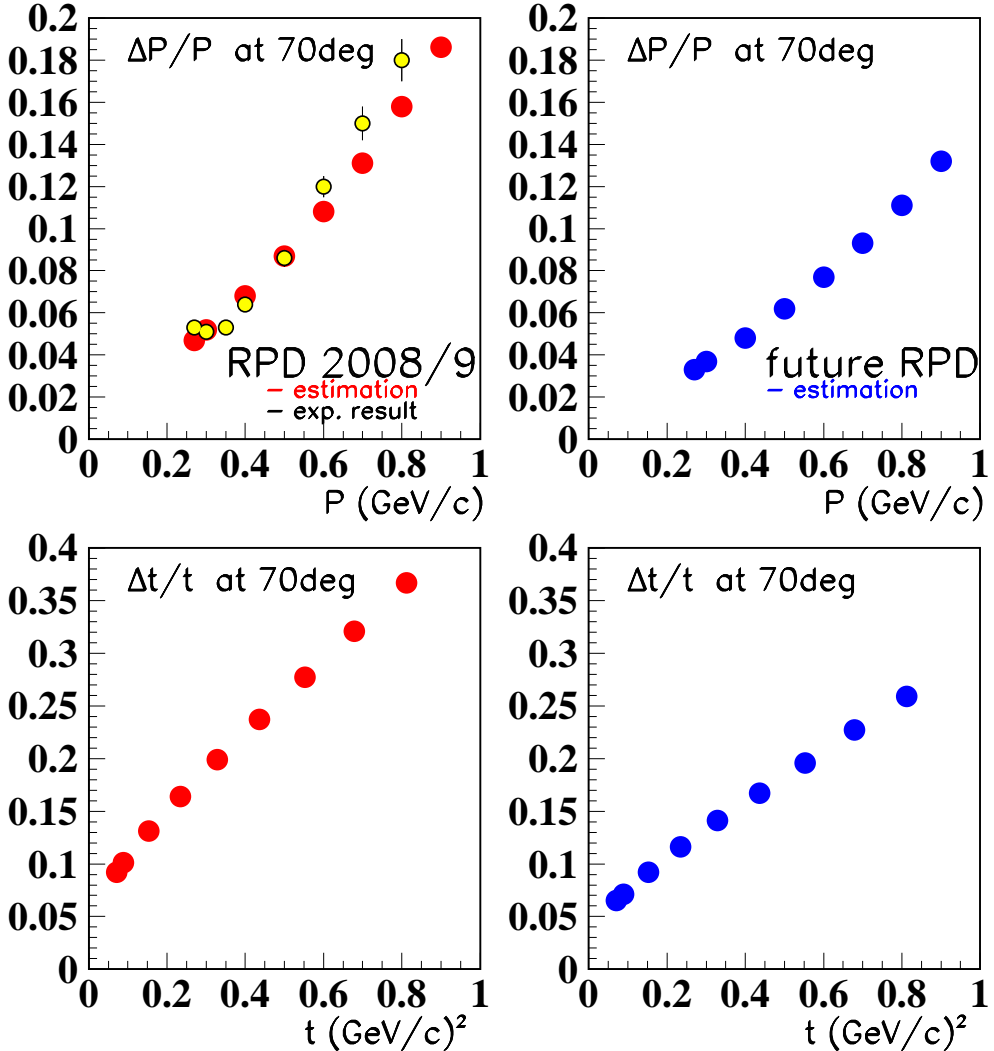


Figure 57: Expectation for the resolution in  $P$  and  $t$  for the RPD used in 2008, compared (for  $P$ ) with preliminary results (left). Expectation for the future RPD (right).

a fast 128 channel trigger matrix for complex trigger decisions. The VXS backplane bus combines the information of up to 18 GANDALF modules. Every module has 16 high-speed lines for the data transfer to a central VXS switch module, which can be used to form fast global trigger decisions based on pulse shapes, time or logic patterns of the individual channels from all GANDALF modules in a single crate. As illustrated in Fig. 58, each GANDALF board has a variety of interfaces for physics data transfer, configuration and monitoring like USB 2.0, VME64x, S-Link and Ethernet.

The tests of the full system performance during the 2009 DVCS test run are being analysed.

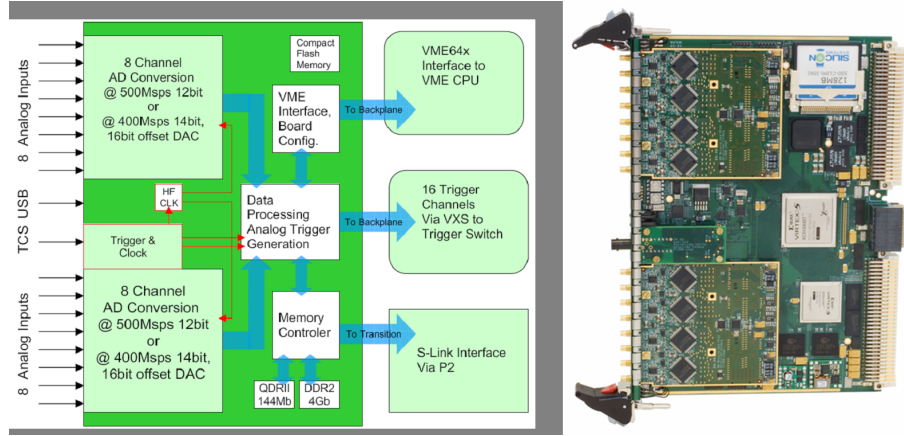


Figure 58: GANDALF board.

## 7 Upgrades of the electromagnetic calorimetry

The electromagnetic calorimetry has been initially developed for the COMPASS hadron programme with the goal of accessing neutral channels for the search of exotic meson production and also for the study of Primakoff reactions. The spectrometer is presently equipped with two electromagnetic calorimeters, ECAL1 and ECAL2. The initial position of ECAL1 (COMPASS former proposal) was at  $z = 9.7$  m but space necessary for detectors required it to be moved to  $z = 11.1$  m. ECAL2 is positioned at  $z = 33.2$  m. At this position and given the size of the ECAL1 central hole of  $1.06 \times 0.59$  m $^2$  (H×V) and the ECAL2 overall size of  $2.45 \times 1.84$  m $^2$  (H×V), there remains a significant mismatch in the horizontal coordinate due to the reduced 2.45 m width of ECAL2.

Figure 59 illustrates the effect of such incomplete coverage for two particular kinematic situations in DVCS. It results in a significant variation in the acceptance for the azimuthal angle  $\phi$  between lepton plane and real-photon production plane (Fig. 4), which leads to unwanted systematic effects in the detection of single-photon events.

Similar effects were expected for the detection of photons from neutral channels in the hadron spectroscopy measurements. In order to cure the poor matching of the ECAL1 and ECAL2 geometries, ECAL1 was moved downstream by 3 m prior to the 2008 hadron run, which resulted in a major reshuffling of the set-up. This change led to a significant acceptance loss for photons emitted at large  $\theta_\gamma$ . In addition, a significant shadowing effect of the boundary of HCAL1 on ECAL2 (vertical coordinate) was also observed for this not fully optimised setup. As illustrated in Sect. 1.3.1, the programme proposed in this document would strongly benefit from an increased angular acceptance for high-energy photon detection, which also motivates the foreseen construction of the new large-angle electromagnetic calorimeter ECAL0. Note that ECAL0 will have a central hole matching the ECAL1 acceptance (given its position), which will restrict the acceptance for charged particles in the upstream part of the spectrometer. The more upstream ECAL1 will be positioned, the larger the central hole of ECAL0 can be made. Hence further upgrades of ECAL1 and ECAL2 will be based on the assumption that ECAL1 is at its nominal position of 11.1 m.

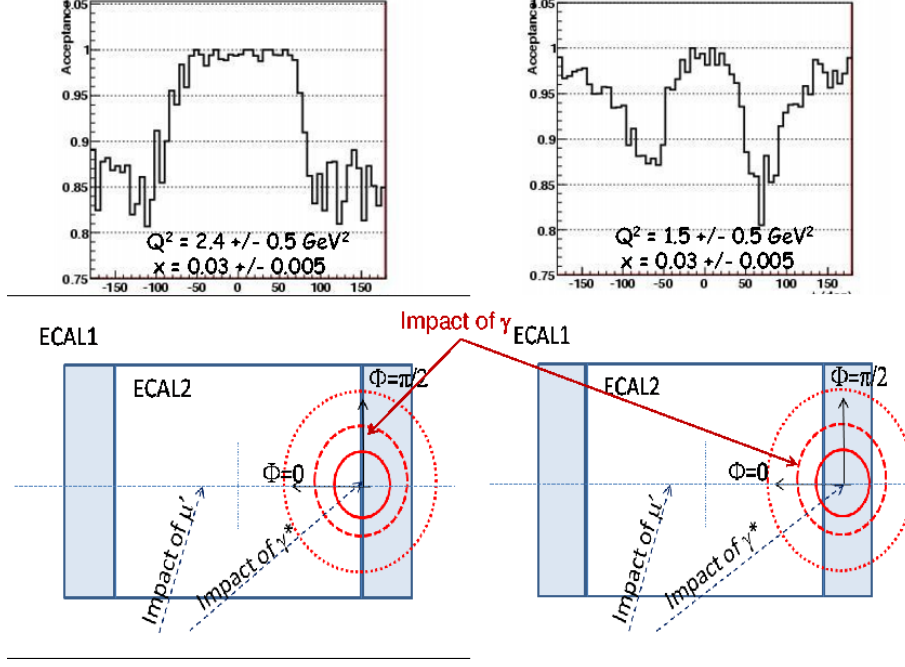


Figure 59: Effect of incomplete  $\phi$  acceptance between ECAL1 and ECAL2, illustrated for two particular kinematic situations in DVCS.

## 7.1 ECAL1 and ECAL2 upgrades

The present ECAL1 and ECAL2 positions are not optimised for the proposed measurements of hard exclusive high-energy photoproduction. The two options for an adequate electromagnetic calorimetry are:

1. Modification of ECAL2 size and structure, aiming at extending the horizontal width to 3.6 m,
2. upstream shift of ECAL2 by a few meters (4 to 6 m) in order to better match the size of ECAL1 while keeping the present size and structure of ECAL2.

Option 1 was already proposed for ECAL2 along with a new layout for ECAL1 keeping its present size (Fig. 60).

### *Upgrade of ECAL2:*

The ECAL2 width is presently 2.45 m. Ideally, a width of 4.4 m would provide the required matching of the widths of ECAL2 and HCAL2 (downstream of ECAL2). However, the need for such “width matching” has not been demonstrated and it was shown that an ECAL2 width of 3.6 m is the optimum for photon detection. Given this, ECAL2 will consist of (going from the centre to outer section): 1736 Shashlik modules ( $3.8 \times 3.8 \text{ cm}^2$ ), 400 GAMS Radiation Hard (GAMS RH) (idem size), 1400 GAMS normal (idem size) and 624 Mainz ( $7.5 \times 7.5 \text{ cm}^2$ ), which represent in total 4160 modules [171].

### *New layout of ECAL1:*

The proposed change consists of removing the 572 Mainz modules ( $7.5 \times 7.5 \text{ cm}^2$ ) and replacing them by 2296 GAMS modules ( $3.8 \times 3.8 \text{ cm}^2$ ) and also implementing Shashlik and GAMS RH in the centre. The Olga modules ( $14.3 \times 14.3 \text{ cm}^2$ ) will stay. Repartition will be as follows (going from the centre to outer section): 200 Shashlik modules ( $3.8 \times 3.8 \text{ cm}^2$ ), 2696 GAMS (*i.e.* 400 GAMS RH and 2296 GAMS modules ( $3.8 \times 3.8 \text{ cm}^2$ )) and 320 Olga modules ( $14.3 \times 14.3 \text{ cm}^2$ ), which represent in total 3216 modules, to be compared to the

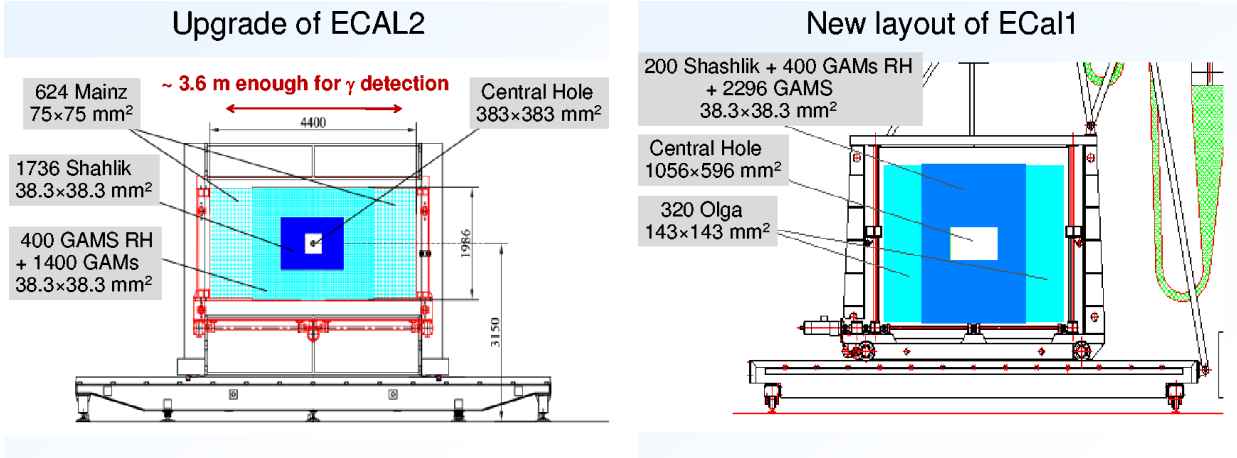


Figure 60: The new ECAL2 of 3.6 m full width (left). The new layout of ECAL1 (right).

1500 modules of the present ECAL1. Finally, an optimisation of the HCAL1 central hole, not properly matched to the ECAL1 hole, may be required to avoid the shadowing effect mentioned above.

An estimate for the ECALs upgrade Option 1 was provided in 2009. A cost estimate of about 1 MEuro was mentioned along with a planning requirement of about two years. Option 2, which requires a displacement of ECAL2 and HCAL2, implies a major reshuffling of several tracking devices in the downstream section of the spectrometer. It would result in a reduction of lever arm for tracking in this section. Preliminary estimates show that an optimum positioning of the high-resolution straw trackers should compensate this reduction. In addition, there would be a large gap of almost 7 m between HCAL2 and the muon identifier. Studies are ongoing to evaluate the overall impact of such a modification. Finally, an Option 3 which consists of reducing the central hole of ECAL1 was also proposed. A preliminary estimate shows that the addition of 3 vertical rows of GAMS blocks on each side of ECAL1 hole would provide ECAL1/ECAL2 hermeticity without having to displace ECAL2. The central hole of HCAL1 would also have to be adjusted to the one of ECAL1 to prevent the already mentioned shadowing effect.

A significant upgrade of the readout electronics of ECAL1 and ECAL2 had been launched and was already fully operational for the 2008 and 2009 hadron runs. It concerns the replacement of previous (slow) analog-to-digital converters, the FIADC, by modern converters, the SADCs (10 bits) and the MSADCs (12 bits) which permit sampling of the ECALs signals and provide a precise timing information for the ECAL signal (an important feature to guarantee excellent single-photon selection and background rejection). Additional channels of MSADCs will be needed given the proposed upgrade. A new laser monitoring system was developed and installed for ECAL1. It was fully operational for the 2009 run. The extension of this monitoring system to ECAL2 is foreseen, also additional channels will be needed for ECAL2 to match the new ECAL1 layout.

## 7.2 Large-angle electromagnetic calorimeter ECAL0

An entirely new calorimeter ECAL0 covering larger photon angles is under development at the JINR Dubna. It will increase the accessible domain in  $x_B$  and therefore provide a good overlap with the HERMES and JLAB experiments. An illustration of the impact of ECAL0 is given in Fig. 6 which shows the projected improvement in the un-

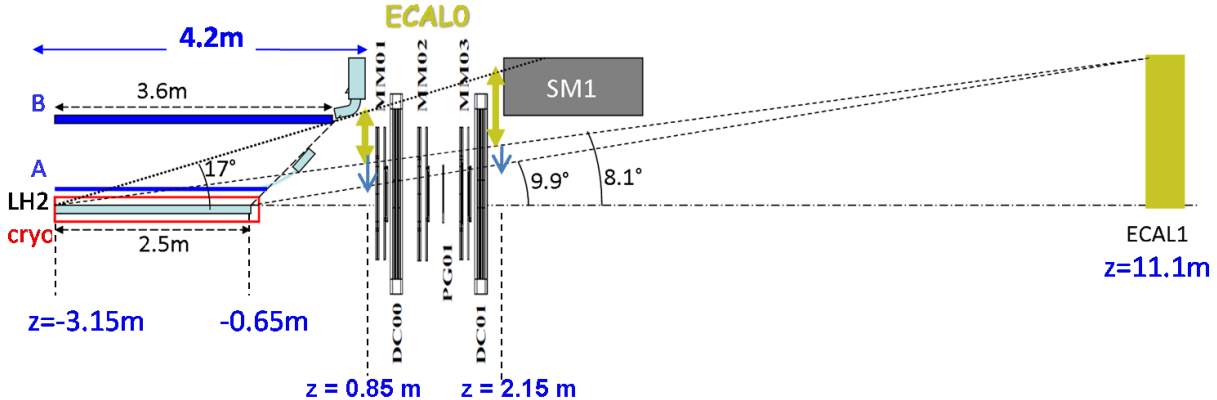


Figure 61: The two  $z$  positions envisaged for ECAL0,  $z = 0.85$  m and  $z = 2.15$  m with the corresponding overall sizes and also two options for the central hole: large hole (dark yellow), small hole (blue).

certainty of the measurement of the  $t$ -slope parameter  $B(x_B)$  at large  $x_B$  values. ECAL0 will also provide an improved hermeticity for detection of exclusive events and contribute to reduce backgrounds from neutral pions and other decays. From Monte Carlo studies, the following requirements have been defined for ECAL0:

- The energy range for photon detection (DVCS and background) is 0.2 to 30 GeV.
- The maximum geometrical size is  $3.6 \times 3.6$  m $^2$ . Assuming that it is located in front of the SM1, such calorimeter will cover the polar angular range 0.3–0.6 rad. (At another location the geometrical size of the calorimeter will be smaller, see below).
- ECAL0 should have a modular structure with the dimensions of a module cell 40 × 40 mm $^2$  in the region close to the beam (inner) and 60 × 60 mm $^2$  at the periphery (outer), subject to optimisations.
- The required energy resolution is about 10% at 1 GeV or better.
- Taking into account the space limitations in the target region and the rather high fringe field of the SM1 magnet, the total length of the calorimeter should be less than 50 cm and the photodetector should be insensitive to the magnetic field.

Figure 61 shows two possible options for the position and also the geometrical size of ECAL0. Optimisation of the overall ECAL0 size and also of its central hole will result from several compromises, among which are the tracking requirements. A small central hole will guarantee good hermeticity between ECAL0 and ECAL1, however it will restrict the acceptance for the charged hadrons detected in the first spectrometer section. A preliminary illustration of the impact of ECAL0 is given in Fig. 62 which shows the  $\phi$  angle acceptance for DVCS events for a specific  $(Q^2, x_B)$  bin without and with ECAL0 at  $z = 0.85$  m.

This project uses a Multipixel Avalanche PhotoDiode (MAPD) as photodetector. It is developed for particle physics and medical applications, in collaboration between JINR/Dubna [172] and the Zecotek company in Singapore. There are several types of MAPDs. The novel type, MAPD-3A, with a micowell structure and high density of pixels was tested for the first time. This device has a common p-n junction on the n-type silicon substrate and a clear sensitive surface. Both, the matrix of avalanche channels and individual passive quenching elements are placed inside the substrate. The avalanche channels (vertical channels) with individual micowells for charge trapping/collection are created at a depth of about 3–5 microns using a special distribution of the inner electric

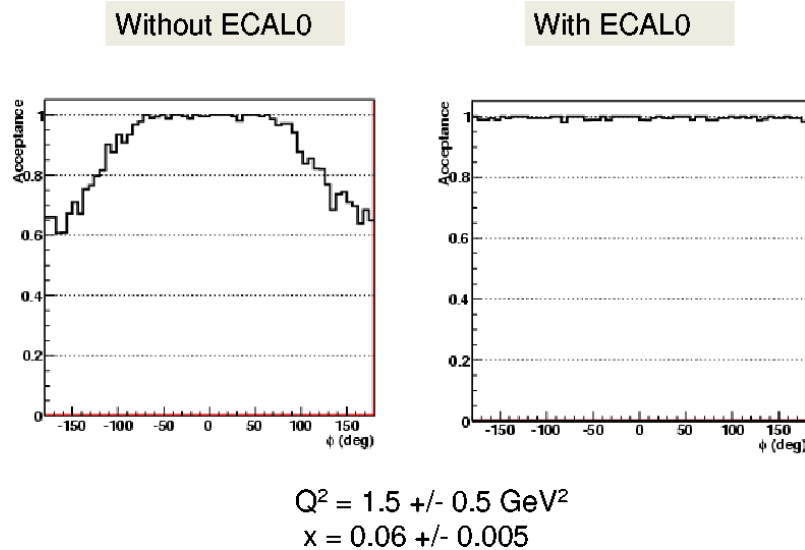


Figure 62: Impact of ECAL0 on the DVCS  $\phi$  angle acceptance: acceptance without ECAL0 (left), acceptance with ECAL0 (right).

field. The MAPD-3A has a gain of 20000, photon detection efficiency of 10% in the green region, density of 15000 pixels per  $\text{mm}^2$  and an area of  $3 \times 3 \text{ mm}^2$ .

The ECAL0 module prototypes have been constructed and tested by the JINR/Dubna group at the CERN East Hall T9 beam line (with electrons of 1 to 7 GeV). Results from these tests are provided in the next section. The team is also pursuing tests at higher energies at the North Area H2 beam line. Two items require more investigation:

- The gain of the MAPD is sensitive to temperature variations, thus a thermal stability (provided by a Peltier device) should be in the range of  $\pm 0.2$  degrees.
- The single pixel recovery time is of about 100 microseconds, therefore the optimum pixel density depends on the instant rate on the photodetector. A test *in situ* at COMPASS was performed during the DVCS test run in 2009 with the goal of providing more definite answers to these questions. Also, more simulations are needed to clarify certain aspects of the specifications like optimum geometry, given the large photon incident angles.

### 7.3 Test of the new ECAL0 prototypes

Several prototypes for the electromagnetic calorimeter ECAL0 have been constructed by the JINR/Dubna team and tested at CERN in 2007–2009. The latest two prototypes of modules, one for the outer part and one for the inner part of ECAL0, have the sampling 'shashlik' structure. Each of them consists of a lead/scintillator stack, fibres, a fibre protection cover on its front side, fibre bundles and a fibre protection cover on the rear side. A module stack is constructed from the alternating layers of 2 mm thick lead, white reflecting 120  $\mu\text{m}$  thick TYVEK paper (DuPont TyvekR) and 4 mm thick scintillator tiles. The total number of lead/scintillator elements of  $12 \times 12 \text{ cm}^2$  in cross section is 66 corresponding to the total length of 42 cm equivalent to 25 radiation lengths. The scintillator tiles are produced by molding under pressure of polystyrene-based PSM-115 with 2.5% p-terphenyl and 0.01% POPOP admixtures.

The two prototype modules differ from each other in scintillator tiles dimensions and in the light collection systems. The light from scintillator tiles is collected, re-emitted

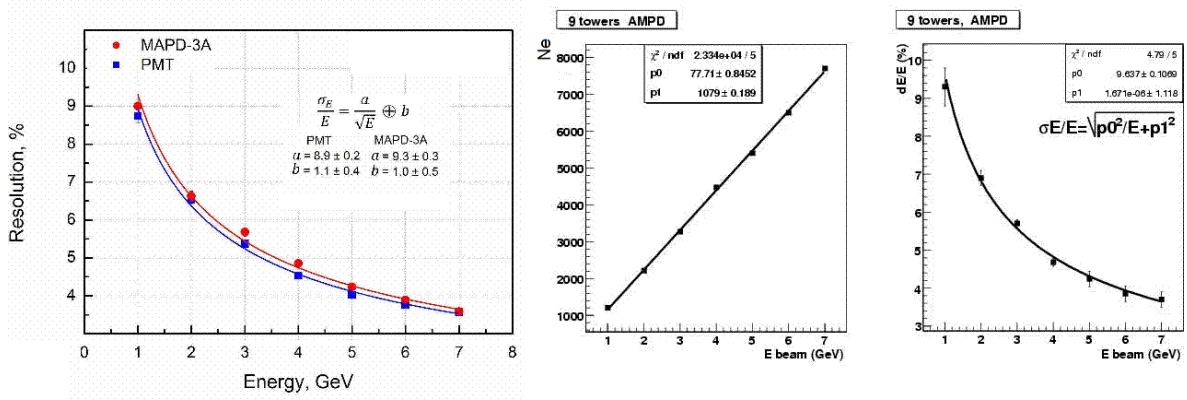


Figure 63: Comparison of the energy resolutions (left) of the modules with PMT EMI9814B and MAPD-3A read outs, response (middle) and resolution (right) of the nine-tower module with MAPD-3A, versus electron beam energy.

and transported by 1.2 mm diameter WLS fibres penetrating the entire module. In the first module (outer) the tiles are combined in a one-tower light collection system, while in the second one (inner) in a nine-tower light collection system. The one-tower module has the tile size of  $12 \times 12 \text{ cm}^2$ . It is read out by 64 fibres inserted in holes at the centre of each  $1.5 \times 1.5 \text{ cm}^2$  square with a distance between centres of 15.25 mm. The fibres are grouped in four bundles, 16 fibres per bundle, each equipped with the MAPD. The nine-tower module has a common lead plates and 9 separated scintillator tiles in each pair. It is read out by 144 fibres inserted in the holes at the centre of each  $1.0 \times 1.0 \text{ cm}^2$  square with a distance between centres of 10.10 mm. The fibres are grouped in nine bundles, 16 fibres per bundle, each corresponding to the  $4 \times 4 \text{ cm}^2$  cell size of the tower. Each bundle is equipped with an MAPD and read out separately. The same type of MAPD, MAPD-3A, is used for both modules. They have a window  $3 \times 3 \text{ mm}^2$  in cross section and contain 135000 pixels. The MAPDs of the module are fixed to the metal plate cooled with the Peltier element. The response of the MAPDs and electronics is monitored with a light from the LED, conveyed to the conical light guides between the ends of bundles and MAPD through the optical connector on the rear face of module and clear fibres.

The prototype modules have been constructed by an outside firm in Vladimir town near Moscow. Similar modules are constructed by this firm for the LHCb experiment. The rear parts of the modules were modified at Dubna in order to use the MAPDs and the Peltier coolers, instead of photomultipliers (PMT). Tests were performed in 2008 at the T9 beam at the CERN PS [173]. The results are summarised as follows (see also Fig. 63):

- The comparison of the module responses to the beam with the MAPD-3A and PMT readouts has shown that MAPD-3A can be used in read-out of ECAL0: the performances of these two photodetectors are the same.
- The yield of the light is found to be in a linear part of the MAPD-3A responses for the electron energies of 1–7 GeV.
- The energy resolution and its dependence on the beam energy for the nine-tower module are found to be in agreement with the requirements for ECAL0. The resolution of the one-tower module is a bit worse, but also in agreement with requirements.

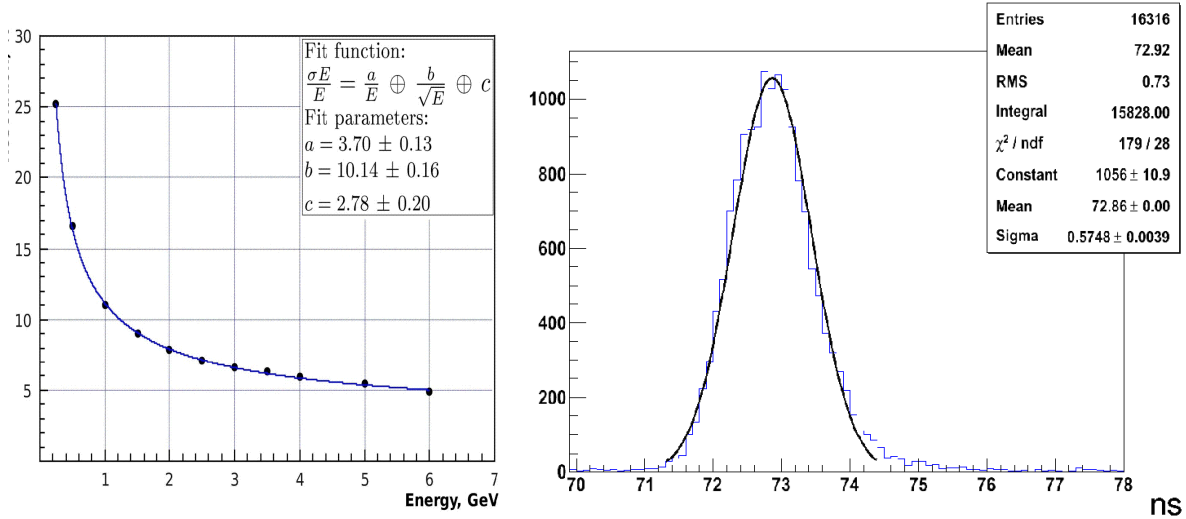


Figure 64: The energy resolution (left) versus the electron beam energy and the time resolution (right) at 4 GeV for the short module with MAPD-3B.

- The tests of the temperature stabilisation system based on Peltier elements were performed and found to be important and necessary for the MAPD-3A gain stabilisation.
- The system of the LED/PIN calibration and monitoring system was designed and tested. It can be used for the whole ECAL0.

The modules described above were too long to be installed at COMPASS (about 65 cm including the light collection system, cooling elements and read out). A new shorter module of 42 cm total length was constructed. It has the same structure as above, but the active material corresponds to 15 radiation length. The light collection system was improved by matching the bundle's surface and the MAPD surface with a Winston-cone light guide glued to the MAPD surface. The latest MAPD type, MAPD-3B, was used instead of MAPD-3A. The MAPD-3B has a gain of 10000, photon detection efficiency of  $\sim 10\%$  in the green region, density of pixels 40000 per  $\text{mm}^2$ , active area  $3 \times 3 \text{ mm}^2$  and total number of pixels 360000.

Beam tests of this module have been done at DESY in the energy range 0.2–6 GeV. The energy and time resolutions are shown in Fig 64.

At COMPASS two modules, the old one with the MAPD-3A and the new one (short) with the MAPD-3B, were tested in a real environment, close to the target, and have shown similar behaviour. In summary, the short ECAL0 module prototype has satisfied the COMPASS requirements for the design and characteristics.

One possible location of ECAL0 is just behind the RPD, as shown in Figure 61. In that case the maximal geometrical size of the ECAL0 is about  $2.2 \times 2.2 \text{ m}^2$  with a central hole of about  $0.5 \times 0.5 \text{ m}^2$  and a distance from the centre of the target of about 2.7 m. The energy range for photon detection is 0.15 to 30 GeV and the polar angle range is 0.15–0.6 rad (upper limit is fixed by the RPD design). ECAL0 will have a modular structure with only one type of module cell of  $4 \times 4 \text{ cm}^2$ , this cell being part of a  $12 \times 12 \text{ cm}^2$  module with 9 towers, each of them equipped with an MAPD. The total number of modules is less than 300. The module will consist of 109 lead-scintillator sandwiches, the thickness of scintillator and lead is 1.5 and 0.8 mm, respectively. Monte Carlo studies yield an energy resolution for this module of about (5–7)% at 1 GeV. The location of ECAL0 just behind

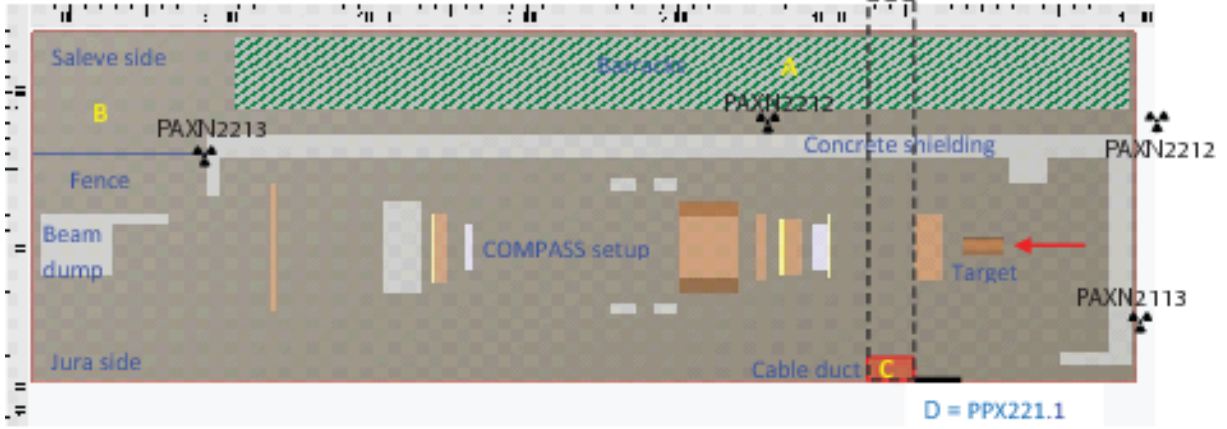


Figure 65: Sketch of the COMPASS experimental hall (top view).

the RPD compared with the location of ECAL0 in the front of SM1, has the following advantages:

- minimal material (from the frames of tracking detectors ),
- reduced cost of ECAL0 (only  $\sim 300$  modules instead of  $\sim 800$ ),
- single type of module cell,
- wider kinematical range,
- simplified installation.

The main disadvantage of this ECAL0 location is a higher background, which will be the subject of further tests. An additional hodoscope in front of ECAL0, as in the case of ECAL0 in front of SM1, will be useful for the separation of photons and electrons.

In 2010 the JINR/Dubna team, with the help of other COMPASS institutions, will construct a small prototype of the calorimeter ECAL0 consisting of a matrix of  $3 \times 3$  modules and geometrically compatible with a location behind the RPD.

## 8 Radiation Protection issues for Drell–Yan measurements

Radiation aspects of the COMPASS facility were presented for the first time in the Radiation Protection Committee (RPC) meeting on March 18, 1999. At that time, the facility was approved for muon and hadron beam operation with the following limitations:  $2 \times 10^8$  muons at 190 GeV/c per SPS supercycle of 16.8 seconds for the muon beam, and  $1 \times 10^8$  hadrons at 190 GeV/c per SPS supercycle of 16.8 seconds for the hadron beam. The maximum amount of material in the beam line had to be limited to about 5% of a nuclear interaction length during hadron beam operation.

In the DY part of the proposal a beam intensity up to  $6 \times 10^8$  hadrons per SPS supercycle (48 seconds) and a considerable longer target are requested. The hadron absorber will be placed immediately downstream of the target to stop the hadron component of the secondary particle's flux. These are major changes with respect to the configuration approved in 1999 and it requires new estimations of radiation levels in accessible areas around the facility, especially at unshielded or weakly shielded locations.

The following four areas in the COMPASS experimental hall are of special interest: the experimental barracks (A in Fig. 65); an unshielded area in the downstream end of the hall (B); the underground tunnel Jura–Salève (C); and an area outside the door on the Jura side (D). The experimental barracks (A) are located on the Salève side, behind

a 160 cm thick and 6.4 m high concrete shielding. Besides the radiation penetrating the shielding, there is also a contribution that is reflected by the roof of the hall (“sky-shine”) that has to be taken into account. The 11.5 m long gap in the concrete shielding (B) at the downstream end of the hall on the Salève side must also be considered, as this area is separated from the beam line only by an interlocked gate (PPG 221.3) and an interlocked door (PPX 221.2). There exists an underground tunnel (GHN22), five meters downstream from the target centre, crossing the experimental hall from the Jura to the Salève side (C). This tunnel is connected with the experimental hall via a 2.5 m × 1 m cable duct, which is partially covered by a 0.5 cm thick steel plate. Presently the tunnel can be entered at any time. Radiation passing through the cable duct has to be estimated. Finally, the area outside door PPX 221.1 (D) is presently accessible, even during beam operation, thus requiring also particular studies.

Accessible areas in the CERN North Area in hall EHN2 (Building 888) are classified as supervised radiation areas according to CERN’s classification of radiation areas [174]. Consequently, the ambient dose equivalent rate must not exceed 3  $\mu\text{Sv}/\text{hour}$  in permanently used work areas like the control room and must stay below 15  $\mu\text{Sv}/\text{hour}$  in low occupancy areas like passage ways.

Radiation levels are monitored in EHN2 by six permanently installed radiation monitors. Four monitors are located in the accessible area of EHN2 and another two are in the beam line area. The monitors in the accessible areas will trip the beam (during beam operation) when exceeding the limits of supervised radiation areas.

During the two Drell–Yan beam tests in 2007 and 2008 the radiation levels have been calculated with the Monte Carlo particle transport code FLUKA [175] [176] and were compared with measurements [177]. In addition to the fixed radiation monitors, also portable monitors were placed around the facility. The radiation level was found low in the areas of permanent occupancy ( $\leq 0.1 \mu\text{Sv}/\text{hour}$  for the beam intensity of  $\approx 2 \times 10^7$  pions per spill) and very good agreement between the monitor readings and the calculated radiation levels was found (the calculated value of the radiation level is  $\approx 30\%$  higher with respect to the measured one).

For the 2009 DY beam test performed at a beam intensity up to  $1.5 \times 10^8$  pions per spill the shielding requirements were determined again with FLUKA and excellent agreement between measurement and calculation was once more confirmed. The radiation level in the test with the hadron absorber was found low,  $\leq 0.5 \mu\text{Sv}/\text{hour}$  (the limit in the area of permanent occupancy is  $\leq 3 \mu\text{Sv}/\text{hour}$ ).

The shielding configuration for future Drell–Yan data taking (pion beam intensity is  $6 \times 10^8$  pions per spill) is under study. Sufficient shielding will be installed around the absorber and the target in order to stay below the radiation limits allowed in the accessible areas of EHN2 during beam operation.

## 9 Transversely polarised target for Drell–Yan measurements

The proposed experiment requires a transversely polarised proton target. The existing COMPASS polarised-target system can be used for this purpose.

The longitudinal polarisation of the target is obtained by the Dynamic Nuclear Polarisation (DNP) method, with a high-cooling-power dilution refrigerator, a 2.5 T solenoid magnet and two microwave systems of about 70 GHz corresponding to the Zeeman splitting for electrons [178, 179]. The polarisation value is measured by NMR techniques from the integral of the NMR absorption signal which is proportional to the polarisation [180]. The spin can be oriented perpendicular to the beam direction by using a 0.6 T dipole

magnet. Under this magnetic condition the polarisation can not be enhanced by the DNP method but can be maintained at a lattice temperature below 100 mK. As time passes, the polarisation decreases by the spin relaxation which depends on the magnetic field, the lattice temperature and the target material (frozen spin mode).

Each polarised target is characterised by a figure of merit  $PT_{FoM}$ , defined as

$$PT_{FoM} = f^2 P_T^2 \rho F_f \quad (63)$$

where  $f$  is the dilution factor, *i.e.* the fraction of polarisable nucleons in the target material,  $P_T$  is the polarisation,  $\rho$  is the density of the polarised target material in g/cm<sup>3</sup>, and  $F_f$  is its packing factor. The  $PT_{FoM}$  is inversely proportional to the data taking time. Ammonia (NH<sub>3</sub>) as polarised proton material is well suited for the Drell–Yan measurements. It reaches a polarisation of 80% after one day and a maximum of 90% after three days. A spin relaxation time of about 4000 hours was measured at 0.6 T and 60 mK in 2007.

In order to obtain the highest possible luminosity as much target material as possible has to be used. A high polarisation requires to stay in the flat field region with high homogeneity. For a better control of the systematical error of the asymmetry measurements it is mandatory to have two consecutive target cells with opposite polarisation simultaneously exposed to the beam.

Due to multiple scattering in the hadron absorber behind the target the vertex resolution is worse than in previous COMPASS measurements. Thus it is more difficult to associate the proper polarisation to each event due to event migration between the target cells. A distance of more than 20 cm between them appears necessary. This would result in a maximum length of 55 cm for each target cell.

The effects of the hadron beam and back scattering from the absorber to the target material and the cryogenic system have to be controlled. The total heat input into the mixing chamber caused by the pion beam is expected to be about 2 mW, which will not affect the spin relaxation time because the refrigerator has a cooling power of 5 mW at 70 mK [181]. Therefore, no modifications of the refrigerator are required. Note that in order to monitor precisely the target polarisation the beam diameter should be of the order of 1 cm FWHM.

The radiation load to the sensitive elements of the cryogenic system was calculated using FLUKA simulations. The results appear to be far below the limits.

## 10 Absorber for Drell–Yan measurements

### 10.1 Concept and design

A spectrometer configuration with a hadron absorber downstream of the polarised target has been chosen as a result of the Drell–Yan beam tests performed in 2007 and 2008. The installation of the hadron absorber will reduce the high secondary particle flux produced by the interaction of the pion beam in the target and, consequently, the tracking detector occupancies. This will make an increase in the intensity of the incident pion beam possible.

The choice of materials for the absorber must follow two main criteria: maximise the number of interaction lengths crossed by the hadrons produced in the collision in order to stop them while minimising the radiation length in order to have energy loss and multiple scattering of the muons as small as possible. In Table 19 one can find the basic characteristics of the various hadron absorbers used in CERN Drell–Yan experiments so

Table 19: Information relevant for the absorber design from past CERN Drell–Yan experiments as compared to the proposed COMPASS DY experiment.

Experiment	NA3 [145]	NA10 [103]	NA50 [146]	COMPASS
Beam mom. ( $\text{GeV}/c$ )	$\pi, p$ 200	$\pi^-$ , 200	$p$ , 400	$\pi^-$ , 150–200
Intensity (p/s)	$4 \times 10^7$	$6.5 \times 10^8$	$1 \times 10^9$	$6 \times 10^7$
Absorber length (m)	1.5 (Fe)	4.8 (C+Fe)	5.4 (Al+C+Fe)	1.5 $\text{Al}_2\text{O}_3 + 0.6 \text{ Fe}$
Beam dump (m)	1.5 (W)	4. (W+U)	4. (W+U)	1.8 (W)
Number of $\lambda_{int}$	7	13	13	7.1
Mass resol. ( $\text{MeV}/c^2$ )	130	100	100	$\approx 100$

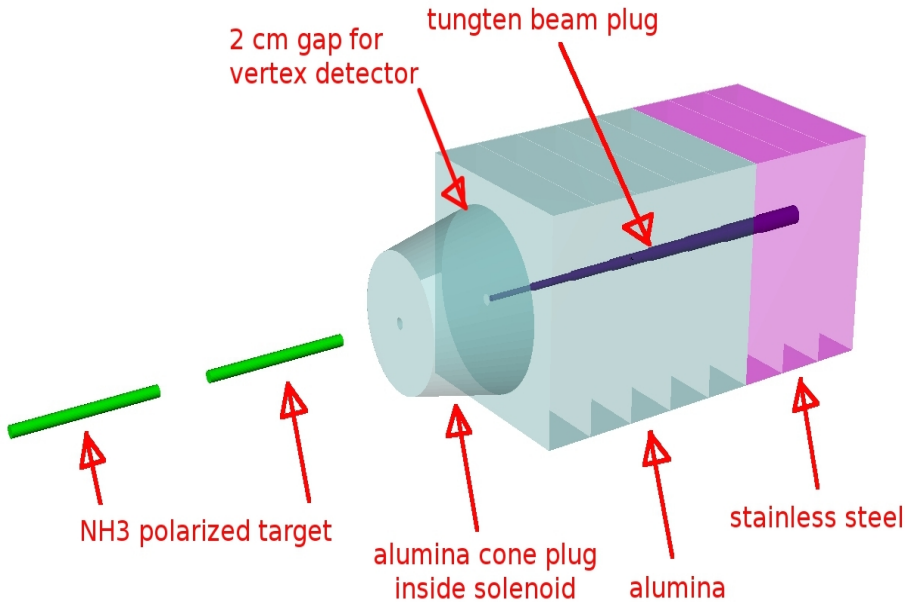


Figure 66: Drawing of the hadron absorber. The two  $\text{NH}_3$  target cells of 55 cm length and 4 cm radius each, are also shown. They are spaced by 20 cm and placed 30 cm upstream of the absorber.

far. The best absorber configuration was found in the NA50 experiment for protons at an intensity of  $10^9$  particles/s, achieving a particle reduction factor of  $I/I_0 = 1.74 \times 10^{-6}$ . We selected a NA50-like absorber for our final design taking into account the lower beam intensity of the COMPASS Drell–Yan experiment, which will be  $6 \times 10^7$  particles/s, *i.e.* 16.7 times less than for NA50. As the background increases quadratically with the beam intensity, the particle reduction factor  $I/I_0$  could be increased by a factor of  $16.7^2$  in COMPASS with respect to NA50, *i.e.*  $I/I_0 = 4.85 \times 10^{-4}$ , leading to a number of interaction lengths of  $L/\lambda_{int} = 7.6$ .

The configuration proposed is an absorber of aluminium oxide ( $\text{Al}_2\text{O}_3$ ) with a total length of 150 cm, followed by a 65 cm long stainless steel absorber, corresponding to a total number of interaction lengths of  $L/\lambda_{int} = 7.5$ . A schematic drawing of the absorber is shown in Fig. 66 together with the target cells. The two blocks of absorber materials have a central hole, centred with respect to the beam line, for the installation of the beam dump (plug), made of tungsten. The first 30 cm inside the aluminium oxide absorber are left empty (filled with air), in order to minimise back-scattering of particles produced by the beam interacting in the beginning of the plug. The plug itself is made

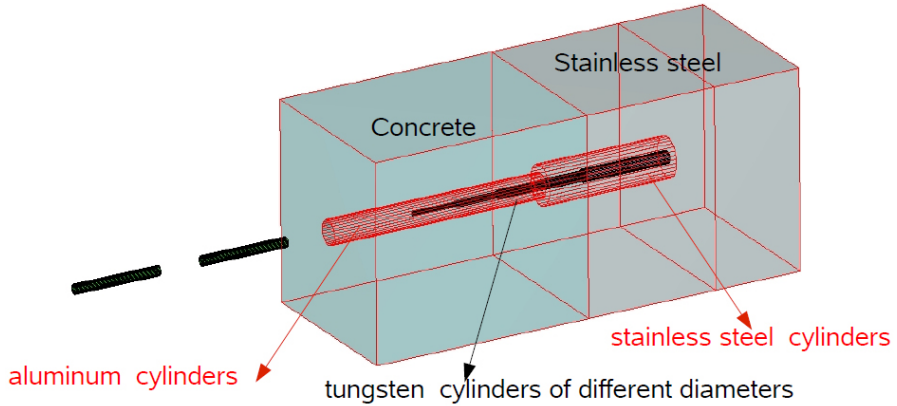


Figure 67: Drawing of the hadron absorber built for the 2009 beam test: in green the concrete part, in grey the stainless steel block. The two hollow aluminium cylinders are in red; inside them, in black, the tungsten cylinders of the plug are shown. The two polyethylene target cells of 40 cm length and 2.5 cm radius each are also shown. They are spaced by 20 cm and placed 20 cm upstream of the absorber.

of tungsten rods of increasing radius, covering a constant angle; it has to be optimised in order to stop the incoming beam particles and, on the other hand, to limit shadowing of the second spectrometer (SAS). The maximum transverse dimension of the absorber must match the maximum acceptance of the spectrometer, namely of the Muon Wall 1 detector (140 mrad). An additional cone-shaped aluminium oxide piece is plugged into the target solenoid with a 2 cm gap before the absorber itself for a possible installation of vertex detectors. A concrete shielding will be placed around the whole structure to reduce the dose rate.

## 10.2 Results from the beam test in 2009

In 2009 a Drell–Yan beam test was performed with a hadron absorber placed downstream of the target. The absorber used for the beam test, which is very close to the configuration described in Sect. 10.1, is shown in Figs. 67 and 68. As a temporary substitute for aluminium oxide concrete was used for the first block of the absorber while the second block was made of non-magnetic stainless steel (AISI 316L). Both blocks were of equal size,  $80 \times 80 \times 100$  cm $^3$ . Additional concrete shielding (80 cm thick on top, 40 cm thick on the sides) was placed around the absorber to reduce the dose rate. Radiation levels were monitored in the COMPASS hall by five permanently installed radiations monitors (Sect. 8). Figure 69 shows the results of the measurements by the five monitors placed in the beam line area (PAXN2111 and PAXN2113) or in the accessible areas. The measured dose rate does not exceed 0.5  $\mu\text{Sv}/\text{h}$  in the permanently used areas, like the control room and the experimental barracks (PAXN2112 and PAXN2212) where the allowed limit is 3  $\mu\text{Sv}/\text{h}$ .

The results of the two beam tests performed in 2007 and 2008 with an open configuration of the spectrometer has shown that the occupancy was too high on the tracking detector stations immediately downstream of the target, in particular on the Micromegas and drift chamber stations closest to the target, DC00 and MM01. The insertion of a hadron absorber suppresses considerably the high secondary particle flux produced by the inter-



Figure 68: Photograph of the absorber and target setup for the 2009 beam test: on the right, inserted in two vertical supports, the two polyethylene target cells; on the left the concrete part of the absorber, with a section of the hollow aluminium cylinder filled with tungsten, followed by the stainless steel part on the very end of the picture. An additional concrete shielding was placed around the absorber to reduce the dose rate.

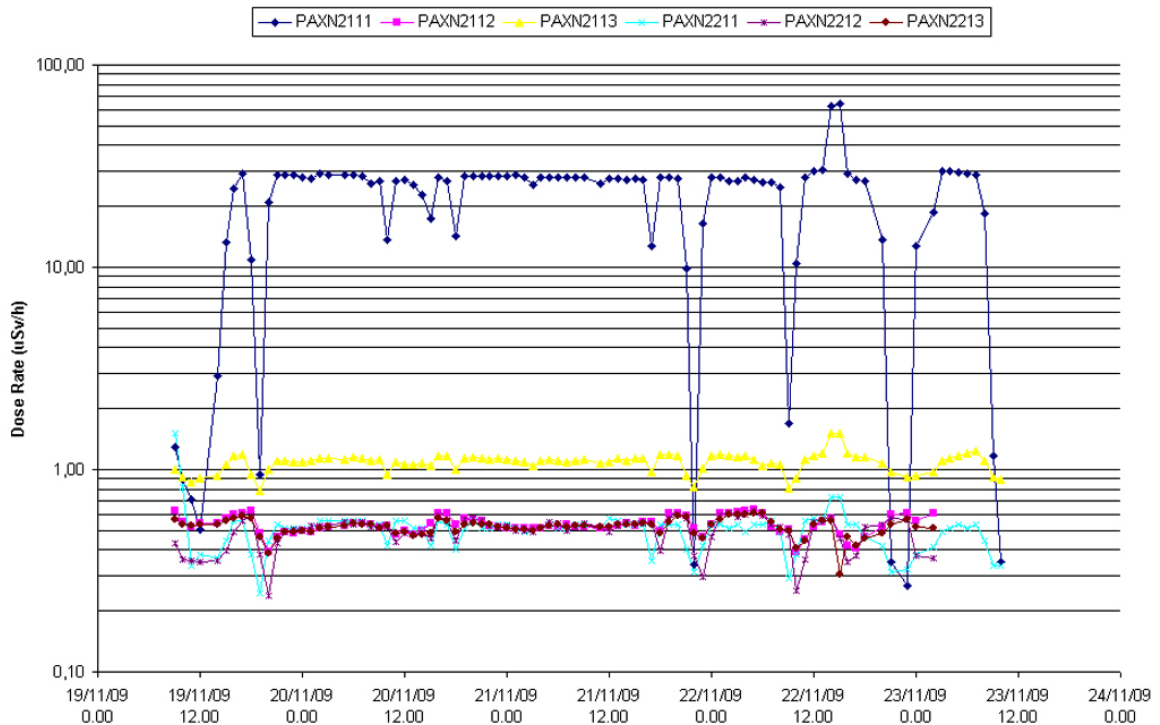


Figure 69: Dose rates measured in the COMPASS hall during the Drell–Yan beam test in November 2009, with an average beam intensity of  $I = 7 \times 10^7$  pions per spill (spill time = 9.6 s, SPS supercycle time = 39.6 s). The beam intensity was increased up to about  $1.5 \times 10^8$  during a short period on 22/11/2009. The different curves show measurements taken by several radiation monitors placed in different positions in the hall.

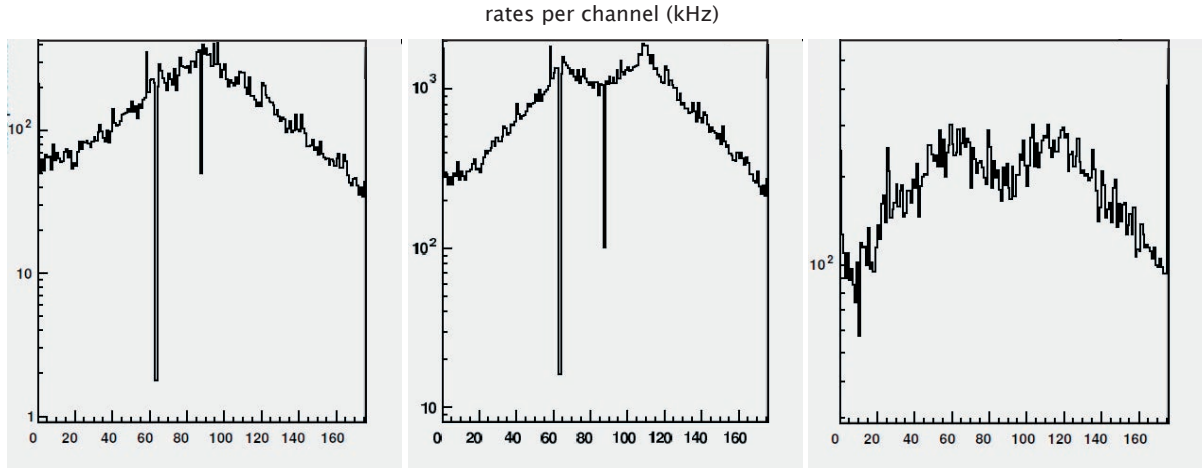


Figure 70: Occupancy of one plane of DC00 for three different runs: muon run in 2007 (left); Drell–Yan beam test run in 2007 without absorber (centre, intensity  $6.4 \times 10^7$  pion per spill) and Drell–Yan beam test run in 2009 with absorber (right, intensity  $1.5 \times 10^8$  pions per spill).

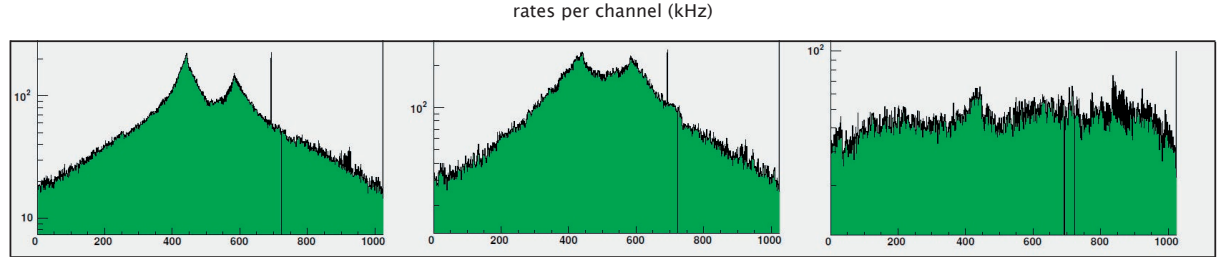


Figure 71: Occupancy of one plane of MM01 for three different runs: muon run in 2007 (left); Drell–Yan beam test run in 2007 without absorber (centre, beam intensity  $6.4 \times 10^7$  pion per spill) and Drell–Yan beam test run in 2009 with absorber (right, intensity  $1.5 \times 10^8$  pions per spill).

action of the pion beam in the target thus reducing, consequently, the tracking detector occupancy. In Figures 70 and 71 a comparison is shown between the rates per channel on one plane of DC00 and MM01 during a muon run in 2007 and two runs taken during the Drell–Yan beam tests in 2007 (without absorber) and 2009 (with absorber). At the maximum achieved beam intensity of  $1.5 \times 10^8$  pions/spill the presence of the absorber significantly reduced the occupancy on the drift chamber planes, which in the 2007 beam test was higher than 1 MHz for the central channels at the maximum achievable intensity of  $6.4 \times 10^7$  pions/spill (without absorber). The particle flux downstream of the absorber was calculated with the Monte Carlo particle code FLUKA. In Figure 72 the charged particle flux through the absorber is shown for a 190 GeV/c incident pion beam. The maximum flux is confined inside the upstream part of the tungsten beam plug inserted in the 100 cm long concrete block, which precedes the stainless steel block. The obtained mean-charged particle flux immediately downstream of the absorber is  $7.9 \times 10^{-5}$  particles/cm<sup>2</sup>/primary, the total particles flux (charged + neutral) is  $4.8 \times 10^{-4}$  particles/cm<sup>2</sup>/primary .

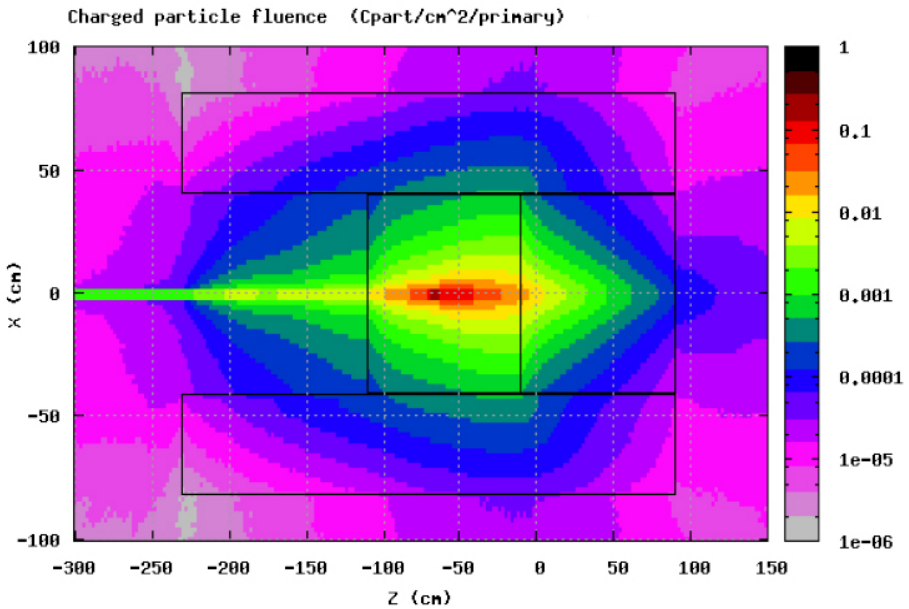


Figure 72: Charged particle flux through the 2009 beam test absorber simulated with FLUKA;  $z$  is along the beam axis,  $x$  is in the horizontal plane.

## 11 Pixelised Micromegas detectors

The physics programmes of this proposal deal with low cross section processes, which require high intensity of the incident muons or hadrons beams. As little as possible material should be introduced by the detectors which should also stand high hadron flux. This poses new constraints on the tracking system. Since 2007/2008 five GEM stations have been upgraded with new detectors offering a pixelised readout structure in the centre using the APV-based readout system. They have been successfully operated in the hadron beam runs 2008/2009. However, due to their overall size of  $10\text{ cm} \times 10\text{ cm}$ , they do not fulfil the tracking requirements right downstream of the target region, presently equipped with the large size  $40\text{ cm} \times 40\text{ cm}$  micro-pattern gaseous Micromegas detectors. The Micromegas detectors are read by strips which cover the full length of the active area and are prolonged in order to move the material of the front-end electronics (SFE16 amplifier cards and F1 TDC cards) out of the spectrometer acceptance. To avoid a too high occupancy in the vicinity of the beam and to minimise the material in the beam region, the detectors were designed with a  $5\text{ cm}$  diameter central dead zone. In order to cope with the new requirements, we plan to replace the Micromegas built ten years ago by new ones of similar size and designed to:

- stand higher beam intensities and up to a factor of five higher rates of hadrons, which are highly ionising particles, and
- detect particles in the centre of the detector without any extra cost in terms of material budget.

The new detectors will also satisfy additional requirements: they will have improved robustness, and will be read out with light and integrated electronics. The central area will be read by pixels. Since the present detectors measure a single coordinate per plane, a rectangular shape of the pixels was chosen thus preserving the spatial resolution (Fig. 73).

Tracking of particles from the beam or scattered at very low angles will become possible with high resolution. The non-central region of the detector will be read out

via strips and the large size of the detector will be preserved. Special care is taken to reduce the frequency of the discharges, which limit the performance of the detector for high intensity hadron beams. A specific R&D program was initiated exploring two lines:

- use resistive layers in order to spread out the electrical charge,
- preamplify the signal using a GEM foil thus allowing for a reduction of the gain in the amplification gap.

Two prototypes with  $1 \text{ mm}^2$  pixels in the centre and 30 cm long strips in the periphery were operated during several months in the hottest region of the COMPASS spectrometer with both muon and hadron beams. The first prototype was built with the new robust “bulk” technology, where a  $20 \mu\text{m}$  woven stainless steel mesh is assembled with the board. This prototype is the first Micromegas detector, in which a large size thin bulk structure was glued to a honeycomb board. A second prototype was built with the standard techniques using a thin  $5 \mu\text{m}$  copper mesh for comparison. Pixels and strips were read out by a compact and integrated electronics using APV chips (128 channels per chip) installed on new cards with a specific protection circuit. The gas mixture was the one used for all standard COMPASS Micromegas, 80%/10%/10% of neon/ethane/CF<sub>4</sub>.

The prototypes operated well, validating both the use of the APV front-end readout and the new technology bulk structure on a thin board. However, the issue of reducing the discharge rate in presence of hadrons was not addressed here.

Several small ( $10 \text{ cm} \times 10 \text{ cm}$ ) prototypes featuring different techniques of resistive coating were tested in a dedicated set-up. Standard bulk Micromegas and a Micromegas equipped with a GEM foil were tested in the same conditions for comparison. The discharge rates of all the prototypes were monitored for various intensities of hadron and muon beams in the SPS H4 test beam line. The preliminary results obtained with the Micromegas equipped with a GEM foil show that the discharge rate can be reduced by more than an order of magnitude (Fig. 74). For the resistive Micromegas prototypes, the discharge amplitudes were so much reduced that the discharge rates could not be measured as a signal on the mesh. Additional beam tests are ongoing to understand the impact of this technology on the reduction of the discharge rate. All other performances (efficiency, spatial resolution, cluster size) of the prototypes were similar to the standard Micromegas ones. A final decision on the technology to be implemented will be taken in the beginning of 2011. Before the production of the twelve new detectors a final prototype will be built and validated in the beam.

## 12 Upgrade of the RICH-1 gaseous photon detectors

The large majority of the topics of the COMPASS physics programme performed so far and presented in this proposal requires hadron identification. In the COMPASS spectrometer, it is provided by a large size Cherenkov imaging counter, RICH-1, operated in its initial version since 2001 [182] and in its upgraded version characterised by a more powerful photon detection system since 2006 [183, 184]. In RICH-1 particles cross 3 m of gaseous radiator, C<sub>4</sub>F<sub>10</sub>. During the years 2001–2004, RICH-1 photodetection has been performed with Multi-Wire Proportional Chambers (MWPC) equipped with solid state CsI photocathodes [185–187]. One of the two cathode planes of the proportional chamber is a Printed Circuit Board (PCB) segmented into  $8 \times 8 \text{ mm}^2$  pads coated with a CsI film. The Cherenkov photons enter the chamber via a fused silica window and hit the photocathode PCB. The photo-electrons produced by the converted photons are multiplied in the MWPC. The detectors are operated at low gain (below  $5 \times 10^4$ ), as imposed by the presence of the CsI photocathode. Since 2006 the peripheral region (75% of the surface)

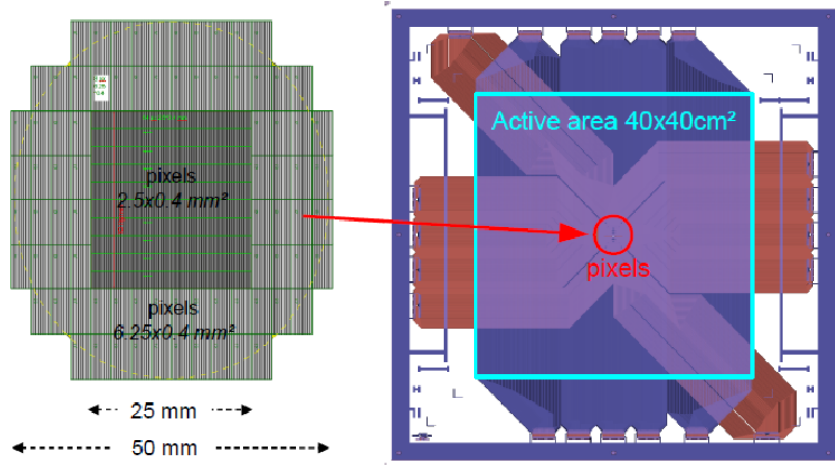


Figure 73: Board design of the pixelised Micromegas.

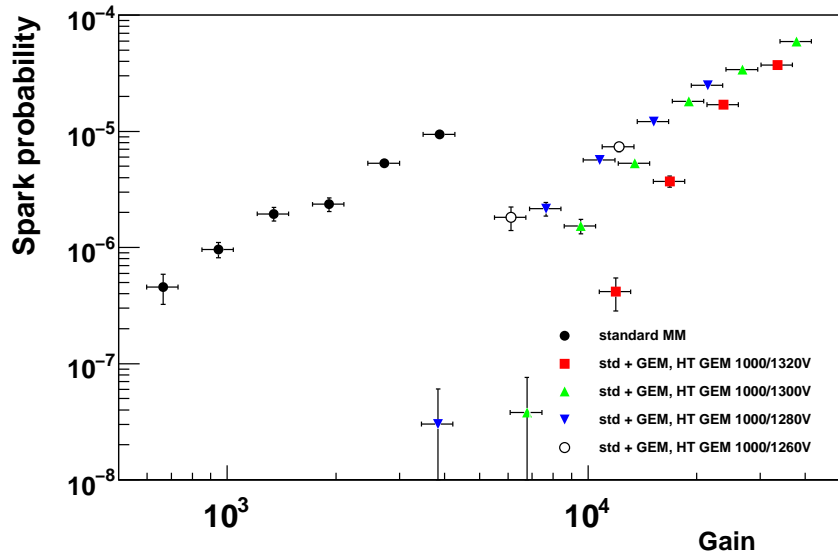


Figure 74: Discharge rates per incident hadron for standard Micromegas and Micromegas with an added GEM foil.

with the images of lower-momentum particles is read out by a system [188] based on the APV chip [189]. The Cherenkov images produced by the high-momentum particles are detected in the central photon detection area (25% of the surface), a region highly populated by uncorrelated background images. This region is instrumented with a fast detection system based on MultiAnode PhotoMultiplier Tubes (MAPMT) [183, 184] coupled to individual telescopes of fused silica lenses (a prismatic field lens followed by a concentrator lens) to enlarge the effective active area of the photon detectors. The effective pad size, resulting from the MAPMT pixel size and the lens telescope magnification is about  $12 \times 12 \text{ mm}^2$ . Presently the resolution on the measured Cherenkov angle for particles with  $\beta \rightarrow 1$  is 0.3 mrad for the central photon-detection area and 0.9 mrad for the peripheral area.

The MWPCs in operation for RICH-1 are examples of the first generation of gaseous photon detector with a solid state photoconverter. In spite of the remarkable success of proving that solid state photoconverters can operate in gaseous atmospheres, MWPCs

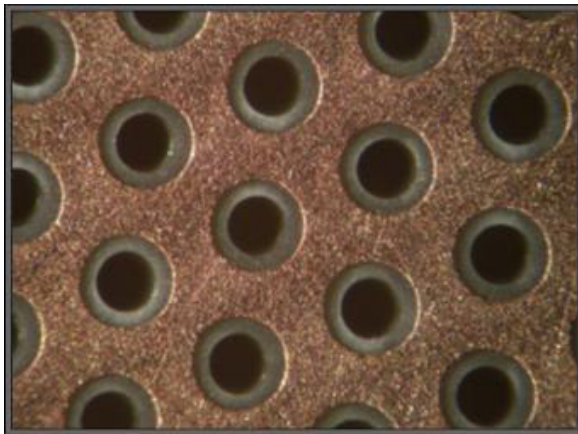


Figure 75: Detail of a THGEM PCB

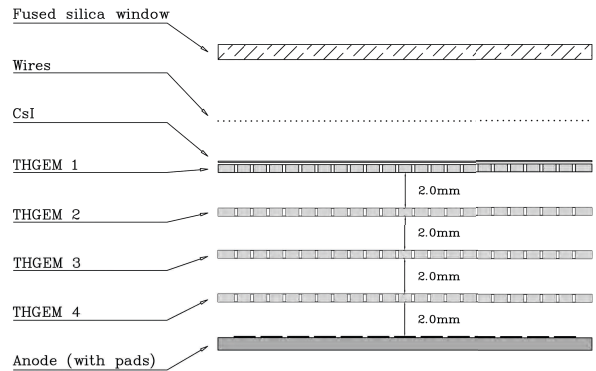


Figure 75: Scheme of the basic architecture of a THGEM-based photon detector (not to scale).

with CsI photocathodes suffer because of some performance limitations: ageing, causing a severe decrease of the quantum efficiency after a collected charge of the order of some  $\text{mC}/\text{cm}^2$  [190, 191] and long recovery time (about 1 day) after a detector discharge [182]. Therefore, they must be operated at low gain, reducing the single photo-electron detection efficiency. These limitations are related to the bombardment of the CsI photocathode film by the positive ions and photons generated in the multiplication process. In COMPASS RICH-1, these features limit the number of detected photons and, at high beam rate, cause instabilities of the photon detector performance related to the long recovery time after a discharge. To overcome these limitations, a large-gain gaseous photon detector is developed, characterised by a closed geometry architecture and based on the use of THick GEM (THGEM) [192–195] electron multipliers, coupled to a solid-state CsI photocathode. In fact, in a multilayer structure of electron multipliers, a good fraction of the ions is trapped in the intermediate layers, and no photons can reach the photocathode [192–194, 196–198].

The THGEM electron multiplier is derived from the GEM [199] one. The copper-coated kapton foil of the GEM multipliers is replaced by a standard PCB and the holes are produced by drilling. The conical shape of the GEM holes that forms uncoated polyamide rings around the holes themselves are replaced by a clearance ring, the rim, surrounding the hole and obtained by copper etching (Fig. 75). Typical values of the geometrical parameters are PCB thicknesses of 0.4–1 mm, hole diameters ranging between 0.3 mm and 1 mm, hole pitches of 0.7–1.2 mm and rim width values between 0 mm and 0.1 mm. The electron multiplication is obtained applying an appropriate voltage between the two conductive faces of the PCB, which are electrically insulated with respect to each other. Large gains have been reported for detectors with single or double THGEM layers as well as good rate capabilities.

The basic architecture of a THGEM-based photon detector (Fig. 75) comprises a multiplication structure of three THGEM, where the first is coated with a CsI film and acts as a reflective photocathode. The electrical field above and below the multiple THGEM structure is defined by additional electrodes. A plane of metallic wires parallel to the THGEM PCB to keep side from which the particles enter as transparent as possible. A PCB segmented into pads, again parallel to the THGEM PCBs, is used both to define the electric field at the exit side of the structure and to collect the signals. Its segmentation

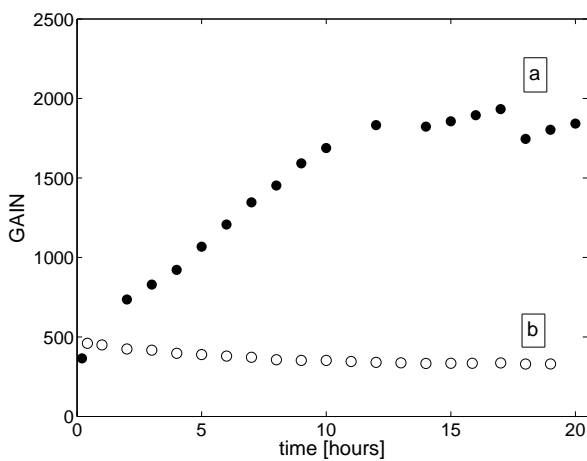


Figure 76: Gain versus time behaviour for two THGEMs with the following geometry: thickness 0.4 mm, pitch 0.8 mm and hole diameter 0.4 mm (common parameters); different parameter: 0.1 mm rim for (a), no rim for (b). Continuous detector irradiation;  $\Delta V = 1750$  V for (a) and 1330 V for (b).

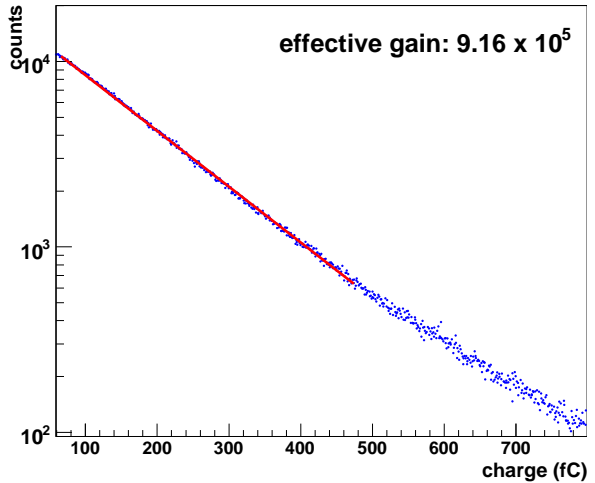


Figure 76: Single photo-electron amplitude spectrum measured with the THGEM detector described in the text.

makes it possible to preserve the space information. The particles enter through an UV-transparent window, closing the volume of the detector chamber.

We have performed a systematic study [200–203] of the properties of the THGEM electron multipliers, in particular disentangling the role of the various geometrical, electrical and production-related parameters to determine the optimal geometry for photon detection applications. In particular, we have shown that stable gain can be obtained for THGEM with no or small ( $10\ \mu\text{m}$ ) rim, while a large rim ( $\sim 0.1$  mm) causes severe gain variations versus time (Fig. 76).

For single photon detection, both simulation studies and laboratory measurements indicate that THGEM geometries for which the electric field at the CsI photocathode surface is large enough to guarantee a good photo-electron extraction are those for which the ratio between the hole diameter and the hole pitch is large ( $\geq 0.5$ ). At the same time the larger this ratio is the larger is the detector dead zone. Selecting a diameter of 0.4 mm and a pitch of 0.8 mm a good compromise can be obtained. Gains up to 10<sup>6</sup> have been obtained with a triple layer detector employing THGEM PCBs with these parameters (Fig. 76), to be compared with the gain of the present gaseous photon detectors of  $5 \times 10^4$ . The measured ion feedback rate is reduced to about 25%. Further reduction can be obtained introducing one more wire plane electrode between the first and the second THGEM layer. This improved geometry is presently under test. The measured time resolution is about 10 ns. The intrinsic space resolution is of the order of 1 mm.

Small-size prototypes of THGEM-based photon detectors have been employed so far. The engineering aspects related to the extension of the size to detectors of about  $60 \times 60\ \text{cm}^2$  is ongoing. Good quality THGEM PCB of this size have already been produced. For these studies the digital read-out system presently used to read-out the MAPMTs employed in the centre of the RICH-1 detection area [184] has been successfully used to

detect with good efficiency the photo-electron signals, thanks to the large detector gain. Alternatively, the present readout technology operated for the CsI-coated MPWC of the RICH and based on the APV chip is envisaged. This system is sucessfully operated on all thin GEM stations within COMPASS.

The proposed upgrade of the RICH-1 gaseous photon detectors consists in replacing the MWPCs with CsI photocathode with THGEM-based detectors of large size, coupled to CsI photocathodes. The pad size will remain the same of the MWPCs, namely,  $8 \times 8 \text{ mm}^2$ . The major improvements of the new gaseous photon detectors are the larger gain, which results in a larger efficiency of the single photo-electron detection, the reduced ion feedback allowing for more stable detector operation and better time resolution.

### 13 Cost estimate

The proposed measurements will make use of the existing COMPASS spectrometer as described in Ref. [133] and of the upgrades performed during the years 2005–2010. However, the new physics programmes require a number of additions and modifications. Furthermore, some of the original equipments are by now 10 years old or more and need to be refurbished or replaced. Typical cases are the DAQ, the pumps of the polarised target (more than 25 years old) and the silicon trackers in the beam, which suffer from radiation damage. The responsibility for maintenance and operation of an existing equipment will in general stay with the same group as in the present COMPASS experiment. In Table 20 these responsibilities are summarised together with those for new equipment and a first estimate of the necessary investment for construction, refurbishment or upgrade.

The major new equipments for the GPD programme are the new electromagnetic calorimeter ECAL0 close to the target and the proton recoil detector RPD with its liquid hydrogen target. For the DY programme the modified polarised target with the hadron absorber are the new key elements. The considerable upgrade of ECAL1 is required for the DVCS part of the GPD programme. Here, for the cost evaluation it was assumed that ECAL2 remains unchanged and that the central holes of ECAL1 and HCAL1 are somewhat reduced (“Option 3” on page 99). The upgrade of the peripheral part of the RICH-1 photon detection is important for a stable operation of the RICH in a high-flux environment. The RICH itself is essential for the exclusive meson production part of the GPD programme as well as for the simultaneously performed measurements of unpolarised SIDIS.

The cost estimate is in an early stage and numbers are very preliminary. The total projected investment is roughly 7 MCHF, about one quarter of the total fresh COMPASS-I investment. COMPASS is inviting and actively searching for new collaborators. Therefore changes in the responsibilities should be expected in the further development of the project. The present sharing between the participating countries is shown in Fig. 77. Within the German groups the sharing is still under discussion. The item concerned is temporarily marked by “BMBF” in Table 20.

Apart from the requested contributions by CERN as collaborating institute listed in Table 20, the new experiment would require from CERN as host laboratory the continuation of the services granted for the present COMPASS experiment, in particular in cryogenics and central data recording. The question of cost for recording media should be rediscussed. A major problem is the temperature in the experimental hall EHN2 (888). In summer it grows well over 30 degree and causes severe problems for the chambers due to thermal expansion as well as to the electronics. Before a new round of experiments is started a refurbishment of the about 35 years old ventilation system is indispensable.

Table 20: Tentative responsibilities in COMPASS-II for detector operation and maintenance as well as estimated cost of repair, modification of existing and of construction of new equipment in kCHF.

Item	Institution	Invest	Remarks
Beam Momentum Station	Bonn HISKP		
Scintillating Fibres	Bonn HISKP/Erlangen	150	more det.
Silicon Beam Telescope	TU Munich	100	new wafers
MicroMegas	Saclay		
Pixel MicroMegas	Saclay	420	new
DC Drift Chambers	Saclay		
GEMs & PixelGEMs	TU Munich		
Straws	Freiburg/Munich LMU		
MWPCs	Turin		
Rich Wall	Turin		
Muon Wall 1	JINR		
W45 drift Chambers	CERN	30	repair
Muon Wall 2	IHEP Protvino		
Total trackers		<b>700</b>	
ECAL0			new
Modules (250)	JINR	372	
Housing & Temp. Stab.	JINR	100	
LED Monitoring	JINR	40	
Readout (MSADCs)	TU Munich	250	
MAPD	Saclay	60	
	Warsaw UT	90	
Preamplifiers	Warsaw SINS/WU	30	
Frame	CERN	50	
ECAL1			upgrade
Shashlik Modules (600)	BMBF	80	
	Mainz	50	
	Freiburg	50	
	Saclay	30	
GAMs Modules (1700)	IHEP Protvino		exist
PMs	IHEP Protvino	270	exist
HV Bases	Freiburg	106	
Readout (MSADCs) & cables	Mainz	110	
	Saclay	50	
	TU Munich	70	
Monitoring ext.	Saclay	75	
ECAL2 Monitoring	Lisbon	50	new
HCAL1 Modification	JINR	50	
Total Calorimeters		<b>1983</b>	

Table 20: (cont'd) Tentative responsibilities in COMPASS-II for detector operation and maintenance as well as estimated cost of repair, modification of existing and of construction of new equipment in kCHF.

Item	Institution	Invest	Remarks
RPD/LH Target			new
RPD Structure	Saclay	150	
PMs	Saclay	60	
	Warsaw SINS/WU	30	
	Calcutta	30	
Scintillators/Lightguides	Saclay	210	
	Mainz/Bonn PI	70	
Readout	Freiburg	190	
HV, Crates, Electronics	Saclay	80	
	Warsaw SINS/WU	50	
	Warsaw UT	20	
LH Target	Saclay	75	
	CERN	75	
	Yamagata	25	
Total RPD&LH Target		<b>1065</b>	
RICH-1 Upgrade			upgrade
Peripheral Chambers	Trieste/Turin	1080	
	Prague	20	
Read-out (under study)	Trieste/Turin	700	
CEDAR Upgrade	Mainz	100	upgrade
Total RICH & CEDAR		<b>1900</b>	
Polarised Target			
Pumps refurbishment	Yamagata	150	maintenance
EIO Microwave Tube	Yamagata	100	replacement
Target material (NH3)	Bochum	80	replacement
Target holder	Bochum	50	modification
Cavity	Bochum	20	modification
	Prague	30	
Hadron Absorber	Turin	110	new
	Lisbon	30	new
	CERN	60	new
Total PT & Absorber		<b>630</b>	
Veto/Matrices	Mainz/Bonn PI	100	new
DAQ	TU Munich	150	replacement
	Turin/Trieste	150	
	Prague	60	
	Tel Aviv	25	
DCS	Lisbon	50	upgrade
Total DAQ/Trigger/DCS		<b>535</b>	
Infrastructure	CERN	<b>250</b>	modification
Total		<b>7063</b>	

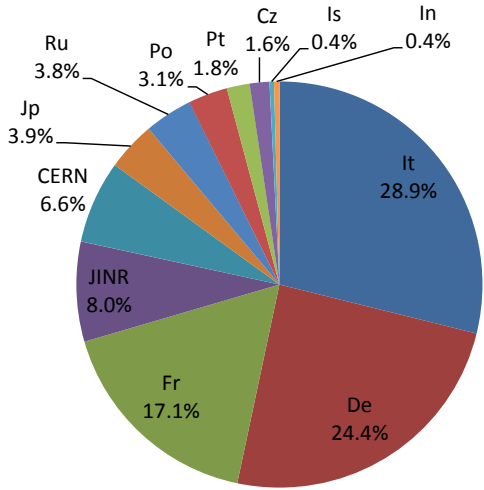


Figure 77: Tentative sharing of new investment cost between the participating countries in per cent.

## Acknowledgements

The authors remember with gratitude Jan P. Nassalski and Alexei N. Sissakian who untimely passed away. Both were strong supporters of the COMPASS-II project and made important contributions to it.

The authors thank M. Anselmino, A. Bacchetta, E. Barone, A. Bianconi, M. Burkardt, M. Diehl, G. Fäldt, L. Gatignon, P. Guichon, Ph. Hägler, N. Kaiser, P. Kroll, D. Müller, A. Prokudin, M. Radici, Ph. Ratcliffe, A. Schäfer, L. Schöffel, H. Vincke, B. Vullierme, W. Weise, and Ch. Weiss for useful advice and comments, critical reading, and/or technical help.

## References

- [1] D. Mueller et al., *Fortschr. Phys.* 42 (1994) 101.
- [2] X.-D. Ji, *Phys. Rev. Lett.* 78 (1997) 610.
- [3] X.-D. Ji, *Phys. Rev. D*55 (1997) 7114.
- [4] A. V. Radyushkin, *Phys. Lett.* B385 (1996) 333.
- [5] A. V. Radyushkin, *Phys. Rev. D*56 (1997) 5524.
- [6] M. Burkardt, *Phys. Rev. D*62 (2000) 071503, Erratum *ibid.* D66 (2002) 119903.
- [7] M. Burkardt, *Int. J. Mod. Phys. A*18 (2003) 173.
- [8] M. Burkardt, *Phys. Lett.* B595 (2004) 245.
- [9] J. C. Collins et al., *Phys. Rev. D*59 (1999) 074009.
- [10] LHPC, Ph. Hägler et al., *Phys. Rev. D*77 (2008) 094502.
- [11] QCDSF-UKQCD, D. Brommel et al., *PoS LAT2007* (2007) 158.
- [12] LHPC, J. D. Bratt et al., [arXiv:1001.3620](https://arxiv.org/abs/1001.3620).
- [13] Conceptual Design Report (CDR) for The Science and Experimental Equipment for The 12 GeV Upgrade of CEBAF (Prepared for the DOE Science Review, April 6–8, 2005), Editors J. Arrington et al., Jefferson Lab (2005),  
[http://www.jlab.org/div\\_dept/physics\\_division/GeV/doe\\_review/CDR\\_for\\_Science\\_Review.pdf](http://www.jlab.org/div_dept/physics_division/GeV/doe_review/CDR_for_Science_Review.pdf).
- [14] LHPC, Ph. Hägler et al., *Phys. Rev. Lett.* 93 (2004) 112001.
- [15] M. Diehl, *Eur. Phys. J. C*25 (2002) 223.
- [16] M. Burkardt, [arXiv:0711.1881](https://arxiv.org/abs/0711.1881).
- [17] J. W. Negele et al., *Nucl. Phys. Proc. Suppl.* 128 (2004) 170.
- [18] H1, F. D. Aaron et al., *Phys. Lett.* B659 (2008) 796.
- [19] M. Strikman et al., *Phys. Rev. D*69 (2004) 054012.
- [20] M. Strikman et al., *Phys. Rev. D*80 (2009) 114029.
- [21] K. Kumericki et al., [arXiv:0904.0458](https://arxiv.org/abs/0904.0458).
- [22] L. Frankfurt et al., *Phys. Rev. D*69 (2004) 114010.
- [23] Z. J. Ajaltouni et al., in *Proceedings of HERA and the LHC: 2nd Workshop on the Implications of HERA for LHC Physics*, Geneva, Switzerland, 6–9 Jun 2006, Hamburg, Germany, 12–16 Mar 2007, Geneva, Switzerland, 26–30 May 2008, [arXiv:0903.3861](https://arxiv.org/abs/0903.3861).
- [24] L. Frankfurt et al., *Annalen Phys.* 13 (2004) 665.
- [25] L. Frankfurt et al., *Phys. Rev. Lett.* 101 (2008) 202003.
- [26] L. Frankfurt et al., *Phys. Rev. D*75 (2007) 054009.
- [27] FP420 R&D Collaboration, M. G. Albrow et al., *JINST* 4 (2009) T10001.
- [28] M. Deile et al., *To appear in:* Proceedings of 13th International Conference on Elastic and Diffractive Scattering (Blois Workshop) – Moving Forward into the LHC Era, [arXiv:1002.3527](https://arxiv.org/abs/1002.3527).

- [29] L. Frankfurt et al., Ann. Rev. Nucl. Part. Sci. 55 (2005) 403.
- [30] I. Balitsky, Nucl. Phys. B463 (1996) 99.
- [31] Y. V. Kovchegov, Phys. Rev. D54 (1996) 5463.
- [32] J. Jalilian-Marian et al., Phys. Rev. D55 (1997) 5414.
- [33] L. D. McLerran et al., Phys. Rev. D49 (1994) 3352.
- [34] L. D. McLerran et al., Phys. Rev. D49 (1994) 2233.
- [35] H. Kowalski et al., Phys. Rev. Lett. 100 (2008) 022303.
- [36] H. Kowalski et al., Phys. Rev. D68 (2003) 114005.
- [37] T. Rogers et al., Phys. Rev. D69 (2004) 074011.
- [38] H1, A. Aktas et al., Eur. Phys. J. C46 (2006) 585.
- [39] ZEUS, S. Chekanov et al., Nucl. Phys. B695 (2004) 3.
- [40] A. V. Belitsky et al., Nucl. Phys. B629 (2002) 323.
- [41] HERMES, A. Airapetian et al., JHEP 06 (2008) 066.
- [42] J. C. Collins et al., Phys. Rev. D56 (1997) 2982.
- [43] BABAR, B. Aubert et al., Phys. Rev. D80 (2009) 052002.
- [44] A. V. Radyushkin, Phys. Rev. D80 (2009) 094009.
- [45] J. C. Collins et al., Nucl. Phys. B193 (1981) 381.
- [46] J. C. Collins et al., Nucl. Phys. B194 (1982) 445.
- [47] R. K. Ellis et al., Nucl. Phys. B207 (1982) 1.
- [48] J. Botts et al., Nucl. Phys. B325 (1989) 62.
- [49] S. V. Goloskokov et al., Eur. Phys. J. C53 (2008) 367.
- [50] HERMES, A. Airapetian et al., Phys. Lett. B679 (2009) 100.
- [51] M. Vanderhaeghen et al., Phys. Rev. D60 (1999) 094017.
- [52] A. Sandacz, April 27, 2009,  
<http://wwwcompass.cern.ch/compass/gpd/index.html>.
- [53] H1, A. Aktas et al., Eur. Phys. J. C44 (2005) 1.
- [54] ZEUS, S. Chekanov et al., JHEP 05 (2009) 108.
- [55] M. Diehl et al., Eur. Phys. J. C39 (2005) 1.
- [56] M. Guidal et al., Phys. Rev. D72 (2005) 054013.
- [57] K. Kumericki et al., Nucl. Phys. B794 (2008) 244.
- [58] HERMES, A. Airapetian et al., JHEP 11 (2009) 083.
- [59] ZEUS, S. Chekanov et al., PMC Phys. A1 (2007) 6.
- [60] A. Sandacz, Feb. 27, 2008,  
<http://wwwcompass.cern.ch/compass/gpd/index.html>.
- [61] NMC, M. Arneodo et al., Nucl. Phys. B429 (1994) 503.
- [62] J. Koivuniemi, logbook entries 60 & 68,  
[http://wwwcompass.cern.ch/elog/target\\_polar/60](http://wwwcompass.cern.ch/elog/target_polar/60).
- [63] W. Meyer, internal communication.
- [64] J. Bernhard et al., COMPASS Note 2009-4, April 30, 2009,  
[http://wwwcompass.cern.ch/compass/notes\\_public/2009-4.pdf](http://wwwcompass.cern.ch/compass/notes_public/2009-4.pdf).
- [65] The COMPASS collaboration, COMPASS Medium and Long Term Plans, CERN-SPSC-2009-003, SPSC-I-238, 2009.
- [66] J. Bernhard et al., COMPASS Note 2009-11, October 7, 2009,  
[http://wwwcompass.cern.ch/compass/notes\\_public/2009-11.pdf](http://wwwcompass.cern.ch/compass/notes_public/2009-11.pdf).
- [67] R. Sassot et al., *To appear in:* Proceedings of 17th International Workshop on Deep-Inelastic Scattering and Related Subjects (DIS 2009), Madrid, Spain, 26–30 April, 2009, arXiv:0906.5521.
- [68] D. Boer et al., Phys. Rev. D57 (1998) 5780.

- [69] R. N. Cahn, Phys. Lett. B78 (1978) 269.
- [70] D. de Florian et al., Phys. Rev. D75 (2007) 114010.
- [71] A. D. Martin et al., Eur. Phys. J. C63 (2009) 189.
- [72] P. M. Nadolsky et al., Phys. Rev. D78 (2008) 013004.
- [73] HERMES, A. Airapetian et al., Phys. Lett. B666 (2008) 446.
- [74] COMPASS, M. Alekseev et al., Eur. Phys. J. C64 (2009) 171.
- [75] COMPASS, M. Alekseev et al., Phys. Lett. B680 (2009) 217.
- [76] S. D. Bass et al., Phys. Lett. B684 (2010) 216.
- [77] E. Christova et al., Phys. Rev. D79 (2009) 014019.
- [78] A. D. Martin et al., Phys. Lett. B531 (2002) 216.
- [79] A. Bacchetta et al., JHEP 02 (2007) 093.
- [80] M. Anselmino et al., Phys. Rev. D71 (2005) 074006.
- [81] EMC, M. Arneodo et al., Z. Phys. C34 (1987) 277.
- [82] EMC, J. Ashman et al., Z. Phys. C52 (1991) 361.
- [83] FNAL-E665, M. R. Adams et al., Phys. Rev. D48 (1993) 5057.
- [84] ZEUS, J. Breitweg et al., Phys. Lett. B481 (2000) 199.
- [85] COMPASS, W. Käfer, in *Proceedings of Transversity 2008: II International Workshop on Transverse Polarization Phenomena in Hard Scattering Processes*, 27-31 May 2008, Ferrara, Italy; World Scientific, ed. by G. Ciullo et al., April 2009, ISBN:978-981-4277-77-8, p. 169, [arXiv:0808.0114](https://arxiv.org/abs/0808.0114).
- [86] HERMES, F. Giordano et al., AIP Conf. Proc. 1149 (2009) 423.
- [87] V. Barone et al., [arXiv:0912.5194](https://arxiv.org/abs/0912.5194).
- [88] G. Bunce et al., Phys. Rev. Lett. 36 (1976) 1113.
- [89] FNAL-E581, D. L. Adams et al., Phys. Lett. B261 (1991) 201.
- [90] FNAL-E704, D. L. Adams et al., Phys. Lett. B264 (1991) 462.
- [91] HERMES, A. Airapetian et al., Phys. Rev. Lett. 84 (2000) 4047.
- [92] HERMES, A. Airapetian et al., Phys. Rev. Lett. 94 (2005) 012002.
- [93] COMPASS, V. Yu. Alexakhin et al., Phys. Rev. Lett. 94 (2005) 202002.
- [94] PHENIX, S. S. Adler et al., Phys. Rev. Lett. 95 (2005) 202001.
- [95] STAR, J. Adams et al., Phys. Rev. Lett. 92 (2004) 171801.
- [96] STAR, B. I. Abelev et al., Phys. Rev. Lett. 101 (2008) 222001.
- [97] BRAHMS, I. Arsene et al., Phys. Rev. Lett. 101 (2008) 042001.
- [98] Belle, K. Abe et al., Phys. Rev. Lett. 96 (2006) 232002.
- [99] Belle, R. Seidl et al., Phys. Rev. D78 (2008) 032011.
- [100] S. Arnold et al., Phys. Rev. D79 (2009) 034005.
- [101] J. Zhou et al., [arXiv:0909.2238](https://arxiv.org/abs/0909.2238).
- [102] V. Barone et al., Phys. Rept. 359 (2002) 1.
- [103] NA10, S. Falciano et al., Z. Phys. C31 (1986) 513.
- [104] E. Anassontzis et al., Phys. Rev. D38 (1988) 1377.
- [105] J. S. Conway et al., Phys. Rev. D39 (1989) 92.
- [106] C. S. Lam et al., Phys. Rev. D18 (1978) 2447.
- [107] C. S. Lam et al., Phys. Rev. D21 (1980) 2712.
- [108] COMPASS, E. S. Ageev et al., Nucl. Phys. B765 (2007) 31.
- [109] COMPASS, M. Alekseev et al., Phys. Lett. B673 (2009) 127.
- [110] HERMES, M. Diefenthaler, doi:10.3360/dis.2007.91.
- [111] M. Anselmino et al., Nucl. Phys. Proc. Suppl. 191 (2009) 98.
- [112] HERMES, A. Airapetian et al., Phys. Rev. Lett. 103 (2009) 152002.
- [113] M. Anselmino et al., Eur. Phys. J. A39 (2009) 89.

- [114] COMPASS, in preparation.
- [115] COMPASS, S. Levorato, in *Proceedings of Transversity 2008*: II International Workshop on Transverse Polarization Phenomena in Hard Scattering Processes, 27–31 May 2008, Ferrara, Italy; World Scientific, ed. by G. Ciullo et al., April 2009, ISBN: 978-981-4277-77-8, p. 49, [arXiv:0808.0086](https://arxiv.org/abs/0808.0086).
- [116] A. Kotzinian, COMPASS Note 2010-2, February 10, 2010,  
[http://wwwcompass.cern.ch/compass/notes\\_public/2010-2.pdf](http://wwwcompass.cern.ch/compass/notes_public/2010-2.pdf).
- [117] J. C. Collins et al., Phys. Rev. D16 (1977) 2219.
- [118] J. C. Collins, Phys. Lett. B536 (2002) 43.
- [119] M. Anselmino et al., Phys. Rev. D75 (2007) 054032.
- [120] M. Anselmino et al., Nucl. Phys. Proc. Suppl. 191 (2009) 98.
- [121] COMPASS, A. Kotzinian, [arXiv:0705.2402](https://arxiv.org/abs/0705.2402).
- [122] NA10, S. Guanziroli et al., Z. Phys. C 37 (1988) 545.
- [123] FNAL-E866/NuSea, L. Zhu et al., Phys. Rev. Lett. 99.
- [124] FNAL-E866/NuSea, L. Zhu et al., Phys. Rev. Lett. 102.
- [125] Z. Lu et al., Phys. Rev. D81 (2010) 034023.
- [126] COMPASS, A. Bressan, *To appear in*: Proceedings of 17th International Workshop on Deep-Inelastic Scattering and Related Subjects (DIS 2009), Madrid, Spain, 26–30 April, 2009, [arXiv:0907.5511](https://arxiv.org/abs/0907.5511).
- [127] R. Vogt, Phys. Rept. 310 (1999) 197.
- [128] M. Anselmino et al., Phys. Lett. B594 (2004) 97.
- [129] V. Barone et al., Eur. Phys. J. C49 (2007) 967.
- [130] A. Sissakian et al., Eur. Phys. J. C59 (2009) 659.
- [131] T. Sjostrand et al., PYTHIA 6.2 Physics and Manual, [hep-ph/0108264](https://arxiv.org/abs/hep-ph/0108264).
- [132] R. Brun et al., GEANT 3 Manual, CERN Program Library Long Writeup W5013 (1994).
- [133] COMPASS, P. Abbon et al., Nucl. Instrum. Meth. A577 (2007) 455.
- [134] M. Anselmino et al., Eur. Phys. J. A39 (2009) 89.
- [135] M. Chiosso et al., COMPASS Note 2010-4, April 13, 2010,  
[http://wwwcompass.cern.ch/compass/notes\\_public/2010-4.pdf](http://wwwcompass.cern.ch/compass/notes_public/2010-4.pdf).
- [136] P. Bordalo, PhD thesis, Centre d’Orsay, Universite Paris-Sud, 1986.
- [137] M. Anselmino et al., in *Proceedings of Transversity 2008*: II International Workshop on Transverse Polarization Phenomena in Hard Scattering Processes, 27–31 May 2008, Ferrara, Italy; World Scientific, ed. by G. Ciullo et al., April 2009, ISBN: 978-981-4277-77-8, p. 138.
- [138] D. Boer, Phys. Rev. D60 (1999) 014012.
- [139] B. Zhang et al., Phys. Rev. D77 (2008) 054011.
- [140] V. Barone et al., Phys. Rev. D56 (1997) 527.
- [141] A. V. Efremov et al., Phys. Lett. B612 (2005) 233.
- [142] J. C. Collins et al., Phys. Rev. D73 (2006) 014021.
- [143] A. Bianconi et al., Phys. Rev. D73 (2006) 114002.
- [144] A. Bacchetta et al., Phys. Rev. D78 (2008) 074010.
- [145] NA3, J. Badier et al., Z. Phys. C20 (1983) 101.
- [146] NA50, B. Alessandro et al., Eur. Phys. J. C48 (2006) 329.
- [147] RICH Spin, [http://spin.riken.bnl.gov/rsc/write-up/dy\\_final.pdf](http://spin.riken.bnl.gov/rsc/write-up/dy_final.pdf).
- [148] Y. Goto et al., <http://indico.cern.ch/conferenceDisplay.py?confId=85721>.
- [149] FNAL-E906, <http://www.phy.anl.gov/mep/drell-yan/index.html>.
- [150] J-PARC, [http://j-parc.jp/NuclPart/Proposal\\_e.html](http://j-parc.jp/NuclPart/Proposal_e.html).

- [151] PAX, V. Barone et al., [arXiv:hep-ex/0505054](https://arxiv.org/abs/hep-ex/0505054).
- [152] PANDA, [http://www-panda.gsi.de/auto\\_home.htm](http://www-panda.gsi.de/auto_home.htm).
- [153] NICA, <http://nica.jinr.ru/>.
- [154] J. Gasser et al., Ann. Phys. 158 (1984) 142.
- [155] J. Bijnens, in *Proceedings of CD'09*, Bern, 2009, [arXiv:0909.4635](https://arxiv.org/abs/0909.4635).
- [156] J. Gasser et al., Nucl. Phys. B745 (2006) 84.
- [157] N. Kaiser et al., Eur. Phys. J. A36 (2008) 181.
- [158] J. Portoles et al., in *The 2<sup>nd</sup> DaΦne Physics Handbook*, [arXiv:hep-ph/9407295](https://arxiv.org/abs/hep-ph/9407295).
- [159] C. A. Wilmot et al., Phys. Rev. C65 (2002) 035206.
- [160] L. V. Fil'kov et al., Phys. Rev. C73 (2006) 035210.
- [161] B. Pasquini et al., in *Proceedings of CD'09*, Bern, 2009, [arXiv:0908.4291](https://arxiv.org/abs/0908.4291).
- [162] L. Fil'kov et al., in *Proceedings of CD'09*, Bern, 2009, [arXiv:0909.4849](https://arxiv.org/abs/0909.4849).
- [163] I. Y. Pomeranchuk et al., Nucl. Phys. 23 (1961) 452.
- [164] N. Kaiser et al., Nucl. Phys. A812 (2008) 186.
- [165] N. Kaiser et al., Eur. Phys. J. A39 (2009) 71.
- [166] G. Fäldt et al., Phys. Rev. C79 (2009) 014607.
- [167] Th. Walcher, Prog. Part. Nucl. Phys. 61 (2008) 106.
- [168] Y. M. Antipov et al., Phys. Lett. B121 (1983) 445.
- [169] Y. M. Antipov et al., Phys. Rev. D36 (1987) 21.
- [170] C. Bernet et al., Nucl. Instrum. and Meth. A 550 (2005) 217.
- [171] V. Polyakov, [https://espace.cern.ch/na58-mgt-tb/Technical%20Board/Lists/Agenda/Attachments/108/ECAL12\\_upgrade\\_jan2009.pdf](https://espace.cern.ch/na58-mgt-tb/Technical%20Board/Lists/Agenda/Attachments/108/ECAL12_upgrade_jan2009.pdf).
- [172] Z. Sadigov, Russian Patent No. 2316848, 01.06.2006, <http://www.zecotek.com>.
- [173] N. Anfimov et al., JINR preprint E13-2009-87, 2009, subm. to Nucl. Instrum. Meth.
- [174] General safety instruction “area classification”, RGE section 9/S3-GSI1, No EDMS 810149 (December 2006).
- [175] G. Battistoni et al., AIP Conference Proceeding 896 (2007) 31.
- [176] A. Fassó et al., CERN-2005-10.
- [177] G. Dumont, CERN-SC-2007-092-RP-TN.
- [178] COMPASS Collaboration, G. Baum et al., Compass: A proposal for a COmmon Muon and Proton Apparatus for Structure and Spectroscopy, CERN/SPSLC 96-14, SPSC/P 297 (March 1996).
- [179] J. Ball et al., Nucl. Instrum. and Meth. A 498 (2003) 101.
- [180] K. Kondo et al., Nucl. Instrum. and Meth. A 526 (2004) 70.
- [181] N. Doshita et al., Nucl. Instrum. and Meth. A 526 (2004) 138.
- [182] E. Albrecht et al., Nucl. Instrum. and Meth. A 553 (2005) 215, and references therein.
- [183] P. Abbon et al., Nucl. Instrum. and Meth. A, doi:10.1016/j.nima.2010.02.069.
- [184] P. Abbon et al., Nucl. Instrum. Meth. A587 (2008) 371.
- [185] RD26 Collaboration, RD26 status report, CERN/DRDC 93-36 (1993).
- [186] ALICE Collaboration, Detector for high momentum PID, technical design report, CERN/LHCC 98-19 (August 1998).
- [187] F. Piuz, Nucl. Instrum. Meth. A502 (2003) 76.
- [188] P. Abbon et al., Nucl. Instrum. Meth. A567 (2006) 104.
- [189] M. J. French et al., Nucl. Instrum. and Meth. A 466 (2001) 359.
- [190] A. Braem et al., Nucl. Instrum. Meth. A553 (2005) 187.
- [191] H. Hoedlmoser et al., Nucl. Instrum. Meth. A574 (2007) 28.

- [192] R. Chechik et al., Nucl. Instrum. Meth. A535 (2004) 303.
- [193] R. Chechik et al., Nucl. Instrum. Meth. A553 (2005) 35.
- [194] C. Shalem et al., Nucl. Instrum. Meth. A558 (2006) 475.
- [195] J. M. Bidault et al., Nucl. Phys. Proc. Suppl. 158 (2006) 199.
- [196] A. Kozlov et al., Nucl. Instrum. Meth. A523 (2004) 345.
- [197] Z. Fraenkel et al., Nucl. Instrum. Meth. A546 (2005) 466.
- [198] A. Milov et al., J. Phys. G34 (2007) S701.
- [199] F. Sauli, Nucl. Instrum. and Meth. A 386 (1997) 531.
- [200] M. Alexeev et al., Nucl. Instrum. Meth. A610 (2009) 174.
- [201] M. Alexeev et al., doi:10.1016/j.nima.2009.08.087; subm. to Nucl. Instrum. Meth.
- [202] M. Alexeev et al., doi:10.1016/j.nima.2010.02.171; subm. to Nucl. Instrum. Meth.
- [203] E. Rocco, Ph.D. thesis, University of Torino, Torino, Italy (2010).